Optimal Control for Quantum Sensing with Spins in Crystal

Inaugural-Dissertation
zur
Erlangung des Doktorgrades
der Mathematisch-Naturwissenschaftlichen Fakultät
der Universität zu Köln

vorgelegt von

Thomas Reisser

aus

Ulm

Köln, 2024

Berichterstatter:	Prof. Dr. Tommaso Calarco
(Gutachter)	Prof. Dr. Frank Wilhelm-Mauch
Tag der mündl. Prüfung:	19.12.2024
Vorsitzender:	Prof. Dr. Paul van Loosdrecht
Beisitzer:	Dr. Matthias M. Müller

Diese Dissertation wurde von der Mathematisch-Naturwissenschaftlichen Fakultät der Universität zu Köln angenommen.

Abstract

The precise control of quantum systems is crucial for, e.g., the implementation of gate operations, to prepare specific quantum states, or to enhance the sensitivity or polarization for quantum sensing. To tackle such challenges, quantum optimal control (QOC) provides a set of tools in order to bring quantum technologies to their full potential. Electromagnetic fields are used to manipulate and guide the state of quantum systems for specific purposes. QOC shapes these fields in order to perform quantum gates and circuits used for quantum sensing, computing or simulation applications.

This thesis revolves around the development of control strategies, with a focus on spins in crystals used predominantly for quantum sensing and metrology applications. I will have a look at polarization techniques under elaborate experimental conditions, the assessment of gate evaluation metrics, and the development of a software package for practical utilization on optimization problems in simulation and experiment.

In particular, I present a strategy to speed up and increase the polarization of protons in a naphthalene crystal through dynamic nuclear polarization from the optically accessible electron spin of pentacene molecules [1]. Due to a complex experimental setup, involving a microwave cavity and various coupling parameters, we use closed-loop control to optimize the applied microwave pulse shapes. The resulting protocol enables an efficient strategy for enhanced macroscopic hyperpolarization of the sample for use in nuclear magnetic resonance experiments, that can potentially be transferred to different experimental scenarios.

Control strategies need to be viewed in the context of experimental constraints and the control hyperparameters have to be tuned together with the specific control problem. We therefore created a software package called the Quantum Optimal Control Suite (QuOCS) in Python, to provide a unified framework for the development of control algorithms [2]. Its modular and open-source nature enables a straightforward extension with new ideas. It is easy to use and thus lowers the hurdle to make use of QOC for a wide range of problems. We discuss its features and show examples for the application through open-loop optimizations based on simulation as well as closed-loop control with communication to an experiment.

The software is then used to investigate various gate and gate-set evaluation metrics for their suitability in closed-loop optimization [3]. An ensemble of nitrogen vacancy centers in diamond serves as the experimental test-bed for control objectives derived from methods such as quantum process tomography, gate-set tomography and randomized benchmarking. It becomes clear that gate operations have to be viewed in the context of their application and an extensive cross-comparison provides a better understanding for the choice among the tested methods for control tasks.

This thesis follows a path from the importance of a clever approach to a control problem, over the relevance of the employed control algorithm and supporting features, to the choice of the correct figure of merit that best encodes the important information.

Contents

1 Introduction

This thesis is written in a time where the use of quantum systems is transitioning from fundamental research and proof-of-concept implementations to real-life applications. To the established devices such as transistors, lasers, QLEDs, atomic clocks, solar cells, MRI scanners and electron microscopes, more and more technologies based on quantum mechanics join the party. Often called the second quantum revolution, the understanding of quantum effects in bulk material is advancing to the control of single atoms, molecules and spins. Advances in each of the four pillars of quantum technology, namely quantum computing, quantum simulation, quantum communication and cryptography, and quantum sensing (and metrology), can be found aplenty. Accessible quantum computers are available from companies such as IBM, Google, IonQ, QuiX, D-Wave, Quantum Brilliance, XeedQ, PASQUAL, Rigetti and Xanadu and quantum processors can reach numbers of more than 1,000 physical qubits [4, 5]. Several claims for quantum advantage over classical computers have been made in the past years [6–9] but were later retracted or disproved. In principle, Shor's algorithm [10] provides a significant speedup for the factorization of prime numbers that is needed to crack today's encryption methods. The current record for prime factorization on a quantum device was achieved using a D-Wave quantum annealer [11] for the number 8,219,999. What sets the quantum computer apart from it's classical pendant is superposition and entanglement. The hunt for ever growing entangled states [12–15] is happening on numerous platforms. More companies such as Daimler and Hyundai [16–18] are investigating methods of quantum simulation to explore, e.g., battery chemistry [19] to improve their performance and durability. Bosch has founded a start-up to focus on bringing quantum sensors for medical applications to the market [20, 21]. Quantum annealers like the D-Wave machines and Aquila from QuEra aim to find the ground state of a specifically configured quantum system that represents the solution to a real-life problem. In that way, flight gate assignment [22] and aircraft scheduling problems [23] can be cast into a Hamiltonian for which the lowest energy state corresponds to the optimal solution of the given task. Another task for quantum computers and simulators are calculations of proton folding [24, 25] which are relevant for the research of diseases and the development of medical drugs. Financial market applications such as portfolio optimization, risk assessment and price prediction sprout [26–29] and are investigated by researchers and companies alike. In order to share secrets such that even the most powerful supercomputers can not refactor the information, quantum cryptography [30–32] and communication [33] can be used. They spark interest in security companies and the military and may even be included in the electronics of mobile phones in the form of random number generators in the near future. Finally, quantum sensing [34–37] can enhance the detection of very weak signals to a high precision used, e.g., for medical applications and biosensors or the detection of particles in real time [38]. Quantum metrology [39–41], on the other hand, focuses on the measurement of physical parameters and constants to ever higher accuracy.

In order to overcome some of the obstacles and pave the way towards the realization and improvement of these technologies, it becomes apparent that precise control of the used quantum system, and the operations performed on it, is a must. The fundamental physics of the most widely used quantum systems is usually well understood [42]. It is the interaction of the system with it's environment that leads to errors in the state preparation, the execution of state manipulations and the preservation of quantum information. To be able to manipulate the state of a

system and interact with it, it has to be sensitive to electromagnetic fields. These fields are used to drive transitions between different states in the energy spectrum and couple to other systems in order to exchange information. However, if such interactions happen unintentionally it can lead to, e.g., the loss of coherence, the decay of a state into another, or leakage to undesired subspaces. The sources of these detrimental effects can either be inherent to the system due to the nature of its properties, they can be introduced during its fabrication or unavoidably occurring defects or vibrations in the surrounding host material, or can be caused by imperfections and fluctuations of the electronics used for the control and read-out [43, 44]. Typically, the quantum systems are controlled by irradiation with laser light, oscillating microwave of radio-frequency fields, or potential wells in order to trap, move and excite particles. Since these controls are not just static values but are varied over time, their exact modulation is crucial for the success of a desired operation. To find the optimal way to design these controls, Quantum Optimal Control (QOC) offers a set of methods and strategies to accomplish the implementation of an operation on a quantum system in the best way possible [45]. These controls can be constant but variable parameters such as bias voltages, dwell times and laser attenuation or time-dependent functions of, e.g., the amplitude for a voltage ramp [46]. By the definition of a quality or cost functional that depends on the provided controls and the fidelity of the resulting action, a number of algorithms can be employed to find an optimal solution [47]. Depending on the problem at hand and the amount of knowledge about the system, the methods can range from analytical solutions over numerical approaches to black-box optimization. If a trustworthy model of the system can be written down in equations, gradient-based optimization has proven very effective for open-loop optimization, where the controls are found in simulation [48]. To take specific properties of the conditions in the lab or on a machine into account, closed-loop optimization with information from measurements on an experimental setup can be performed.

In this thesis, we want to focus on the latter part of closed-loop QOC in particular and see, how it can be applied in the laboratory using two different quantum systems [1, 3] in combination with specifically for this purpose developed control software [2]. Chapter 2 gives an introduction to QOC, followed by an overview of gate evaluation metrics. The nitrogen vacancy center in diamond is discussed and some applications are illustrated. On the example of pentacene in naphthalene, methods for dynamic nuclear polarization are explained and the system is extended with a cavity. Equipped with this knowledge, the first publication in Chapter 3.1 shows our advances in the polarization of the protons in naphthalene molecules through the optically accessible pentacene electron spin. Closed-loop optimization of the applied microwave pulses lead to the development of a protocol called ARISE to facilitate the design and optimization of hyperpolarization sequences. In Chapter 3.2, the Quantum Optimal Control Suite (QuOCS) is highlighted, its features are explained and some application examples are demonstrated. Finally, the work shown in Chapter 3.3 investigates the suitability and properties of gate and gate-set evaluation metrics for their use in closed-loop optimization through experiments using a nitrogen vacancy ensemble in diamond.

2 Fundamentals and Methods

This chapter introduces the fundamental concepts of the investigated quantum systems and the methods used for the theoretical understanding, simulation and optimal control in this thesis.

2.1 Quantum Optimal Control

2.1.1 Control Theory

In the 17$^{\text{th}}$ century great minds like Galileo Galilei [49], Johann Bernoulli [50], Isaac Newton [51], Gottfried-Wilhelm Leibniz [52] and Marquis de l'Hôpital [53] were already concerned with optimal control problems. Bernoulli proposed one of the first and most famous optimal control problems, later to become known as the brachistochrone problem. Similar to a problem that Galilei discusses 58 years earlier, he wants to find the fastest way to get from one point to a lower point in space under gravity in the shortest time possible. Not unlike today's problems, where we often want to navigate through the state-space of a quantum system [54], this problem can be tackled by variational calculus and optimal control. One of the fundamental theorems for modern control theory is Pontryagin's maximum principle, that connects the solution of an optimization problem to the Hamiltonian description of the system [55].

A quantum system in the simplest case is usually described by two parts: the drift Hamiltonian $H_d(t)$ and control Hamiltonians $H_{c,i}(t)$, which both might depend on time. The drift Hamiltonian describes the dynamics of the system itself left alone or possibly under external fields that cannot be manipulated directly. The control part describes external perturbations that can be shaped in order to execute an operation or stir the system in a desired direction. The evolution of the whole system is then governed by

$$H(t) = H_d(t) + \sum_i u_i(t) \cdot H_{c,i}(t) \tag{2.1}$$

with the control amplitudes $u_i(t)$. Assuming Eq. (2.1) contains the full description of the system, the time evolution of a state $\rho = \sum_j p_j |\psi_j\rangle\langle\psi_j|$ with $\sum_j p_j = 1$ can be written as the Liouville-von Neumann equation [56]

$$\frac{\partial}{\partial t}\rho = \frac{i}{\hbar}\left[\rho, H(t)\right] \tag{2.2}$$

where from now on we are going to set $\hbar = 1$. Markovian as well as non-Markovian effects can be included via Lindblad operators, Kraus operators or linear maps (see Secs. 2.2 and 3.1). The time-evolution in a closed system can be expressed by the transformation of an initial state $\rho_0 = \rho(t = 0)$ with a unitary operator U such that

$$\rho(T) = U\,\rho_0\,U^\dagger \tag{2.3}$$

where the unitary gate is a solution of Eq. (2.2). This connects the control functions $u_i(t)$ to the resulting final state under their influence and the effective action performed on the system.

In order to fully state the control problem, we now need to define the cost functional $J\left(\rho_0, \{u_i(t)\}, t\right)$

as the control objective that needs to be minimized to obtain the optimal solution for the given control task. It is in general a functional of the initial state, the controls and the time. Ideally, it is a convex and steady function with a single global minimum and can encode information about the state of the system and the fidelity of operations on it, as is discussed in the next section.

2.1.2 Control Objectives: The Figure of Merit

The control objectives include any condition that needs to be fulfilled to achieve a successful operation. The cost functional for quantum control is mostly called the Figure of Merit (FoM) and contains any relevant information about the quality of the applied manipulation to the system and can be extended with additional conditions for constraints on the controls and the state of the system itself during the evolution. One of the most commonly used objectives is the fidelity F [57–59]. The definition of a fidelity changes depending on the context of its use. For example can the fidelity of a state overlap between two quantum states be written as

$$F_\psi = |\langle\, \psi \,|\, \xi \,\rangle|^2 \quad \text{or} \quad F_\rho = \left(\mathrm{tr}\left(\sqrt{\sqrt{\rho}\, \nu \sqrt{\rho}} \right) \right)^2 \tag{2.4}$$

where ψ and ρ are the evolved states and ξ and ν the targets. For unitary operations (gates) it can be formulated in terms of a gate fidelity

$$F_U = \frac{1}{N^2} \left| \mathrm{tr}\left(U^\dagger V \right) \right|^2 \tag{2.5}$$

where U is the control gate, V the target gate and N the dimension of the Hilbert space. This representation disregards global phases, since they often are not relevant on the experiment. A definition including the global phase can be made via

$$F_{U,\mathrm{Re}} = \frac{1}{N} \mathrm{Re}\Big[\mathrm{tr}\left(U^\dagger V \right) \Big] \,. \tag{2.6}$$

To get the discrepancy between any two matrices A and B, regardless of their properties such as unitarity, hermiticity or dimensions, the Frobenius norm of their difference can be used with

$$\mathrm{FoM}_{\mathrm{Frob}} = ||A - B||_{\mathrm{Frob}} = \sqrt{\sum_{k=1}^{m} \sum_{l=1}^{n} |A_{k,l} - B_{k,l}|^2} \tag{2.7}$$

as a quantity to be minimized. One can note that $\frac{1}{2N} \cdot ||U - V||^2_{\mathrm{Frob}} = 1 - F_{U,\mathrm{Re}}$ in the case of U and V being unitary. In optimization, it does not matter if the FoM is maximized or minimized. For consistency and due to conventions we are always going to define the FoM as a functional for minimization. Therefore, the appropriate FoM used to maximize fidelities is the infidelity $\mathcal{I} = 1 - F$, if the fidelity is properly normalized to always result in a value between 1 and 0.
However, more application-specific FoMs can be used as well. For sensing protocols the sensitivity can be optimized using Bayesian approaches [60] or the Fisher information [61]. Experimentally, other quality or performance measures such as the polarization of nuclei in a sample using, e.g., nuclear magnetic resonance (NMR) or the photoluminescence contrast for state preparation

can be used and appear in publications [1] and [2] and sections 3.1 and 3.2, respectively.

Most often several effects contribute to the total cost function. Thus, constraints or undesired effects can be added to the FoM using weighted penalty terms. These so-called Lagrange multipliers balance the gain of the fidelity and negative contributions and in the optimal case the infidelity as well as the penalty terms can be put to zero. These terms can include the population of "lossy" states during the time-evolution, large amplitude peaks of the control functions or the total energy pumped into the system (see fluence in Supplementary of Ref. [3]).

2.1.3 Control Algorithms

The goal of optimal control is to find controls such that the cost functional is minimized. This task can be done by numerous control algorithms of which some are summarized in this section, where we will focus on methods developed specifically for Quantum Optimal Control.

One method is the design of a perpendicular pulse so that it compensates for the errors introduced by the main pulse for a state transformation via the Derivative Removal by Adiabatic Gate (DRAG) [62–64]. It is specifically useful to suppress leakage to close levels outside of the computational subspace of the qubit.

Detailed knowledge about the quantum system and access to a reliable model opens up the possibility to calculate the gradient of the cost functional with respect to the control pulses. The development of optimal control algorithms for quantum systems to shape the control pulses using gradients started in the end of the 1980s by Rabitz and Tannor [65–67]. Krotov's method [57, 68–71] calculates sequential updates for the control pulses at different times by considering the overlap of a back-propagation with the old controls and a forward propagation with the new control functions. The slightly younger GRadient Ascend Pulse Engineering (GRAPE) [72] method uses the gradient of a performance function to update the controls at each time-discretized step in one iteration concurrently. This is done using two full time-evolutions, one forward and one backwards, and has its origins in NMR and electron paramagnetic resonance (EPR) applications [73, 74]. Those methods usually adapt the amplitudes of piece-wise constant pulses and can lead to sharp spikes that have large jumps between two adjacent time bins. The response time of the experimental hardware often imposes bandwidth limitations on the controls that have to be taken into account [75]. Extensions to generate smoother pulses have thus been developed [76, 77].

However, the calculation of an exact gradient of the figure of merit with respect to each control parameter is not always easy or efficient and can even be near impossible, e.g., in an experiment. Furthermore, methods that generate smooth, bandwidth-limited pulses by design can be favourable in many situations [78, 79]. The chopped random basis (CRAB) method aims to find such pulses without using gradient information [80, 81]. The controls are hereby expanded in a suitable basis of functions [82], like the Fourier basis or Chebyshev polynomials, that is truncated at some order to enforce bandwidth restrictions. The remaining function space is then chopped into smaller pieces and one specific basis function is selected randomly from each piece. This strategy allows for an improved convergence of the algorithm [80]. Each basis element is assigned one (or more) parameters such as their amplitude of how much they contribute in the

composition of the final pulse. A control pulse with CRAB can then be written in the form

$$u_i(t)_{\mathrm{CRAB}} = g(t) + \sum_{k=1}^{N_b} c_{1,k} \sin(\nu_k t) + c_{2,k} \cos(\nu_k t) \tag{2.8}$$

in the case of the Fourier basis. The update pulse composed of sine and cosine functions on the interval $\left[\frac{2\pi \cdot n^{\min}}{T}, \frac{2\pi \cdot n^{\max}}{T}\right]$ is added to a provided guess pulse $g(t)$. The integer N_b is the order of basis discretization, $n^{\min}$ and $n^{\max}$ define the frequency range (typically $n^{\min} = 0$) and $c_{1,k}$ and $c_{2,k}$ are variable parameters. These parameters are then optimized to minimize the FoM of the control problem using a suitable search method. By carefully selecting the number of basis elements to contain as little parameters as possible but give the shaped control pulse enough complexity to fulfil its purpose [83], the parameter-space can be kept to a minimum. In that way, even very simple gradient-free methods as the Nelder-Mead simplex search algorithm can be employed to find the best CRAB parameters. This advantage is especially useful for black-box-like optimization scenarios, such as closed-loop experimental control, where no analytical gradient is accessible and estimation would be too resource- and time-consuming. Although the CRAB method has led to advances in control for various platforms [84–86] the restrictions on the search-space can lead to false traps and local minima that are hard to escape from. In order to circumvent such problems and improve the convergence of the optimization, the method can be extended to what is called the dressed CRAB (dCRAB) algorithm [59, 87]. Instead of just using one instance of a randomized basis, the optimization can be restarted once the current control parameters have resided in a (possibly local) optimum. Keeping the so far improved pulse shape, the controls can be updated with a fresh set of newly randomized basis vectors in what is called a new super-iteration (SI). Similar to Eq. (2.8) the control pulse can then be written as

$$u_i(t)_{\mathrm{dCRAB}} = g(t) + \sum_{j=1}^{N_{\mathrm{SI}}} \sum_{k=1}^{N_b} c_{1,k}^{(j)} \sin\left(\nu_k^{(j)} t\right) + c_{2,k}^{(j)} \cos\left(\nu_k^{(j)} t\right) \tag{2.9}$$

where N_{SI} is the number of super-iterations. This changes the shape of the parameter landscape and enables the algorithm to escape local minima and false traps to converge to a global optimum, given the pulse restrictions and number of optimization steps. Successful usage examples of the dCRAB method can be found for numerous quantum platforms [1, 3, 14, 88–94], which have to deal with their own methodological or experimental oddities. Strategies to make this powerful algorithm easily accessible and support the user with features to cope with experiment-specific constraints and nuisances are provided in publication [2] and Sec. 3.2 of this thesis.
Naturally, gradient information can still be leveraged to improve the search for the optimal expansion parameters [76]. Methods like gradient optimization using parameterization (GROUP) [95], gradient optimization of analytic controls (GOAT) [96] and gradient ascent in function space (GRAFS) [97] aim to combine the idea of CRAB expansions with efficient gradient-based optimization. Automatic differentiation (AD) has become popular in the machine learning community [98] and the availability of many libraries, e.g., in Python such as PyTorch, TensorFlow, and JAX or for Julia (see [99]) help to further advance numerical optimization [100, 101].

Now that we have seen how operations on quantum systems can be optimized, the question

arises: "How do we extract information about the quality of a quantum operation?". This question is tackled in the next section.

2.2 Gate Evaluation Metrics

In Sec. 2.1.2 we have already seen the state and gate fidelity that can be used to assess how well they overlap with a target. This, however, assumes the knowledge of the full state or matrix representing the unitary quantum gates and is usually only accessible in calculations or simulation. In this section, we want to have a look at a more general description of quantum operations and processes and how they can be extracted and estimated by measurements on the system.

To make meaningful use of the system, one needs to be able to implement several gates that can be combined into quantum circuits, i.e. sequences of gates, that perform a desired task. We will call such a gate-set $\mathcal{G}$ and it can contain any gate that you can perform on the system, such as for example

$$\begin{aligned}\mathcal{G} &= \{G_0, G_1, G_2, G_3, G_4, G_5, G_6\} \\ &= \{\mathbb{1}, \mathcal{X}_{\pi/2}, \mathcal{Y}_{\pi/2}, \mathcal{X}_{\pi}, \mathcal{H}, \mathcal{S}\}\,.\end{aligned} \tag{2.10}$$

Here, the identity $\mathbb{1}$ is sometimes also called the null gate and denoted with $\{\}$ to signify that it means to "do nothing for no time" [102]. Its purpose is to simplify the equations later in this section. The $\mathcal{X}$ and $\mathcal{Y}$ gates are called Pauli gates and denote rotations of a qubit about the x- or y-axis as generated by the spin-$\frac{1}{2}$ operators $S_x = \frac{1}{2}\sigma_x$ and $S_y = \frac{1}{2}\sigma_y$, where σ_x and σ_y are the respective Pauli matrices. The index indicates the angle of rotation so that we get, e.g.,

$$\mathcal{X}_{\varphi} = e^{-i\varphi S_x}\,. \tag{2.11}$$

The Hadamard gate $\mathcal{H}$ is basically a rotation about the axis $(x+z)/\sqrt{2}$ on the Bloch sphere and transforms the pure states $|0\rangle$ and $|1\rangle$ into equal superpositions with an opposite phase. The phase gate $\mathcal{S}$ is a rotation of $\frac{\pi}{2}$ about the z-axis. Both gates can be decomposed into Pauli gates [103] as done in Sec. 3.3.

In order to have the minimum set of gates needed to prepare any relevant state, we define

$$\begin{aligned}\mathcal{F} &= \{F_0, F_1, F_2, F_3\} \\ &= \{G_0, G_1, G_2, G_3\}\,.\end{aligned} \tag{2.12}$$

It is also needed for the readout of specific components of a state. These state preparation and measurement (SPAM) gates are often also called the fiducials and the gate-set in Eq.(2.10) can be named the germs [104].

The description of quantum operations as gates is sufficient if everything is perfectly unitary. But in real life and on experimental setups noise sources acting on the system and the controls can cause incoherent and statistical errors that do not preserve the unitarity, since most of the times the full environment can not be considered. A way to elegantly represent such effects into the description of a quantum process is the process matrix formulation discussed in the following

section.

2.2.1 Quantum Maps

Operations on quantum systems can be represented by linear maps $\Lambda : \mathcal{H} \to \mathcal{H}$ with the Hilbert space $\mathcal{H} = \mathbb{C}^d$ of dimension d that act on a density operator and transform it to another state $\rho \mapsto \Lambda(\rho)$. Such a map can be written as

$$\Lambda(\rho) = \sum_{i=1}^{M} K_i \rho K_i^\dagger \tag{2.13}$$

which is called the operator-sum representation [105] with the so-called Kraus operators $\{K_i\}$ [106]. Since we want to describe a physical process, the density matrix should always stay positive semidefinite under this transformation. This is also called complete positivity (CP) and fulfilled if the linear map $\tilde{\Lambda} : \tilde{\mathcal{H}} \to \tilde{\mathcal{H}}$ acting on the extended Hilbert space $\tilde{\mathcal{H}} = \mathcal{H} \otimes \mathcal{H}'$ with any other space $\mathcal{H}'$ acts only on the original subspace, i.e $\tilde{\Lambda}(\rho \otimes \rho') = \Lambda(\rho) \otimes \rho'$ [107]. Usually, we also want to preserve the trace of ρ and this trace preservation (TP) is achieved by the completeness condition

$$\sum_{i=1}^{M} K_i^\dagger K_i = \mathbb{1} \tag{2.14}$$

on the Kraus operators [102]. Such maps can be used to describe the actions of gates directly but also be added on top to represent effects of noise that, e.g., lead to the depolarizing channel with

$$K_1 = \sqrt{1 - \frac{3p}{4}} \cdot \mathbb{1}\,, \quad K_2 = \sqrt{\frac{p}{4}} \cdot \sigma_x\,, \quad K_3 = \sqrt{\frac{p}{4}} \cdot \sigma_y\,, \quad K_4 = \sqrt{\frac{p}{4}} \cdot \sigma_z \tag{2.15}$$

which shrinks the length of the Bloch vector so that for $p = 1$ the system ends up in a completely mixed state.
The CPTP map in Eq. (2.13) can be extended by writing the Kraus operators K_i in terms of a fixed set of operators that form a basis for the set of operators acting on ρ [105]. These can be the Pauli matrices $P_j \in \mathcal{P} = \mathbb{1}, \sigma_x, -i\sigma_y, \sigma_z$ so that we write

$$\Lambda(\rho) = \sum_{j,k=1}^{d^2} \chi_{jk}\, P_j \rho P_k^\dagger\,. \tag{2.16}$$

This form is called the chi matrix representation and we will call χ the process matrix. If the Kraus operators are written as $K_i = \sum_{j=1}^{d^2} c_{ij} P_j$ then chi is $\chi_{jk} = \sum_i c_{ij} c_{ik}^*$. The process matrix has the advantage that the full effect of a quantum process can be captured and described by a single matrix, i.e. the action of the gate itself plus phenomena like decoherence and relaxation to the ground state.

This leads us to the question of how to determine the transformation that an unknown quantum operation or a set of operations induce in a system by performing measurements on said system.

2.2.2 Tomography

Quantum Process Tomography

A well known method that uses state tomography to determine the process matrix of a quantum operation is called quantum process tomography (QPT). Following Ref. [105], for a single qubit this can be done by the preparation of the input states

$$|0\rangle\,,\quad |1\rangle\,,\quad |x\rangle = \frac{1}{\sqrt{2}}\left(|0\rangle + |1\rangle\right) \quad \text{and} \quad |y\rangle = \frac{1}{\sqrt{2}}\left(|0\rangle + i|1\rangle\right) \tag{2.17}$$

via application of the appropriate fiducials on the state that can be prepared reliably on the system (usually $|0\rangle$). For example can $|y\rangle$ be prepared by the application of a $\mathcal{X}_{\pi/2}$ gate on $|0\rangle$ which is the SPAM gate F_1 in the set defined in Eq. (2.12). Then the resulting output states under the operation of interest are recorded as

$$\begin{aligned}
\rho_1' &= \Lambda(|0\rangle\langle 0|) \\
\rho_2' &= \Lambda(|x\rangle\langle x|) - i\Lambda(|y\rangle\langle y|) - \frac{(1-i)}{2}(\rho_1' + \rho_4') \\
\rho_3' &= \Lambda(|x\rangle\langle x|) + i\Lambda(|y\rangle\langle y|) - \frac{(1+i)}{2}(\rho_1' + \rho_4') \\
\rho_4' &= \Lambda(|1\rangle\langle 1|)
\end{aligned} \tag{2.18}$$

which have to be mapped out by state tomography [108]. This can again be done using the SPAM-set in Eq. (2.12) to determine the projection along each axis of the state on the Bloch sphere by rotating it to the z-axis, assuming this is the accessible observable. Therefore, measurements of the type

$$p_{ij} = \langle\langle E|F_i G_{\text{tomog}} F_j|\rho\rangle\rangle \tag{2.19}$$

are used, where F_j prepares the states in Eq (2.17), the application of the gate of interest G_{tomog} is the Λ in Eq. (2.18) and the F_i are used to determine the resulting state. The double brackets $\langle\langle\cdot|$ denote that we take the density matrices and operators in Hilbert-Schmidt space to simplify the notation (see Refs. [3, 102] and Sec. 3.3). The initially prepared density matrix $|\rho\rangle\rangle$ is evolved by the gates and SPAM gates and projected onto the measurement operator $\langle\langle E|$. From the specific choice of operators for Eq. (2.16) and the set of experiments in Eq. (2.18) that map

$$\rho_1 = |0\rangle\langle 0|\,,\quad \rho_2 = \rho_1 \cdot \sigma_x\,,\quad \rho_3 = \sigma_x \cdot \rho_1 \quad \text{and} \quad \rho_4 = \sigma_x \cdot \rho_1 \cdot \sigma_x \tag{2.20}$$

such that $\rho_j' = \Lambda(\rho_j)$ for $j = 1, 2, 3, 4$, a convenient expression for the process matrix can be found as

$$\chi = \Theta \begin{bmatrix} \rho_1' & \rho_2' \\ \rho_3' & \rho_4' \end{bmatrix} \Theta \qquad \text{with} \qquad \Theta = \frac{1}{2}\begin{bmatrix} \mathbb{1} & \sigma_x \\ \sigma_x & -\mathbb{1} \end{bmatrix}. \tag{2.21}$$

Repeating these measurements for all gates in the gate-set $\mathcal{G}$ can be used to characterize the whole set. However, in QPT the SPAM-set is assumed to be faultless and all errors are attributed to the investigated gate. If the SPAM gates are already imperfect, this can lead to false estimates

of the process matrix. A method that analyzes the whole gate-set holistically, also acknowledging errors and noise in the SPAM-set, is called gate-set tomography (GST). Therefore, some variants of GST are discussed in the next sections.

Linear Inversion Gate-Set Tomography

Gate-set tomography can be used to estimate the total gate-set as a whole, including the state that is prepared and the state for projective measurement. Linear inversion gate-set tomography (LGST) is similar to QPT. Instead of measuring the effects of a single gate, we sandwich all gates in our gate-set between every possible combination of state preparation and measurement to obtain the expectation values

$$p_{ijk} = \langle\langle E|F_i G_k F_j|\rho\rangle\rangle = \left(\tilde{G}_k\right)_{ij} \tag{2.22}$$

and define $\left(|\tilde{\rho}\rangle\rangle\right)_i = \langle\langle E|F_i|\rho\rangle\rangle = \left(\langle\langle\tilde{E}|\right)_i$. The quantities marked with a tilde then contain the sorted, recorded expectation values. We have selected the first gate of $\mathcal{G}$ as the identity or null gate, which by definition does not do anything, so we can use it to convert the measured expectations values back to matrices that represent gate operations. Since $\tilde{G}_0^{-1}\tilde{G}_0 \stackrel{!}{=} \mathbb{1}$ we can use the Gram matrix $g = \tilde{G}_0$ so that

$$\begin{aligned} \hat{G}_k &= g^{-1}\tilde{G}_k \\ |\hat{\rho}\rangle\rangle &= g^{-1}|\tilde{\rho}\rangle\rangle \\ \langle\langle\hat{E}| &= \langle\langle\tilde{E}| \,. \end{aligned} \tag{2.23}$$

The gates and states obtained in this way can be in a different gauge from the definitions in Eq. (2.10) and Eq. (2.12). For the systems considered in this thesis, the z-axis is typically defined through the experimental preparation and readout procedure. However, x and y are arbitrary and only given by a relative phase shift of $\pi/2$. A global rotation of the coordinate system can thus lead to the same expectation values for two different sets of gates, if they can be related by a gauge transformation $T'_k = \hat{B}^{-1}T_k\hat{B} \quad \forall k$. The sets $\{T_k\}$ and $\{T'_k\}$ are then called gauge invariant. Therefore, such a gauge transformation $\hat{B}$ is used to match the estimates as close as possible to the target definitions in the gate-set via

$$\hat{B}^* = \underset{\hat{B}}{\operatorname{argmin}} \sum_{k=1}^{K+1} \operatorname{Tr}\left\{ \left(\hat{G}_k - \hat{B}^{-1}T_k\hat{B}\right)^\dagger \left(\hat{G}_k - \hat{B}^{-1}T_k\hat{B}\right) \right\} \tag{2.24}$$

with the $K+1^{th}$ gate defined to be $|\rho\rangle\rangle\langle\langle E|$. The final estimates by LGST are then given by the optimized gauge matrix $\hat{B}^*$ via

$$\hat{G}_k^* = \hat{B}^*\hat{G}_K\left(\hat{B}^*\right)^{-1} \qquad |\hat{\rho}^*\rangle\rangle = \hat{B}^*|\hat{\rho}\rangle\rangle \quad \text{and} \quad \langle\langle\hat{E}^*| = \langle\langle\hat{E}|\left(\hat{B}^*\right)^{-1} \,. \tag{2.25}$$

At this point we could use the starred estimates to understand the gate-set at hand and its actions. However, these gates and states are in general not physically correct, i.e. not normalized and unitary, which is no surprise because they are build up from noisy measurement data and

can't represent decoherence effects properly. For this reason, typically process matrices are reconstructed from the values in Eq. (2.22) using the estimates of Eq. (2.25) with a maximum likelihood estimation.

Maximum Likelihood Estimation

In the context of gate-set tomography, the maximum likelihood estimation (MLE) aims to find the most likely and physical description of the prepared states, projection operators and actions of the quantum operations on the system. Especially for the LGST method described above, where all entities are reconstructed from "noisy" measurements, the closest estimate to a physical representation of the system is desired. A suitable likelihood function for the LGST measurements can be written with a normal distribution as [102]

$$\mathcal{L}\left(\hat{\mathcal{G}}\right) = \prod_{ijk} \exp\left(-\left(p_{ijk} - \hat{p}_{ijk}(\vec{\xi})\right)^2 / \sigma_{ijk}^2\right) \tag{2.26}$$

where p_{ijk} describes the measured values, $\hat{p}_{ijk}(\vec{\xi})$ the estimators expressed through a parameterization with the parameters $\vec{\xi}$, and σ_{ijk} being the sampling variance of the measurement. A maximization of this likelihood function is then the same as minimizing the negative logarithm of $\mathcal{L}$. Written in terms of process matrices this results in the minimization of the least-squares problem

$$l\left(\hat{\mathcal{G}}\right) = \sum_{ijk}\left(p_{ijk} - \sum_{mnrstu} \left(\chi_{F_i}\right)_{tu} \left(\chi_{G_k}\right)_{rs} \left(\chi_{F_j}\right)_{mn} \mathrm{Tr}\{E P_t P_r P_m \rho P_n P_s P_u\}\right)^2 / \sigma_{ijk} \tag{2.27}$$

where ρ, E, and all χ depend on $\vec{\xi}$. A parameterization for the maximally likely initially prepared state, the state onto which the measurements projects and the actions of the gates can be done via a concatenation of several Kraus maps that describe rotations on the Bloch sphere and effects like decoherence. These can then be combined in the process matrix or expression of the states in Eq. (2.27). Using the guesses obtained from Eq. (2.25) these expansion parameters $\vec{t}$ can then be found through a suitable minimization method implemented in packages such as `SciPy` or `Optim.jl`, depending on the used programming language. Unfortunately, these minimizations usually take several minutes on standard hardware [104, 109, 110] so the procedure can be impractical for a closed-loop optimization.

Randomized Linear Gate-Set Tomography

A strategy that does not rely on the rigorous definition of fixed and predetermined circuits is randomized linear gate-set tomography (RLGST) [111]. It aims to find the error matrices e_k or noise maps for a set of gates as well as $\hat{\rho}$ and $\hat{E}$. To this end, following Ref. [111], the noise maps are defined as

$$\hat{G}_k = (\mathbb{1} + e_k) \cdot T_k\,, \qquad |\hat{\rho}\rangle\rangle = (\mathbb{1} + e_\rho) \cdot |\rho_T\rangle\rangle \quad \text{and} \quad |\hat{E}\rangle\rangle = (\mathbb{1} + e_E) \cdot |E_T\rangle\rangle \tag{2.28}$$

for a set of gates $\hat{\mathcal{G}}$ where T_k, $|\rho_T\rangle\rangle$ and $|E_T\rangle\rangle$ are the expected, ideal targets. Similarly to

Eq. (2.22) in LGST, a number N of gate-strings $\hat{\mathcal{C}}$ with the length L (number of gates in a gate-string) are generated randomly from the gate-set. In that sense the gate-strings can bee seen as a combination of state preparation, a subsequent operation on the state, and a measurement sequence before the readout

$$\hat{\mathcal{C}}^{(i)} = \underbrace{\hat{G}_{\gamma(L)} \cdot \hat{G}_{\gamma(L-1)} \cdot \hat{G}_{\gamma(L-2)} \cdots}_{\text{measurement}} \underbrace{\ldots \hat{G}_{\gamma(j+1)} \cdot \hat{G}_{\gamma(j)} \cdot \hat{G}_{\gamma(j-1)} \cdots}_{\text{operation}} \underbrace{\ldots \hat{G}_{\gamma(3)} \cdot \hat{G}_{\gamma(2)} \cdot \hat{G}_{\gamma(1)}}_{\text{preparation}} \,. \tag{2.29}$$

The lookup-table $\gamma(j) \to \{1, ..., |\mathcal{G}|\} \quad \forall j$ maps the randomized index $j = 1...L$ to the gates in the set $\mathcal{G}$ and takes care of the randomization. The number N of these gate-strings depends on the size of the gate-set and should be larger than the number of noise parameters, i.e. the number of entries in the error matrices. The expectation value of a "noisy" circuit $\hat{\mathcal{C}}$ can then be expanded as

$$\begin{aligned}
\hat{p}^{(i)} &= \langle\langle \hat{E} | \hat{\mathcal{C}}^{(i)} | \hat{\rho} \rangle\rangle \\
&= \langle\langle \mathcal{C}^{(i)} \rangle\rangle \\
&\quad + \langle\langle e_E \mathcal{C}^{(i)} + \sum_{j=1}^{L} T^{(i)}_{\gamma(L:k+1)} e_{\gamma(j)} T^{(i)}_{\gamma(j:1)} + \mathcal{C}^{(i)} e_\rho \rangle\rangle \\
&- \\
&\quad + \langle\langle e_E T^{(i)}_{\gamma(L:2)} e_{\gamma(1)} T^{(i)}_{\gamma(1)} + T^{(i)}_{\gamma(L:3)} e_{\gamma(2)} T^{(i)}_{\gamma(2)} e_{\gamma(1)} T^{(i)}_{\gamma(1)} \\
&\quad + \; ... \; + \; T^{(i)}_{\gamma(L:2)} e_{\gamma(1)} T^{(i)}_{\gamma(1)} e_\rho \rangle\rangle \; + \; ...
\end{aligned} \tag{2.30}$$

where $\mathcal{C}$ is the idealized circuit. A linear approximation can be made if we have $L\epsilon \ll 1$ where ϵ is an upper bound with $||e_k||$, $||e_\rho||$, $||e_E|| \leq \epsilon$ and $0 < \epsilon \ll 1$ for some matrix norm $|| \cdot ||$. In that case, the last two lines in Eq. (2.30) are cut off and the differences between the measured and expected values can be written as

$$\begin{aligned}
\Delta p^{(i)} = \hat{p}^{(i)} - p^{(i)} &= \; \langle\langle \hat{E} | \hat{\mathcal{C}}^{(i)} | \hat{\rho} \rangle\rangle - \langle\langle \mathcal{C}^{(i)} \rangle\rangle \\
&\simeq \langle\langle e_E \mathcal{C}^{(i)} + \sum_{j=1}^{L} T^{(i)}_{\gamma(L:j+1)} e_{\gamma(j)} T^{(i)}_{\gamma(j:1)} + \mathcal{C}^{(i)} e_\rho \rangle\rangle
\end{aligned} \tag{2.31}$$

and only one insertion of the error matrix at each possible position in the gate-string is kept. With the introduction of an orthonormal basis $\{|B_a\rangle\rangle\}_{a=1}^{d^2}$ and using the identity $\sum_a |B_a\rangle\rangle\langle\langle B_a| = \mathbb{1}$, we can write [111]

$$\begin{aligned}
e_k &= \sum_{a,b} \langle\langle B_a | e_k | B_b \rangle\rangle |B_a\rangle\rangle\langle\langle B_b| = \sum_{a,b} e_{k;ab} |B_a\rangle\rangle\langle\langle B_b| \\
e_\rho |\rho\rangle\rangle &= \sum_a \langle\langle B_a | e_\rho | \rho \rangle\rangle |B_a\rangle\rangle = \sum_a e_{\rho;a} |B_a\rangle\rangle \\
\langle\langle E | e_E &= \sum_a \langle\langle E | e_{E;a} | B_a \rangle\rangle \langle\langle B_a| = \sum_a e_{E;a} \langle\langle B_a|
\end{aligned} \tag{2.32}$$

which can be linked to Eq. (2.31) through

$$\Delta p^{(i)} \simeq \sum_a c^{(i)}_{\rho;a} e_{E;a} + \sum_{a,b} c^{(i)}_{k;ab} e_{k,ab} + \sum_a c^{(i)}_{E;a} e_{\rho;a} \ . \tag{2.33}$$

The coefficients are then given by

$$\begin{aligned} c^{(i)}_{\rho;a} &= \langle\langle B_a | \mathcal{C}^{(i)} | \rho \rangle\rangle \\ c^{(i)}_{k;ab} &= \sum_{j|\gamma(j)=k} \langle\langle E | T^{(i)}_{\gamma(L:j+1)} | B_a \rangle\rangle \langle\langle B_b | T^{(i)}_{\gamma(j:1)} | \rho \rangle\rangle \\ c^{(i)}_{E;a} &= \langle\langle E | \mathcal{C}^{(i)} | B_a \rangle\rangle \end{aligned} \tag{2.34}$$

so that Δp can be related to the error matrices, or more exact to a vector of the entries of all error matrices, in the form

$$\Delta \boldsymbol{p} = \mathbf{C}\boldsymbol{e} \quad \xrightarrow{\text{(pseudo) inverse}} \quad \boldsymbol{e} = \mathbf{C}^{-1}\Delta \boldsymbol{p} \tag{2.35}$$

where $\mathbf{C}$ is called the design matrix. By inversion of $\mathbf{C}$, the systems of equations can be solved directly from the deviations of the measured to the ideal expectation values and the knowledge of the selected random gate-strings. The inversion is done through a pseudo-inverse, since $\mathbf{C}$ is in general not a square matrix. From the error matrices one could reconstruct the estimates of the gates and reach something similar to the results from LGST that can be further processed with an MLE or used as a quick estimate for the gate-set's quality. In the context of optimization, however, the error matrices can be used directly to serve as a minimization target through optimal control and is further discussed in Sec. 3.3 and Ref. [3].

2.2.3 Randomized Benchmarking

Randomized benchmarking (RB) is a well-known technique and a de facto standard protocol used for systems based on, e.g., superconducting qubits [112–116], trapped ions [117–120], or liquid-state NMR [121, 122]. The idea behind RB is to prepare the quantum system in an initial state that can be prepared in a reproducible way. Then one randomly selects a number L of gates from a set and finds the $(L+1)^{\text{th}}$ gate such that it brings back the system in its initial state. After the application of the random gate-string, the survival probability, i.e. the probability to come back to the initial state, is determined (see Fig. 2.2.1). Therefore, this randomized selection is repeated several times so that sufficient combinations in the gate-strings are averaged. The experiment is repeated for varying gate-string lengths L.

The average fidelity of a unitary gate V under the completely positive map characterizing the noise Λ is given by [123]

$$\overline{F_g}(\Lambda, V) = \int \mathrm{d}\psi \ \langle\psi| V^\dagger \Lambda \left(V|\psi\rangle\langle\psi|V^\dagger \right) V |\psi\rangle \tag{2.36}$$

integrating over every state in the Hilbert space. We want to put all the experimental control errors and inherent decoherence of the system into the map Λ and prepare a fixed, arbitrary

input state $|\psi\rangle$ so that the average gate fidelity over all unitaries $\mathcal{U}$ is [124]

$$F_g(\Lambda^{\text{twirl}}) = \int_{\mathcal{U}} \mathrm{d}\mu(U)\ \langle\psi|\, U^\dagger\, \Lambda\left(U|\psi\rangle\langle\psi|U^\dagger\right) U\,|\psi\rangle \tag{2.37}$$

where $\mathrm{d}\mu(U)$ means that the unitary U is selected from the Haar-measure [125]. This way the channel Λ is *twirled* over the Bloch sphere to capture all possible effects and get a proper average. The so twirled and Haar-averaged map Λ^{twirl} can then be seen as a depolarizing channel that decays the survival probability exponentially with the length of the twirling sequence [123]. In order to measure this average gate fidelity, the integral in Eq. (2.37) needs to be replaced by a discrete set of measurements. This can be done if the set of gates from which the U are selected forms at least a unitary 2-design [126]. Fortunately, the Clifford group fulfills this property [127, 128] and even has the advantage that the final gate in a sequence, to bring back the state to its initial position, can be found efficiently [129].

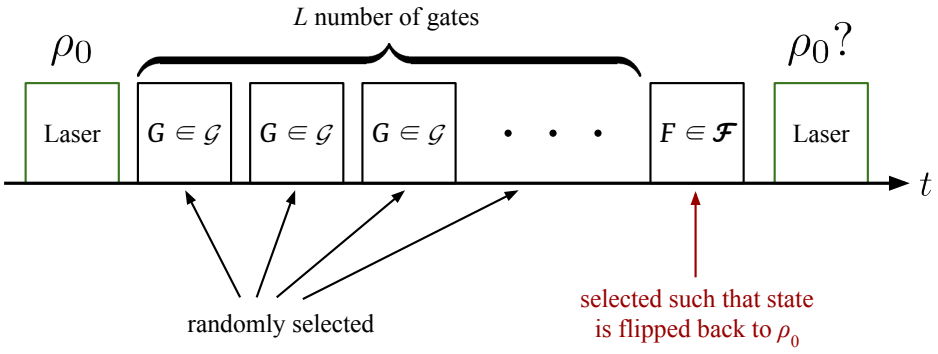

Figure 2.2.1: Visualization of an RB measurement. The initial state ρ_0 is prepared with a laser pulse (as done, e.g., for NV centers). A number L of randomly selected gates is applied, whereas the last gate is selected such that it brings back the state to the initial ρ_0 in the ideal case. A second laser pulse is used for the readout (and renewed preparation for the next measurement).

By increasing the number of Cliffords, L, an exponential decay of the survival probability can be expected. For a single qubit the Clifford group consists of 24 unique elements that can be composed of the gates defined in the gate-set as used in Sec. 3.3 [103]. On average one Clifford gate corresponds to 1.833 gates of the gate-set. The decaying survival probability is typically fitted by a model

$$F_{\text{seq}}(L) = A \cdot p_{\text{ref}}^L + B \tag{2.38}$$

to obtain p_{ref}, where L is the length of the Clifford sequences. Higher order fit models are also possible [130]. The parameters A and B absorb the SPAM errors and the error on the final gate. The decay parameter p_{ref} is related to the average error per Clifford $r = 1 - F_{\text{ave}} = 1 - p_{\text{ref}} - (1 - p_{\text{ref}})/d$, with $d = 2^n$ being the dimension of the Hilbert space, so that the average

(Clifford) gate fidelity is [121]

$$\overline{F}_{\text{ave}} = p_{\text{ref}} + \frac{1 - p_{\text{ref}}}{d} \,. \tag{2.39}$$

Interleaving a target gate of interest between each individual Clifford and performing the same fit to obtain p_{gate} leads, after subtraction of the reference, to the interleaved gate error [131]

$$r_{\text{gate}} = \left(1 - \frac{p_{\text{gate}}}{p_{\text{ref}}}\right)\left(\frac{d-1}{d}\right) \,. \tag{2.40}$$

Optimization of the gate fidelities directly via RB can be done via a method called optimized randomized benchmarking for immediate tune-up (ORBIT) [132]. Here, the sequence fidelity, i.e. the survival probability, at a fixed length L is optimized. This also enables us to vary the length of the randomized gate-string to see the effect of an optimization on different regimes, similar to RLGST. Based on these principles, even more advanced methods such as for example randomized compiling [133] can be used for error mitigation and the improvement of the average gate fidelity.

The methods discussed in this chapter have been used and investigated for gate and gate-set optimization in Ref. [3] and Sec. 3.3 with an experimental application to an ensemble of nitrogen vacancy centers in diamond. Therefore, an overview of this platform and its properties is given in the next section.

2.3 The Nitrogen-Vacancy Center

2.3.1 Overview

The nitrogen-vacancy (NV) center is a point defect in diamond [134]. It is formed by the replacement of two carbon atoms in a diamond lattice by one nitrogen atom and the creation of an adjacent vacancy [135]. The resulting structure is also called a color center due to its photoluminescent properties. Besides the NV center, other defects such as germanium- [136], silicon- [137–139] and tin-vacancy [140] have been investigated and display similar properties. Recently, point defects in the lattice of silicon carbide have become more and more popular [141, 142]. In this thesis, however, we want to focus on the NV center in diamond.

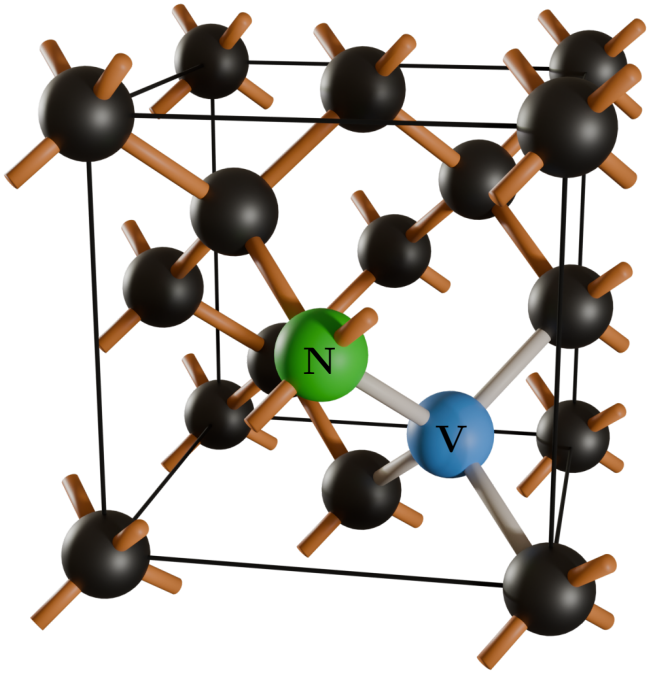

Figure 2.3.1: Nitrogen Vacancy in the Diamond Lattice. The nitrogen atom is shown in green and the adjacent vacancy in blue. Carbon atoms of one unit cell are colored black with their covalent bonds in brown.

When a nitrogen atom is injected into the diamond lattice, the three free electrons of the N-atom bind to three surrounding carbon atoms. The two unbound valence electrons of the nitrogen atom and the three remaining electrons of the carbons around the vacancy form the nitrogen vacancy center in its neutral charge state [143]. Typically, another electron is caught from a nearby donor in the diamond lattice, leading to what is called the NV^- charge state. NV centers can occur in different charge states, namely NV^0, NV^- and in principle in NV^+ [144]. Due to its optical spin properties explained in the following, we limit the discussion to the NV^- center which will simply be called NV center in this work. This electron configuration results in an effective spin $S = 1$ system with a ground state $|m_s = 0\rangle = |0\rangle$ and the degenerate states $|m_s = \pm 1\rangle = |\pm 1\rangle$. They are split by $D_{gs} = 2.87\,\mathrm{GHz}$ if no electromagnetic fields are ap-

plied to the system [145] as indicated in Fig. 2.3.2. From these levels the NV can be excited optically with a wavelength of typically 532 nm while preserving the spin state (green arrows in Fig. 2.3.2). After dissipation of vibronic excitations to the diamond lattice, the states can decay radiatively back to the ground states under emission of a photon with 637 nm at the zero phonon line (ZPL) (red arrows in Fig. 2.3.2) and a wide phonon side-band at higher wavelengths [145]. For the $m_s = \pm 1$ states of the excited triplet, however, there is a chance that they decay back to the ground state via a pair of singlet states, also called inter-system crossing [146], as shown in Fig. 2.3.2. This process happens under emission of a photon with much lower energy and is mostly filtered out in experiments, which is why $|\pm 1\rangle$ are also called the dark states. A decay via this path is not spin preserving and ends up in the $m_s = 0$ projection of the ground triplet states. In that way the NV center can be optically pumped into the $|0\rangle$ ground state [147] and initialized for the use in experiments. At the same time this mechanism is utilized to measure the integrated emission of fluorescence for repeated sequences in order to determine the final state of the electron spin afterwards [148]. The readout and initialization conveniently happen simultaneously.

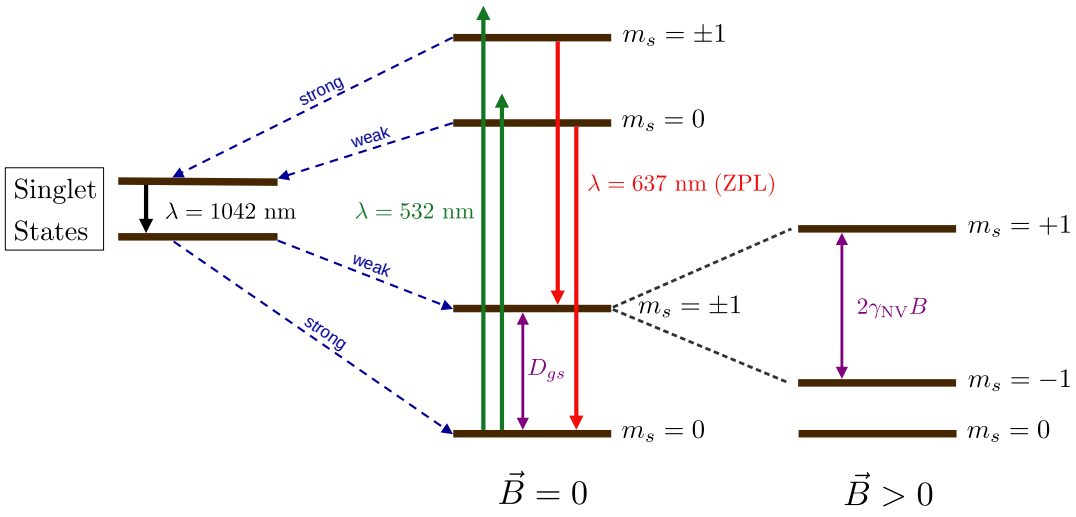

Figure 2.3.2: Energy level scheme of the NV center. The $|m_s\rangle = 0$ and $|m_s\rangle = \pm 1$ ground state levels are split by the zero-field splitting D_{gs} if no magnetic field is applied. Irradiation with a green laser ($\lambda = 532$ nm) excites the states to higher energy levels from which two decay paths are possible. A radiative decay directly back to the ground state emits a photon with a wavelength of 637 nm at the zero phonon line (ZPL). A second path via two meta-stable singlet states is possible and more likely if the NV was in the excited $|m_s = \pm 1\rangle$ spin projection. Under Application of a static magnetic field, the degeneracy between $|m_s = +1\rangle$ and $|m_s = -1\rangle$ is lifted and they are split by $2\gamma_{NV}B$ through the Zeeman effect. The $|m_s\rangle = 0$ state is left untouched.

Setting $\hbar$ to 1, the Hamiltonian for the electron spin part of the NV center can be written as [58, 148–151]

$$\begin{aligned} H_{\text{el}} \;=\; & \overbrace{D_{gs}\left(S_z^2 - \frac{2}{3}\right)}^{\text{ZFS}} + \overbrace{\gamma_{\text{NV}}\mathbf{B}\cdot\mathbf{S}}^{\text{magnetic}} \\ & + \underbrace{\epsilon_{\parallel}E_z\left(S_z^2 - \frac{2}{3}\right) - \epsilon_{\perp}\left[E_x\left(S_xS_y + S_yS_x\right) + E_y\left(S_x^2 + S_y^2\right)\right]}_{\text{electric}} \end{aligned} \tag{2.41}$$

where $\mathbf{E} = (E_x, E_y, E_z)^{\intercal}$ and $\mathbf{B} = (B_x, B_y, B_z)^{\intercal}$ are constant electric and magnetic fields, respectively, and $\mathbf{S} = (S_x, S_y, S_z)^{\intercal}$ is the vector of spin matrices for $S = 1$. The first term describes the aforementioned zero-field splitting (ZFS) in the absence of external electromagnetic fields. Magnetic fields couple to the NV via the second term in Eq. (2.41) with the gyromagnetic ratio for the NV center of $\gamma_{\text{NV}} = 28\,\text{GHz/T}$ [148]. The electric part in the second line of Eq. (2.41) describes the effects of both, external electric fields as well as effective fields arising from strain on the crystal. The simplification of the coupling coefficients to only be along the NV axis ($\epsilon_{\parallel}$) or perpendicular to it ($\epsilon_{\perp}$) can be made due to the C_{3v} symmetry of the defect [150]. Since the strength of the electric coupling is much weaker than γ_{NV}, being only around $\epsilon_{\parallel} = 17\,\text{Hz/(V cm}^{-1})$ and $\epsilon_{\perp} = 0.35\,\text{Hz/(V cm}^{-1})$ [150], they are often neglected or absorbed into the effective transition frequency of the states.

Apart from these effects, other spins surrounding the NV center can also have an influence and are discussed in the next subsection.

2.3.2 Interaction with Nuclear Spins

Nuclear spins in the vicinity of the color defect can interact with the electron spin of an NV center [152]. The first candidate is the inherent nitrogen that comes with the NV center. The naturally more abundant ^{14}N has a spin of $I = 1$ while the isotope ^{15}N, that can be introduced during synthesis of the defect, is an $I = \frac{1}{2}$ nucleus [145]. They have the strongest interaction strength due to their small distance to the electron cloud. Next up are the carbon atoms of the hosting diamond lattice. The common ^{12}C, with an abundance of 98.9 % [153], have a spin of zero and, therefore, do not interact with the electron spin, allowing for long coherence times due to the spin-free environment. Diamonds that are enriched with ^{13}C, however, can contain an adjustable amount of the carbon isotope that is seen by the NV center and connects with $I = \frac{1}{2}$. The extended Hamiltonian, that includes also interactions with nuclear spins, is [145]

$$H_{\text{NV}} \;=\; H_{\text{el}} + \cdot\sum_k \left(\mathbf{S}\cdot\underline{\mathbf{A}}_k\cdot\mathbf{I}_k + \mathbf{I}_k\cdot\underline{\mathbf{P}}_k\cdot\mathbf{I}_k - \gamma_k\cdot\mathbf{B}\cdot\mathbf{I}_k\right)\,. \tag{2.42}$$

The hyperfine tensor $\underline{\mathbf{A}}_k$ describes the interaction between the electron spin and nucleus k. Some nuclei can exhibit quadrupole interaction, which is encoded in $\underline{\mathbf{P}}_k$. Coupling constants for nitrogen are in the range of a few MHz whereas ^{13}C reaches over 130 MHz [154, 155]. Similar as in Eq. (2.41) can the magnetic field influence the other spins and in this case it couples via

the species-specific gyromagnetic ratio γ_k to the nuclear spin. The most relevant examples are $\gamma_{^{14}\mathrm{N}} \approx 3.1\,\mathrm{kHz/mT}$, $\gamma_{^{15}\mathrm{N}} \approx -4.3\,\mathrm{kHz/mT}$, and $\gamma_{^{13}\mathrm{C}} \approx 10.7\,\mathrm{kHz/mT}$ [156].

Typically, a static magnetic field along the symmetry-axis of the NV center is applied to induce a Zeeman splitting (see Fig. 2.3.3)), usually between $400 - 500\,\mathrm{G}$ ($40 - 50\,\mathrm{mT}$). This lifts the degeneracy between the $|+1\rangle$ and $|-1\rangle$ projections of the electron spin so that these transitions can be driven selectively. If the splitting is large enough, only one transition can be selected and serve as an effective two level system, i.e. our qubit. Furthermore, if the splitting between the two selected states along the z-axis is large enough, Eqs. (2.41) and (2.42) can be simplified because only the terms parallel to the NV axis remain and perpendicular terms for the electron spin part are rendered negligible. This is also called the secular approximation [157].

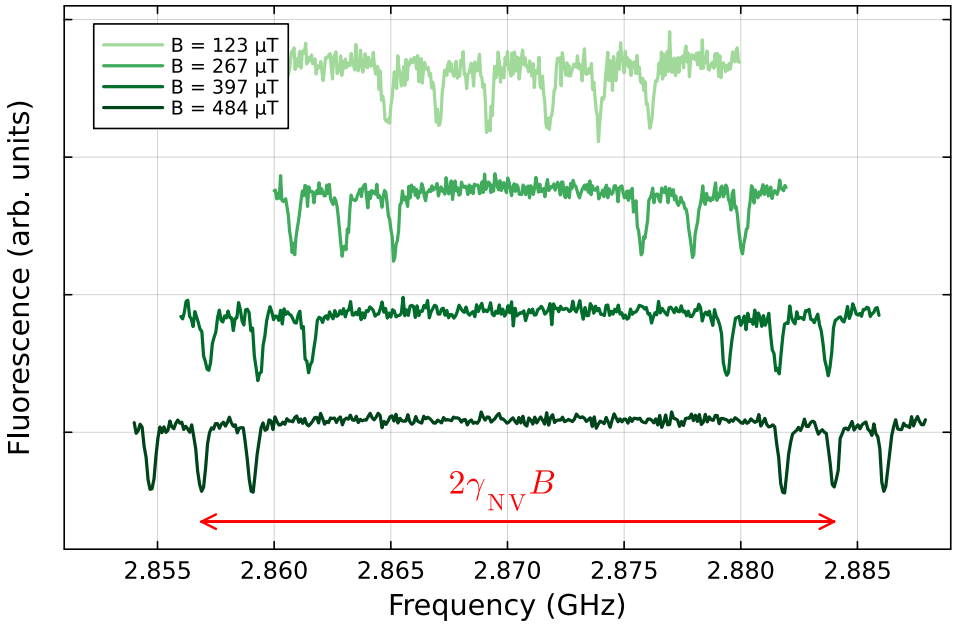

Figure 2.3.3: ODMR Spectra of an NV center with fluorescence dips for the transitions from $m_s = 0$ to $|-1\rangle$ and $|+1\rangle$ at different magnetic fields shifted by the Zeeman effect. The main dips are split by the hyperfine interactions with an ^{14}N triplet.

2.3.3 Driving and ODMR

To drive the NV center between the ground and one of the excited states in the lower level, a microwave (MW) field that generates an oscillating magnetic field in the form $H_D = \Omega \cos(\omega_D t) S_x$ can be added to the system in Eq. (2.41) where Ω depends on the magnitude of the applied magnetic fields. If the frequency of the driving field matches the transition frequency ω_{ab} of two levels of the energy spectrum, the spin states start performing Rabi oscillations with the

flip-flop probability

$$P_{a\to b}(\tau) = \frac{\Omega^2}{\Omega^2 + \Delta^2} \sin^2\left(\frac{\sqrt{\Omega^2 + \Delta^2}}{2} \cdot \tau\right) = \frac{\Omega^2}{\Omega_{\text{eff}}^2} \sin^2\left(\frac{\Omega_{\text{eff}}}{2} \cdot \tau\right) \tag{2.43}$$

where Ω is called the Rabi frequency, that corresponds to the magnitude of the driving field and influences the speed of the oscillations, and $\Delta = \omega_D - \omega_{ab}$ denotes the detuning of the drive frequency ω_D to the resonance frequency ω_{ab} between states a and b. If the drive frequency is swept while continuous illumination with green laser light, a dip in the detected fluorescence is detected if the MW frequency hits a resonance condition (population of dark states). This phenomenon is called optically detected magnetic resonance (ODMR) [158].
Instead of continuous wave irradiation, pulsed ODMR [159] can be used to apply narrow-band pulses that can even resolve the hyperfine and quadrupole splitting of the NV due to the nitrogen atoms (see Fig. 2.3.3)).

2.3.4 Applications of Color Centers

NV centers live in the inert host material diamond. That means their bio-compatibility enables applications in biological systems such as living cells [160–162]. What favours applications in life sciences is the possibility to work with the system at room temperature, which also reduces the complexity of experimental setups and the cost of hardware. Nonetheless, they can be cooled down to cryogenic temperatures to significantly enhance their lifetime and coherence times [163]. In bulk diamond the color defects are located at a fixed position but they can also be placed into nanostructures [164] or attached to atomic force microscope (AFM) tips and used as scanning probe spin sensors [165]. Nanodiamonds containing NVs can be functionalized to act, e.g., as biomarkers [166] or used for drug delivery [167]. Since color defects in diamond are not composed of molecules that can decompose or react, they display no problematic photobleaching or blinking [168], especially if used in bulk diamond.
3D electric field sensing for alternating current (ac) as well as direct current (dc) can be performed with single NV centers [169]. Scanning electrometry with NVs in an AFM tip [170] can be used to probe materials and *in-situ* monitoring of the electrolyte to determine battery degradation was shown [171]. Due to the stronger coupling to magnetic fields, a plethora of applications for magnetic field sensing with NV centers exists. They range from sensing ac and dc fields [172–174] over scanning probes [175, 176], also with temporal resolution [177], and even resulted in magnetometer prototypes [178].
The zero-field splitting parameter D_{gs} is temperature-dependent, so NV-based thermometers were demonstrated [179, 180] that can be used, in the form of nanodiamonds, to detect temperature changes in living cells [160]. Furthermore, applications to sensing pressure [181, 182] and even keeping time for GPS localization [183] were proposed. A comprehensive overview of quantum sensing in general and with NV centers can be found in Ref. [184] and Ref. [35].
In order to go towards quantum computing with NV centers, a network of the NV's electron spin coupled to individual nuclear spins can be used [185]. This is often called a spin register. The electron spin, which can easily be initialized, read out and manipulated, serves as a mediator to encode states stored in the nuclei, to entangle them and perform operations on the register [13]. Fig. 2.3.4 a) shows an illustration of such a spin register. To sense and detect the nuclear spin

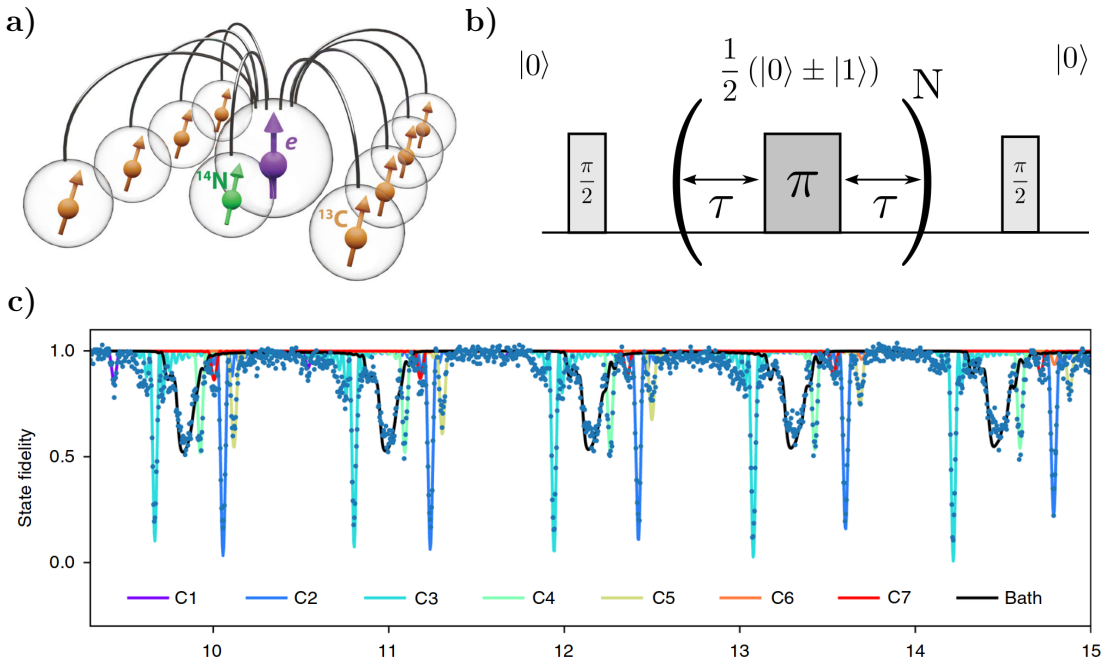

Figure 2.3.4: Sensing nuclear spins. **a)** Illustration of the NV electron spin coupled to the inherent nitrogen and eight carbon atoms [13], **b)** Dynamical decoupling sequence used for sensing individual nuclei, **c)** Dynamical decoupling spectrum that shows the fingerprints of individual ^{13}C atoms (adapted from [163]).

environment, dynamical decoupling (DD) sequences can be used, where repeated π-pulses on the electron spin with a temporal spacing matching the frequency of a nuclear spin's Larmor precession leads to a dip in the recorded spectrum (see Fig. 2.3.4 b) and c)) [163]. In fact, the same DD sequences can be used to control the individual nuclear spins [186] or to decouple and protect the electron spin from decoherence. More complex operations can be used to build up specific quantum circuits, e.g. using CNOT gates [187], to achieve universal control of a spin register [185]. Lastly, quantum jumps on a single nuclear spin can be detected in real time with a single-shot readout strategy using the electron spin [188].
NV centers can also be used as a single photon source, even at room temperature [189, 190]. This enables the entanglement between two distant NVs via photons over large distances [191, 192] and the design of quantum repeaters [193].

2.3.5 Ensembles of NV Centers

Ensembles of nitrogen vacancy centers allow for the accumulation of the fluorescence of many color centers simultaneously, boosting the signal-to-noise ratio (SNR) of the measurement. Since the SNR is proportional to the square root of the NV concentration $SNR \propto \sqrt{N}$, such ensembles can lead to a much faster readout and improved sensitivity [194]. Their coherence times at room

temperature have been shown to be $T_2 > 600\,\mu s$ for Hahn-echo measurements [195] which can be improved by, e.g., depleting the host diamond of impurities and the naturally abundant ^{13}C. Various fabrication methods to produce diamonds containing ensembles of NVs with different concentrations, depths, and compositions of the nuclear spin environment enables tailored properties for applications as sensors [195, 196]. Most prominent and promising is the use of NV ensembles as magnetometers with high sensitivities and a large field-of-view [173, 197, 198] also for wide-field microscopy [199–202] and under high pressure [203]. They can also be used for the imaging of thin films [204] to reconstruct the current flow in, e.g., thin graphene ribbons. Figure 2.3.5 shows the magnetic fields and reconstructed currents flowing through a graphene ribbon measured using a thin layer of nitrogen vacancy centers [205].

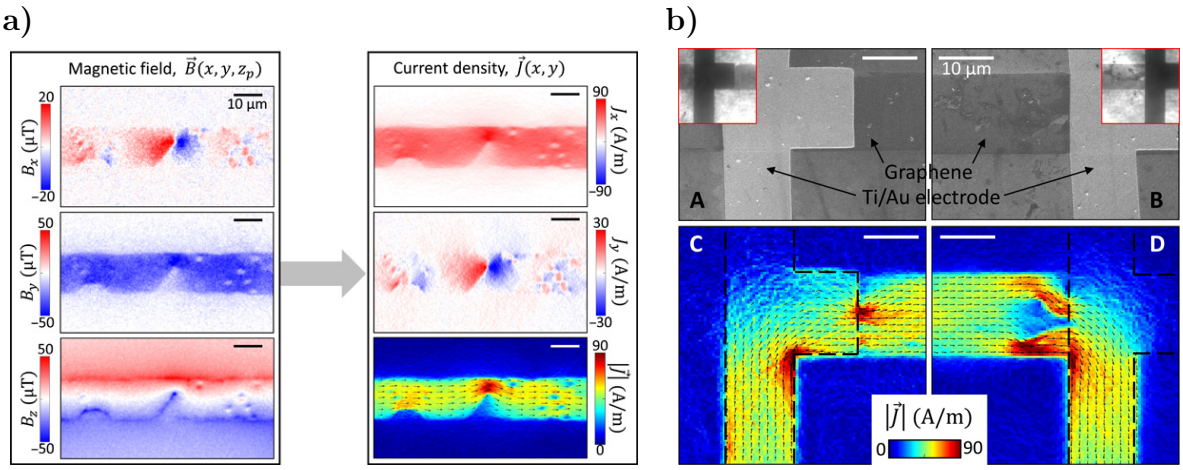

Figure 2.3.5: Imaging the current flow in graphene with NV ensembles. **a)** Maps of the magnetic field in x-, y-, and z-direction produced by a current (left) and reconstructed current density (right). **b)** Flow of currents near metallic contacts connected to the graphene ribbon. (Figures adapted from [205])

Besides magnetic fields, electric field sensing with ensembles to investigate and characterize charge environments has been performed [206]. Lastly, new phases of matter with properties such as a discrete time-crystalline order are explored using ensembles NVs [207, 208].

2.4 Dynamic Nuclear Polarization

2.4.1 Overview

Magnetic resonance imaging (MRI) is based on the use of very strong magnetic fields to introduce a, albeit tiny, polarization of the nuclear spins inside the object that is examined. In order to increase the spin polarization given by the Boltzmann distribution, either the magnetic field needs to be increased, or the temperature has to be lowered. This would result in a higher resolution of the image or shorter measurement times, which benefit living patients inside the scanner. The world's most powerful MRI scanner uses a magnetic field of 11.7 Tesla with even

stronger ones on the way [209]. Lower temperatures are often not an option due to the detrimental effects on a living organism. Therefore, other ways to increase the nuclear polarization are of high interest. Hyperpolarized samples have so been successfully used for, e.g., sensitivity enhancement of NMR experiments [210–213] or to develop broadband neutron spin filters [213–216].

2.4.2 The Integrated Solid Effect

Dynamic nuclear polarization (DNP) is a hyperpolarization technique where the spin polarization of an electron spin is transferred to nuclear spins. These polarizable electron spins are usually introduced into the sample artificially and then manipulated to interact with the nuclei. In this thesis the focus lies on DNP schemes based on the solid effect [217]. Let's assume a Hamiltonian of the form

$$H \;=\; \omega_S S_z \;+\; 2\Omega\cos(\omega_d t) S_x \;+\; \omega_I \sum_i I_z^i \;+\; \sum_i \mathbf{S}\cdot\underline{\mathbf{A}}^i\cdot\mathbf{I}^i \tag{2.44}$$

for an electron spin with $S = \frac{1}{2}$ and a number of nuclear spins with $I = \frac{1}{2}$ and $\hbar$ is set to 1. The oscillation frequency ω_S includes the ZFS and the Zeeman effect. The electron spin is driven by an oscillating field with frequency ω_d and Rabi frequency Ω. The nuclear spins have a Larmor frequency ω_I and couple to the electron according to the last part of Eq. (2.44). In a rotating frame about the z-axis with the drive frequency and assuming only one nuclear spin for readability, the Hamiltonian can be written as

$$H_{\mathrm{IP}} \;=\; \Delta S_z \;+\; \Omega S_x \;+\; \omega_I\, I_z \;+\; S_z\,(A_{zx}I_x + A_{zy}I_y + A_{zz}I_z) \tag{2.45}$$

where we have used the rotating wave approximation (RWA) to truncate the Hamiltonian of fast oscillating terms. Additionally, the secular approximation was used because, due to the large ZFS and Zeeman splitting of the electron, the perpendicular coupling terms are orders of magnitude smaller than the S_z components [157] for the systems considered in this thesis [173, 218–221]. The detuning Δ describes the mismatch of drive and resonance frequency $\Delta = \omega_S - \omega_d$. To access the polarization and make the two spins talk to each other, the electron spin needs to be flipped away from the z-axis. Following Ref. [222], this can be described by tilting the frame of reference about the y-axis about an angle

$$\sin(\beta) = \frac{\Omega}{\sqrt{\Delta^2+\Omega^2}} = \frac{\Omega}{\Omega_{\mathrm{eff}}} \tag{2.46}$$

with the operator $U = \exp(i\beta S_y)$ so that the new z-axis is along S_z'. The tilted Hamiltonian then is

$$\begin{aligned} H' \;=\; & \Omega_{\mathrm{eff}}\, S_z' \;+\; \omega_I\, I_z \;+\; \frac{1}{2}\cos(\beta)\, S_z'\,(A_{z+}I_- + A_{z-}I_+ + 2A_{zz}I_z) \\ & +\; \frac{1}{4}\sin(\beta)\,(S_+ + S_-)\,(A_{z+}I_- + A_{z-}I_+ + 2A_{zz}I_z) \end{aligned} \tag{2.47}$$

with

$$\begin{aligned} S_\pm &= S'_x \pm i S'_y \\ I_\pm &= I_x \pm i I_y \\ A_{z\pm} &= A_{zx} \pm i A_{zy} \,. \end{aligned} \tag{2.48}$$

Subsequently, another transformation into a frame rotating about the first term of Eq. (2.47), i.e. $\Omega_{\text{eff}}\, S'_z + \omega_I\, I_z$, can be made to average over a time $t > \frac{2\pi}{\omega_I}$. Since for polarization transfer to occur the Hartmann-Hahn condition [223]

$$\Omega_{\text{eff}} = \sqrt{\Delta^2 + \Omega^2} \approx \omega_I \tag{2.49}$$

needs to be fulfilled, so that the rotations of the electron spin induced by the drive happen with the same frequency as the Larmor precession of the nuclei and they are therefore on "speaking terms" with each other. This drops out fast oscillating contributions perpendicular to the new z-axis. After a final transformation back into the previous frame, we arrive at

$$H'' = \Omega_{\text{eff}}\, S'_z + \omega_I\, I_z + \cos(\beta)\, A_{zz} S'_z I_z - \frac{1}{4}\sin(\beta)\,(A_{z+} S_+ I_- + A_{z-} S_- I_+) \tag{2.50}$$

and can recognize the flip-flop terms $S_+ I_-$ and $S_- I_+$ that are responsible for the polarization transfer. For an electron spin with $S = 1$ which is reduced to an effective 2-level system, the z-spin operator looks like $S_z = |1\rangle\langle 1| = \frac{1}{2}\,(\mathbb{1} - \sigma_z)$ and leads to a shift of the Larmor frequency by $\frac{1}{2}A_{zz}$ and therefore to the adapted Hartmann-Hahn condition of $\sqrt{\Delta^2 + \Omega^2} = |\omega_I \hat{\mathbf{z}} + \frac{1}{2}\mathbf{A}|$ [224, 225]. In that case the prefactor of the drive also needs to be changed to a $\sqrt{2}$ in Eq. (2.44).

One method to perform DNP is called nuclear spin orientation via electron spin locking (NOVEL) [222, 226–228] where the electron spin is flipped with a $\pi/2$-pulse and then driven by a microwave perpendicular to the flipping pulse. In that case $\beta = \frac{\pi}{2}$ and the polarization is flipped after a duration of $\frac{2\pi}{|A_{z\pm}|}$. After transfer the polarization is distributed to surrounding nuclear spins through what is called spin diffusion [229]. The whole process is then repeated numerous times to slowly build up a significant polarization in the sample.

However, if the electron spin resonance line is broader than the resonance frequencies due to the hyperfine interaction with the nucleus, DNP with the solid effect is strongly hindered [230]. Therefore, an improved scheme called the integrated solid effect (ISE) is often used. ISE uses the idea of a Landau-Zener transition [231, 232] where either the microwave frequency of the drive on the electron is swept at constant external magnetic field, or by sweeping the magnetic field while fixing the drive frequency and amplitude. By doing so, the Hartmann-Hahn resonance condition in Eq. (2.49) is passed twice as is illustrated in Fig. 2.4.1. Performing such an adiabatic fast passage through the electron resonance line drastically increases the polarization transfer rate [233] and has even led to a proton polarization of 80 % [214]. It can be very helpful if there are several nuclei coupling with similar magnitudes. Then the resonance condition can be fulfilled for all of them on the way during the variation of the detuning and the overall polarization transfer is improved.
NOVEL [225, 228] as well as ISE [228, 234, 235] were experimentally investigated with NV

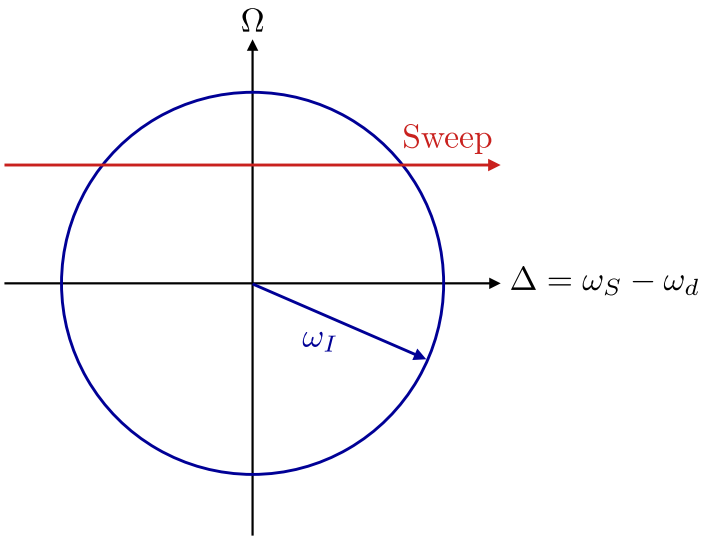

Figure 2.4.1: Illustration of the Integrated Solid Effect. The blue circle indicates the Hartmann-Hahn condition in Eq. (2.49) which is met twice if the frequency of the driving MW is varied around the electron spin resonance frequency at constant amplitude Ω.

centers to polarize its surrounding spin bath (see Sec. 2.3.2). Other interesting systems that were used as a test bed for the ISE development are p-type silicon wavers doped with boron [230] and the electron spin of pentacene molecules embedded in, e.g., a naphthalene host to polarize the protons of one or both molecules [233]. In this thesis we want to have a closer loot at the system of pentacene in naphthalene in the next section.

2.4.3 Pentacene-doped Naphthalene

Pentacene molecules can be inserted into the crystal structure of a naphthalene host by replacing two translationally equivalent $C_{10}H_8$ molecules along the c-axis [236]. The pentacene molecules are slightly tilted by 10° from that axis [237] so the structure looks as depicted in Fig. 2.4.2. The electron spin of pentacene can be excited from a singlet ground state to an excited state $\mathcal{S}_1$ from which it converts into triplet states $\mathcal{T}_1$ via inter system crossing [238] as is shown in Fig. 2.4.3. Since the lifetime of the singlet state is much shorter than the decay from the triplet states, the system can be pumped into $\mathcal{T}_1$ by repeated laser excitation [239]. The levels are then mainly populated in the $m_s = 0$ with $P(|T_0\rangle) = 0.76$ and $P(|T_+\rangle) = P(|T_-\rangle) = 0.12$ [240]. The lifetime of the triplet state is on the order of 20 µs [237] and can be extended by using deuterated pentacene (pentacene-d_{14}) instead of normal molecules with hydrogen atoms, which also narrows the ESR linewidth [241]. A static magnetic field aligned along the x-axis of the pentacene induces a Zeeman splitting and can be used to tune the resonance frequency of the triplet state transitions. By using a microwave filed to manipulate the electron spin states and DNP strategies discussed above, the optically induced polarization can be transferred to the surrounding nuclear spins. In the case of pentacene-d_{14} the resonance condition can be tuned such that only the protons of naphthalene are addressed. The concrete terms for the hyperfine tensor can be calculated from the relative position of the nuclei in the lattice with respect to

the electron spin [224].

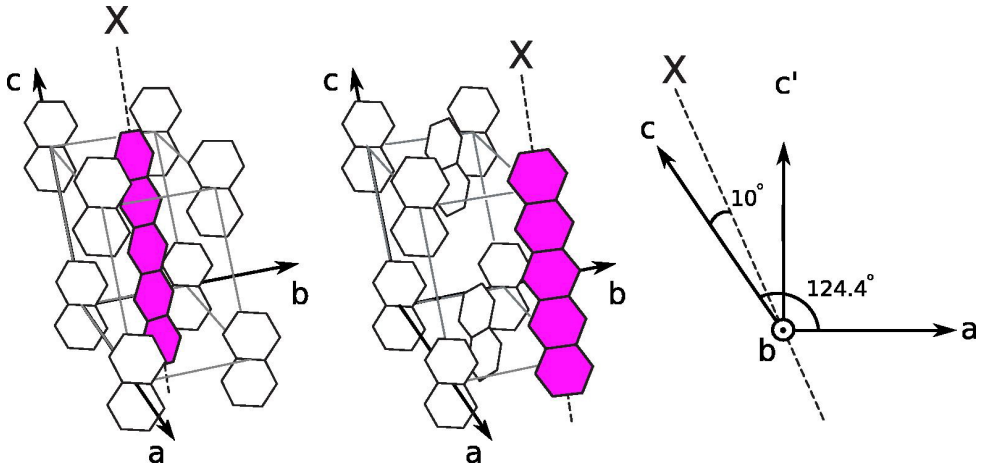

Figure 2.4.2: Crystal structure of naphthalene doped with pentacene. The pentacene (purple) molecule can be in two different positions tilted by 10° with respect to the c-axis of the naphthalene crystal lattice [242].

Image reprinted from T. Eichhorn, M. Haag, B. van den Brandt, P. Hautle, W. Wenckebach, S. Jannin, J. van der Klink, and A. Comment, "An apparatus for pulsed ESR and DNP experiments using optically excited triplet states down to liquid helium temperatures", Journal of Magnetic Resonance, Vol. 234, pp. 58–66, Copyright (2013), with permission from Elsevier.

2.4.4 Spins inside a Cavity

In some experiments, the sample with the spins and polarization target is put inside of a resonator [243]. This can be done, e.g., to obtain a stronger field for higher Rabi frequencies [244] or a more homogeneous field distribution.

The Hamiltonian for the system of cavity, electron spins, and external driving field can be written in a Jaynes–Cummings form with the creation and annihilation operators $a_\mathrm{c}^\dagger$ and a_c for the cavity and the raising and lowering operators for the spins inside as σ_+^j and σ_-^j. It reads [245]

$$\begin{aligned} H_\mathrm{csd} = \; & \Delta_\mathrm{cs} a_\mathrm{c}^\dagger a_\mathrm{c} \; + \; \frac{1}{2}\sum_j \Delta_j \sigma_z^j \\ & + \; i\sqrt{2\gamma_\mathrm{cav}}\left(\beta(t)a_\mathrm{c}^\dagger - \beta(t)^* a_\mathrm{c}\right) \; + \; \sum_j g_j \left(\sigma_+^j a_\mathrm{c} + \sigma_-^j a_\mathrm{c}^\dagger\right) \end{aligned} \tag{2.51}$$

in the frame rotating with the spin frequency ω_s. The first term describes the field inside the cavity with the detuning from the spins $\Delta_\mathrm{cs} = \omega_\mathrm{c} - \omega_\mathrm{s}$ and the second term describes the spins that can be detuned from their average frequency by $\Delta_j = \omega_j - \omega_s$. The interaction of the drive $\beta(t)$ via the cavity response γ_cav is given by the third term. The last part shows the exchange between cavity and spins with each spin's potentially individual coupling strength g_j. Assuming the field inside the cavity is strong enough to be treated classically the average of the

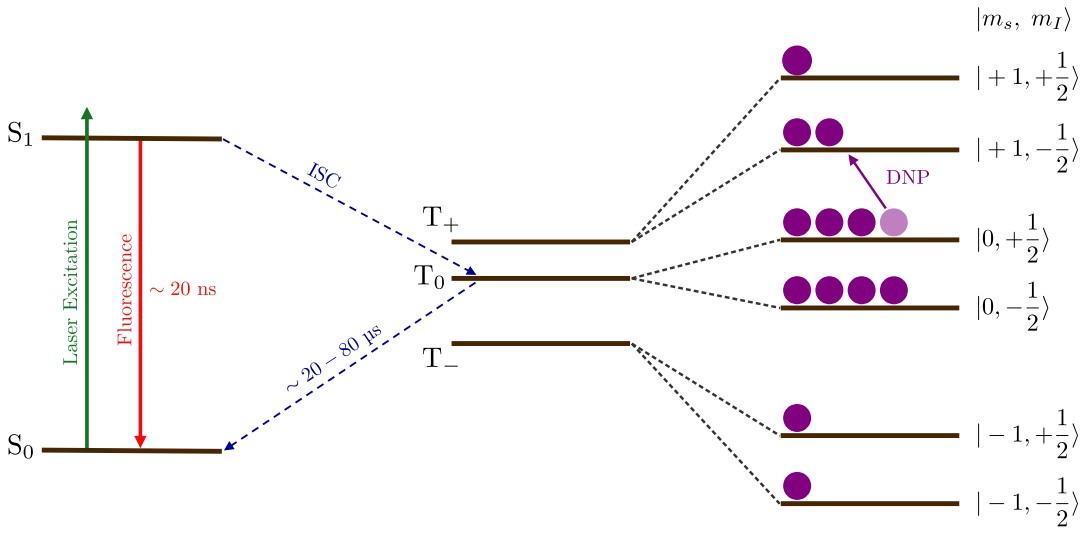

Figure 2.4.3: Energy level scheme of pentacene coupled to a nucleus. Excitation with a laser drives the electron spin state to S_1 and via inter system crossing to the triplet states. The longer lifetime of the triplet states compared to a direct decay creates an overhead of population in T_0. DNP techniques can be used to transfer this polarization to nuclear spins.

annihilation operator is found to be [245]

$$\frac{\partial}{\partial t}\langle a_c\rangle \;=\; -\gamma_{cav}\langle a_c\rangle \;-\; i\sum_j g_j\langle\sigma_-^j\rangle \;+\; \sqrt{2\gamma_{cav}}\beta(t) \;-\; i\Delta_{cs}\langle a_c\rangle \tag{2.52}$$

which can be further simplified, if we also assume that there are only few spins that interact with the field inside the cavity and therefore do not influence it much, so we get

$$\frac{\partial}{\partial t}\langle a_c\rangle \;=\; \gamma_{cav}\left(\Omega(t) - \langle a_c\rangle\right) \;-\; i\Delta_{cs}\langle a_c\rangle \tag{2.53}$$

where we defined $\Omega(t) = \frac{\sqrt{2\gamma_{cav}}}{\gamma_{cav}}\beta(t)$. From this equation we can see how the field builds up inside the cavity based on the drive, the excitation already inside and the perturbation through a mismatch of the driving frequency.

3 Publications

In this chapter, the main results of the three publications presented in this thesis are reviewed and set into current research perspective:

- Alastair Marshall†, **Thomas Reisser**†, Phila Rembold†, Christoph Müller, Jochen Scheuer, Martin Gierse, Tim Eichhorn, Jakob M. Steiner, Patrick Hautle, Tommaso Calarco, Fedor Jelezko, Martin B. Plenio, Simone Montangero , Ilai Schwartz, Matthias M. Müller, Philipp Neumann; "*Macroscopic hyperpolarization enhanced with quantum optimal control*", In: Phys. Rev. Res. 4.4 (2022), p. 043179, DOI: `https://doi.org/10.1103/PhysRevResearch.4.043179`

- Marco Rossignolo†, **Thomas Reisser**†, Alastair Marshall, Phila Rembold, Alice Pagano, Philipp J. Vetter, Ressa S. Said, Matthias M. Müller, Felix Motzoi, Tommaso Calarco, Fedor Jelezko and Simone Montangero; "*QuOCS: The quantum optimal control suite*", In: Computer Physics Communications 291 (2023), p. 108782, DOI: `https://doi.org/10.1016/j.cpc.2023.108782`

- Philipp J. Vetter†, **Thomas Reisser**†, Maximilian G. Hirsch, Tommaso Calarco, Felix Motzoi, Fedor Jelezko and Matthias M. Müller; "*Gate-set evaluation metrics for closed-loop optimal control on nitrogen-vacancy center ensembles in diamond*", In: npj Quantum Information 10.1, 96 (2024), DOI: `https://doi.org/10.1038/s41534-024-00893-y`

(† These authors contributed equally to this work.)

Each section starts with a summary of one article, followed by the metadata, an overview of the contributions by the author of this thesis, and ends with the content of the publication itself.

3.1 Macroscopic Hyperpolarization enhanced with Quantum Optimal Control

3.1.1 Summary

NMR finds its applications, inter alia, in magnetic resonance spectroscopy (MRS) and magnetic resonance imaging (MRI). In order to boost sensitivity and to improve the quality of the acquired spectra and images, hyperpolarized materials are of high interest [246, 247]. With many use cases in chemistry [248] and biology [249], methods of DNP and subsequent utilization in NMR experiments are an active field of research. Medical use cases are, e.g., the use of hyperpolarized xenon to increase the signal for brain imaging in rats [250] and companies like NVision [251] even provide commercial offers of machines to produce hyperpolarized samples for injection. The goal of the publication discussed in this section [1] is to employ optimal control strategies in order to enhance the macroscopic polarization of a crystalline sample of naphthalene doped with pentacene and find a simple recipe to reproduce the results in similar experimental scenarios.

In the publication, we perform DNP from the highly optically polarized electron spins in deuterated pentacene to the nuclear spins (protons) of naphthalene. The sample was grown in-house by NVision in Ulm and is placed in a polarizer device under a static magnetic field of 230 mT and a temperature of 130 K. The crystal sample, mounted on a motorized stage, can be shuttled between a microwave cavity and an NMR coil. A pulsed laser generates the polarization in the triplet state of the electron spin. To transfer the polarization, shaped microwave pulses are used to manipulate the system. To calibrate the simulation model, parameters such as the lifetimes of the electron states, the conversion of voltages to Rabi amplitudes and the distribution of detuning values between single electrons and the cavity resonance are determined. Furthermore, the cavity response γ_{cav} is required. In order to determine it, we recorded the Rabi oscillations on the electron spins for an applied, constant external drive field and varying values of the cavity-spin detuning Δ_{cs} (see Sec. 2.4.4). Doing the same with the simulation model and taking a Fourier transform to find the Rabi frequency distribution Ω leads to heat-map plots as shown in Fig. 3.1.1 a). The mismatch between simulation and experiment is calculated from the integral over the difference of both data-sets and denoted as ΔI. Varying the cavity response factor in simulation to obtain the curve shown in Fig. 3.1.1 b) suggests a value of $\gamma_{\mathrm{cav}} = 9.24\,\mathrm{MHz}$ after finding the minimum of a Gaussian fit to the ΔI values.
Simulations of the polarization buildup are performed considering the 30 most strongly coupled nuclear spins, calculated from their relative positions to the electron spin in the crystal lattice formed by pentacene and naphthalene. For each curve shown in Fig. 3.1.2, the time evolution of the system, including the distortions by the cavity, the decay rates of the used triplet spin states and three nuclear spins is calculated 1000 times and averaged. For each instance, three different nuclei are selected randomly. In this way, effects like the repolarization of the electron and redistribution of polarization between the nuclei can be captured to some degree. To investigate the best approach for DNP, we start off with a linear detuning sweep at fixed microwave amplitude for the externally applied field, similar to the ISE. The cavity distorts the field inside, but the crossings of the Hartmann-Hahn resonance condition remain, as can bee seen by the orange indication lines in Fig. 3.1.2. Evidently, polarization is built up as measured in the bottom row of Fig. 3.1.2. The parameters of the sweep, i.e., the amplitude, sweep rate, and duration, have been tuned manually. This initial guess serves as the benchmark of further optimized pulses and is used as the input pulse for a dCRAB optimization using the RedCRAB

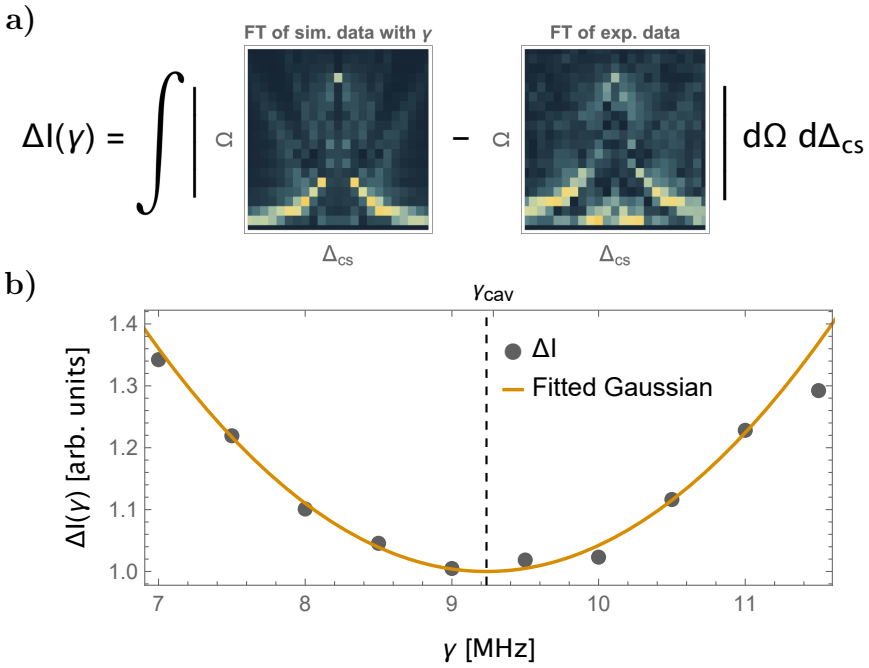

Figure 3.1.1: Determination of the cavity response factor γ_{cav}. **a)** To quantify the mismatch between simulation and experiment, ΔI, the driven oscillations for different values of the cavity-spin detuning Δ_{cs} are Fourier transformed to give the plotted Ω. **b)** The integral of the differences between the two heat-maps is then calculated for a range of cavity response values in simulation to find the best overlap at $\gamma_{\mathrm{cav}} = 9.24\,\mathrm{MHz}$ (dashed black line) after a Gaussian fit to get the minimum of ΔI. (Reprinted from [1])

software package [252], which implements a remote version of the dCRAB algorithm [1, 14, 91–93]. The first step we perform is to optimize this "Linear" sweep (left column in Fig. 3.1.2) by varying the externally applied amplitude and phase of the microwave pulse. This results in the "Optimal (Linear)" pulse shown in the second column of the figure. We can see a much faster initial polarization buildup and the overall higher polarization achieved, with an improvement of about 19 % compared to the "Linear" ISE-like approach. Especially the repeated crossing of the resonance line is expected to give the main contribution to the enhancement. For that reason, a "Sinusoidal" pulse is constructed, that repeatedly sweeps through the resonance, indicated by the orange colored lines and areas in Fig. 3.1.2, in a sinusoidal fashion for the detuning Δ with constant amplitude. Also, the pulse duration is increased to 160 µs so that more time for spin-diffusion is allowed and to utilize as much polarization of the electron spin as possible, before it decays to the ground state S_0. We see that the general improvement of the "Optimal (Linear)" pulse is maintained in the "Sinusoidal" pulse, albeit with a slightly lower final polarization of the sample. Another closed-loop optimization of the amplitude and phase with RedCRAB leads to the final "Optimal (Sin.)" pulse shown in the last column of Fig. 3.1.2. It has the best final polarization, beating the initial guess by $\sim 28\,\%$. The initial slow-down of the first crossing sweep is responsible for the very fast polarization increase in the first few microseconds of the pulse, as experimental tests shown in the Appendix of the publication confirm. The performed

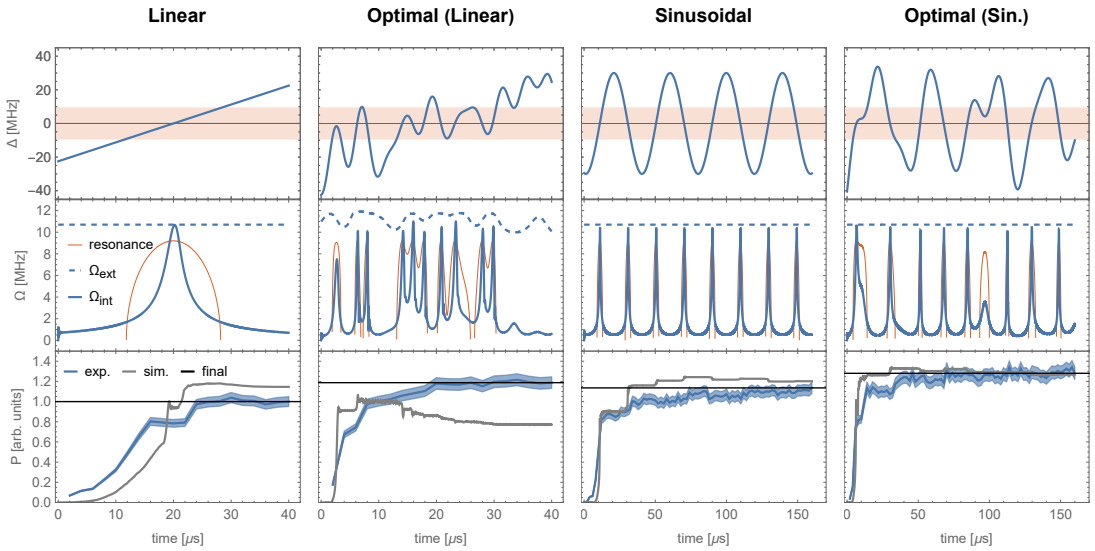

Figure 3.1.2: Optimization progression. The rows show, from top to bottom, the detuning of the pulse from the spin resonance over time, the amplitude of the externally applied field (dotted blue line) and the field inside the cavity (blue line) where the resonance condition depending on the detuning is indicated in orange. The bottom plots show the measured (blue) and simulated (black) buildup of the polarization during the pulse. The final polarization reached is indicated with a black line to guide the eye. From left to right, the columns correspond to the linear (ISE-like) guess pulse, the optimized pulse based on that, a sinusoidal pulse design based on the optimization result in column 2, and the final optimized pulse in the fourth column after starting from column 3. (Reprinted from [1])

simulations reproduce the main qualitative features of the polarization buildup curves, although with some significant mismatches especially for the "Optimal (Linear)" pulse. We attribute this to the fast time-dynamics of the pulse amplitude and detuning and the lack of knowledge about the true transfer function of the setup's electronics, causing distortions to the actual pulse seen by the pentacene spins.

Investigations of a long-term polarization buildup, where the optical preparation of the electron spin and subsequent transfer with the pulses is repeated over the course of several hours, show the practical use of the optimized technique. With the "Optimal (Sin.)" pulse the sample polarization reaches an overall higher final polarization (increase by 26 %) than the "Linear" pulse. Furthermore, the time to reach the same polarization as 98 % of the saturation observed for the "Linear" pulse is shortened by over 5 hours for the optimized pulse.

To generalize the whole optimization process, we propose a 3-step scheme called autonomously optimized repeated linear sweep (ARISE). Since a good initial guess is very beneficial of optimization, the first step is to tune a linear sweep by finding the best sweep range $\Delta_{\max}$ and duration T_{linear} for the setup at hand. From these parameters, a repeated sweep between $\pm\Delta_{\max}$ back and forth for N_{osc} times with a period $\tau_0 = T_{\text{linear}}$ is constructed. The parameters N_{osc} and τ are then optimized by a simple search. Finally, the resulting pulse shape is fed as a guess into

a closed-loop optimization to fine-tune the time-dependent detuning $\Delta(t)$ in order to obtain the best performance for polarization buildup.

In conclusion, we have shown that closed-loop optimal control can enhance the polarization transfer for a spin ensemble in a complex experimental setup, starting from conventional techniques, by at least 26 %. The much shorter time it needs to reach a high polarization enables experimentalists to prepare several samples per day. The developed ARISE protocol can help to take advantage of the discovered features of the final sequence and can be used to improve DNP for similar systems such as, e.g., NV centers coupled to ^{13}C nuclei as mentioned in Sec. 2.3.2. Furthermore, it serves as a good starting point for other macroscopic ensembles and also for further optimization and investigation of the system dynamics. Finally, the gained experience and feedback for the usage of the control software RedCRAB has immensely helped in the improvement of the software and the development of new features. The obtained know-how also led to the development of its open-source successor, the quantum optimal control suite QuOCS, which is highlighted in the following Sec. 3.2.

Title: Macroscopic Hyperpolarization enhanced with Quantum Optimal Control

Authors: Alastair Marshall†, **Thomas Reisser**†, Phila Rembold†, Christoph Müller, Jochen Scheuer, Martin Gierse, Tim Eichhorn, Jakob M. Steiner, Patrick Hautle, Tommaso Calarco, Fedor Jelezko, Martin B. Plenio, Simone Montangero , Ilai Schwartz, Matthias M. Müller, Philipp Neumann

Journal: Physical Review Research

Publisher: American Physical Society

Year: 2022

Volume: 4

Issue: 4

DOI: 10.1103/PhysRevResearch.4.043179

Link: https://link.aps.org/doi/10.1103/PhysRevResearch.4.043179

† These authors contributed equally to this work.

3.1.2 Author's Contribution

Thomas Reisser contributed to the planning of this project, the theory and the simulations, the conceptualization of the measurements, as well as writing the manuscript. He performed most of the simulations for the system and cavity and was involved in discussions on the characterization of the setup. Thomas supported the implementation of closed-loop optimal control with RedCRAB and contributed to the discussion and analysis of the experimental results. He provided the simulation data for Figures 3 and 5 and for discussions about the characterization of the setup and protocol design.

3.1.3 Data Availability

The simulation data shown in Publication [1] is stored on the backed-up data servers of PGI-8 at Forschungszentrum Jülich (FZJ) and available upon request to the author of this thesis or the Institute for Quantum Control (PGI-8). The experimental data shown is stored at NVision in Ulm and can be requested from Alastair Marshall (see publication).

PHYSICAL REVIEW RESEARCH **4**, 043179 (2022)

Macroscopic hyperpolarization enhanced with quantum optimal control

Alastair Marshall,[1,2,*] Thomas Reisser,[3,4,*] Phila Rembold,[3,4,5,6,*] Christoph Müller,[1] Jochen Scheuer,[1] Martin Gierse,[1,2] Tim Eichhorn,[1] Jakob M. Steiner,[1,7] Patrick Hautle,[7] Tommaso Calarco,[3,4] Fedor Jelezko,[2] Martin B. Plenio,[8] Simone Montangero,[5,6,9] Ilai Schwartz,[1] Matthias M. Müller,[3] and Philipp Neumann[1]

[1]*NVision Imaging Technologies GmbH, D-89081 Ulm, Germany*

[2]*Institute for Quantum Optics (IQO) and Center for Integrated Quantum Science and Technology (IQST), Albert-Einstein-Allee 11, Universität Ulm, D-89081 Ulm, Germany*

[3]*Forschungszentrum Jülich GmbH, Peter Grünberg Institute - Quantum Control (PGI-8), D-52425 Jülich, Germany*

[4]*Institute for Theoretical Physics, University of Cologne, D-50937 Cologne, Germany*

[5]*Dipartimento di Fisica e Astronomia "G. Galilei," Università degli Studi di Padova, I-35131 Padua, Italy*

[6]*Istituto Nazionale di Fisica Nucleare (INFN), Sezione di Padova, I-35131 Padua, Italy*

[7]*Paul Scherrer Institute, CH-5232 Villigen PSI, Switzerland*

[8]*Institute of Theoretical Physics (ITP) and Center for Integrated Quantum Science and Technology (IQST), Albert-Einstein-Allee 11, Universität Ulm, D-89081 Ulm, Germany*

[9]*Padua Quantum Technologies Research Center, Università degli Studi di Padova, I-35131 Padua, Italy*

(Received 14 March 2022; revised 4 April 2022; accepted 8 September 2022; published 12 December 2022)

Hyperpolarization of nuclear spins enhances nuclear magnetic resonance signals, which play a key role for imaging and spectroscopy in the natural and life sciences. This signal amplification unlocks previously inaccessible techniques, such as metabolic imaging of cancer cells. In this paper, electron spins from the photoexcited triplet state of pentacene-doped naphthalene crystals are used to polarize surrounding protons. As existing strategies are rendered less effective by experimental constraints, they are replaced with optimal control pulses designed with REDCRAB. In contrast to previous optimal control approaches, which consider one or two effective nuclei, this closed-loop optimization is macroscopic. A 26% improvement in signal and 15% faster polarization rate are observed. Additionally, a strategy called autonomously optimized repeated linear sweep (ARISE) is introduced to efficiently tailor existing hyperpolarization sequences in the presence of experimental uncertainty to enhance their performance. ARISE is expected to be broadly applicable in many experimental settings.

DOI: 10.1103/PhysRevResearch.4.043179

I. INTRODUCTION

Sensitive nuclear magnetic resonance (NMR) spectroscopy and magnetic resonance imaging (MRI) are key drivers in research areas from life sciences through material science to quantum computing. The feasibility and sensitivity of such experiments critically depend on the polarization of the utilized spins. Dynamic nuclear polarization (DNP) techniques have been shown to increase NMR signals by multiple orders of magnitude [1], enabling previously inaccessible imaging techniques [2]. DNP transfers the polarization from highly polarized electron spins to a target species of nuclear spins [3] used for NMR protocols. Electron spins are polarized, for example, by thermalization at low temperatures and high magnetic fields or by optical polarization of atoms and suitable molecules in gases, liquids, and solids [1,4–11]. In this paper, the electron spins of photoexcited triplet states in pentacene are used as the source of polarization, and the proton spins of naphthalene are used as the target. The final polarization of the sample is enhanced via the application of quantum optimal control (QOC) techniques to a dynamic nuclear polarization scheme in a closed-loop fashion. The efficiency of the overall proton polarization process is increased by optimizing the DNP transfer process using closed-loop QOC. To guide the algorithm towards a solution which produces a strongly increased signal, it is helpful to provide a good initial guess. Consequently, a new multistep protocol is introduced called autonomously optimized repeated linear sweep (ARISE). It provides a systematic approach to the improvement of "integrated solid effect"-like (ISE-like) linear sweep DNP sequences in the presence of an unknown experimental transfer function. The macroscopic properties of the polarized crystals have been further investigated in a separate publication [12] confirming an improved sample polarization of 25%.

Some background regarding the target quantum system and existing DNP strategies, as well as an introduction to QOC, is given in Sec. II. In Sec. III A the measurement techniques are explained in more detail, and a description of the

*These authors contributed equally to this work.

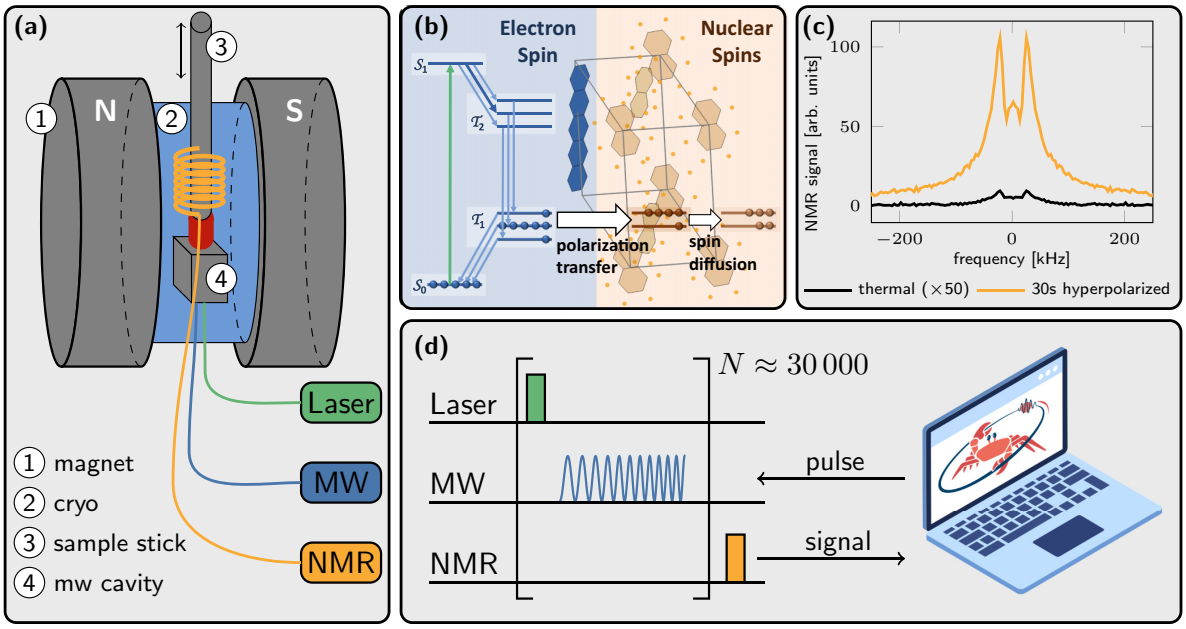

FIG. 1. Experimental realization. (a) Schematic of the in-house polarizer device. The sample (red) is mounted on a sample stick, which allows it to be moved between a MW cavity and an NMR coil inside a magnetic field at cryogenic temperatures. The laser is coupled to the system via an optical fiber. (b) Level scheme of pentacene (electron spin) and naphthalene-based protons (nuclear spins), including the effect of laser excitation (green) and natural decay (blue). Spin diffusion to external nuclear spins [17] is indicated. (c) 30 s of hyperpolarization show a clear signal enhancement compared with a 1-h thermal buildup; the thermal signal is scaled by a factor of 50 to emphasize its faint polarization peaks. (d) Schematic of the pulse sequence, consisting of a laser pulse for electron spin initialization and a MW pulse (of variable frequency) for polarization transfer to the nuclear spins. This basic block is repeated with a repetition rate of 1 kHz (i.e., 30 000 repetitions are performed in 30 s). After the polarization, the sample is shuttled into the NMR coil, where the magnetization is measured. An integral over the detected proton polarization is passed to REDCRAB, which provides the shape of the next MW pulse.

experimental setup is given in Sec. III B. The polarization results are introduced in Sec. IV A, and a description of the ARISE protocol is given Sec. IV B. The model used in the simulation is introduced in Sec. V, and details of the simulation are given in Sec. V A. In Sec. VI the results of the paper are put into context.

II. BACKGROUND

A. Pentacene-doped naphthalene crystals as a target

The system of naphthalene doped with pentacene, shown in Fig. 1(b), exhibits unique properties. In its ground state, the electron spin is in a singlet state, and therefore the host crystal is free of paramagnetic defects. Consequently, proton relaxation times of 50 h and above have been demonstrated at 77 K and 0.5 T [13].

In its metastable triplet state, the pentacene molecule exhibits a highly polarized electron spin with favorable lifetimes. Together with surrounding nuclear spins, this forms a central spin system that resembles other well-known systems such as nitrogen vacancy (NV) centers in diamond or phosphorus in silicon. This quantum resource for DNP leads to record values of 80% proton polarization [14], which amounts to a polarized proton concentration of 50 M. Exemplary applications of these nuclear-spin-polarized crystals are portable neutron spin filters in neutron scattering experiments [13,15] and polarization agents for NMR spectroscopy [12,16].

Under typical operating conditions (e.g., high magnetic field), electron and nuclear spins are mutually off-resonant, prohibiting direct polarization transfer. Advanced spin control methods, such as DNP, can be used to transfer polarization. Real-world experimental constraints such as material quality, field inhomogeneities, and limited power and bandwidth commonly impair the ideal performance of existing DNP methods. Under such constraints, the maximum achievable polarization is reduced, and the time to reach a certain polarization increases.

B. Existing DNP strategies

In the case where the heterogeneity among spins is sufficiently small, they are all equally well controllable. As a result, techniques such as nuclear orientation via electron-spin locking (NOVEL) [18,19] can be employed to transfer polarization. As the environmental complexity and inhomogeneity increase, other techniques are needed. Transferring polarization while counteracting a broad electron spin resonance (ESR) is done with the so-called "integrated solid effect" (ISE) [20,21]: After the electron spin initialization, either a linear magnetic field sweep is performed, while the sample is driven by a constant microwave (MW) field B_1, or a

linear MW frequency sweep is performed at a static magnetic field. The ISE method is notable for both its simplicity and its robustness and has been shown to reach up to 80% total nuclear polarization in naphthalene under optimized conditions (e.g., liquid He cooling, sample quality) [14]. It has also been applied to NV centers in diamond at room temperature [11,22–24]. While optimizing DNP sequences on a model, i.e., performing open-loop quantum optimal control, is one method to recover some of their performance [25–27], another is to employ closed-loop QOC by allowing an algorithm to directly control the experiment [shown in Fig. 1(d)] [28–32]. The latter approach is particularly appealing when the experimental setting is very complex or impossible to accurately model. Due to the complex molecular environment, coupled with experimental constraints, the system's true transfer function is obscured, making accurate simulation difficult.

C. Quantum optimal control

Many advances in quantum technology were only possible due to the design of sophisticated control strategies using methods of QOC [28–32]. Established methods of QOC include gradient-based algorithms such as gradient ascent pulse engineering (GRAPE) [33,34], the Krotov algorithm [35,36], or gradient-based algorithms based on automatic differentiation [37], as well as algorithms based on an expansion of the control pulse into a truncated basis such as the dressed chopped random basis (dCRAB) algorithm [32,38,39], typically coupled with direct search maximization algorithms. This pulse expansion ansatz can also be combined with the gradient approach [40–42]. The dCRAB algorithm is readily applicable to closed-loop control as it can be integrated directly with an experiment, allowing the user to treat the system as a black box. For this purpose, the dCRAB algorithm was implemented in the QOC software packages Remote-dCRAB (REDCRAB) [43–46] and its open-source version, Quantum Optimal Control Suite (QUOCS) [47]. Recently, REDCRAB enabled automatic calibration of quantum gates [45] and robust sensing operations [48] with NV centers in diamond, optimization of Bose-Einstein condensate (BEC) creation in ultracold atoms [46], and the creation of a 20-atom Schrödinger cat state with Rydberg atoms in an optical lattice [49].

III. METHODS

A naphthalene crystal doped with pentacene-d_{14} grown in-house provides the electron spin system used as the polarization target. The crystal is placed in a magnetic field of 230 mT at around 130 K. This temperature is chosen because this is the limit of the polarizer. A series of laser pulses initialize the pentacene molecules into their metastable spin-polarized triplet state $\mathcal{T}_2$ [see Fig. 1(a)] via the singlet state $\mathcal{S}_1$, from which it decays to the lower $\mathcal{T}_1$ triplet via intersystem crossing (ISC) [50]. Depending on the occupation of the $\mathcal{T}_1$ states, the pentacene returns to its ground state $\mathcal{S}_0$ after 80–180 μs. During this intermediate time, a MW DNP sequence transfers electron spin polarization to the densely packed proximal proton spins. Strong dipolar coupling among protons distributes polarization throughout the entire crystal via spin diffusion. The macroscopic proton polarization is measured via NMR spectroscopy after a 30-s buildup [see Fig. 1(c)].

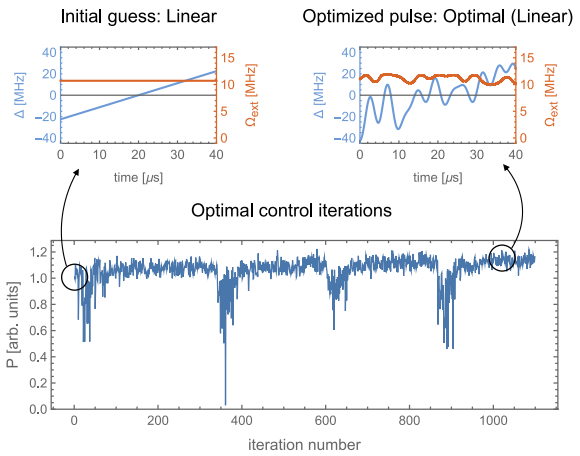

FIG. 2. Optimization procedure. Comparison between the linear sweep pulse (top left) and the pulse after optimization (top right). The MW amplitudes are shown in orange, and the detuning from cavity resonance is shown in blue, representing the control pulses, which are shaped during the optimization. Bottom: The change in the final polarization after the pulse over different sub- and superiterations during the optimization.

Starting from an external linear sweep (similar to ISE), and altering the amplitude and phase of the MW pulse using REDCRAB, this polarization is optimized (for more details, see Sec. IV B). The optimization starting from a linear sweep is shown in Fig. 2. Closed-loop QOC implicitly accounts for all experimental conditions influencing the transfer from optically initialized pentacene spins to macroscopic polarization. These could be, for example, the different lifetimes in the metastable state for different electron spin states or variations of the pentacene lifetimes throughout the crystal which might impact the final polarization.

Another potential source of uncertainty could be the strong variation of couplings between the electron and surrounding proton spins or the distribution of polarization via spin diffusion during and after the MW DNP sequence. Fluctuations in the experimental setup might also play a role, as bandwidth limitations of microwave equipment, spatial and spectral MW field variation inside the MW resonator, and spatial variation of laser intensity can also impact the efficiency. Additionally, it is challenging to control the amplitude of the MW field while its frequency is scanned across the resonance. Black-box (closed-loop) QOC does not directly incorporate variations in these parameters, whose role in polarization transfer is not understood; however, if they play a role, it can be captured by such an optimization. Importantly, some of these influences are very hard to predict theoretically.

A. Measurement technique

The crystal grown in-house is cleaved along the *ab* crystallographic plane and mounted on a sample holder [see

Fig. 1(a)] oriented along the b crystallographic axis. The sample holder is then attached to a motorized stage, enabling it to be shuttled into the MW cavity, where it is cooled to 130 K. Optically detected magnetic resonance (ODMR) can be observed in pentacene-doped naphthalene crystals, where the triplet state is created using a 556-nm laser pulse. By observing the fluorescence of the crystal under constant MW illumination, while changing the magnetic field, the electron spin resonance of pentacene can be found. The high-field transition of the pentacene triplet is used for both alignment and polarization. The crystal is then aligned by monitoring the ODMR spectrum while the sample is rotated; the best alignment is found when the resonance field is maximized. Rabi oscillations are observed with a maximum Rabi frequency of 19.3 MHz, by varying the duration of a resonant MW pulse.

B. Experimental realization

The experimental results are obtained in an in-house polarizer device, shown in Fig. 1(a), consisting of an optically accessible MW cavity inside an electromagnet operating at fields up to 800 mT. The experimental sequence used to hyperpolarize the sample is shown in Fig. 1(d). Within the MW cavity, photoexcited triplet states are created using a 556-nm pulsed laser with a repetition rate of 1 kHz delivering 0.35 mJ optical power in a 600-ns laser pulse every 1 ms and setting the timing of experiments. The spin state is then manipulated using a MW pulse in between laser pulses. Sophisticated pulse shapes can be sampled and uploaded to an arbitrary waveform generator (AWG) using the experiment control software QUDI [51]. The sample is attached to a holder that allows it to be shuttled into an NMR coil, which is located next to the MW cavity. Here, an NMR spectrometer (Magritek Kea^2) is used to read out the polarization of the proton spins using a 1Pulse measurement. This round trip takes approximately 40 s from the pulse engineered by the REDCRAB software to the NMR measurement, and the optimizations typically ran for 12 h. Integrating over the peak of the resulting NMR spectrum provides a relative estimate of the proton polarization. The REDCRAB algorithm is fed with this integrated signal and its estimated uncertainty to produce the next guess pulse.

An optional 532-nm continuous wave laser additionally allows the readout of the pentacene's electronic spin state optically; it is not used during closed-loop optimizations, but during the pentacene spin characterization experiments. Cooling of the sample is provided by a nitrogen gas flow system, which allows precise control of the temperature from 130 K to above room temperature; as previously mentioned the experiments are carried out at this lower limit.

IV. RESULTS

A. Polarization buildup

The optimization directly adjusts the pulse phase for experimental convenience, but as the detuning modulation Δ contains the same information and connects directly to the system dynamics, it is displayed in Fig. 3 instead. The first row of Fig. 3 shows the detuning modulation Δ as a function of time during the pulse. In the second row, the y axis shows the amplitude Ω during the pulse for both the externally applied field and the internal cavity field. The Hartmann-Hahn resonance [52], shown in orange, is calculated using the time-dependent detuning assuming the target spin is a proton. In the third row of Fig. 3, experimental data and simulation are compared, showing how the polarization builds up during the pulse.

The first initial guess pulse is an ISE-like linear sweep whose parameters (amplitude, sweep rate, and duration) had already been manually tuned in the experimental setup. The externally applied amplitude is kept constant, while the frequency is swept across the resonance. This pulse serves as the benchmark against which the optimized pulses are compared both in the experiment and in the simulation.

During the experiment, the polarization plateaus at the center of the pulse before continuing to rise in the second half of the pulse. The simulation results contain the same features. However, the plateau is shorter and the initial rise is slightly delayed compared with the experimental data. These differences might be caused by the lack of a full analytical model that extends the existing description of the cavity with distortions due to electronics and other components of the setup. It should be noted that polarization plateaus occur in the simulated results across all pulses when the detuning is above the resonance condition.

The optimization of this guess results in the pulse labeled "optimal (linear)," which shows a relative polarization improvement of approximately 19%. The evolution of the figure of merit (FoM) during the search for an optimized pulse and the comparison between the initial and the optimized version are shown in Fig. 2.

The "optimal (linear)" pulse transfers the majority of its polarization during the first 10 μs. It is notable that the detuning is oscillating during that time, and it crosses the cavity resonance several times. The algorithm slows the sweep down as the detuning approaches the resonance. Both features appear in multiple optimization outcomes. Arguably, if some electron population is left untransferred, subsequent sweeps through the resonance in both directions (from positive to negative detuning and back) can serve as additional opportunities for the polarization of more weakly coupled nuclear spins.

The relative speedup of the polarization transfer during this pulse is visible in both the simulation and the experiment. However, a divergence between the measurement and the simulation arises in the latter part of the pulse. This could be explained by the very fast oscillations in cavity field amplitude, which are not captured in full detail in the simulation, due to the unknown transfer function of the setup's electronics.

After analyzing the effect of the amplitude and phase of the pulse independently (see Appendix A for more details), the MW amplitude is kept constant in later optimizations. To further explore the idea that repeated sweeps through the resonance are beneficial, pulses with phase oscillations that use a range of frequencies and pulse durations are tested; see Appendix B for more details. The "sinusoidal" pulse shown in the third column of Fig. 3 is guessed in this manner. It outperforms the linear sweep by approximately 14%. The "sinusoidal" protocol in Fig. 3 then becomes the new guess pulse for the optimal control algorithm. After adding more frequency components, REDCRAB obtains the "optimal

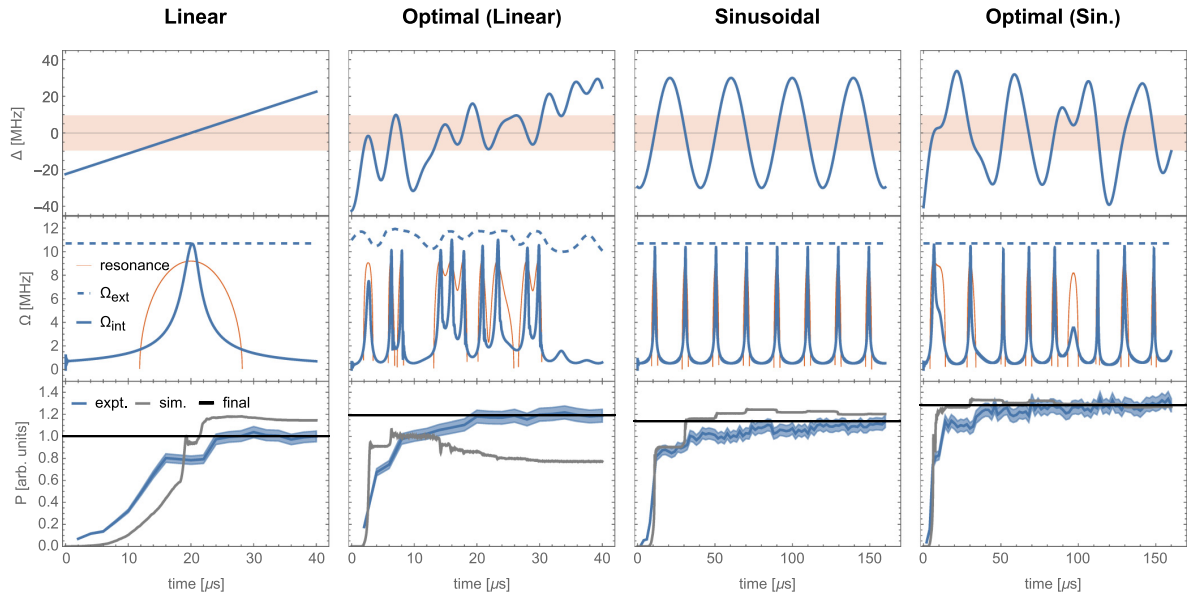

FIG. 3. Implementation of a selection of polarization pulses. From left to right, the figure presents the following MW pulse schemes on the resonator: The externally applied linear sweep, a linear sweep-based QOC-generated pulse, a sinusoidal sweep of the detuning, and a corresponding QOC-generated pulse. The first row gives the detuning applied by the drive with respect to time. The orange area comprises the window in which the Hartmann-Hahn resonance condition lies ($\Delta^2 = \omega_{0I}^2 - \Omega^2$). The second row shows the Rabi frequency as applied externally (dashed line), the field inside the cavity (solid blue line), and the resonance condition for the given detuning (thin orange line). The last row shows how the polarization builds up over the course of the pulse. Experimental values (expt.) are shown in blue, and theoretical values (sim. for simulation) are shown in gray. To make the comparison between the panels easier, we inserted a solid black line representing each pulse's final polarization. Optimal (Sin.), Optimal (sinusoidal).

(sinusoidal)" pulse. It outperforms all other pulses in both final polarization (approximately 28% higher with respect to the linear sweep for the short-buildup measurement) and polarization rate in our setup. When the pulse is significantly detuned from the resonance, as in the first 5 μs, the energy gap between the spins is large, and so very little polarization can be transferred. As this gap closes, the nuclei are more likely to be polarized, and the pulse slows down to allow for an extended transfer period. The detuning "slowdown" was re-created with an analytical polynomial function. (For details, see Appendix C.) The resulting "fitted optimal" pulse largely retains the polarization capability of the optimized pulse. The comparable efficiency corroborates that the "slowdown" feature contributes to the substantial polarization buildup during the first 30 μs. This behavior is reminiscent of optimal adiabatic passages with Landau-Zener protocols and optimal controlled crossings of quantum phase transitions. Both have been investigated in different theoretical and experimental scenarios [53–57] providing a basis for further exploration.

The simulated polarization of both the "sinusoidal" pulse and the "optimal (sinusoidal)" pulse matches the experimental data closely. Again, the initial step-plateau-step shape of the "sinusoidal" pulse is reduced after optimization. Almost all the performance gained by optimizing the pulses arises from the behavior during the first 40–50 μs of the pulse. This is on a timescale similar to that of the electron's decay to the singlet state. In the simulation, the polarization of the longer pulses slowly decreases after approximately 80 μs. This was not seen in the experiment, most likely due to spin diffusion. Many weakly coupled nuclear spins could lead to a slow distribution of polarization away from the electron spin. Spin diffusion is expected on a timescale of approximately 100 μs according to calculations of the dipolar interaction strength between the protons [17].

The key result of the paper is shown in Fig. 4, where the REDCRAB-optimized "optimal (sinusoidal)" pulse demonstrates two clear improvements over the linear sweep. Firstly, the magnitude of polarization increases by 26% when using the optimized pulse. Secondly, the optimized pulse reaches, in only 3.35 h, the same polarization that the linear sweep approach obtains after 9 h of continuously repeating the protocol, making it a factor of 2.6 faster. These times correspond to $\sim$98% of the maximum polarization of the linear sweep, which is within the error margin of the polarization measurements. The rate of polarization buildup is 15% faster compared with the linear sweep. This allows for more than doubling the number of polarized crystals in a given time. Previously, crystals were left to polarize overnight to reach sufficiently high polarization. Using the optimal protocol, it is now possible, in the current experimental setup, to polarize several crystals per day. Due to its increased performance, the "optimal (sinusoidal)" pulse was also applied as the hyperpolarization method of choice by Eichhorn *et al.* [12]. In that paper, a bulk crystal polarization of 25% is achieved using the optimized pulse.

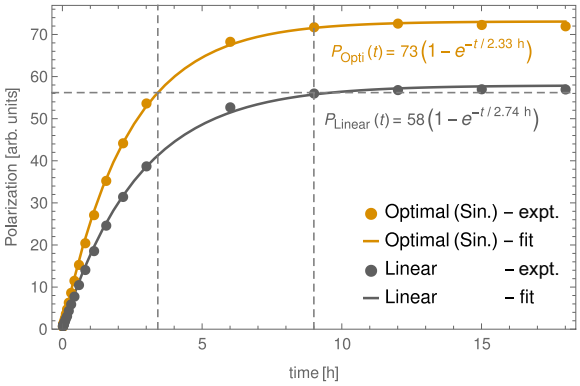

FIG. 4. Long-term polarization buildup: Comparing the polarization buildup using the optimal settings for the linear sweep and the REDCRAB-optimized pulse, shown in Fig. 3. Using closed-loop optimal control, a higher final polarization is reached in a shorter buildup time before saturation. The vertical dashed lines mark the times at which the polarization reaches 98% of the maximum polarization of the linear sweep pulse. This level is reached in 3.35 h using the optimized pulse, in contrast to 9 h with the linear sweep. The formulas placed in the figure correspond to the exponential fits, P_{Opti} and P_{Linear}, of the polarization buildup during the optimized pulse and the linear sweep, respectively.

The saturation of the polarization at this higher level is likely due to an equilibrium being reached between the polarizing sequence and the competing T_1 decay process of the nuclear spins [17]. The lifetime of the nuclear states is measured to be approximately 3–4 h under laser illumination, considering the specific values for the magnetic field B_0 and temperature. In this case, it is limited due to the laser illumination and MW fields causing, for example, additional heating. While this is the limit for the lifetime during polarization transfer, the polarization can be stored in the sample afterwards for much longer. Lifetimes between 50 h [12] and 800 h [13] have been reported for similar crystals at different temperatures and magnetic fields.

Additionally, by examining the shape of the optimized pulse and fitting its main features, a simplified analytical function is obtained describing the pulse (shown in Appendix C), labeled "fitted optimal"). This retains most of the enhanced performance of the optimized sweep.

B. ARISE

Generalizing the steps taken to achieve the results of the previous section, the autonomously optimized repeated linear sweep (ARISE) procedure is introduced. Each step provides a recipe for finding a good initial guess for the proceeding optimization. While this should be unimportant for an infinite-dimensionally parametrized optimization without limits and infinite measurement precision, in practice those restrictions apply, leading the algorithm to local instead of global optima. Despite the dCRAB algorithm's approach allowing it to escape local minima under certain circumstances, the optimization time is also drastically reduced if the initial guess is chosen carefully [32]. The protocol consists of three steps:

(i) Tune the linear sweep. Do a parameter search for the sweep range $\Delta_{\max}$ and duration t_{Linear} producing the most efficient polarization transfer.

(ii) Construct a multisweep. Set up a protocol which sweeps the detuning repeatedly between $\Delta_{\max}$ and $-\Delta_{\max}$ for N_{osc} times with a period τ. Do a parameter search for N_{osc} and τ, starting from $\tau = t_{\text{Linear}}$.

(iii) Apply quantum optimal control. Search the full function space of the detuning $\Delta(t)$ using an optimal control algorithm. The initial guess is provided by the multisweep protocol from the previous step.

In this paper, steps (i) and (ii) are accomplished through a simple parameter sweep. During step (ii), the detuning is swept with the function $-\Delta_{\max}\cos(2\pi t/\tau)$; however, this could be replaced by linear sweeps. As the setup requires the pulse phase $\varphi_{\text{ext}}(t)$ as an input, all detunings are translated to phase modulations (see Sec. V). In general, experimental feedback determines the best solution for the respective step. Here, it took the form of the proton NMR signal after 30 000 repetitions of the sequence. The third step is implemented using the REDCRAB software, which suggests different shapes for the phase of the pulse (see Appendix H).

V. THEORY

The spin system is modeled as an electron spin coupled to three nuclear spins. Both the electron and nuclear spins are considered to be spin-$\frac{1}{2}$ particles. A strong, constant magnetic field $\boldsymbol{B}_0 = B_0\hat{z}$ is aligned along the long axis of the pentacene molecule, representing the z axis. The total spin Hamiltonian of the electron can be written as

$$H_{\text{el}} = \frac{\hbar}{2}\omega_{0S}\sigma_z + \frac{\hbar^2}{4}\left[D\left(\sigma_z^2 - \frac{1}{3}\boldsymbol{\sigma}(\boldsymbol{\sigma}+1)\right) + E\left(\sigma_x^2 - \sigma_y^2\right)\right], \tag{1}$$

where $\boldsymbol{\sigma} = \{\sigma_x, \sigma_y, \sigma_z\}$ are the Pauli matrices. The Zeeman interaction is described by $\omega_{0S} = -\gamma_S B_0$, where γ_S is the electron spin's gyromagnetic ratio. The factors D and E correspond to the zero-field splitting [50,58]. The exact transition frequency is determined experimentally, and the magnetic field is aligned such that the splitting is symmetric.

As shown in Fig. 1(b) the electron spin of the pentacene molecule is excited to the $\mathcal{S}_1$ state with a short laser pulse. From there it decays to the triplet states $\mathcal{T}_2$ and subsequently $\mathcal{T}_1$ via intersystem crossing (ISC) [50]. $\mathcal{T}_1$ then couples to the nuclear spins in the vicinity of the molecule. The three states of the triplet correspond to spin quantum numbers $m_s = 0$ and $m_s = \pm 1$. An external magnetic field induces a Zeeman splitting of the $m_s = \pm 1$ levels, allowing for a two-level approximation. As the pentacene is deuterated, the resonances of the pentacene's own nuclear spins are shifted far enough from the other protons in the crystal that they can be neglected. The electron spin is assumed to have its origin at the center of the pentacene molecule. To extract the parallel and perpendicular dipolar coupling to the pentacene's electron spin, 574 protons of the nearest naphthalene molecules contained

in the $3 \times 3 \times 3$ unit cells around the pentacene molecule are modeled.

The driving field has a carrier frequency which is resonant with the electron spin $\omega_{\text{res}} = D - \omega_{0S}$. Its amplitude $\Omega_{\text{ext}}(t)$ and phase $\varphi_{\text{ext}}(t)$ are modulated to control the system. It is then transformed into the field inside the cavity Ω_{int} [the details are given below in Eq. (4)].

Coupling between the electron and nuclear spins is described by the hyperfine interaction tensor $\mathbf{A}^i$ with the nuclear spin indices $i = \{1, 2, 3\}$. A detuning Δ_{es} is introduced, describing the deviation of the field inside the cavity from the electron resonance frequency. In the rotating frame of the MW, and after applying the rotating wave approximation, the Hamiltonian is given by [59]

$$H = \hbar\Bigg(\text{Re}[\Omega_{\text{int}}(t)]S_x + \text{Im}[\Omega_{\text{int}}(t)]S_y + \Delta_{\text{es}}S_z + \omega_{\text{L}}\sum_{i=1}^{3} I_z^i + \sum_{i=1}^{3}\mathbf{S}\cdot\mathbf{A}^i\cdot\mathbf{I}^i\Bigg), \tag{2}$$

where $\mathbf{S} = \{S_x, S_y, S_z\}$ with $S_k = \frac{1}{2}\sigma_k \otimes \mathbb{1} \otimes \mathbb{1} \otimes \mathbb{1}$ $(k \in \{x, y, z\})$ are the electron's spin operators. $\mathbf{I}^i$ and I_k^i are the equivalent operators for the nuclear spin with index i, Ω_{int} is the complex, time-dependent field inside the cavity, and $\omega_{\text{L}} \approx 9.2$ MHz corresponds to the Larmor frequency of the nuclei. The voltage signal, which is fed into the AWG, is given by

$$V_{\text{ext}} = V(t)\cos\left((\omega_{\text{res}} + \Delta_{\text{cs}})t + \varphi_{\text{ext}}(t)\right). \tag{3}$$

The conversion between $V(t)$ and $\Omega_{\text{ext}}(t)$ is determined directly from experimental data. The phase modulation $\varphi_{\text{ext}}(t)$ can be translated into the drive detuning $\Delta(t) = \dot{\varphi}_{\text{ext}}(t)$.

The effect of the cavity on the external driving field is characterized by the cavity response factor γ_{cav} and given by the differential equation

$$\frac{\partial}{\partial t}\Omega_{\text{int}}(t) = \gamma_{\text{cav}}(\Omega_{\text{ext}}(t)\cdot e^{-i\varphi_{\text{ext}}(t)} - \Omega_{\text{int}}(t)) - i\Delta_{\text{cs}}\Omega_{\text{int}}, \tag{4}$$

where Δ_{cs} describes the constant detuning of the cavity from the resonance of the electron spin transition frequency [60].

In the secular approximation [61], only the dominant coupling terms along z are kept, giving

$$\mathbf{S}\cdot\mathbf{A}^i\cdot\mathbf{I}^i \approx S_z\cdot\left(A_{zx}^i I_x^i + A_{zy}^i I_y^i + A_{zz}^i I_z^i\right). \tag{5}$$

They are calculated for the respective position of the nucleus in the crystal structure by considering a purely dipolar interaction [62].

The static detuning values Δ_{es} for the Hamiltonian shown in Eq. (2) are drawn from a normal distribution with a full width at half maximum (FWHM) of 10 MHz to mimic additional frequency shifts due to magnetic field inhomogeneities and other impurities.

The system description includes the dephasing of the electron spin via a Lindblad operator $R_1 = \sqrt{\frac{\Gamma_{\text{el}}}{2}}S_z$, where Γ_{el} is the dephasing rate [63]. The only electron states that interact with surrounding nuclei are the $|0\rangle$ and $|1\rangle$ states in the $\mathcal{T}_1$ triplet (see Fig. 1). To account for the decay from $\mathcal{T}_1$ to $\mathcal{S}_0$, the model includes a shelf state, which does not interact with the drive. It is only coupled via the loss rates $\Gamma_{\text{loss},0}$ and $\Gamma_{\text{loss},1}$ from the respective triplet states. The corresponding Lindbladians are given by $R_2 = \sqrt{\Gamma_{\text{loss},0}}\,\sigma_{-,0}$ and $R_3 = \sqrt{\Gamma_{\text{loss},1}}\,\sigma_{-,1}$ with $\sigma_{-,0} = |s\rangle\langle 0|$ and $\sigma_{-,1} = |s\rangle\langle 1|$.

The evolution of the density matrix is then solved using the Lindblad master equation

$$\dot{\rho} = -\frac{i}{\hbar}[H, \rho] + \sum_{j=1,2,3}\left(R_j\rho R_j^\dagger - \frac{1}{2}R_j^\dagger R_j\rho - \frac{1}{2}\rho R_j^\dagger R_j\right), \tag{6}$$

where ρ is the density matrix of the system.

A. Simulation

The solutions to the differential equations in Eqs. (6) and (4) are calculated numerically using DIFFERENTIALEQUATIONS.JL [64] and other JULIA packages [65–78]. To obtain a realistic polarization buildup, Eq. (6) is solved for and averaged over 1000 instances. For each instance, three random but distinct nuclei are picked from the 30 most strongly coupled nuclei, and the detuning Δ_{es} is sampled from a Gaussian distribution. This way, mechanisms which are neglected in the common weighted-sum single-nucleus approximation are captured. Examples include the repolarization of the electron spin through partially polarized nuclei or the redistribution of polarization from one nucleus to another. The mean over many runs with different coupling combinations takes into account the variety of couplings in the system with reasonable computational resources.

The cavity response γ_{cav} is determined by repeatedly applying constant external drive fields with different cavity detunings Δ_{cs}, obtaining a photon count that corresponds to the electron state.

B_0 is adjusted such that the spin always stays resonant with the drive frequency. Oscillations are recorded for times up to 0.6 μs from the start of the drive pulse. The detuning is swept through a range of ± 25 MHz around the resonance. The maximum of the Fourier transform of the photon count then corresponds to the Rabi frequency Ω for a detuning Δ_{cs}. The cavity dynamics are complex, leading to a response similar to the example shown at the top right of Fig. 5. These measurements are modeled for an electron spin inside a cavity with a response factor γ_{cav} between 5 and 14 MHz (range suggested by response time based on the measured Q factor of the resonator using a spectrum analyzer). The resulting Fourier transforms are compared with the experimental values. The comparison was done by calculating the overlap of the normalized measurement and simulation grids, as shown in Fig. 5. The minimum of the sum of the absolute difference between each grid point of the measurement and simulation data is obtained by a Gaussian fit resulting in $\gamma_{\text{cav}} = 9.24$ MHz.

The values for the decoherence rate, Γ_{el}, of the electron spin and the loss rates to the shelf state, $\Gamma_{\text{loss},0}$ and $\Gamma_{\text{loss},-1}$, are found by performing a Hahn echo measurement and state-dependent lifetime measurements. For the dephasing time of the electron, $1/\Gamma_{\text{el}} = 10$ μs is obtained, and the

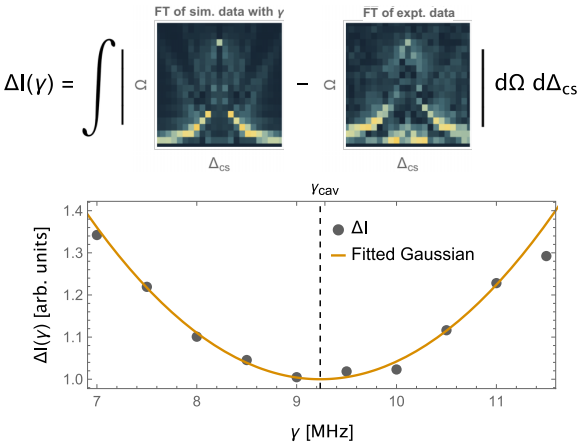

FIG. 5. Characterization of the setup via response factor γ. The agreement between experiment and simulation, ΔI, is calculated via the Fourier transform Ω of the driven Rabi signal for varying cavity detunings (top). The integral indicates the overlap of measured and simulated distributions, which is shown for different values of cavity response fed to the simulation in the bottom plot. The dashed black line indicates the minimum of the error in overlap between simulation end experiment at $\gamma_{\text{cav}} = 9.24$ MHz (bottom). FT, Fourier transform.

triplet-state decay times are measured to be $1/\Gamma_{\text{loss},0} = 80\ \mu$s and $1/\Gamma_{\text{loss},-1} = 180\ \mu$s.

VI. DISCUSSION AND OUTLOOK

The use of closed-loop optimal control provides a strategy for improving hyperpolarized NMR signals in complex experimental setups despite the unknown transfer function. A concern often raised about numerically optimized sequences is that they lose generality and only apply to a specific setup or sample. In contrast, the "optimal (sinusoidal)" protocol has been successfully applied on different crystals with varying spin relaxation times across an extended period of time [12]. It is now the gold-standard pulse in the laboratory.

The combination of a 15% faster polarization rate and a 26% higher polarization level provides a factor of 2.6 reduction in the time taken to polarize crystals to within the margin of error of the previous method. As a result, multiple crystals can be polarized per day to be used in external hyperpolarization experiments [12]. Furthermore, these improvements lead to higher levels of polarization in a shorter time, resulting in an overall polarization within the crystal of about 25% [12]. Such strongly polarized crystals are necessary to transfer polarization to external nuclear spins. By operating under liquid helium conditions and with improved crystal quality, even higher values are anticipated [14]. Mimicking the features of the optimized pulse by fitting an analytical function to it (as shown in Appendix C) retains almost all the improved performance. It represents a good starting point not only for future optimization, but also for further investigations of the system dynamics.

A key feature of all the sequences that outperform the linear sweep is that they repeatedly sweep through the cavity resonance. Hence the sequences are given an extra opportunity to transfer polarization, suggesting that the first sweep leaves some electron polarization untransferred. The simulation shows that the first sweep primarily transfers to one of the most strongly coupled nuclear spins, while subsequent sweeps redistribute the polarization to a wider range of couplings. This type of dynamics can only be accounted for when multiple nuclear spins are considered or the optimization is done on a macroscopic system.

The ARISE protocol offers a starting point for future optimizations of DNP sequences using both open- and closed-loop protocols. Inherently flexible, the protocol is easily customized to fit any number of setups, including the complex molecular environment seen here.

In conclusion, the application of the ARISE protocol results in a 26% improvement in the polarization level and 15% faster polarization rate. Consequently, crystals were efficiently polarized to 25% bulk proton polarization. These crystals were then used as the polarization source for an external hyperpolarization experiment [12] which demonstrated strong transfer to external spins.

ACKNOWLEDGMENTS

The authors would like to acknowledge receiving funding from the European Union's Horizon 2020 research and innovation program under the Marie Skłodowska-Curie project QuSCo (Grant No. 765267), EU Quantum Flagship projects ASTERIQS (Grant No. 820394) and PASQuANS (Grant No. 817482), and the ERC Synergy grant HyperQ (Grant No. 856432).

APPENDIX A: AMPLITUDE VERSUS PHASE VARIATION

To separate the respective effects of amplitude and phase modulation, these two parameters are investigated independently (Fig. 6). The first test was a basic linear sweep and the "optimal (linear)" pulse, where it was observed that the optimized pulse leads to higher polarization. To test only the optimized amplitude modulation, the optimized phase is reset to the initial guess while the phase modulation was kept ("optimal amplitude + linear phase"). Similarly, to test the optimized phase modulation, the amplitude is held constant, as in the linear sweep, and the optimized phase is applied ("linear amplitude + optimal phase").

By comparing those four pulses, it becomes clear that the amplitude modulation plays no role in the polarization transfer and only the pulses with optimally controlled phase modulation lead to enhanced polarization (highlighted in Fig. 6). Testing the phase of the optimized pulses with different constant MW amplitudes shows that using a higher MW amplitude always leads to better polarization transfer (see Fig. 8 in Appendix C).

APPENDIX B: SINE OSCILLATION FREQUENCY TESTS

Following the idea that subsequent sweeps through the resonance in alternating directions further enhance the

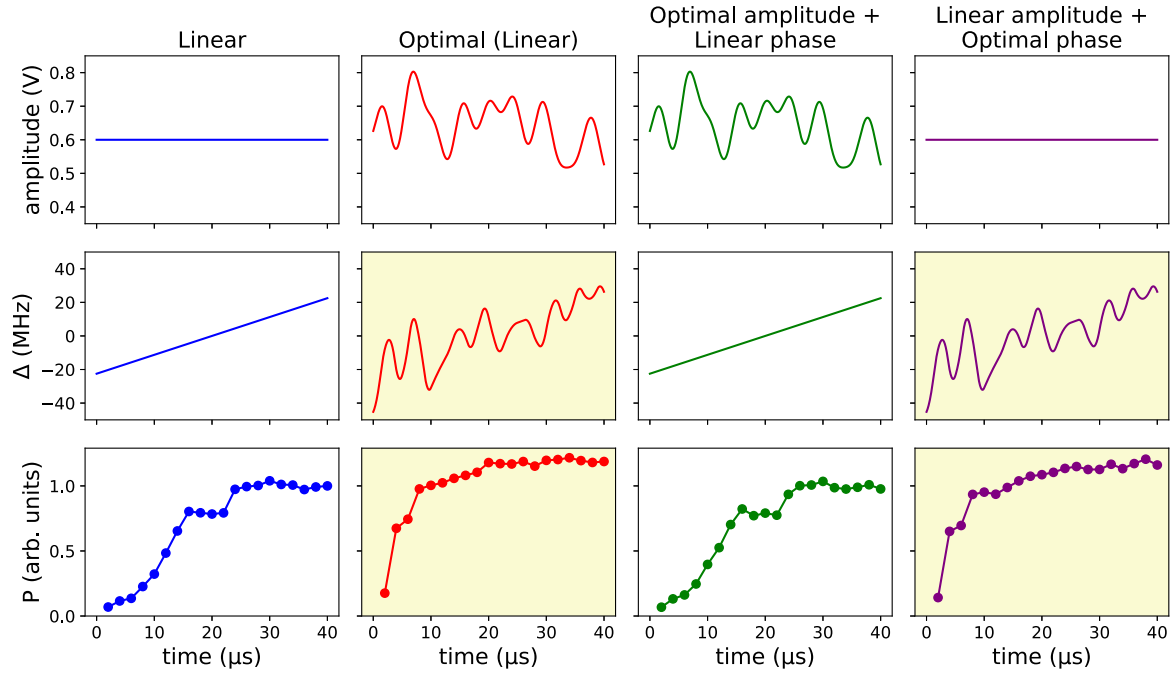

FIG. 6. Amplitude vs phase variations: Comparing the linear sweep ("linear") with the corresponding QOC-generated pulse ["optimal (linear)"], as well as combinations of both. In the third and fourth columns the amplitude array of one is combined with the phase array of the other ("optimal amplitude + linear phase" and "linear amplitude + optimal phase"). The increase in polarization over the optimization is caused solely by the changes in phase rather than amplitude (compare highlighted plots).

polarization, a sinusoidal pulse is tried. To find the optimal pulse, both the frequency of the oscillation and the number of resonance passages were varied. For better comparison, the length of a half oscillation is used as a parameter instead of the frequency, which means passing through the resonance once, similar to a basic ISE-like linear sweep [Fig. 7(a)]. The second parameter, which describes the passages through the resonance, is then given by the number of half oscillations [examples given in Fig. 7(c)].

In Fig. 7(b) the polarization for different parameter sets (length and number of half oscillation) is compared with the standard linear sweep (dashed line). Increasing the number of resonance passages leads to an increase in polarization for all lengths. While most of the applied pulses beat the standard linear pulse, a maximum polarization for a length of 20 μs and eight half oscillations was found [Fig. 7(d)]. This pulse was characterized in the main text and used a new starting point for the sinusoidal-based optimal control.

APPENDIX C: FITTED OPTIMIZED PULSE

The "fitted optimal" pulse shown on the right-hand side in Fig. 8 was designed by modeling the shoulder feature of the sinusoidal-based optimal control (OC) pulse resulting from closed-loop optimizations of the sinusoidally varying pulse in the detuning regime. Repeating mirrored polynomial functions emulate the slowdown of the detuning sweep around resonance. A variation of the externally applied voltage kept constant during the pulses displays an improvement of polarization transfer for higher external drive amplitude. Except for the highest driving amplitudes, at the limit of the experimental capabilities, the fitted pulse is equal to or outperforms the pulse resulting from the closed-loop iterations. Therefore it serves as a good starting point for use in other, similar setups and further optimizations as well as theoretical and analytical transfer calculations and numerical simulations.

APPENDIX D: NAÏVE SWEEP CORRECTIONS

While a linear sweep is applied outside the cavity, the mentioned effects lead to a nonlinear sweep inside the cavity. However, the drive would appear faster when passing through the cavity resonance, compared with the part of the sweep far outside the resonance. Measuring the cavity linewidth and Q factor allows the calculation of the expected deviation from the linear sweep. Calculating an input function with modified amplitude that takes the cavity properties into account would be the first naïve approach to overcome this issue. Trying this did not, however, improve the polarization values.

APPENDIX E: COHERENCE MEASUREMENTS

The nuclear spin relaxation time T_1 and the electron spin coherence time T_2 were measured. For the nuclear spin relaxation time T_1 measured under experimental conditions (e.g., temperature, laser illumination), a value of around 223 min (Fig. 9, top) was recorded. For the coherence time of the electron spin, T_2, a standard Hahn-echo sequence [79] was

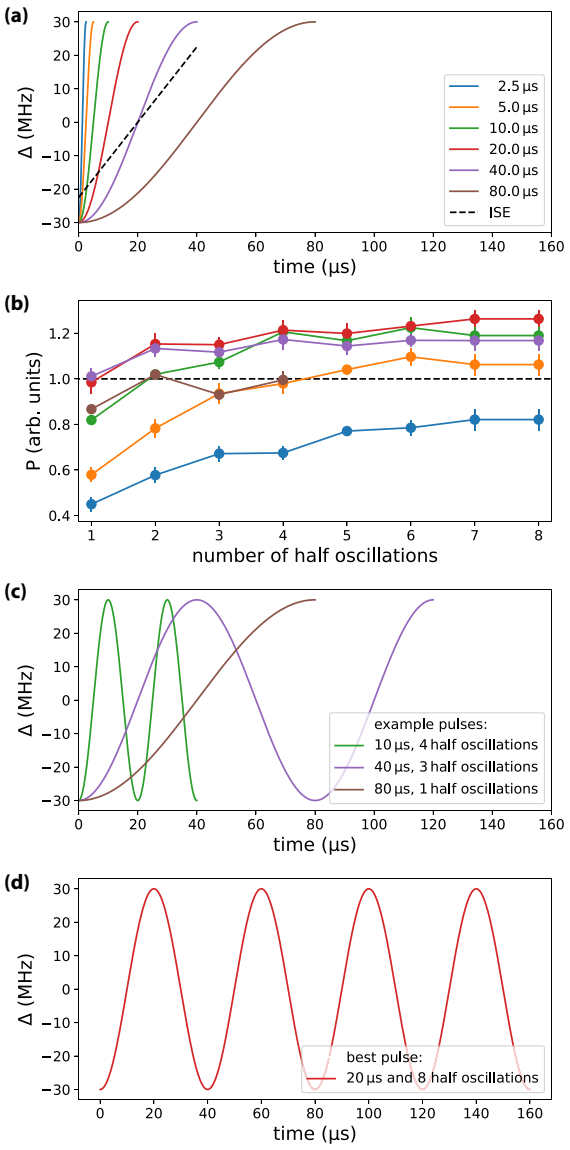

FIG. 7. Comparing different sinusoidal pulses. (a) Half oscillations with different frequencies comparable to different speeds of the ISE-like linear sequences. (b) For all six frequencies in (a), the polarization after up to eight half oscillations is measured and compared with the polarization after the linear sweep (dashed line). (c) Example pulses to visualize the idea of the measurement. (d) Sinusoidal pulse that gave the highest polarization.

used, and a value of around 9 μs was obtained (Fig. 9, bottom).

APPENDIX F: POLARIZATION BUILDUP

Polarization p in the crystal is built up by iteratively applying the basic polarization sequence many times (see Fig. 3 in the main text). The final polarization will be given at the

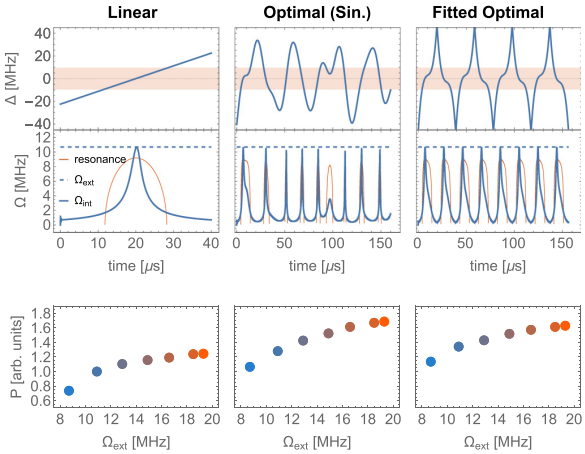

FIG. 8. Polarization performance of the linear sweep ("linear"), the QOC pulse generated from a sinusoidal initial guess ["optimal (sinusoidal)"], and its fit ("fitted optimal") for increasing constant drive amplitudes. Guided by the outcome of the optimal control algorithm, the first ~20 μs of the "optimal (sinusoidal)" pulse are remodeled analytically by tuning polynomial functions to match the detuning's shoulder feature. Even for lower Rabi frequencies, the optimized pulses outperform the initial ISE-like linear approach.

equilibrium of two competing effects: Each time the basic sequence is applied, a fraction $\alpha(1-p)$ of the remaining unpolarized nuclear spins will be polarized, where α is the polarization power of the sequence. At the same time, the polarized nuclear spins decay at a constant rate γ.

$$\frac{dp}{dt} = \alpha(1-p) - \gamma p. \tag{F1}$$

Solving Eq. (F1) leads to the equation

$$p(t) = p_{\max}(1 - e^{-\tilde{\gamma}t}), \tag{F2}$$

where $p_{\max} = \alpha/(\gamma+\alpha)$ and the parameter $\tilde{\gamma} = \gamma + \alpha$ can be obtained from a fit to the data. From the polarization built up while applying a linear sweep, $\tilde{\gamma} \approx 0.0061$ min^{-1} and $p_{\max} \approx 14\,140$ arb. units are obtained. When applying the optimal sequence, $\tilde{\gamma} \approx 0.0071$ and $p_{\max} \approx 17\,850$ arb. units are obtained. An additional measurement, T_1, gives $1/\gamma \approx 223$ min (Fig. 9, top). This translates into estimates for the final polarization of $p_{\max} \approx (27.8 \pm 1.3)\%$ for the linear sweep and $p_{\max} \approx (35.1 \pm 1.7)\%$ for the optimal sequence. Note that the true value of γ is probably slightly larger than in the T_1 measurement due to the polarization pulse sequences. If, for example, $1/\gamma \approx 200$ min (or $1/\gamma \approx 180$ min) is considered, the polarization for the optimal sequence drops to $p_{\max} \approx (26.2 \pm 3.4)\%$ [or $p_{\max} \approx (16.5 \pm 5.2)\%$] and similarly for the linear sweep.

APPENDIX G: EFFECT OF THE NUMBER OF NUCLEI ON THE MODEL

Each electron spin is surrounded by a large number of protons, forming the nuclear spin bath. As only a limited number can be simulated at a time, subgroups of nuclei are considered

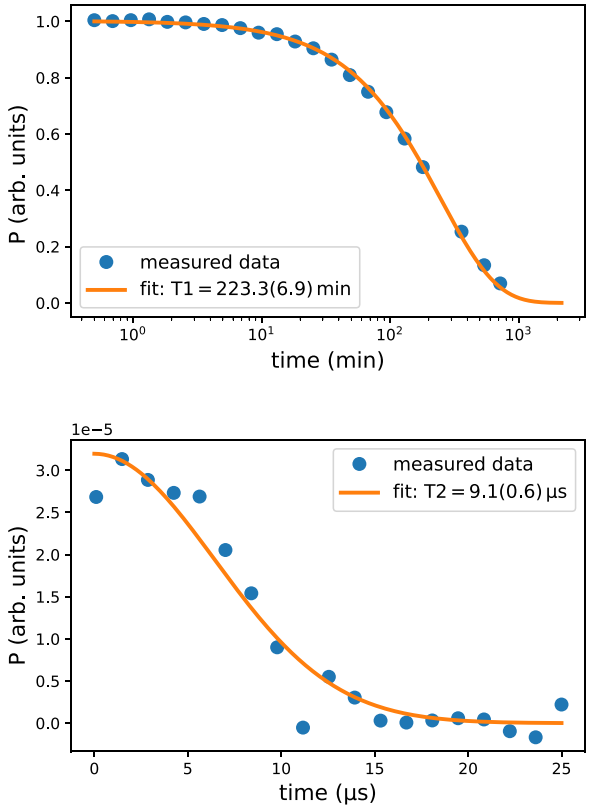

FIG. 9. Top: T_1 measurement of the nuclear spins under experimental conditions. Bottom: T_2 measurement of the electron spin via Hahn echo.

and averaged over. Fortunately, the molecular and crystallographic properties of the naphthalene-h_8 specimen doped with pentacene-d_{14} are well known. Hence the orthogonal (A^i_{zx}, A^i_{zy}) and parallel (A^i_{zz}) parts of the hyperfine tensor can be directly calculated [62] for the surrounding protons in the crystal. Instead of including the entire bath as a single effective nuclear spin [59], several nuclei are considered individually in the polarization dynamics. This step is necessary to reflect the effects caused by complex pulse shapes obtained by the optimization, as well as the distortion by the cavity. Since the pulses cross the resonance line multiple times and are repeated successively for polarization buildup, strongly coupled nuclei are usually polarized first but can be depolarized again so that excitation is transferred to other nuclear spins. Because the electron spin is reinitialized before each pulse application, each iteration can polarize different nuclei. Up to six nuclei were considered during the initial investigation. However, for the figures presented in this paper, the following combination of spins was used to keep computational resources within an acceptable range: The electron spin is coupled to three nuclear spins, where the hyperfine coupling values are randomly selected from the top 30 most strongly coupled protons. This simulation is repeated and averaged for 1000 sets using three different random nuclei in each run. This captures the dynamics of multiple protons coupling to the electron at the same time, as well as the repetition of the transfer operation in the experiment.

APPENDIX H: QUANTUM OPTIMAL CONTROL

Optimal control methods aim to optimize a functional f by modifying time-dependent control functions $u_i(t)$. This functional is the figure of merit (FoM); it includes all the relevant information contributing to the quality of an operation. To simplify the optimization problem, the controls can be parametrized in terms of N_{be} basis functions $v_\ell(t)$ with corresponding parameters c_ℓ

$$u_i(t) = \sum_{\ell=1}^{N_{\mathrm{be}}} c_\ell v_\ell(t). \tag{H1}$$

The FoM therefore depends on the coefficients of these basis functions:

$$\mathrm{FoM}(u_i) = f(c_\ell, v_\ell, t). \tag{H2}$$

The solution to the problem is found using an iterative optimization algorithm, which takes in the FoM for a defined set of parameters and returns a new set of parameters. Closed-loop control involves the algorithm directly interacting with the experimental setup. Hence it automatically takes into account real-world imperfections. Specifics of the measurement technique can be found in Sec. III A of the main text. The algorithm improves the FoM by comparing the results from different iterations. It follows the direction of improvement, while exploring the parameter landscape and exploiting its features. An optimal set of controls is eventually obtained after a number of iterations and FoM evaluations.

Limiting the size of the parameter landscape reduces the number of experimental runs and hence the total optimization time. The dCRAB algorithm [32,38,39,80], in combination with the Nelder-Mead [81,82] simplex optimization algorithm, is a good choice for this. A small parameter space is created by randomly picking a number of basis functions, finding the optimal parameters for them, and then switching to a new basis set. An optimization in a single parameter space is called a superiteration. This allows the optimization to start afresh and continue, even if it temporarily gets stuck in a local optimum.

For the parametrization the Fourier basis is chosen, which provides a simple method to restrict the bandwidth of the controls by limiting their maximum oscillation frequency component through a capping of $\omega_{d,\ell}$ in

$$u(t) = \sum_{d=1}^{N_{\mathrm{SI}}} \sum_{\ell=1}^{N_{\mathrm{be}}} \left[A^{\mathrm{opt}}_{d,\ell} \sin(\omega_{d,\ell} t) + B^{\mathrm{opt}}_{d,\ell} \cos(\omega_{d,\ell} t) \right]. \tag{H3}$$

N_{be} represents the number of basis elements (i.e., the size of the parameter space in each superiteration), while N_{SI} corresponds to the number of superiterations. The parameter space of the optimization is spanned by $c_{d,\ell} = \{A^{\mathrm{opt}}_{d,\ell}, B^{\mathrm{opt}}_{d,\ell}\}$, while $\omega_{d,\ell}$ is randomly initialized with frequencies within a predefined interval for each superiteration defining the basis functions $v_{d,\ell} = \{\sin(\omega_{d,\ell} t), \cos(\omega_{d,\ell} t)\}$. Meanwhile, the length of the pulses is kept constant.

The combination of this limited search space for efficient closed-loop optimization together with the three-step ARISE protocol (see Sec. IV B in the main text) enables the encoding of a sufficient amount of information in the control pulse to substantially increase its performance [83].

[1] J. H. Ardenkjaer-Larsen, B. Fridlund, A. Gram, G. Hansson, L. Hansson, M. H. Lerche, R. Servin, M. Thaning, and K. Golman, Increase in signal-to-noise of >10,000 times in liquid-state NMR, Proc. Natl. Acad. Sci. USA **100**, 10158 (2003).

[2] Z. J. Wang, M. A. Ohliger, P. E. Z. Larson, J. W. Gordon, R. A. Bok, J. Slater, J. E. Villanueva-Meyer, C. P. Hess, J. Kurhanewicz, and D. B. Vigneron, Hyperpolarized ^{13}C MRI: State of the art and future directions, Radiology **291**, 273 (2019).

[3] K. Tateishi, M. Negoro, S. Nishida, A. Kagawa, Y. Morita, and M. Kitagawa, Room temperature hyperpolarization of nuclear spins in bulk, Proc. Natl. Acad. Sci. USA **111**, 7527 (2014).

[4] D. M. Lilburn, G. E. Pavlovskaya, and T. Meersmann, Perspectives of hyperpolarized noble gas MRI beyond ^{3}He, J. Magn. Reson. **229**, 173 (2013).

[5] M. S. Albert Jr, G. Cates, B. Driehuys, W. Happer, B. Saam, C. Springer Jr, and A. Wishnia, Biological magnetic resonance imaging using laser-polarized ^{129}Xe, Nature (London) **370**, 199 (1994).

[6] M. Auzinsh and R. Ferber, *Optical Polarization of Molecules* (Cambridge University Press, Cambridge, 2005).

[7] T. E. Lee, S. Gopalakrishnan, and M. D. Lukin, Unconventional Magnetism via Optical Pumping of Interacting Spin Systems, Phys. Rev. Lett. **110**, 257204 (2013).

[8] G. Liu, S.-H. Liou, N. Enkin, I. Tkach, and M. Bennati, Photo-induced radical polarization and liquid-state dynamic nuclear polarization using fullerene nitroxide derivatives, Phys. Chem. Chem. Phys. **19**, 31823 (2017).

[9] J. P. King, K. Jeong, C. C. Vassiliou, C. S. Shin, R. H. Page, C. E. Avalos, H.-J. Wang, and A. Pines, Room-temperature *in situ* nuclear spin hyperpolarization from optically pumped nitrogen vacancy centres in diamond, Nat. Commun. **6**, 8965 (2015).

[10] P. London, J. Scheuer, J.-M. Cai, I. Schwarz, A. Retzker, M. B. Plenio, M. Katagiri, T. Teraji, S. Koizumi, J. Isoya, R. Fischer, L. P. McGuinness, B. Naydenov, and F. Jelezko, Detecting and Polarizing Nuclear Spins with Double Resonance on a Single Electron Spin, Phys. Rev. Lett. **111**, 067601 (2013).

[11] J. Scheuer, I. Schwartz, Q. Chen, D. Schulze-Sünninghausen, P. Carl, P. Höfer, A. Retzker, H. Sumiya, J. Isoya, B. Luy, M. B. Plenio, B. Naydenov, and F. Jelezko, Optically induced dynamic nuclear spin polarisation in diamond, New J. Phys. **18**, 013040 (2016).

[12] T. R. Eichhorn, A. J. Parker, F. Josten, C. Müller, J. Scheuer, J. M. Steiner, M. Gierse, J. Handwerker, M. Keim, S. Lucas, M. U. Qureshi, A. Marshall, A. Salhov, Y. Quan, J. Binder, K. D. Jahnke, P. Neumann, S. Knecht, J. W. Blanchard, M. B. Plenio *et al.*, Hyperpolarized solution-state NMR spectroscopy with optically polarized crystals, J. Am. Chem. Soc. **144**, 2511 (2022).

[13] Y. Quan, B. van den Brandt, J. Kohlbrecher, W. Wenckebach, and P. Hautle, A transportable neutron spin filter, Nucl. Instrum. Methods Phys. Res., Sect. A **921**, 22 (2019).

[14] Y. Quan, N. Nekitic, B. van den Brandt, and P. Hautle, A novel broad-band neutron spin filter based on dynamically polarized protons using photo-excited triplet states, EPJ Web Conf. **219**, 10006 (2019).

[15] Y. Quan, B. van den Brandt, J. Kohlbrecher, and P. Hautle, Polarization analysis in small-angle neutron scattering with a transportable neutron spin filter based on polarized protons, J. Phys.: Conf. Ser. **1316**, 012010 (2019).

[16] H. Kouno, Y. Kawashima, K. Tateishi, T. Uesaka, N. Kimizuka, and N. Yanai, Nonpentacene polarizing agents with improved air stability for triplet dynamic nuclear polarization at room temperature, J. Phys. Chem. Lett. **10**, 2208 (2019).

[17] A. C. Pinon, J. Schlagnitweit, P. Berruyer, A. J. Rossini, M. Lelli, E. Socie, M. Tang, T. Pham, A. Lesage, S. Schantz, and L. Emsley, Measuring nano- to microstructures from relayed dynamic nuclear polarization NMR, J. Phys. Chem. C **121**, 15993 (2017).

[18] A. Henstra, P. Dirksen, J. Schmidt, and W. Wenckebach, Nuclear spin orientation via electron spin locking (NOVEL), J. Magn. Reson. (1969–1992) **77**, 389 (1988).

[19] H. Brunner, R. H. Fritsch, and K. H. Hausser, Notizen: Cross polarization in electron nuclear double resonance by satisfying the Hartmann-Hahn condition, Z. Naturforsch., A, Phys. Sci. **42**, 1456 (1987).

[20] A. Henstra, P. Dirksen, and W. Wenckebach, Enhanced dynamic nuclear polarization by the integrated solid effect, Phys. Lett. A **134**, 134 (1988).

[21] A. Henstra, T.-S. Lin, J. Schmidt, and W. Wenckebach, High dynamic nuclear polarization at room temperature, Chem. Phys. Lett. **165**, 6 (1990).

[22] K. Miyanishi, T. F. Segawa, K. Takeda, I. Ohki, S. Onoda, T. Ohshima, H. Abe, H. Takashima, S. Takeuchi, A. I. Shames, K. Morita, Y. Wang, F. T.-K. So, D. Terada, R. Igarashi, A. Kagawa, M. Kitagawa, N. Mizuochi, M. Shirakawa, and M. Negoro, Room-temperature hyperpolarization of polycrystalline samples with optically polarized triplet electrons: Pentacene or nitrogen-vacancy center in diamond? Magn. Reson. **2**, 33 (2021).

[23] I. Schwartz, J. Scheuer, B. Tratzmiller, S. Müller, Q. Chen, I. Dhand, Z.-Y. Wang, C. Müller, B. Naydenov, F. Jelezko, and M. B. Plenio, Robust optical polarization of nuclear spin baths using Hamiltonian engineering of nitrogen-vacancy center quantum dynamics, Sci. Adv. **4**, eaat8978 (2018).

[24] Q. Chen, I. Schwarz, F. Jelezko, A. Retzker, and M. B. Plenio, Optical hyperpolarization of ^{13}C nuclear spins in nanodiamond ensembles, Phys. Rev. B **92**, 184420 (2015).

[25] H. Yuan, R. Zeier, N. Pomplun, S. J. Glaser, and N. Khaneja, Time-optimal polarization transfer from an electron spin to a nuclear spin, Phys. Rev. A **92**, 053414 (2015).

[26] N. Pomplun, B. Heitmann, N. Khaneja, and S. J. Glaser, Optimization of electron–nuclear polarization transfer, Appl. Magn. Reson. **34**, 331 (2008).

[27] N. Pomplun and S. J. Glaser, Exploring the limits of electron-nuclear polarization transfer efficiency in three-spin systems, Phys. Chem. Chem. Phys. **12**, 5791 (2010).

[28] C. Brif, R. Chakrabarti, and H. Rabitz, Control of quantum phenomena: Past, present and future, New J. Phys. **12**, 075008 (2010).

[29] S. J. Glaser, U. Boscain, T. Calarco, C. P. Koch, W. Köckenberger, R. Kosloff, I. Kuprov, B. Luy, S. Schirmer, T. Schulte-Herbrüggen, D. Sugny, and F. K. Wilhelm, Training Schrödinger's cat: Quantum optimal control, Eur. Phys. J. D **69**, 279 (2015).

[30] C. P. Koch, Controlling open quantum systems: Tools, achievements, and limitations, J. Phys.: Condens. Matter **28**, 213001 (2016).

[31] P. Rembold, N. Oshnik, M. M. Müller, S. Montangero, T. Calarco, and E. Neu, Introduction to quantum optimal control for quantum sensing with nitrogen-vacancy centers in diamond, AVS Quantum Sci. **2**, 024701 (2020).

[32] M. M. Müller, R. S. Said, F. Jelezko, T. Calarco, and S. Montangero, One decade of quantum optimal control in the chopped random basis, Rep. Prog. Phys. **85**076001 (2022).

[33] N. Khaneja, T. Reiss, C. Kehlet, T. Schulte-Herbrüggen, and S. J. Glaser, Optimal control of coupled spin dynamics: Design of NMR pulse sequences by gradient ascent algorithms, J. Magn. Reson. **172**, 296 (2005).

[34] S. Machnes, U. Sander, S. J. Glaser, P. de Fouquières, A. Gruslys, S. Schirmer, and T. Schulte-Herbrüggen, Comparing, optimizing, and benchmarking quantum-control algorithms in a unifying programming framework, Phys. Rev. A **84**, 022305 (2011).

[35] A. I. Konnov and V. F. Krotov, On global methods for the successive improvement of control processes, Avtomat. i Telemekh. **60**, 77 (1999) [Autom. Remote Control (Engl. Transl.) **60**, 1427 (1999)].

[36] M. H. Goerz, D. Basilewitsch, F. Gago-Encinas, M. G. Krauss, K. P. Horn, D. M. Reich, and C. P. Koch, Krotov: A Python implementation of Krotov's method for quantum optimal control, SciPost Phys. **7**, 080 (2019).

[37] N. Leung, M. Abdelhafez, J. Koch, and D. Schuster, Speedup for quantum optimal control from automatic differentiation based on graphics processing units, Phys. Rev. A **95**, 042318 (2017).

[38] P. Doria, T. Calarco, and S. Montangero, Optimal Control Technique for Many-Body Quantum Dynamics, Phys. Rev. Lett. **106**, 190501 (2011).

[39] N. Rach, M. M. Müller, T. Calarco, and S. Montangero, Dressing the chopped-random-basis optimization: A bandwidth-limited access to the trap-free landscape, Phys. Rev. A **92**, 062343 (2015).

[40] S. Machnes, E. Assémat, D. Tannor, and F. K. Wilhelm, Tunable, Flexible, and Efficient Optimization of Control Pulses for Practical Qubits, Phys. Rev. Lett. **120**, 150401 (2018).

[41] D. Lucarelli, Quantum optimal control via gradient ascent in function space and the time-bandwidth quantum speed limit, Phys. Rev. A **97**, 062346 (2018).

[42] J. J. W. H. Sørensen, M. O. Aranburu, T. Heinzel, and J. F. Sherson, Quantum optimal control in a chopped basis: Applications in control of Bose-Einstein condensates, Phys. Rev. A **98**, 022119 (2018).

[43] J. Zoller, Optimal quantum engineering, Ph.D. thesis, Faculty of Natural Sciences, University of Ulm, 2018.

[44] F. Hoeb, F. Angaroni, J. Zoller, T. Calarco, G. Strini, S. Montangero, and G. Benenti, Amplification of the parametric dynamical Casimir effect via optimal control, Phys. Rev. A **96**, 033851 (2017).

[45] F. Frank, T. Unden, J. Zoller, R. S. Said, T. Calarco, S. Montangero, B. Naydenov, and F. Jelezko, Autonomous calibration of single spin qubit operations, npj Quantum Inf. **3**, 48 (2017).

[46] R. Heck, O. Vuculescu, J. J. Sørensen, J. Zoller, M. G. Andreasen, M. G. Bason, P. Ejlertsen, O. Elíasson, P. Haikka, J. S. Laustsen, L. L. Nielsen, A. Mao, R. Müller, M. Napolitano, M. K. Pedersen, A. R. Thorsen, C. Bergenholtz, T. Calarco, S. Montangero, and J. F. Sherson, Remote optimization of an ultracold atoms experiment by experts and citizen scientists, Proc. Natl. Acad. Sci. USA **115**, E11231 (2018).

[47] M. Rossignolo, A. Marshall, T. Reisser, P. Rembold, A. Pagano, P. Vetter, R. Said, M. Müller, T. Calarco, S. Montangero, and F. Jelezko, QuOCS: A Quantum Optimal Control Suite (unpublished).

[48] N. Oshnik, P. Rembold, T. Calarco, S. Montangero, E. Neu, and M. M. Müller, Robust magnetometry with single nitrogen-vacancy centers via two-step optimization, Phys. Rev. A **106**, 013107 (2022).

[49] A. Omran, H. Levine, A. Keesling, G. Semeghini, T. T. Wang, S. Ebadi, H. Bernien, A. S. Zibrov, H. Pichler, S. Choi, J. Cui, M. Rossignolo, P. Rembold, S. Montangero, T. Calarco, M. Endres, M. Greiner, V. Vuletić, and M. D. Lukin, Generation and manipulation of Schrödinger cat states in Rydberg atom arrays, Science **365**, 570 (2019).

[50] T. Eichhorn, B. van den Brandt, P. Hautle, A. Henstra, and W. T. Wenckebach, Dynamic nuclear polarisation via the integrated solid effect II: Experiments on naphthalene-h_8 doped with pentacene-d_{14}, Mol. Phys. **112**, 1773 (2014).

[51] J. M. Binder, A. Stark, N. Tomek, J. Scheuer, F. Frank, K. D. Jahnke, C. Müller, S. Schmitt, M. H. Metsch, T. Unden, T. Gehring, A. Huck, U. L. Andersen, L. J. Rogers, and F. Jelezko, Qudi: A modular python suite for experiment control and data processing, SoftwareX **6**, 85 (2017).

[52] S. R. Hartmann and E. L. Hahn, Nuclear Double Resonance in the Rotating Frame, Phys. Rev. **128**, 2042 (1962).

[53] D. Stefanatos and E. Paspalakis, Speeding up adiabatic passage with an optimal modified Roland–Cerf protocol, J. Phys. A: Math. Theor. **53**, 115304 (2020).

[54] J. Roland and N. J. Cerf, Quantum search by local adiabatic evolution, Phys. Rev. A **65**, 042308 (2002).

[55] T. Caneva, T. Calarco, R. Fazio, G. E. Santoro, and S. Montangero, Speeding up critical system dynamics through optimized evolution, Phys. Rev. A **84**, 012312 (2011).

[56] S. van Frank, M. Bonneau, J. Schmiedmayer, S. Hild, C. Gross, M. Cheneau, I. Bloch, T. Pichler, A. Negretti, T. Calarco, and S. Montangero, Optimal control of complex atomic quantum systems, Sci. Rep. **6**, 34187 (2016).

[57] N. Malossi, M. G. Bason, M. Viteau, E. Arimondo, R. Mannella, O. Morsch, and D. Ciampini, Quantum driving protocols for a two-level system: From generalized Landau-Zener sweeps to transitionless control, Phys. Rev. A **87**, 012116 (2013).

[58] A. Van Strien and J. Schmidt, An EPR study of the triplet state of pentacene by electron spin-echo techniques and laser flash excitation, Chem. Phys. Lett. **70**, 513 (1980).

[59] A. Henstra and W. Wenckebach, Dynamic nuclear polarisation via the integrated solid effect I: Theory, Mol. Phys. **112**, 1761 (2014).

[60] B. Julsgaard, C. Grezes, P. Bertet, and K. Mølmer, Quantum Memory for Microwave Photons in an Inhomogeneously Broadened Spin Ensemble, Phys. Rev. Lett. **110**, 250503 (2013).

[61] T. Can, Q. Ni, and R. Griffin, Mechanisms of dynamic nuclear polarization in insulating solids, J. Magn. Reson. **253**, 23 (2015).

[62] A. Henstra, The integrated solid effect, Ph.D. thesis, Rijksuniversiteit te Leiden, 1990.

[63] F. Marquardt and A. Püttmann, Introduction to dissipation and decoherence in quantum systems, arXiv:0809.4403.

[64] C. Rackauckas and Q. Nie, DifferentialEquations.jl - A performant and feature-rich ecosystem for solving differential equations in Julia, J. Open Res. Software **5**, 15 (2017).

[65] T. Besard, C. Foket, and B. De Sutter, Effective extensible programming: Unleashing Julia on GPUs, IEEE Trans. Parallel Distrib. Syst. **30**, 827 (2019).

[66] T. Besard, V. Churavy, A. Edelman, and B. D. Sutter, Rapid software prototyping for heterogeneous and distributed platforms, Adv. Eng. Software **132**, 29 (2019).

[67] S. Bromberger *et al.*, JuliaGraphs/LightGraphs.jl: An optimized graphs package for the Julia programming language, 2017, https://doi.org/10.5281/zenodo.889971.

[68] J. Chen, J. Revels, and A. Edelman, Robust benchmarking in noisy environments, in *HPEC'16 Proceedings of the Twentieth IEEE High Performance Extreme Computing Conference* (IEEE, Waltham, MA, 2016).

[69] M. Besançon, VertexSafeGraphs.jl, 2019, https://github.com/matbesancon/VertexSafeGraphs.jl.

[70] P. K. Mogensen and A. N. Riseth, Optim: A mathematical optimization package for Julia, J. Open Source Software **3**, 615 (2018).

[71] C. Rackauckas and Q. Nie, Adaptive methods for stochastic differential equations via natural embeddings and rejection sampling with memory, Discrete Contin. Dyn. Syst. Ser. B **22**, 2731 (2017).

[72] Y. Ma, S. Gowda, R. Anantharaman, C. Laughman, V. Shah, and C. Rackauckas, ModelingToolkit: A composable graph transformation system for equation-based modeling, arXiv:2103.05244.

[73] C. Fieker, W. Hart, T. Hofmann, and F. Johansson, Nemo/Hecke: Computer algebra and number theory packages for the Julia programming language, in *Proceedings of the 2017 ACM on International Symposium on Symbolic and Algebraic Computation*, ISSAC '17 (ACM, New York, 2017), pp. 157–164.

[74] S. G. Johnson, QuadGK.jl: Gauss–Kronrod integration in Julia, 2016, https://github.com/JuliaMath/QuadGK.jl.

[75] M. Innes, Don't Unroll Adjoint: Differentiating SSA-form programs, arXiv:1810.07951.

[76] M. Udell, K. Mohan, D. Zeng, J. Hong, S. Diamond, and S. Boyd, Convex optimization in Julia, in *Proceedings of the 1st First Workshop for High Performance Technical Computing in Dynamic Languages* (IEEE, Piscataway, NJ, 2014), pp. 18–28.

[77] B. Legat, O. Dowson, J. D. Garcia, and M. Lubin, MathOptInterface: A data structure for mathematical optimization problems, INFORMS J. Comput. **34**, 671 (2022).

[78] M. Frigo and S. G. Johnson, The design and implementation of FFTW3, Proc. IEEE **93**, 216 (2005).

[79] E. L. Hahn, Spin Echoes, Phys. Rev. **80**, 580 (1950).

[80] T. Caneva, T. Calarco, and S. Montangero, Chopped random-basis quantum optimization, Phys. Rev. A **84**, 022326 (2011).

[81] F. Gao and L. Han, Implementing the Nelder-Mead simplex algorithm with adaptive parameters, Comput. Optim. Appl. **51**, 259 (2012).

[82] J. A. Nelder and R. Mead, A simplex method for function minimization, Comput. J. **7**, 308 (1965).

[83] S. Lloyd and S. Montangero, Information Theoretical Analysis of Quantum Optimal Control, Phys. Rev. Lett. **113**, 010502 (2014).

3.2 QuOCS: The Quantum Optimal Control Suite

3.2.1 Summary

To make best use of quantum control algorithms, they need to be programmed in code form in order to make them accessible for a computer. In recent years, numerous QOC software packages have been developed for different platforms and with different features. Some interesting examples are given in the following. MATLAB is a commercial software designed for engineers and scientists and commonly used for, e.g., numerical simulations. A library that extends MATLAB with capabilities for spin dynamics simulation, deep learning, and control through GRAPE is called `Spinach` [253] and specifically designed for MRS experiments. Implementations of Krotov and GRAPE can be found in `DYNAMO` [254] together with efficient ways for time evolution and computational resource management. `QEngine` [255] is written in C++ and contains implementations of GRAPE and tailored variants of GROUP. For the fairly new programming language Julia, the `QuantumControl.jl` package [256] can be found to contain Krotov and GRAPE together with ready-to-use implementations for control functionals.
The most widespread programming language in the control community is Python with a number of useful packages. Among them is the Quantum Toolbox in Python (`QuTiP`) [257] with control features through the GRAPE and CRAB algorithm and it can be extended with a Krotov package that is build on top of it [258]. A strategy leveraging automatic differentiation can be found in `GRAPE-Tensorflow` [100]. Techniques that are more focused on the communication with an experiment are captured in the integrated open-source tool set for control, calibration, and characterization $\mathbb{C}^3$ [48, 259] and `QOPT` [260]. Based on such efforts, commercial offers for control software are sprouting from the ground due to the increased demand by the quantum technology industry. The company Qruise [261] offers closed-loop calibration, model learning, and optimal control to develop high-fidelity digital twins of experimental setups and get deeper insight and diagnostics of their performance. Another example is the company Q-CTRL [262], which offers strategies to improve the performance of quantum sensors and quantum computation platforms.

In this section, we will discuss our approach to make quantum control accessible via a Python package called the Quantum Optimal Control Suite (QuOCS). Based on the remote dCRAB implementation in the RedCRAB software [1, 14, 91–93], the predecessor of the open-source package discussed here, QuOCS puts a focus on the optimization of the controls through direct communication with an experiment or custom simulation written by a user. It unites black-box optimization strategies with useful features to overcome some issues like drift and measurement uncertainties and to respect experimental constraints, which can also come in handy in certain simulation scenarios. Therefore, QuOCS does not necessarily need to know, how the FoM value is generated explicitly. However, if enough information about the model is provided, QuOCS can also perform gradient-based optimization. If the simulation is written in the appropriate format and uses the according syntax, automatic differentiation via the JAX library [263] for Python is possible. In this summary, however, we will mainly discuss a dCRAB optimization approach, since it demonstrates most of the features and structure of the software. Due to its object-oriented and modular design, the control suite can be adapted and extended by any user to fit to their needs and it provides a helpful foundation for testing, e.g., new or tailored control algorithms, parameter search methods and bases for pule expansion.

To characterize the performance of one or more control pulses, a user of QuOCS needs to define a FoM for their problem in the first step. This is done via a specific class defined in QuOCS with a function that takes the pulses, time-grids, and a list of additional parameters, that can also be adjusted by the optimization, as an input. It returns a real-valued number which is targeted for minimization or maximization. The job of the FoM object then is to evaluate the pulses and parameters and construct the FoM such that it reflects the quality of their performance, but also contains penalty terms for undesired effects like leakage or high power intake. By a call to the evaluation function, the controls can be sent to an experiment for measurement in the lab, but also other code can be executed that runs a simulation in another programming language. Only if gradient methods are used, more information such as the drift- and control-Hamiltonian and, e.g., the target state of the quantum system have to be provided.

The rest of the control schematics are performed by QuOCS. All the available settings for the optimization and information about the controls are combined in a JSON file for good readability and the possibility to provide and alter them with a dictionary datatype in Python. The controls have attributes like the corresponding time, so that several pulses, i.e. any time-dependent function, can be associated with different time-grids. Limitations on the maximum and minimum amplitude and a guess pulse can be defined. The entry for each pulse also contains the information about the basis in which to expand it. So can the type of basis, e.g. Fourier or Sigmoid functions, be selected including further options such as bandwidth limitations and the number of basis vectors to use during each SI of the dCRAB algorithm. Investigations on the effect of different bases depending on the optimized problem have recently been studied [82] and provide helpful insight in the basis choice. A separate section with parameters, that are single-valued variables to optimize, accepts a guess value, limits for the value, and an estimate for the initial variation to help the search reach a faster convergence to the optimum. These parameters can, as examples among other purposes, be used to describe bias voltages or dwell-times.

In a separate section for the algorithm settings, the main QOC method is described. If dCRAB is chosen, the options include the number of super-iterations (SI) and general stopping criteria such as a maximum number of function evaluations, a maximum time, or the goal value for the FoM to reach. The direct search method for the basis and additional parameters is selected next and can be fine-tuned with a local set of stopping criteria for each SI, so that no time is wasted if the search gets stuck in a local optimum. Furthermore, options for drift-compensation can be set, so that the current FoM is re-measured periodically to refocus shifts in the optimization target due to, e.g., temperature changes in the lab. A method we call re-evaluation steps can be used to repeat the evaluation of the same set of pulses and parameters if the obtained FoM together with an estimated or determined measurement uncertainty suggests the possibility of an improvement while showing a slightly worse FoM than the current optimum.

In the publication, we describe the structure of the code in more detail and also show-case the software with practical examples. The illustrations include three model-based optimizations with GRAPE, AD-dCRAB and normal dCRAB and an experimental closed-loop example for the optimization of the photo-luminescence contrast of an ensemble of NV centers. QuOCS can be directly integrated in Qudi [264], an open-source software for the control of experimental

setups.
In summary, in QuOCS we provide a software package that comes with implementations of commonly used algorithms, both for open- and closed-loop optimization. Its modular and open-source structure provides a platform for further development and implementation of user-defined variations or new approaches for optimizations schemes. Numerous helpful structures for parameteriaztion and supporting restrictions of experimental hardware as well as a customizable FoM class aid in the connection to simulations and setups in the lab. Besides the applications of its predecessor RedCRAB [252], QuOCS has been used successfully in a handful of scenarios already [3, 82, 90, 94, 265] and we are looking forward to extending this list and spark interest in development contributions across many research areas. QuOCS can be found on GitHub (`https://github.com/Quantum-OCS/QuOCS`) and can be installed from the Python package index (PyPI).

Title:	QuOCS: The Quantum Optimal Control Suite [1]
Authors:	Marco Rossignolo†, **Thomas Reisser**†, Alastair Marshall, Phila Rembold, Alice Pagano, Philipp J. Vetter, Ressa S. Said, Matthias M. Müller, Felix Motzoi, Tommaso Calarco, Fedor Jelezko, Simone Montangero
Journal:	Computer Physics Communications
Publisher:	Elsevier
Year:	2023
Volume:	291
Page:	108782
DOI:	10.1016/j.cpc.2023.108782
Link:	`www.sciencedirect.com/science/article/pii/S0010465523001273`
Copyright:	

† These authors contributed equally to this work.

3.2.2 Author's Contribution

Thomas Reisser contributed to the code conceptualization of the software as well as the manuscript. He wrote large parts of the theory, software description and examples. Thomas was involved in the design of the experimental closed-loop example and development of features of the software. He streamlined and wrote the example scripts and notebooks and created the resulting figures (4, 5, 6 and 8). He also worked on the documentation of the software online and maintained and extended the program further. Thomas implemented new features and adapted existing ones based on feedback from experimental testers.

[1] This article was published in Computer Physics Communications, Vol. 291, Marco Rossignolo, Thomas Reisser, Alastair Marshall, Phila Rembold, Alice Pagano, Philipp J. Vetter, Ressa S. Said, Matthias M. Müller, Felix Motzoi, Tommaso Calarco, Fedor Jelezko and Simone Montangero, "*QuOCS: The quantum optimal control suite*", Page 108782, Copyright Elsevier (2023).

3.2.3 Data Availability

The software code is published on GitHub (`https://github.com/Quantum-OCS/QuOCS`) and some detailed examples in the form of Jupyter are found on another repository (`https://github.com/Quantum-OCS/QuOCS-jupyternotebooks`). Additional code for the connection with Qudi can be found under `https://github.com/Quantum-OCS/Qudi-plugin`. Further data for the simulations and experiments shown in the publication in this section is stored on the backed-up data servers of PGI-8 at Forschungszentrum Jülich (FZJ) and available upon request to the author of this thesis or the Institute for Quantum Control (PGI-8).

Computer Physics Communications 291 (2023) 108782

Contents lists available at ScienceDirect

Computer Physics Communications

journal homepage: www.elsevier.com/locate/cpc

Computer Programs in Physics

QuOCS: The quantum optimal control suite ☆,☆☆

Marco Rossignolo [a,b,c,d,1], Thomas Reisser [e,f,*,1], Alastair Marshall [a,d,g], Phila Rembold [b,c,f], Alice Pagano [b,c,h], Philipp J. Vetter [a], Ressa S. Said [a], Matthias M. Müller [e], Felix Motzoi [e,f], Tommaso Calarco [e,f], Fedor Jelezko [a], Simone Montangero [b,c]

[a] Institute for Quantum Optics, Ulm University, Albert-Einstein-Allee 11, 89081 Ulm, Germany
[b] Dipartimento di Fisica e Astronomia "G. Galilei" & Padua Quantum Technologies Research Center, Università degli Studi di Padova, I-35131, Padova, Italy
[c] INFN, Sezione di Padova, via Marzolo 8, I-35131, Padova, Italy
[d] Qruise GmbH, Saarbrücken, D-66113, Germany
[e] Peter Grünberg Institute – Quantum Control (PGI-8), Forschungszentrum Jülich GmbH, D-52425, Germany
[f] Institute for Theoretical Physics, University of Cologne, D-50937, Germany
[g] NVision Imaging Technologies, Albert-Einstein-Allee 11, 89081 Ulm, Germany
[h] Institute for Complex Quantum Systems & Center for Integrated Quantum Science and Technology, Ulm University, Albert-Einstein-Allee 11, 89081 Ulm, Germany

ARTICLE INFO

Article history:
Received 17 January 2023
Received in revised form 9 May 2023
Accepted 10 May 2023
Available online 23 May 2023

Keywords:
Python 3
Optimal control
Adaptive (feedforward) optimization
Closed-loop
Customization
Algorithm
Quantum

ABSTRACT

Quantum optimal control includes a family of pulse-shaping algorithms that aim to unlock the full potential of a variety of quantum technologies. The Quantum Optimal Control Suite (QuOCS) unites experimental focus and model-based approaches in a unified framework. Easy usage and installation presented here and the availability of various combinable optimization strategies is designed to improve the performance of many quantum technology platforms, such as color defects in diamond, superconducting qubits, atom- or ion-based quantum computers. It can also be applied to the study of more general phenomena in physics. In this paper, we describe the software and the toolbox of gradient-free and gradient-based algorithms. We then show how the user can connect it to their experiment. In addition, we provide illustrative examples where our optimization suite solves typical quantum optimal control problems, in both open- and closed-loop settings. Integration into existing experimental control software is already provided for the experiment control software Qudi (Binder et al., 2017 [41]), and further extensions are investigated and highly encouraged.
QuOCS is available from GitHub, under Apache License 2.0, and can be found on the PyPI repository.

Program summary
Program Title: QuOCS - Quantum Optimal Control Suite
CPC Library link to program files: https://doi.org/10.17632/wjjch757fk.1
Developer's repository link: https://github.com/Quantum-OCS/QuOCS
Licensing provisions: Apache-2.0
Programming language: Python
External routines: NumPy [1], SciPy [1], JAX [2]
Nature of problem: Quantum systems are typically controlled by time-dependent electromagnetic fields to perform a certain set of quantum operations. Those operations may in turn provide building blocks for various quantum information processing tasks such as quantum computation, communication, simulation, sensing, and metrology. Numerous control strategies exist to design and improve such operations [3]. While some strategies are constructed to target a rather specific problem with high efficiency, others are more general to solve a wide range of applications [4,5]. To access the different algorithms, one has to download different optimization suites with different input and output parameters, making them hard to compare and combine. To benefit from the variety of algorithms, we have devised a customizable and intuitive optimization suite that simultaneously provides access to some of the most popular quantum optimal control algorithms.

☆ The review of this paper was arranged by Prof. Weigel Martin.
☆☆ This paper and its associated computer program are available via the Computer Physics Communications homepage on ScienceDirect (http://www.sciencedirect.com/science/journal/00104655).
* Corresponding author at: Peter Grünberg Institute – Quantum Control (PGI-8), Forschungszentrum Jülich GmbH, D-52425 Jülich, Germany.
E-mail address: t.reisser@fz-juelich.de (T. Reisser).
[1] These authors contributed equally to this work.

https://doi.org/10.1016/j.cpc.2023.108782

Solution method: We combine, in a unified framework, some of the frequently used optimal control algorithms which are the dressed Chopped Random Basis method (dCRAB) [6], and Gradient Ascent Pulse Engineering (GRAPE) [7], with an extension to make use of Automatic Differentiation (AD) [8]. The software is able to connect to both models of quantum dynamics in simulations and real-time quantum experiments to perform open- and closed-loop optimization, respectively. With minimal knowledge of optimal control theory, the user can manage to run optimizations of quantum processes using a variety of additional features such as stopping criteria and drift compensation. Logging and data management of the optimization progress and results are also handled by the suite. Its modular structure allows for extensions that accommodate customized algorithms and can be implemented by the user straightforwardly.

Additional comments including unusual features: The connection to the experiments is performed by an extension that enables a direct integration to a laboratory control software Qudi [9].

References

[1] T.E. Oliphant, Comput. Sci. Eng. 9 (2007) 10, http://www.scipy.org/.
[2] J. Bradbury, et al., JAX: composable transformations of Python+NumPy programs, http://github.com/google/jax, 2018.
[3] S. Glaser, U. Boscain, T. Calarco, et al., Eur. Phys. J. D 69 (2015) 279.
[4] C.P. Koch, U. Boscain, T. Calarco, et al., EPJ Quantum Technol. 9 (2022) 19.
[5] Schaefer, Ido, Ronnie Kosloff, Phys. Rev. A 101 (2) (2020).
[6] N. Rach, M.M. Müller, T. Calarco, S. Montangero, Phys. Rev. A 92 (2015) 6.
[7] N. Khaneja, et al., J. Magn. Reson. 92 (6) (2015) 296–305.
[8] N. Leung, et al., Phys. Rev. A 95 (2017) 4.
[9] J.M. Binder, et al., SoftwareX 6 (2017) 85–90.

1. Introduction

Quantum optimal control (QOC) is a technique for shaping pulses that can enable and improve the performance of quantum technology and contribute to studying phenomena in quantum physics in general [1–6]. Besides a clever way of combining search algorithms with modeled or measured information about a quantum system, it includes analytical methods such as Pontryagin's maximum principle [7,8], geometric approaches [9,10], shortcuts to adiabaticity [11–16] and dynamical decoupling [17–24]. QOC can be used to develop control sequences for quantum systems [25]. This can include guiding the system from an initial state to some desired target state [26], producing robust quantum gates, or entanglement [27]. To do so, the algorithm either makes use of a simulated model or adaptive learning from the experiment. If optimal control is used in combination with a simulation and theoretical model, we refer to it as open-loop quantum optimal control. If, however, the optimization is performed using information obtained from experimental measurements of the controls provided by QuOCS, we speak of a closed-loop optimization. Closed-loop QOC is primarily applicable to experiments that use variable electromagnetic control fields and are capable of performing fast state preparation and read-out compared to the lifetime and coherence time of the system. When using QOC for closed-loop optimization, regardless of the origin of the feedback, the algorithm iteratively advances the controls until the system reaches the desired target in a reasonable computational and experimental time.

QOC has its roots in the nuclear magnetic resonance community of the 1970s, where, for example, shaped radio frequency pulses were designed to display certain spectral properties [28]. Since then, many methods have been developed specifically catering to quantum problems: The Krotov method [29–31] is a gradient-based approach that can under certain assumptions guarantee monotonic convergence. The field has steadily grown, and with the introduction of the gradient ascent pulse engineering (GRAPE) method in 2005, optimal control became more accessible [32,33]. In 2011, the chopped random basis (CRAB) algorithm [34,35] was introduced and refined in 2015 with the introduction of dressed CRAB (dCRAB) [36]. In the open-source domain, many libraries have implemented algorithms similar to the ones we present here, e.g., the quantum toolkit in Python (QuTiP) [37] includes both CRAB and GRAPE, the `Krotov.py` package [30] contains a Python implementation of the Krotov method. QOpt offers an experiment-oriented qubit simulation and optimization control package [38], DYNAMO [33] and Spinach [39] are MATLAB-based programs running GRAPE, and C^3 is an integrated open-source tool-set for Control, Calibration, and Characterization [40]. In particular, the main focus of C^3 is on superconducting qubit systems and relies on the description of the system via Hamiltonians. What sets the Quantum Optimal Control Suite (QuOCS) apart is that it unites model-based approaches and an (also model-free) experimental focus to provide a unified framework. The common interface and large selection of customizable options make it an ideal platform for application-focused yet efficient optimization. At its core, QuOCS already includes a standard set of gradient-based and gradient-free methods. However, it is the whole environment QuOCS offers to make this software noteworthy: it allows the user to create and benchmark their own tailored QOC algorithms. Furthermore, it is designed to be easily connected to lab control setups (leveraging existing experimental control software such as Qudi [41]) and thus be used as a closed-loop optimizer. QOC algorithms have already demonstrated their capabilities in many different physical platforms, including NV centers in diamond [25,42–49], nuclear magnetic resonance (NMR) [32,50–54], trapped ions [55–63], cold atoms [64–71], and superconducting qubits [72–76]. The optimization tasks range from high-performance sensing and state preparation to the creation of controlled unitary operations for quantum computing and quantum simulation. QuOCS inherits ideas from RedCRAB (Remote dressed Chopped RAndom Basis) [35,36] on optimizing theoretical problems and experimental challenges [77–79] concentrating on a user-friendly and customizable interface. In contrast to RedCRAB, QuOCS is an open-source software with a modular structure and object-oriented nature providing a wider range of customizability to the user. While other projects are still ongoing, QuOCS' optimization of a two-qubit gate with Rydberg atoms was recently published [80]. In this work, we demonstrate its usefulness through a closed-loop example with NV centers in

diamond, hopefully inspiring more complex applications in the future.

The paper is structured as follows. In Sec. 2 we describe the software, the main toolbox and show how to connect to an experiment. Illustrative examples where our optimization suite solves typical quantum optimal control problems, both open- and closed-loop, are given in Sec. 3. Finally, in Sec. 4 we give an outlook and a summary of this work.

2. Software description

Python has gathered a lot of attention in the last decade, especially within the scientific community. As an intuitive, easy-to-read, and flexible programming language, it has become the de facto standard for writing user-friendly code. Whenever its efficiency is not sufficient, a number of application programming interface (API) libraries can be used to connect it to other high-performance programming languages for computationally heavy calculations. To leverage this existing community, QuOCS is written in Python 3 using an object-oriented style and has a robust suite of tests to ensure the code is reliable. This chapter leads the reader through a QOC process, starting from the problem description, through the configuration of the optimizer and ending with the modules that make up the software and available algorithms.

Instructions for the installation of QuOCS can be found in the README as part of the GitHub repository. Likewise, an overview of the available features and configuration options for the optimization are specified under features and settings. To get started with QuOCS the user should identify the available time-dependent and static controls and their limits. Additionally, a rigorous definition of the specified target is required. The next step is to set up the connection between the system (experiment or simulation) and QuOCS. At this point, the user has to choose the optimal control algorithm and hyperparameters before starting the iterative optimization. Ultimately, the algorithm converges to produce the improved final control sequence.

2.1. Problem description

A QOC problem is generally described through the dynamics of a quantum system and an optimization target. The Hamiltonian of a quantum system,

$$H(t) = H_0(t) + \sum_j u_j(t) \cdot H_{c,j}(t) \,, \tag{1}$$

is typically defined by a system term H_0, also called the drift Hamiltonian, and the control Hamiltonian $H_{c,i}$, which represents the effect the control fields $u_i(t)$ have on the system. The system starts in an initial state $|\Psi_0\rangle$ or $\rho_0 = |\Psi_0\rangle\langle\Psi_0|$ and evolves according to the time-dependent Schrödinger equation

$$\frac{\partial}{\partial t} |\Psi(t)\rangle = -\frac{i}{\hbar} H(t) |\Psi(t)\rangle \tag{2}$$

or more generally the Liouville-von Neumann equation.

$$\frac{\partial}{\partial t} \rho(t) = -\frac{i}{\hbar} [H(t), \rho(t)] \,. \tag{3}$$

The latter can be extended to include Lindblad terms to describe decoherence and dissipation (see Appendix C). In the case of a closed quantum system, the solution to equations (2) and (3) is given by

$$|\Psi(t)\rangle = U(t) |\Psi_0\rangle \tag{4}$$

with the unitary propagator,

$$U(t) = \mathbb{T} \exp\left(-\frac{i}{\hbar} \int_0^t H(\tau) d\tau \right) \tag{5}$$

where $\mathbb{T}$ is the Dyson time-ordering operator [33]. The preparation of a quantum state can typically be done by intrinsic properties of the given quantum system, but can also be the objective of a QOC problem. A comparison to the target is done via the Figure of Merit (FoM) which quantifies the distance to the target after the evolution or its preparation fidelity. Such a FoM can be the state overlap fidelity, $F_{\text{state}} = \left(\text{tr}\sqrt{\sqrt{\rho_T}\,\rho_{\text{aim}}\sqrt{\rho_T}}\right)^2$, or gate overlap fidelity, $F_{\text{gate}} = \frac{1}{N^2}\text{tr}\left(U_{\text{aim}}^\dagger U_T\right)^2$. It can also be extended to contain further information such as penalty terms. Such term can, for example, help to reduce the population of forbidden or undesired (usually lossy) states. Alternatively, any term can be included that represents a parameter that should be maximized or minimized during the development of the control sequence. Other examples include the control power or high-frequency pulse components. In order to limit the power transmitted to the system by the control, a factor k can be introduced such that the FoM takes the form $\mathcal{F} = k \cdot (1 - F) + (1 - k) \int |u(t)|^2 dt$ where F is e.g. the gate fidelity. In that way it becomes clear that the FoM is not necessarily the same as the (in)fidelity, and the optimization can be adjusted to be in favor of increasing the fidelity or reducing the power. During the optimization, a FoM is calculated in each iteration of the search and associated with the tested control pulse. The pulses $u_j(t)$ (or control fields) are expanded in an arbitrary type of basis, such as, e.g., the Fourier basis or Chebyshev polynomials, and updated by variation of the basis coefficients (i.e., the optimization-parameters). Additionally, the gradient of the FoM can be calculated with respect to the basis elements of the pulse.

As an example for the user, we have implemented a gradient-based optimization for a state-to-state transfer, where the user sets the initial and target state as well as the model of the quantum system by providing the drift and control Hamiltonian. In that case, QuOCS also works as a simulator. When performing gradient-free optimizations, the user only has to provide the custom FoM class, which is a child of the `AbstractFoM` class, that feeds back the fidelity or cost of a given set of pulses and parameters. The system dynamics are provided by a user-specific coded model. Future extensions to the software might include a set of efficient propagators, sophisticated solvers of the Schrödinger equation, or approximations for ensemble systems if the problem is described in the template structure provided by QuOCS. Regardless of the specific way the FoM is calculated, the aim of the `AbstractFoM` class is to establish a connection to any kind of simulation code or experiment. In the simplest case, this can be done by calling another Python code script from within the FoM class. In principle, any arbitrary structure that takes the pulses, their associated times, and constant but variable parameters as an input, can work for a gradient-free black-box optimization with QuOCS. The only requirement is that a real number to be maximized or minimized is given as an output. As a result, the user can execute code written in other programming languages such as Julia, C, C++, Matlab, or Mathematica. For connections to an experiment, methods of file communication, where the pulses, parameters, and FoM are written into text files and a watcher for timestamp changes is implemented, have been proven very useful in the development and experiences with RedCRAB. Furthermore, TCP/IP socket communication, where the information is sent between local ports on the same computer or remotely accessible ports between different machines, has been investigated and might become available in future updates to the software.

Once the FoM has been calculated for a given set of parameters describing the pulse, QuOCS uses an updating algorithm (such as the Nelder-Mead simplex algorithm [81,82], Powell's method [83], the covariance matrix adaption evolution strategy (CMA-ES) [84], or L-BFGS-B [85]) to find a new pulse. This cycle is repeated until the optimization converges or a specified stopping criterion is reached (see 2.2.2).

2.2. Configuration of the optimizer

After defining the problem to be solved via the `AbstractFoM` class, the settings for the solution method of the problem by QuOCS have to be specified by the user. This is done in a configuration file with JSON format. JSON provides a structured and human-readable way of defining data as a dictionary in a Pythonic style. We have split the information into sections to ease the navigation between different settings and the parameters provide intuitive configuration. Examples can be found in Sec. 3 and in the form of a set of Jupyter notebooks on GitHub [86]. The configuration file is saved automatically together with the optimization results to allow the user to take note of the used parameters and reproduce the results. We will go through the settings in the order as shown in the examples. Each key is an entry in the optimization configuration dictionary and contains the information of a specific setting. A name for the optimization runs, that is then also contained in the folder name for the results, can be specified by the key `optimization_client_name`. The main sections for the optimization are `algorithm_settings`, `pulses`, `parameters` and `times`. The `algorithm_settings` define the information about the type of QOC algorithm and its properties. Among them are, for example, the name of the algorithm (e.g. dCRAB, GRAPE, or AD (for automatic differentiation) (see Appendix A)) via the key `algorithm_name`, the number of super-iterations in the case of dCRAB (see Appendix A.2) by `super_iteration_number`, and if a minimization or maximization of the FoM should be performed (`optimization_direction`). Under `dsm_settings` the name of the direct search method (dsm) is given by `dsm_algorithm_name` (e.g. "NelderMead") in the `general_settings` and stopping criteria are specified in `stopping_criteria` (see Sec. 2.2.2). Via `random_number_generator` a seed can be defined to perform reproducible searches during testing, debugging, or determination of suitable hyperparameters. In this context, the hyperparameters are the settings in the configuration that have a direct influence on the optimization, such as the number of (super-) iterations, the specific basis used for pulse expansion, or the number of basis functions per search during a super-iteration. The stopping criteria and convergence tolerances can also be considered as hyperparameters because they determine the behavior of the optimization.

In experiments, specific issues may arise, such as the need to deal with measurement uncertainty and noise or drift of the detection signal. For simple drift compensation, a regular time interval on which to re-calibrate the current best set of pulses and parameters to the experiment can be specified in `compensate_drift` either as a time-periodic check or after each super-iteration. Noisy measurements might require the re-evaluation of data points to ensure an accurate interpretation of the parameter landscape if the FoM evaluated for two data points are within the measurement error. The `re_evaluation` option uses a list of threshold probabilities and the standard deviation of the FoM as input. A potential improvement of the pulses is verified by repeating the evaluation to lower the measurement uncertainty according to the criteria specified by the threshold probabilities. If this option is activated, a standard deviation of the measured FoM, or at least a reasonable estimate, has to be provided in the `AbstractFoM` class.

Custom designs of search algorithms can be written according to the available templates or by adapting existing scripts coming with QuOCS. The Python files containing the algorithm class (see Sec. 2.5) can be placed in any folder of the user's file structure and linked via the keys `dsm_algorithm_module` for the filename and `dsm_algorithm_class` for the name of the class so that QuOCS can find and use them.

2.2.1. Configuration of pulses and parameters

Time-dependent control functions can be defined under `pulses`. `pulse_name` allows the user to provide a custom name, e.g. "amplitude" or "voltage", and the associated duration is connected by `time_name`. This feature enables the optimization of several pulses on different time scales and to specify the same duration for several pulses. Other parameters for pulses are the amplitude limits (`upper_limit` and `lower_limit`), the number of bins into which to discretize the pulse (typically the sampling rate of the electronics in the experiment or the model resolution) by `bins_number` and an initial amplitude variation scale via `amplitude_variation`. The amplitude variation is specified in the units of the amplitude limits and guess pulse (if provided) and describes the variation of the points in the start simplex in case of Nelder-Mead or the initial width of the Gaussian in case of CMA-ES. Initial guesses can be defined by providing a Python lambda function or a list of values under `initial_guess` that can, e.g., stem from previous optimization runs. This list can also be added programmatically to the settings dictionary before executing the optimization by reading in the results from a previous run or sampling from a function defined elsewhere. The same holds for a scaling function, which can be used to set the pulse amplitudes to zero at the beginning and the end or to include post-processing of the obtained pulse-shape. In the `basis` section, the desired basis in which to expand a pulse can be set and further parameters that are specific to the chosen basis can be defined. These include the distribution (`distribution_name`) from which to select the random variables for the dCRAB algorithm (see Appendix A.2), the number of basis vectors per super-iteration (`basis_vector_number`), etc. QuOCS comes equipped with a set of bases: Fourier, Chebyshev, piece-wise constant, and Sigmoid. However, the user can easily extend this list by writing their own basis according to the available template and link their file to QuOCS in the basis part of the pulse settings. As for the custom algorithm, the Python files containing the new basis class can be placed in any folder of the user's file structure and referenced via the keys `basis_module` for the filename and `basis_class` for the name of the class so that QuOCS can find and use them.

Under `times` the settings so far contain a name to connect it to a pulse, an initial value for the duration and ranges in which the duration might be varied with a reasonable variation size to start with. Currently, the variation and optimization of pulse durations is not supported yet.

The same as for the `times` holds for `parameters`, except that they should be seen as constant but variable values that are optimized besides the pulse amplitudes and are not connected to the pulses (at least not inside QuOCS), e.g. the constant detuning of a control field or a bias voltage. Here, the variation is considered

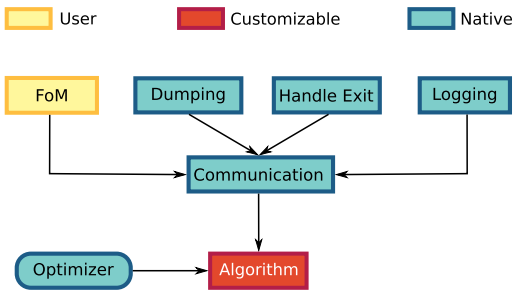

Fig. 1. General structure of QuOCS. The `FoM` class, which is specified by the user, is fed into a communication object together with further utilities for data dumping, logging and exit handling. The optimizer then connects this object to the defined optimization algorithm and initiates the run.

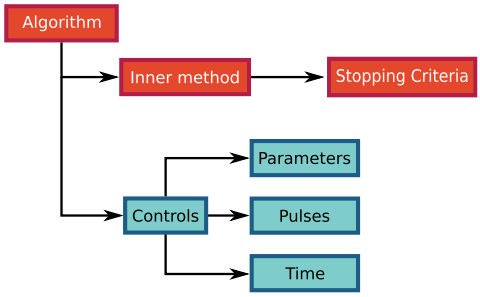

Fig. 2. The algorithm structure of QuOCS. The inner method contains the main part of the algorithm and can be adapted by the user or replaced by a custom code. It is connected to a stopping criteria object to check for, e.g., convergence or timeout. The controls object handles the composition of pulses, constant but variable parameters and times and can be accessed by the optimization algorithm.

in the optimization and the final values are saved with the optimal pulses (see Sec. 2.3).

2.2.2. Stopping criteria

Numerous stopping criteria are available to either end the optimization upon convergence or continue with a new super-iteration if a local search is stuck. Globally, one can set the total number of function evaluations by `max_eval_total`, the total time after which to stop by `total_time_lim` given in minutes, and a goal FoM that is to be reached by `FoM_goal` given in the same units as the FoM provided by the `AbstractFoM` class. These options are defined directly in the algorithm settings. More information on algorithm-dependent criteria can be found in Section 3.

For stopping criteria of individual super-iterations (SI) a `stopping_criteria` entry in the direct search method settings is used. Among them are convergence criteria for the search method defined analogous to numpy like `xatol` and, `fatol` which describe the simplex size and variation of the FoM value over the simplex points, respectively, in the case if Nelder-Mead. Additionally, a time limit for the SI, a maximum number of evaluations, and a change-based stop can be specified. The change-based stop takes the slope of the FoM trend over a given number of evaluations, below which the optimization proceeds with the next SI. This is a very intuitive way to save time in an already sufficiently converged local search.

2.3. The optimizer class

After the configuration of the optimization problem, the iterative optimization process can start.

The `Optimizer` class is the main class of the optimizer. As shown in Fig. 1, it contains all the general modules every optimization algorithm requires, such as an object for the communication, which takes care of the data management (dumping), logging, and the current state of the optimization. Exit handling is also performed in here. One important job of the communication is to take care of the connection to a graphical interface which is currently under development. Also, the visualization and initiation of a run in the lab-software Qudi is enabled by this class.

Each execution of the optimizer will create a folder named "QuOCS_Results" in the current directory of the Python shell with which the script is called. The results of an optimization run are put in a sub-folder therein named with a date- and time-stamp plus the custom optimization name defined by the user. In that folder, all the results are saved. This contains a log file that can be used for investigations of errors during an optimization and to gain more insight in the optimization history. The software generates a `.npz` file containing the best control pulses and parameters, the best achieved FoM and more information like the SI and iteration number required to converge. Lastly, a copy of the settings dictionary in JSON format and a text file with the used QuOCS version number is saved. The files that are saved can be extended manually by extracting desired information from the optimizer object or by adding functions to the FoM class.

2.4. Optimization algorithms

The optimization code is at the core of the Quantum Optimal Control Suite. The chosen optimization algorithm itself is a child class of `OptimizationAlgorithm` and invokes all independent module classes which it needs to perform the optimization as well as information about the communication object. A visualization of the structures shown in Fig. 2.

A routine defined in the `OptimizationAlgorithm` class is called every time a set of controls is evaluated. At every call of the routine, the global stopping criteria are checked and the communication with the linked FoM class is established. The child class for a specific algorithm has an inner routine call that is linked to its parent class and function. In the child, the specific stopping criteria are checked, and the re-evaluation steps are performed.

The algorithm itself contains an object for the controls (pulses, parameters and times), so that the used basis and settings can be handled separately, and the optimization algorithms are kept general. Also, the stopping criteria are taken care of in their own class, so that for each search strategy unique convergence indicators can be considered. During the routine call, only a query if one of the criteria has been reached is done and acted upon accordingly.

2.5. Direct search methods

During each dCRAB super-iteration, a direct search for the set of randomized controls is performed. The `DirectSearchMethod` class implements different direct search algorithms, such as Nelder-Mead and CMA-ES. Further strategies, that each have different advantages depending on the control problem, can easily be added personalized by the user. Direct search methods that are written or adapted by a user can be linked in the JSON configuration file, as already explained for the user `OptimizationAlgorithm` and `basis`. In this way, the new code can be integrated in the local file structure of the user, without the need to update the QuOCS installation (see Sec. 2.2).

2.6. Bases and pulses

Since the time-dependent pulses are expanded in some basis, a separate class for the pulses has been implemented. Each basis type is a child of this class and combines the to be optimized

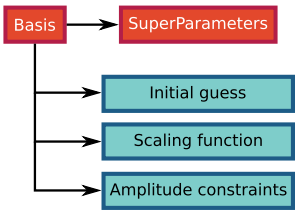

Fig. 3. Structure of pulses in QuOCS. The basis class obtains the information about each pulse, such as the function space in which to expand it and the optimization-parameters used for optimization. An initial guess, a scaling function and possible amplitude constraints are also defined here.

optimization-parameters to describe a certain pulse shape depending on the specified basis and the initial guess provided by the user. Here, also the scaling function is used to post-shape the pulse if needed. Finally, amplitude constraints are enforced. The structure can be visualized in Fig. 3. Several ways are possible here: simply cutting off the parts of a pulse that exceed the limits can introduce sharp edges, which can be useful to achieve shapes similar to bang-bang controls [74]. If bandwidth restrictions are important for the setup or system at hand, the shrink option can be useful, where the pulse is squeezed until it obeys all limitations. Additionally, post-processing steps to enforce bandwidth-limitations by cutting off high or low frequencies after a Fourier transformation could be implemented.

3. Example applications

In the following subsections, we are going to show three optimization examples to illustrate how QuOCS can be used to improve processes using models and experimental feedback. One of the model-based optimizations is demonstrated with a gradient-based and one with a gradient-free algorithm. Lastly, we show the results of a simple closed-loop optimization on an experiment in a laboratory.

Examples for runnable scripts can be found in the Examples folder of the GitHub repository. More guided examples using Jupyter notebooks are located on a separate GitHub repository [86]. An introduction to QuOCS for Qudi, including a Qudi installation guide and Jupyter notebook example, are accessible through QuOCS' Qudi-plugin repository [87].

3.1. Model-based optimization with GRAPE

We show the performance of GRAPE on an Ising problem with a Hamiltonian similar to the one used in Ref. [88]. The optimization problem is given by

$$H(t) = -J\sum_j \sigma_j^z\sigma_{j+1}^z - g\sum_j \sigma_j^z\sigma_{j+2}^z + u(t)\sum_j \sigma_j^x \tag{6}$$

where J and g describe the nearest and next-nearest neighbor interaction, respectively. A global control field in the x-direction $u(t)$ is used for the control of the system. We use a spin-chain of 5 qubits and take $J = 1$ and $g = 2$. A pulse of length 1 (a.u.) is discretized into 100 piece-wise constant elements. In QuOCS, we exploit the GRAPE algorithm to optimize the control field $u(t)$ from an initial guess of $u(t) = 0$ to find an operation that transfers all spins from the ground to the excited state. The figure of merit (FoM) is defined as the fidelity of the overlap of the target state with the state after time evolution under the control pulse according to the Hilbert-Schmidt inner product $F = \mathrm{tr}[\rho(T)^\dagger \rho_{\mathrm{aim}}]$. The time propagation is performed by a piece-wise evolution method using the matrix-exponential provided by QuOCS.

Initially, the modules needed for setting up the QOC problem are imported.

```
from quocslib.utils.inputoutput import readjson
from quocslib.utils.AbstractFoM import AbstractFoM
from quocslib.Optimizer import Optimizer

```

To define the control problem, the user provides a class which handles the dynamics of the system. At this point the drift- and control-Hamiltonian might be provided or the figure of merit (FoM) is handed back directly establishing the connection to the experiment or simulation.

```
class IsingModel(AbstractFoM):

    def __init__(self, args_dict:dict = None):
    """ Initialize the object """
    if args_dict is None:
    args_dict = {}
    ...

    def get_FoM(self, pulses: list = [],
    parameters: list = [],
    timegrids: list = []
    ) -> dict:
    # Compute the dynamics and FoM
    ...

    return {"FoM": fidelity}

    # Create Figure of Merit object
    FoM_object = IsingModel()

```

Details of the used model FoM class can be found in the Examples folder in the GitHub repository. The optimization algorithm is customized via a JSON file that contains information about the number of pulses, stopping criteria, etc.

```
optimization_dictionary = readjson("opt_dictionary.json
 "))

```

The JSON dictionary used for the GRAPE optimization is as follows:

```
{
  "algorithm_settings": {
    "algorithm_name": "GRAPE",
    "stopping_criteria": {
      "max_eval_total": 100,
      "ftol": 1e-6,
      "gtol": 1e-6
    }
  },
  "pulses": [{
    "pulse_name": "Pulse_1",
    "upper_limit": 100.0,
    "lower_limit": -100.0,
    "bins_number": 100,
    "amplitude_variation": 20.0,
    "time_name": "time_1",
    "basis": {
      "basis_name": "PiecewiseBasis",
      "bins_number": 100
    },
    "initial_guess": {
      "function_type": "lambda_function",
      "lambda_function": "lambda t: 0.0 + 0.0*t"
    }
  }],
  "parameters": [],
  "times": [{
    "time_name": "time_1",
    "initial_value": 1.0
  }]
}

```

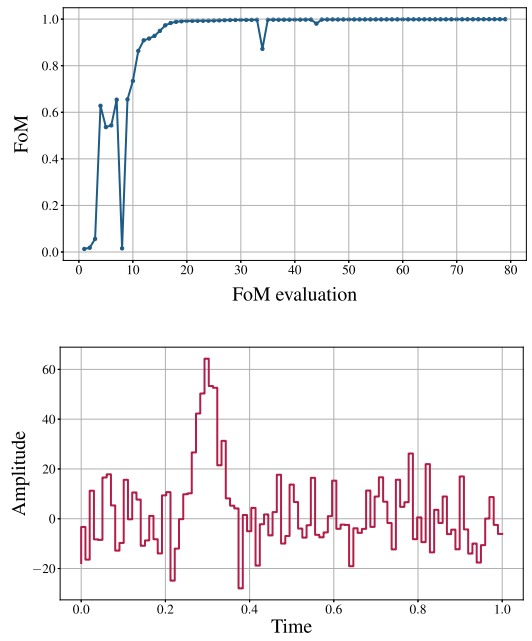

Fig. 4. Optimization results with GRAPE: *Top:* Evolution of the figure of merit during the iterations of the GRAPE algorithm for the system described by the Hamiltonian in eq. (6). *Bottom:* Final optimized amplitude $u(t)$ after the application of GRAPE on the problem.

In the last step, the optimizer object is built from the provided class and dictionary. After that the QuOCS optimization can be started:

```
# Define Optimizer
optimization_obj = Optimizer(optimization_dictionary,
 FoM_object)

# Execute the optimization
optimization_obj.execute()
```

The final optimized amplitude and evolution of the FoM during the run is shown in Fig. 4 and the fidelity reached a value of 99.95% in 79 steps of the GRAPE algorithm. This can be pushed further by decreasing the convergence tolerances (`ftol` and `gtol`) of the L-BFGS-B minimizer used during the optimization [89].

3.2. Model-based optimization with AD-dCRAB

The same problem can be optimized with the dCRAB algorithm. Here, we use gradients with respect to a chosen dCRAB basis. They are calculated via the automatic differentiation library JAX [90], thus we call it AD-dCRAB. To work effectively, all NumPy functions and types used in the FoM calculation have to be replaced by their jax.numpy counterparts. Furthermore, it is recommended to make use of jitting (jit - just in time) [91] for the time evolution to improve performance. For details see the Examples folder on the GitHub repository. The JSON file containing the optimization settings is given in the following:

```
{
  "optimization_client_name": "
 Optimization_AD_IsingModel_100_bins",
  "algorithm_settings": {
    "algorithm_name": "AD",
    "super_iteration_number": 3,
    "max_eval_total": 3000,
    "optimization_direction": "maximization",
    "stopping_criteria": {
      "max_eval": 1000,
      "ftol": 1e-05,
      "gtol": 1e-05
    }
  },
  "pulses": [
  {
    "pulse_name": "Pulse_1",
    "upper_limit": 1000.0,
    "lower_limit": -1000.0,
    "bins_number": 100,
    "amplitude_variation": 10.0,
    "time_name": "time_1",
    "basis": {
      "basis_name": "Fourier",
      "basis_vector_number": 5,
      "random_super_parameter_distribution": {
        "distribution_name": "Uniform",
        "lower_limit": 0.01,
        "upper_limit": 5.0
      },
      "bins_number": 2000
    },
    "initial_guess": {
      "function_type": "lambda_function",
      "lambda_function": "lambda t: 0.0 + 0.0*t"
    }
  }
  ],
  "parameters": [],
  "times": [
  {
    "time_name": "time_1",
    "initial_value": 1.0
  }
  ]
}
```

Fig. 5 shows the improvement over the dCRAB iterations and function evaluations leading to a final FoM of 99.91%. This result might be further improved by reducing the values for the stopping criteria `ftol` and `gtol` , which describe the acceptance for convergence based on the variations of the relative error in the FoM or the gradient norm, respectively. New dCRAB superiterations started after FoM evaluation 28 and 76.

The resulting pulse is much smoother than the GRAPE result. This feature is inherently provided by the dCRAB method and can be added to GRAPE as well by extending this basic implementation example [92,93]. In contrast to piece-wise constant basis used in the GRAPE example, which limits the discretization of the pulse in order to still perform a computationally efficient optimization, a much finer time grid can be used for the pulse. This comes from the expansion of the pulse into analytical basis functions which can be sampled at any time-step and the binning does not influence the complexity of the control problem.

3.3. Model-based optimization with gradient-free dCRAB

We again use the same model as in the previous sections but the optimization is performed via the dCRAB algorithm in combination with a gradient-free search method to give an example for a black-box optimization. However, to slightly modify the problem and to emulate fluctuations of the output of the system, a variation of the next-nearest neighbor coupling is added to the simulation as an example. For this purpose, we sample a random number from a Gaussian distribution around 0 with a variance of 0.1 and add it to the value of g in each evaluation of the FoM. In such a “noisy” scenario the dCRAB algorithm, in combination with Nelder-Mead and a Fourier basis under usage of the re-evaluation steps option of QuOCS, is a good approach to solve the problem. One reason

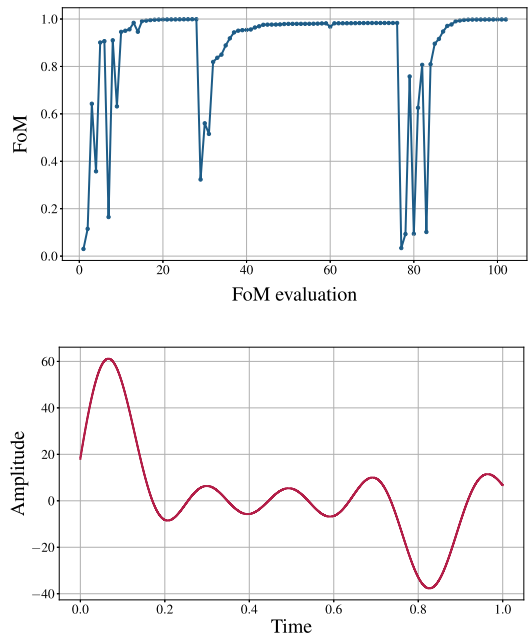

Fig. 5. Optimization results with AD-dCRAB: *Top:* Evolution of the FoM during the iterations of the dCRAB algorithm. We used automatic differentiation to calculate the gradients of the basis components that make up the drive control for the system described by the Hamiltonian in eq. (6). *Bottom:* Final optimized control amplitude $u(t)$ after the application of AD-dCRAB.

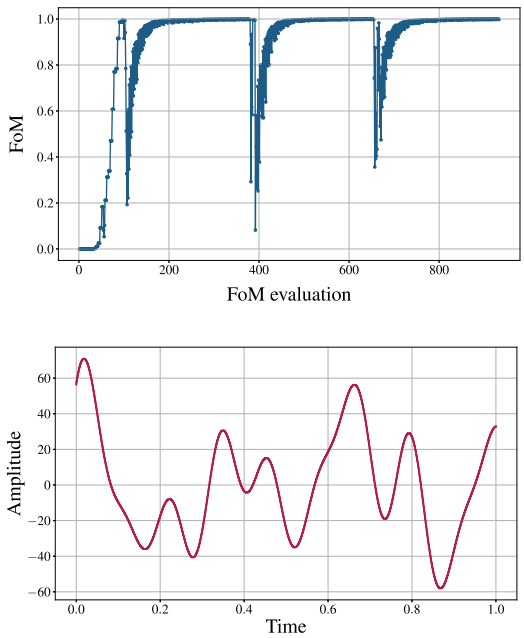

Fig. 6. Optimization results with dCRAB: *Top:* Evolution of the figure of merit during the iterations of the dCRAB algorithm for the system described by the Hamiltonian in eq. (6) with additional noise on the g parameter. *Bottom:* Final optimized amplitude $u(t)$ after the application of dCRAB on the problem.

for this is the natural robustness of Nelder-Mead since its simplex size can be chosen larger than the variations in the parameter landscape. The Fourier basis can produce arbitrary pulse shapes limited by the bandwidth provided in the optimization settings and the re-evaluations option is designed to consider uncertainty in the evaluated FoM. The settings for the optimization were defined as follows:

```
{
  "optimization_client_name": "
 Optimization_dCRAB_IsingModel",
  "algorithm_settings": {
    "algorithm_name": "dCRAB",
    "super_iteration_number": 3,
    "max_eval_total": 3000,
    "dsm_settings": {
      "general_settings": {
        "dsm_algorithm_name": "NelderMead",
        "is_adaptive": true
      },
      "stopping_criteria": {
        "xatol": 1e-14,
        "fatol": 1e-09,
        "change_based_stop": {
          "cbs_funct_evals": 200,
          "cbs_change": 0.01
        }
      }
    },
    "re_evaluation": {}
  },
  "pulses": [
  {
    "pulse_name": "Pulse1",
    "bins_number": 2000,
    "upper_limit": 1000.0,
    "lower_limit": -1000.0,
    "time_name": "time1",
    "amplitude_variation": 10.0,
    "basis": {
      "basis_name": "Fourier",
      "basis_vector_number": 5,
      "random_super_parameter_distribution": {
        "distribution_name": "Uniform",
        "lower_limit": 0.01,
        "upper_limit": 5.0
      }
    },
    "initial_guess": {
      "function_type": "lambda_function",
      "lambda_function": "lambda t: 0.0 + 0.0*t"
    }
  }
  ],
  "times": [
  {
    "time_name": "time1"
  }
  ],
  "parameters": []
}
```

In Fig. 6 the evolution of the FoM during an optimization with the dCRAB algorithm and the resulting control is shown. At step 379 and 654 a new dCRAB super-iteration is started and the new parameter landscape is searched by the NM method with an (initially) larger simplex (see [6,36,69]). The final FoM results in $99.78 \pm 0.02\%$ for an average of the FoM evaluated 50 times with the best pulse provided after the run.

3.4. Closed-loop implementation in an experiment

To improve the usability of QuOCS in an experimental environment, the control suite contains an interface with Qudi [41], a well-established multi-modular software to tune technologies often used for color-centers in diamond, as well as on other setups for experiments on quantum systems. The communication between the two platforms is established by using the signal slot feature of the Qt library and a Jupyter notebook kernel provided by Qudi. The optimization is started via a Jupyter notebook, controlling the

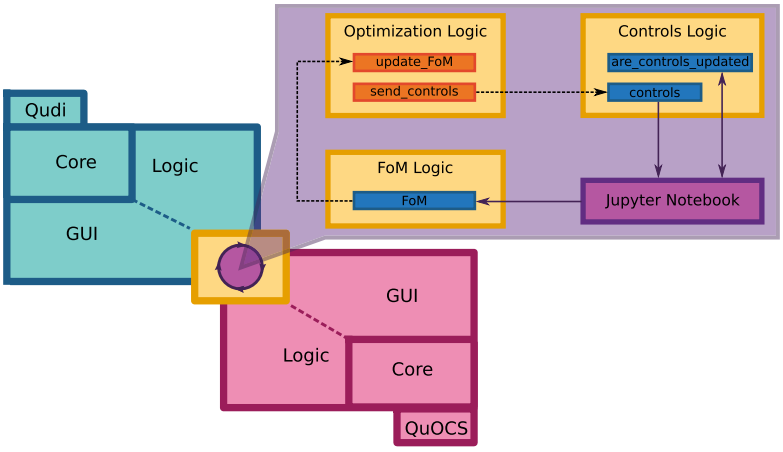

Fig. 7. QuOCS implementation in Qudi. The *optimization logic* class sends the controls to the Controls logic via a signal. The Jupyter notebook is then notified by the class variables *are_controls_updated* when the controls are ready to be used in the measurement. Indeed the Qudi module inside the notebook performs the experiment and returns the feedback to the *fom* variables in the *fom_logic* class. Finally, the feedback result is given back to the *optimization_logic* class via a signal and stored for the optimization algorithm. The red boxes delimit the class functions (orange boxes), and variables (blue boxes). The dashed arrows show the signals action among the logic classes, meanwhile the violet continuous lines represent the declaration and the return interactions between modules. (For interpretation of the colors in the figure, the reader is referred to the web version of this article.)

status of QuOCS and Qudi at each iteration. A schematic of the process is provided in Fig. 7.

To test and verify the applicability of QuOCS in a real experiment, we perform a state-to-state transfer for an ensemble of nitrogen vacancy (NV) centers in diamond. The NV center is a defect in the diamond lattice consisting of a vacancy and a nitrogen atom on the neighboring lattice site [94–96]. Because of its large zero-field splitting of $D \approx 2.87$ GHz, its $m_s = -1$ and $m_s = 0$ ground states can be treated as an effective two-level system when a magnetic field is applied (here $B = 458$ G). The applied magnetic field also leads to polarization of the nuclear spin associated with the nitrogen of the NV center [95]. The diamond sample is grown by chemical vapor deposition and has a natural abundance of ^{13}C and an NV layer thickness of ≈ 10 μm ([N] = 14 ppm). Due to the large NV layer thickness and readout area of $\varnothing \approx 14.5$ μm, the NV centers suffer from strong amplitude variation across the sample during the application of microwave pulses for spin state manipulation. To overcome this problem, we task QuOCS to optimize the amplitude and phase of a 200 ns long pulse to perform a π rotation of the NV spins from $m_s = 0$ to $m_s = -1$. As the $m_s = -1$ state shows a lower fluorescence signal than the $m_s = 0$ state [97], the FoM is given by the fluorescence contrast between those two states. We read out the NV centers spin state by applying a 532 nm laser pulse, which can also be used to re-initialize it back to the $m_s = 0$ state [98]. Generated pulses are sent in form of a microwave signal through a straight microwave antenna on top of the diamond. Further details of the setup can be found in Appendix B.

The optimization is performed for 3 hours where a new SI is started if the FoM does not change more than 0.001 over 50 evaluations. One evaluation step takes ~8.5 s and is mainly limited by the time needed to generate the pulse and process the obtained fluorescence signal. This choice is mainly made to illustrate the behavior of the optimization over a longer timescale and several super-iterations. The improvement of the photoluminescence contrast is only minor after around 250 iterations and the optimization could already have been stopped there for a faster runtime of about 35 minutes. As can be seen in the upper part of Fig. 8, the FoM signal is subject to some drift over time, i.e. iterations. This drift is well mitigated by the compensation methods via a re-calibration of the current best pulse after every 15 minutes that is provided in QuOCS and taken into account for the final optimal pulse components. To investigate the robustness against amplitude errors, we compare the final optimized pulse to a rectangular one with equal length. As shown in the lower part of Fig. 8, the optimized pulse shows a much higher contrast in any case of artificially lowering the applied amplitude as compared to its rectangular counterpart and is therefore able to transfer more population from $m_s = 0$ to $m_s = -1$. Such optimized pulses can

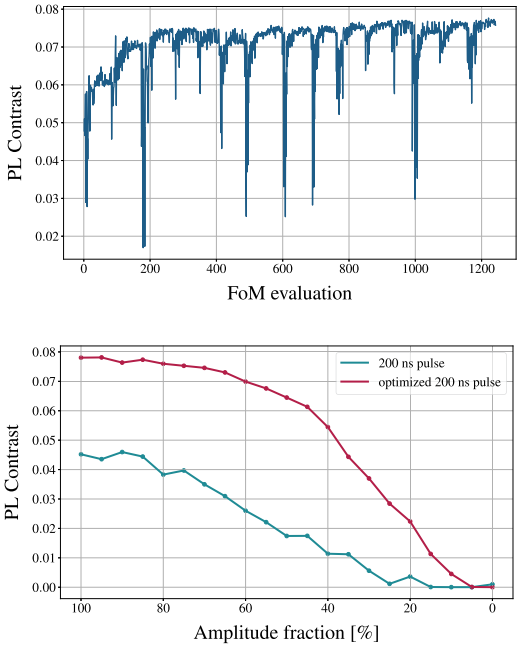

Fig. 8. Closed-loop optimization of a π-pulse on an NV center: *Top:* Evolution of the figure of merit during the iterations of the dCRAB algorithm for the maximization of the photo-luminescence (PL) contrast between the initial $m_s = 0$ and excited $m_s = -1$ state. The PL contrast corresponds to the amount of population flipped from ground to excited state. *Bottom:* Comparison of the achieved PL contrast between the optimized pulse and a simple rectangular pulse (constant amplitude and phase) under reduction of the amplitude from 100% to 0.

enhance the performance of experiments substantially [44,99–102] and due to its simple experimental implementation and fast optimization times QuOCS provides a framework for these kinds of experiment.

4. Conclusions and outlook

The family of QOC methods contains a variety of powerful algorithms to boost quantum technologies. To date, these methods have been implemented in several libraries, but a unified framework is missing. Finding the algorithm that is most suited to solve a problem, or having an heterogeneous approach, could be time demanding for a user in terms of the large amount of interfaces to develop for connecting the optimization algorithms to a given problem. Thus, to exploit the full potential of QOC and make these methods more accessible, even for researchers not in the QOC field, we provide QuOCS: a control suite that allows a problem to be solved by different algorithms in the same framework. Moreover, the modular structure of QuOCS allows an easier customization of the features to satisfy even specific needs of the user. For instance, new algorithms can be intuitively integrated with the many features already available and optimizer-related classes simplify the definition and implementation of new constraints, stopping criteria, etc.

We have shown with some examples that QuOCS simplifies also the process of transitioning from open-loop to closed-loop optimization. The open-loop optimization examples show the strength and weaknesses of two of the implemented algorithms, GRAPE and dCRAB. Instead, the closed-loop optimization is connected to the experiment via Qudi [41], a modular experiment control software often used for experiments with color centers in diamond. While the experiment could also be connected using, for example, a simple user-written bash script, we provide a module that allows the integration of QuOCS with the Qudi graphical user interface.

The field of quantum technology is in the transition phase between publicly funded research efforts and commercial exploitation, and QOC is starting to play a major role in this transition. Color centers in diamond, superconducting qubits, Rydberg atoms and ions in traps are vivid branches of quantum technology. Breakthroughs in these areas increasingly involve the need of tailored control over quantum devices and feedback loops between the device and the control algorithm. By integrating QOC into the lab software Qudi, QuOCS represents another step towards quantum technology based on color centers in diamond, especially with regard to automatic control of quantum computers and quantum sensors. Furthermore, the modular structure allows for straightforward extension to many other platforms. However, any type of setup able to run in closed-loop mode can in principle make use of QuOCS. Additionally - as demonstrated by similar open access control suites like QuTiP - QuOCS has the potential of widespread use across different quantum technology platforms. In particular, the underlying control algorithm dCRAB was used successfully on many different systems such as trapped ions, cold atoms, superconducting qubits or Bose Einstein condensates [5].

Installation and updating is straight-forward due to the availability on the Python Package Index (PyPI). Examples are available on the GitHub repository, as well as an overview of QuOCS' features and settings. More detailed tutorials in the form of Jupyter notebooks can be found on a separate GitHub repository with Jupyter notebooks [86]. For instructions regarding the usage of QuOCS with Qudi, please have a look at the Qudi-plugin repository [87].

The further development of QuOCS and addition of new features is an ongoing project. The main focus currently lies on the implementation of features requested by active users. Besides that, goals include the implementation of more updating algorithms, stopping criteria, and drift-compensation mechanics. To simplify the configuration of the optimization, which is submitted in the form of a JSON file, we are working on an adaptable GUI. Future updates might also include settings in the JSON file to automate regularly-needed processes, such as the visualization of pulses and FoM evolution. The list of possible extensions also includes the adaption of the implemented GRAPE method in order to generate smooth, bandwidth-limited pulses. This could be done by reparameterizing the pulse similar to dCRAB and subsequently optimizing the coefficients via their gradient obtained with the chain-rule (GROUP) [92] or gradient optimization of analytic controls (GOAT) [93]. Another method is the usage of filter functions or interpolation [103]. These features are candidates for potential future additions to the codebase of QuOCS. The priority of future development will be adjusted according to user demands voiced on the repository.

As quantum technology is on the rise, so is the demand for the application of QOC to fully exploit the hardware's potential. QuOCS is designed to bring together well-established but distinct QOC methods. In doing so, it provides a user-friendly framework for quantum scientists and engineers. Its open-source form invites the involvement of others to continuously extend and improve QuOCS.

Required metadata

Github repository: https://github.com/Quantum-OCS/QuOCS.

Declaration of competing interest

The authors declare the following financial interests/personal relationships which may be considered as potential competing interests: Thomas Reisser, Matthias Mueller, Felix Motzoi, Tommaso Calarco reports financial support was provided by Helmholtz Validation Fund project Qruise (HVF-00096). Phila Rembold, Alastair Marshall, Tommaso Calarco, Simone Montangero reports financial support was provided by European Union Horizon 2020 research and innovation program under the Marie Sklodowska-Curie QuSCo (Grant No. 765267). Thomas Reisser, Alastair Marshall, Philipp Vetter, Ressa Said, Matthias Mueller, Felix Motzoi, Tommaso Calarco, Fedor Jelezko reports financial support was provided by EU Quantum Flagship project ASTERIQS (Grant No. 820394). Marco Rossignolo, Alice Pagano, Simone Montangero reports financial support was provided by Italian PRIN 2017 (No. 2017E44HRF). Marco Rossignolo, Alice Pagano, Simone Montangero reports financial support was provided by EU-RyQA (No. 101070144). Marco Rossignolo, Alice Pagano, Simone Montangero reports financial support was provided by EU-QuantERA projects QuantHEP and T-NISQ. Marco Rossignolo, Alice Pagano, Simone Montangero reports financial support was provided by WCRI-Quantum Computing and Simulation Center of Padova University. Marco Rossignolo, Alice Pagano, Simone Montangero reports financial support was provided by BMBF under the funding program quantum technologies — from basic research to market — with the grant QRydDemo (No. 13N15633). Thomas Reisser, Alastair Marshall, Philipp Vetter, Ressa Said, Fedor Jelezko, Matthias Mueller, Felix Motzoi, Tommaso Calarco reports financial support was provided by BMBF SPINNING (No. 13N16210). Thomas Reisser, Matthias Mueller, Felix Motzoi, Tommaso Calarco reports financial support was provided by BMBF VERTICONS (No. 13N14872). Thomas Reisser, Matthias Mueller, Felix Motzoi, Tommaso Calarco reports financial support was provided by BMBF QSolid (No. 13N16149). Alastair Marshall, Philipp Vetter, Ressa Said, Fedor Jelezko reports financial support was provided by DFG (CRC1279, EXC 2154 POLiS — Post Lithium Storage Cluster of Excellence, 445243414, 499424854).

Alastair Marshall, Philipp Vetter, Ressa Said, Fedor Jelezko reports financial support was provided by Center for Integrated Quantum Science and Technology (IQst).

Alastair Marshall, Philipp Vetter, Ressa Said, Fedor Jelezko reports financial support was provided by European Research Council Synergy Grant HyperQ (Grant No. 319130). Thomas Reisser, Matthias Mueller, Felix Motzoi, Tommaso Calarco reports financial support was provided by Quantum Cooperativity of Light and Matter (QuCoLiMa) (No. 429529648) of Deutsche Forschungsgemeinschaft (DFG). Alastair Marshall, Marco Rossignolo reports a relationship with Qruise GmbH that includes: equity or stocks.

Data availability

Data will be made available on request.

Acknowledgements

This work was supported by the Helmholtz Validation Fund project "Qruise" (HVF-00096), the European Union's Horizon 2020 research and innovation program under the Marie Skłodowska-Curie QuSCo (Grant No. 765267) and the EU Quantum Flagship project ASTERIQS (Grant No. 820394). We acknowledge support from the Italian PRIN 2017 (No. 2017E44HRF), the EU project EU-RyQA (No. 101070144), the EU-QuantERA projects QuantHEP and T-NISQ, and the WCRI - Quantum Computing and Simulation Center of Padova University. Furthermore, this project has received funding from the German BMBF (Federal Ministry of Education and Research) under the funding program quantum technologies — from basic research to market — with the QRydDemo grant (No. 13N15633). We also acknowledge funding by the BMBF via the projects SPINNING (No. 13N16210), VERTICONS (No. 13N14872) and QSolid (No. 13N16149). RSS and FJ acknowledge support from the DFG (CRC1279, EXC 2154 POLiS - Post Lithium Storage Cluster of Excellence, 445243414, 499424854), BMBF, BW Stiftung, and the European Research Council Synergy Grant HyperQ (Grant No. 319130).

Finally, the research was supported by the Center for Integrated Quantum Science and Technology (IQ^{ST}) and the Deutsche Forschungsgemeinschaft (DFG, German Research Foundation) - Project-ID 429529648 - TRR 306 QuCoLiMa ("Quantum Cooperativity of Light and Matter").

Appendix A. Optimal control algorithms

A.1. Gradient-free algorithms

QuOCS includes a set of direct search algorithms serving as a base for the dCRAB algorithm. The user has complete control over which algorithm to use and can tweak the hyper-parameters of the algorithm to enhance convergence. Gradient-free optimization algorithms provide a recipe to find local minima in the absence of gradients. Gradients might not be available when the optimal control problem is especially complex or the access to data is limited. The latter is especially true for closed-loop optimizations where each FoM is obtained directly from the experiment. While finite-difference methods aim to approximate the gradient nevertheless, gradient-free optimizers are truly independent from them and commonly more efficient in the lower-dimensional searches we consider. The software comes with a simplex-based algorithm (adaptive Nelder-Mead) as well as the Covariance Matrix Adaption Evolution Strategy (CMA-ES). However, the user can add their own gradient-free algorithms via the `DirectSearchMethod` class. An example implementation can be found under `GradientFreeTemplate.py`. To reduce the number of parameters per optimization, gradient-free algorithms are commonly applied in combination with dCRAB.

A.2. dCRAB

The dressed Chopped RAndom Basis algorithm [6,34–36] is designed to optimize time-dependent pulses by expanding the control field in a truncated basis of functions. Typical used bases are elements of the Fourier series, Chebyshev polynomials, Gaussian functions, or sigmoid functions with certain randomized parameters. The advantage of doing this is two-fold: experimental constraints such as, e.g., bandwidth limitations can be considered directly by limiting the parameters during basis vector selection. Secondly, the search space to find optimal update pulses is drastically lowered in comparison to optimizing the amplitudes of a piece-wise constant pulse because only the so-called optimization-parameters are varied and optimized. These optimization-parameters are the coefficients of the basis elements such as the amplitude and phase of a sine wave or the width of a Gaussian plus any constant but variable coefficients that need to be optimized as well. The basis vectors are randomized by selecting e.g. the frequency of the sine wave randomly from within a certain range. After finding the best-performing optimization-parameters for a set of basis functions, a new set of basis vectors is selected and the resulting pulse variations are added on top of the previous best solution. This scheme, split into several super-iterations, ensures that the improvement does not get stuck in a local optimum but can converge to the optimal solution given by the superordinate constraints (e.g. maximum amplitude, bandwidth, boundary conditions) [104,105].

A.3. Gradient-based algorithms

Gradient-based optimizations are implemented via GRAPE or automatic differentiation. As a basis QuOCS provides the gradient-based updating algorithms BFGS [106] and LFBGS-B [107–109] from Scipy [110] as well as a connection to the automatic differentiation library JAX [90]. Gradient-based optimization offers an efficient method of exploring high dimensional parameter spaces to find local optima. Gradient-based methods typically require prior knowledge of the task at hand so that an analytical gradient can be derived for use in the optimizer. If an expression cannot be found, then a finite difference approximation can be used. This is a numerical approach that approximates the gradient by evaluating it at x and a small perturbation $x + \delta x$. Finite difference-based gradients are not included in this toolbox as their accuracy suffers from round-off error, and they are typically slow. Instead, for the supported problems, exact gradient methods are implemented. For gradient-based optimal control, we implement the Gradient Ascent Pulse Engineering algorithm (GRAPE) [32,33]. Time is discretized it into N piecewise constant slices. During each slice, the system Hamiltonian, governing the dynamics, is assumed to be constant, which is generally a good approximation. The GRAPE algorithm included in this toolbox uses the "auxiliary matrix method" [111–114] to compute the exact gradients of the system. State optimization and unitary gate synthesis are implemented by vectorizing the density matrix and performing the evolution in the Liouvillian space. GRAPE performs well in high dimensional parameter spaces because it can exploit the gradient and make rapid progress. However, it offers no guards against becoming stuck in a local optimum within the parameter space. QuOCS also comes equipped with an implementation of "AD-GRAPE", a reverse-mode automatic differentiation-based version of GRAPE, similar to the version implemented in [115]. By making use of the JAX [90] framework, we are able to compile both the fidelity and gradient calculations functions and execute them rapidly, dramatically reducing the time it takes to optimize. We are also able to implement novel figures of merit where the analytical gradient is difficult or impossible to derive.

Appendix B. Experimental setup

Once QuOCS forwards the optimized pulse shapes to Qudi, Qudi constructs the full measurement sequence. The measurement sequence is then uploaded to a Keysight M8195A arbitrary waveform generator (AWG) which offers a sample rate up to 65 GSa/s and generates the microwave signals. To decrease the upload speed and the overall optimization time, we lower the sample rate to 16.25 GSa/s. The microwave pulses are then send to an AR 30S1G6 amplifier (0.7-6 GHz, 30 W) and afterwards through the microwave antenna on the diamond surface (straight gold line on glass, produced by lithography). The fluorescence counts are collected via a SiPM (Ketek PE3315-WB-TIA-SP) and the obtained voltage signal is recorded with a PCI Express Digitizer (Spectrum Instrumentation, M4i.4420-x8) and analyzed by Qudi.

Appendix C. Lindblad master equation

Using Lindblad's theorem [116] the evolution of a density matrix can be written as the Markov master equation

$$\dot{\rho}(t) = \mathcal{L} \cdot \rho(t) \,, \tag{C.1}$$

where $\mathcal{L}$ is the Liouvillian operator in Lindblad form fulfilling

$$\mathcal{L} \cdot \rho = -\frac{i}{\hbar}[H, \rho] + \sum_j \left(L_j \rho L_j^\dagger - \frac{1}{2} L_j^\dagger L_j \rho - \frac{1}{2} \rho L_j^\dagger L_j \right) . \tag{C.2}$$

The matrices L_j are the Lindblad operators or jump operators that describe effects like dephasing or decoherence. More information can be found in references [117–119]. Examples using a matrix-exponential-based time evolution and an approach to solve Eq. (C.2) directly with an ordinary differential equation (ODE) solver from the JAX library can be found on the GitHub repository. Further generalizations to bring any control problem as defined in Eq. (1) plus Lindblad operators into the form of Eq. (C.1) can be made using e.g. reference [120].

These implementations make use of automatic differentiation. If the Lindblad equation is solved differently (e.g. using QuTiP or any other ode solver that is not suited for JAX) the control pulses and parameters can also be optimized by a black-box search with dCRAB and one of the gradient-free search methods in QuOCS.

References

[1] C. Brif, R. Chakrabarti, H. Rabitz, New J. Phys. 12 (7) (2010) 075008, https://doi.org/10.1088/1367-2630/12/7/075008.
[2] S.J. Glaser, U. Boscain, T. Calarco, C.P. Koch, W. Köckenberger, R. Kosloff, I. Kuprov, B. Luy, S. Schirmer, T. Schulte-Herbrüggen, D. Sugny, F.K. Wilhelm, Eur. Phys. J. D 69 (12) (2015) 279, https://doi.org/10.1140/epjd/e2015-60464-1.
[3] C.P. Koch, J. Phys. Condens. Matter 28 (21) (2016) 213001, https://doi.org/10.1088/0953-8984/28/21/213001.
[4] Christiane P. Koch, Ugo Boscain, Tommaso Calarco, Gunther Dirr, Stefan Filipp, Steffen J. Glaser, Ronnie Kosloff, Simone Montangero, Thomas Schulte-Herbrüggen, Dominique Sugny, Frank K. Wilhelm, EPJ Quantum Technol. 9 (1) (2022) 19, https://doi.org/10.1140/epjqt/s40507-022-00138-x.
[5] M.M. Müller, R.S. Said, F. Jelezko, T. Calarco, S. Montangero, Rep. Prog. Phys. 85 (7) (2022) 076001, https://doi.org/10.1088/1361-6633/ac723c.
[6] P. Rembold, N. Oshnik, M.M. Müller, S. Montangero, T. Calarco, E. Neu, AVS Quantum Sci. 2 (2) (2020) 024701, https://doi.org/10.1116/5.0006785.
[7] R.V. Gamkrelidze, J. Dyn. Control Syst. 5 (4) (1999) 437–451, https://doi.org/10.1023/A:1021783020548.
[8] H.J. Pesch, M. Plail, Doc. Math. 01 (2012).
[9] A. Agrachev, Y. Sachkov, Control theory from the geometric viewpoint, https://doi.org/10.1007/978-3-662-06404-7, 2002.
[10] W. Clark, M. Oprea, A.J. Graven, A geometric approach to optimal control of hybrid and impulsive systems, https://doi.org/10.48550/ARXIV.2111.11645, 2021.
[11] R. Unanyan, L. Yatsenko, K. Bergmann, B. Shore, Opt. Commun. 139 (1) (1997) 48–54, https://doi.org/10.1016/S0030-4018(97)00099-0.
[12] M. Demirplak, S.A. Rice, J. Phys. Chem. A 107 (46) (2003) 9937–9945, https://doi.org/10.1021/jp030708a.
[13] X. Chen, A. Ruschhaupt, S. Schmidt, A. del Campo, D. Guéry-Odelin, J.G. Muga, Phys. Rev. Lett. 104 (2010) 063002, https://doi.org/10.1103/PhysRevLett.104.063002.
[14] E. Torrontegui, S. Ibáñez, S. Martínez-Garaot, M. Modugno, A. del Campo, D. Guéry-Odelin, A. Ruschhaupt, X. Chen, J.G. Muga, in: E. Arimondo, P.R. Berman, C.C. Lin (Eds.), Advances in Atomic, Molecular, and Optical Physics, in: Advances in Atomic, Molecular, and Optical Physics, vol. 62, Academic Press, 2013, pp. 117–169.
[15] D. Guéry-Odelin, A. Ruschhaupt, A. Kiely, E. Torrontegui, S. Martínez-Garaot, J.G. Muga, Rev. Mod. Phys. 91 (2019) 045001, https://doi.org/10.1103/RevModPhys.91.045001.
[16] F. Motzoi, J.M. Gambetta, P. Rebentrost, F.K. Wilhelm, Phys. Rev. Lett. 103 (2009) 110501, https://doi.org/10.1103/PhysRevLett.103.110501.
[17] E.L. Hahn, Phys. Rev. 80 (1950) 580–594, https://doi.org/10.1103/PhysRev.80.580.
[18] H.Y. Carr, E.M. Purcell, Phys. Rev. 94 (1954) 630–638, https://doi.org/10.1103/PhysRev.94.630.
[19] L. Viola, E. Knill, S. Lloyd, Phys. Rev. Lett. 82 (1999) 2417–2421, https://doi.org/10.1103/PhysRevLett.82.2417.
[20] L. Viola, E. Knill, Phys. Rev. Lett. 90 (2003) 037901, https://doi.org/10.1103/PhysRevLett.90.037901.
[21] K. Khodjasteh, D.A. Lidar, Phys. Rev. Lett. 95 (2005) 180501, https://doi.org/10.1103/PhysRevLett.95.180501.
[22] M.J. Biercuk, H. Uys, A.P. VanDevender, N. Shiga, W.M. Itano, J.J. Bollinger, Nature 458 (7241) (2009) 996–1000, https://doi.org/10.1038/nature07951.
[23] J.R. West, D.A. Lidar, B.H. Fong, M.F. Gyure, Phys. Rev. Lett. 105 (2010) 230503, https://doi.org/10.1103/PhysRevLett.105.230503.
[24] C.L. Degen, F. Reinhard, P. Cappellaro, Rev. Mod. Phys. 89 (2017) 035002, https://doi.org/10.1103/RevModPhys.89.035002.
[25] M.M. Müller, S. Gherardini, F. Caruso, Sci. Rep. 8 (1) (2018) 1–17.
[26] V.N. Petruhanov, A.N. Pechen, Int. J. Mod. Phys. A 37 (20n21) (2022) 2243017, https://doi.org/10.1142/S0217751X22430175.
[27] F. Preti, T. Calarco, J.M. Torres, J.Z. Bernád, Optimal two-qubit gates in recurrence protocols of entanglement purification, https://doi.org/10.48550/ARXIV.2205.12091, 2022.
[28] B.L. Tomlinson, H.D.W. Hill, J. Chem. Phys. 59 (4) (1973) 1775–1784, https://doi.org/10.1063/1.1680263.
[29] D.J. Tannor, V. Kazakov, V. Orlov, in: J. Broeckhove, L. Lathouwers (Eds.), Time-Dependent Quantum Molecular Dynamics, Springer US, Boston, MA, 1992, pp. 347–360.
[30] M. Goerz, D. Basilewitsch, F. Gago-Encinas, M.G. Krauss, K.P. Horn, D.M. Reich, C. Koch, SciPost Phys. 7 (6) (2019) 080, https://doi.org/10.21468/SciPostPhys.7.6.080.
[31] D.M. Reich, M. Ndong, C.P. Koch, J. Chem. Phys. 136 (10) (2012) 104103, https://doi.org/10.1063/1.3691827.
[32] N. Khaneja, T. Reiss, C. Kehlet, T. Schulte-Herbrüggen, S.J. Glaser, J. Magn. Reson. 172 (2) (2005) 296–305, https://doi.org/10.1016/j.jmr.2004.11.004.
[33] S. Machnes, U. Sander, S.J. Glaser, P. de Fouquières, A. Gruslys, S. Schirmer, T. Schulte-Herbrüggen, Phys. Rev. A 84 (2011) 022305, https://doi.org/10.1103/PhysRevA.84.022305.
[34] P. Doria, T. Calarco, S. Montangero, Phys. Rev. Lett. 106 (2011) 190501, https://doi.org/10.1103/PhysRevLett.106.190501.
[35] T. Caneva, T. Calarco, S. Montangero, Phys. Rev. A 84 (2011) 022326, https://doi.org/10.1103/PhysRevA.84.022326.
[36] N. Rach, M.M. Müller, T. Calarco, S. Montangero, Phys. Rev. A 92 (2015) 062343, https://doi.org/10.1103/PhysRevA.92.062343.
[37] J.R. Johansson, P.D. Nation, F. Nori, Comput. Phys. Commun. 183 (8) (2012) 1760–1772.
[38] J.D. Teske, P. Cerfontaine, H. Bluhm, Phys. Rev. Appl. 17 (2022) 034036, https://doi.org/10.1103/PhysRevApplied.17.034036.
[39] H.J. Hogben, M. Krzystyniak, G.T.P. Charnock, P.J. Hore, I. Kuprov, J. Magn. Reson. 208 (2) (2011) 179–194, https://doi.org/10.1016/j.jmr.2010.11.008.
[40] N. Wittler, F. Roy, K. Pack, M. Werninghaus, A.S. Roy, D.J. Egger, S. Filipp, F.K. Wilhelm, S. Machnes, Phys. Rev. Appl. 15 (2021) 034080, https://doi.org/10.1103/PhysRevApplied.15.034080.
[41] J.M. Binder, A. Stark, N. Tomek, J. Scheuer, F. Frank, K.D. Jahnke, C. Müller, S. Schmitt, M.H. Metsch, T. Unden, T. Gehring, A. Huck, U.L. Andersen, L.J. Rogers, F. Jelezko, SoftwareX 6 (2017) 85–90, https://doi.org/10.1016/j.softx.2017.02.001.
[42] J. Scheuer, X. Kong, R.S. Said, J. Chen, A. Kurz, L. Marseglia, J. Du, P.R. Hemmer, S. Montangero, T. Calarco, et al., New J. Phys. 16 (9) (2014) 093022.
[43] G. Waldherr, Y. Wang, S. Zaiser, M. Jamali, T. Schulte-Herbrüggen, H. Abe, T. Ohshima, J. Isoya, J. Du, P. Neumann, et al., Nature 506 (7487) (2014) 204–207.
[44] F. Dolde, V. Bergholm, Y. Wang, I. Jakobi, B. Naydenov, S. Pezzagna, J. Meijer, F. Jelezko, P. Neumann, T. Schulte-Herbrüggen, et al., Nat. Commun. 5 (1) (2014) 1–9.
[45] T. Unden, P. Balasubramanian, D. Louzon, Y. Vinkler, M.B. Plenio, M. Markham, D. Twitchen, A. Stacey, I. Lovchinsky, A.O. Sushkov, et al., Phys. Rev. Lett. 116 (23) (2016) 230502.

[46] F. Frank, T. Unden, J. Zoller, R.S. Said, T. Calarco, S. Montangero, B. Naydenov, F. Jelezko, npj Quantum Inf. 3 (1) (2017) 48, https://doi.org/10.1038/s41534-017-0049-8.
[47] S. Schmitt, T. Gefen, F.M. Stürner, T. Unden, G. Wolff, C. Müller, J. Scheuer, B. Naydenov, M. Markham, S. Pezzagna, et al., Science 356 (6340) (2017) 832–837.
[48] F. Poggiali, P. Cappellaro, N. Fabbri, Phys. Rev. X 8 (2) (2018) 021059.
[49] N. Oshnik, P. Rembold, T. Calarco, S. Montangero, E. Neu, M.M. Müller, Phys. Rev. A 106 (2022) 013107, https://doi.org/10.1103/PhysRevA.106.013107.
[50] S. Conolly, D. Nishimura, A. Macovski, IEEE Trans. Med. Imaging 5 (2) (1986) 106–115, https://doi.org/10.1109/TMI.1986.4307754.
[51] A.P. Peirce, M.A. Dahleh, H. Rabitz, Phys. Rev. A 37 (1988) 4950–4964, https://doi.org/10.1103/PhysRevA.37.4950.
[52] S. McDonald, W.S. Warren, Concepts Magn. Reson. 3 (2) (1991) 55–81, https://doi.org/10.1002/cmr.1820030202.
[53] J. Casanova, Z.-Y. Wang, I. Schwartz, M.B. Plenio, Phys. Rev. Appl. 10 (2018) 044072, https://doi.org/10.1103/PhysRevApplied.10.044072.
[54] P.J. Vetter, A. Marshall, G.T. Genov, T.F. Weiss, N. Striegler, E.F. Großmann, S. Oviedo-Casado, J. Cerrillo, J. Prior, P. Neumann, F. Jelezko, Phys. Rev. Appl. 17 (2022) 044028, https://doi.org/10.1103/PhysRevApplied.17.044028.
[55] M.M. Müller, U.G. Poschinger, T. Calarco, S. Montangero, F. Schmidt-Kaler, Phys. Rev. A 92 (5) (2015) 053423.
[56] H. Fürst, M.H. Goerz, U. Poschinger, M. Murphy, S. Montangero, T. Calarco, F. Schmidt-Kaler, K. Singer, C.P. Koch, New J. Phys. 16 (7) (2014) 075007.
[57] T. Pichler, T. Caneva, S. Montangero, M.D. Lukin, T. Calarco, Phys. Rev. A 93 (1) (2016) 013851.
[58] T. Monz, P. Schindler, J.T. Barreiro, M. Chwalla, D. Nigg, W.A. Coish, M. Harlander, W. Hänsel, M. Hennrich, R. Blatt, Phys. Rev. Lett. 106 (13) (2011) 130506.
[59] A. Walther, F. Ziesel, T. Ruster, S.T. Dawkins, K. Ott, M. Hettrich, K. Singer, F. Schmidt-Kaler, U. Poschinger, Phys. Rev. Lett. 109 (8) (2012) 080501.
[60] J. Casanova, L. Lamata, I. Egusquiza, R. Gerritsma, C.F. Roos, J.J. García-Ripoll, E. Solano, Phys. Rev. Lett. 107 (26) (2011) 260501.
[61] K. Singer, U. Poschinger, M. Murphy, P. Ivanov, F. Ziesel, T. Calarco, F. Schmidt-Kaler, Rev. Mod. Phys. 82 (3) (2010) 2609.
[62] J. Zhang, M. Um, D. Lv, J.-N. Zhang, L.-M. Duan, K. Kim, Phys. Rev. Lett. 121 (16) (2018) 160502.
[63] D. Leibfried, R. Blatt, C. Monroe, D. Wineland, Rev. Mod. Phys. 75 (1) (2003) 281.
[64] S. Rosi, A. Bernard, N. Fabbri, L. Fallani, C. Fort, M. Inguscio, T. Calarco, S. Montangero, Phys. Rev. A 88 (2) (2013) 021601.
[65] S. van Frank, A. Negretti, T. Berrada, R. Bücker, S. Montangero, J.-F. Schaff, T. Schumm, T. Calarco, J. Schmiedmayer, Nat. Commun. 5 (1) (2014) 1–6.
[66] S. van Frank, M. Bonneau, J. Schmiedmayer, S. Hild, C. Gross, M. Cheneau, I. Bloch, T. Pichler, A. Negretti, T. Calarco, et al., Sci. Rep. 6 (1) (2016) 1–12.
[67] I. Brouzos, A.I. Streltsov, A. Negretti, R.S. Said, T. Caneva, S. Montangero, T. Calarco, Phys. Rev. A 92 (6) (2015) 062110.
[68] J. Sørensen, M. Aranburu, T. Heinzel, J. Sherson, Phys. Rev. A 98 (2) (2018) 022119.
[69] R. Heck, O. Vuculescu, J.J. Sørensen, J. Zoller, M.G. Andreasen, M.G. Bason, P. Ejlertsen, O. Elíasson, P. Haikka, J.S. Laustsen, et al., Proc. Natl. Acad. Sci. 115 (48) (2018) E11231–E11237.
[70] A. Omran, H. Levine, A. Keesling, G. Semeghini, T.T. Wang, S. Ebadi, H. Bernien, A.S. Zibrov, H. Pichler, S. Choi, et al., Science 365 (6453) (2019) 570–574.
[71] I. Mastroserio, S. Gherardini, C. Lovecchio, T. Calarco, S. Montangero, F.S. Cataliotti, F. Caruso, Experimental realization of optimal time-reversal on an atom chip for quantum undo operations, https://doi.org/10.48550/ARXIV.2206.02746, 2022.
[72] P. Watts, J. Vala, M.M. Müller, T. Calarco, K.B. Whaley, D.M. Reich, M.H. Goerz, C.P. Koch, Phys. Rev. A 91 (6) (2015) 062306.
[73] M.H. Goerz, G. Gualdi, D.M. Reich, C.P. Koch, F. Motzoi, K.B. Whaley, J. Vala, M.M. Müller, S. Montangero, T. Calarco, Phys. Rev. A 91 (6) (2015) 062307.
[74] F. Hoeb, F. Angaroni, J. Zoller, T. Calarco, G. Strini, S. Montangero, G. Benenti, Phys. Rev. A 96 (3) (2017) 033851.
[75] R.W. Heeres, P. Reinhold, N. Ofek, L. Frunzio, L. Jiang, M.H. Devoret, R.J. Schoelkopf, Nat. Commun. 8 (1) (2017) 94, https://doi.org/10.1038/s41467-017-00045-1.
[76] L.S. Theis, F. Motzoi, S. Machnes, F.K. Wilhelm, Europhys. Lett. 123 (6) (2018) 60001, https://doi.org/10.1209/0295-5075/123/60001.
[77] R. Heck, O. Vuculescu, J.J. Sørensen, J. Zoller, M.G. Andreasen, M.G. Bason, P. Ejlertsen, O. Elíasson, P. Haikka, J.S. Laustsen, L.L. Nielsen, A. Mao, R. Müller, M. Napolitano, M.K. Pedersen, A.R. Thorsen, C. Bergenholtz, T. Calarco, S. Montangero, J.F. Sherson, Proc. Natl. Acad. Sci. 115 (48) (2018) E11231–E11237, https://doi.org/10.1073/pnas.1716869115.
[78] F. Angaroni, A. Graudenzi, M. Rossignolo, D. Maspero, T. Calarco, R. Piazza, S. Montangero, M. Antoniotti, Personalized therapy design for liquid tumors via optimal control theory, bioRxiv, https://www.biorxiv.org/content/early/2019/06/07/662858.full.pdf, 2019, https://doi.org/10.1101/662858.
[79] A. Marshall, T. Reisser, P. Rembold, C. Müller, J. Scheuer, M. Gierse, T. Eichhorn, J.M. Steiner, P. Hautle, T. Calarco, F. Jelezko, M.B. Plenio, S. Montangero, I. Schwartz, M.M. Müller, P. Neumann, Phys. Rev. Res. 4 (2022) 043179, https://doi.org/10.1103/PhysRevResearch.4.043179.
[80] A. Pagano, S. Weber, D. Jaschke, T. Pfau, F. Meinert, S. Montangero, H.P. Büchler, Phys. Rev. Res. 4 (2022) 033019, https://doi.org/10.1103/PhysRevResearch.4.033019.
[81] J.A. Nelder, R. Mead, Comput. J. 7 (4) (1965) 308–313, https://doi.org/10.1093/comjnl/7.4.308, http://oup.prod.sis.lan/comjnl/article-pdf/7/4/308/1013182/7-4-308.pdf.
[82] F. Gao, L. Han, Comput. Optim. Appl. 51 (1) (2012) 259–277.
[83] M.J.D. Powell, Comput. J. 7 (2) (1964) 155–162, https://doi.org/10.1093/comjnl/7.2.155, http://oup.prod.sis.lan/comjnl/article-pdf/7/2/155/959784/070155.pdf.
[84] N. Hansen, S.D. Müller, P. Koumoutsakos, Evol. Comput. 11 (1) (2003) 1–18, https://doi.org/10.1162/106365603321828970.
[85] D.C. Liu, J. Nocedal, Math. Program. 45 (1) (1989) 503–528, https://doi.org/10.1007/BF01589116.
[86] Quantum-OCS, Jupyter notebooks for QuOCS, https://github.com/Quantum-OCS/QuOCS-jupyternotebooks. (Accessed 17 December 2022).
[87] Quantum-OCS, Qudi plugin repository for QuOCS, https://github.com/Quantum-OCS/Qudi-plugin. (Accessed 3 April 2023).
[88] M. Dalgaard, F. Motzoi, J. Sherson, Phys. Rev. A 105 (1) (Jan 2022), https://doi.org/10.1103/physreva.105.012402.
[89] SciPy Documentation, Settings for L-BFGS-B, https://docs.scipy.org/doc/scipy/reference/optimize.minimize-lbfgsb.html. (Accessed 19 August 2022).
[90] J. Bradbury, R. Frostig, P. Hawkins, M.J. Johnson, C. Leary, D. Maclaurin, G. Necula, A. Paszke, J. VanderPlas, S. Wanderman-Milne, Q. Zhang, JAX: composable transformations of Python+NumPy programs, http://github.com/google/jax, 2018.
[91] R. Schneider, V. Mikulik, Just in time compilation with JAX, https://jax.readthedocs.io/en/latest/jax-101/02-jitting.html. (Accessed 17 April 2023).
[92] J.J.W.H. Sørensen, M.O. Aranburu, T. Heinzel, J.F. Sherson, Phys. Rev. A 98 (2018) 022119, https://doi.org/10.1103/PhysRevA.98.022119.
[93] S. Machnes, E. Assémat, D. Tannor, F.K. Wilhelm, Phys. Rev. Lett. 120 (2018) 150401, https://doi.org/10.1103/PhysRevLett.120.150401.
[94] M.W. Doherty, N.B. Manson, P. Delaney, F. Jelezko, J. Wrachtrup, L.C. Hollenberg, Phys. Rep. 528 (1) (2013) 1–45, https://doi.org/10.1016/j.physrep.2013.02.001.
[95] V. Jacques, P. Neumann, J. Beck, M. Markham, D. Twitchen, J. Meijer, F. Kaiser, G. Balasubramanian, F. Jelezko, J. Wrachtrup, Phys. Rev. Lett. 102 (2009) 057403, https://doi.org/10.1103/PhysRevLett.102.057403.
[96] J.F. Haase, P.J. Vetter, T. Unden, A. Smirne, J. Rosskopf, B. Naydenov, A. Stacey, F. Jelezko, M.B. Plenio, S.F. Huelga, Phys. Rev. Lett. 121 (2018) 060401, https://doi.org/10.1103/PhysRevLett.121.060401.
[97] M. Steiner, P. Neumann, J. Beck, F. Jelezko, J. Wrachtrup, Phys. Rev. B 81 (2010) 035205, https://doi.org/10.1103/PhysRevB.81.035205.
[98] N.B. Manson, J.P. Harrison, M.J. Sellars, Phys. Rev. B 74 (2006) 104303, https://doi.org/10.1103/PhysRevB.74.104303.
[99] P.J. Vetter, A. Marshall, G.T. Genov, T.F. Weiss, N. Striegler, E.F. Großmann, S. Oviedo-Casado, J. Cerrillo, J. Prior, P. Neumann, F. Jelezko, Phys. Rev. Appl. 17 (2022) 044028, https://doi.org/10.1103/PhysRevApplied.17.044028.
[100] F. Frank, T. Unden, J. Zoller, R.S. Said, T. Calarco, S. Montangero, B. Naydenov, F. Jelezko, npj Quantum Inf. 3 (1) (2017) 1–5.
[101] T. Häberle, D. Schmid-Lorch, K. Karrai, F. Reinhard, J. Wrachtrup, Phys. Rev. Lett. 111 (17) (2013) 170801.
[102] A.F.L. Poulsen, J.D. Clement, J.L. Webb, R.H. Jensen, L. Troise, K. Berg-Sørensen, A. Huck, U.L. Andersen, Phys. Rev. B 106 (2022) 014202, https://doi.org/10.1103/PhysRevB.106.014202.
[103] F. Motzoi, J.M. Gambetta, S.T. Merkel, F.K. Wilhelm, Phys. Rev. A 84 (2011) 022307, https://doi.org/10.1103/PhysRevA.84.022307.
[104] J.-S. Li, J. Ruths, D. Stefanatos, J. Chem. Phys. 131 (16) (2009) 164110, https://doi.org/10.1063/1.3253796.
[105] J. Ruths, J.-S. Li, IEEE Trans. Autom. Control 57 (8) (2012) 2021–2032, https://doi.org/10.1109/TAC.2012.2195920.
[106] J. Nocedal, S.J. Wright, Numerical Optimization, 2nd edition, Springer Series in Operations Research, Springer, New York, 2006.
[107] R.H. Byrd, P. Lu, J. Nocedal, C. Zhu, SIAM J. Sci. Comput. 16 (5) (1995) 1190–1208, https://doi.org/10.1137/0916069.
[108] J.L. Morales, J. Nocedal, ACM Trans. Math. Softw. 38 (1) (dec 2011), https://doi.org/10.1145/2049662.2049669.
[109] C. Zhu, R.H. Byrd, P. Lu, J. Nocedal, ACM Trans. Math. Softw. 23 (4) (1997) 550–560, https://doi.org/10.1145/279232.279236.
[110] P. Virtanen, R. Gommers, T.E. Oliphant, M. Haberland, T. Reddy, D. Cournapeau, E. Burovski, P. Peterson, W. Weckesser, J. Bright, S.J. van der Walt, M. Brett, J. Wilson, K.J. Millman, N. Mayorov, A.R.J. Nelson, E. Jones, R. Kern, E. Larson, C.J. Carey, İ. Polat, Y. Feng, E.W. Moore, J. VanderPlas, D. Laxalde, J. Perktold, R. Cimrman, I. Henriksen, E.A. Quintero, C.R. Harris, A.M. Archibald, A.H. Ribeiro, F. Pedregosa, P. van Mulbregt, Nat. Methods 17 (3) (2020) 261–272, https://doi.org/10.1038/s41592-019-0686-2.
[111] P. de Fouquieres, S.G. Schirmer, S.J. Glaser, I. Kuprov, J. Magn. Reson. 212 (2) (2011) 412–417, https://doi.org/10.1016/j.jmr.2011.07.023.
[112] D.L. Goodwin, Advanced optimal control methods for spin systems, arXiv: 1803.10432 [quant-ph], 2017, https://doi.org/10.5258/soton/t0003.

[113] H.J. Hogben, M. Krzystyniak, G.T.P. Charnock, P.J. Hore, I. Kuprov, J. Magn. Reson. 208 (2) (2011) 179–194, https://doi.org/10.1016/j.jmr.2010.11.008.
[114] F.F. Floether, P. de Fouquieres, S.G. Schirmer, New J. Phys. 14 (7) (2012) 073023, https://doi.org/10.1088/1367-2630/14/7/073023.
[115] N. Leung, M. Abdelhafez, J. Koch, D. Schuster, Phys. Rev. A 95 (2017) 042318, https://doi.org/10.1103/PhysRevA.95.042318.
[116] G. Lindblad, Commun. Math. Phys. 48 (2) (1976) 119–130, https://doi.org/10.1007/BF01608499.
[117] H.-P. Breuer, F. Petruccione, The Theory of Open Quantum Systems, Oxford University Press, 2007.
[118] F. Marquardt, A. Püttmann, Introduction to dissipation and decoherence in quantum systems, https://doi.org/10.48550/ARXIV.0809.4403, 2008.
[119] D. Manzano, AIP Adv. 10 (2) (02 2020) 025106, https://doi.org/10.1063/1.5115323, https://pubs.aip.org/aip/adv/article-pdf/doi/10.1063/1.5115323/12881278/025106_1_online.pdf.
[120] F. Campaioli, J.H. Cole, H. Hapuarachchi, A tutorial on quantum master equations: tips and tricks for quantum optics, quantum computing and beyond, arXiv:2303.16449, 2023.

3.3 Gate-Set Evaluation Metrics for Closed-Loop Optimal Control on Nitrogen-Vacancy Center Ensembles in Diamond

3.3.1 Summary

Accurate control of a quantum system is essential for most applications in quantum technologies. On the way towards fault-tolerant quantum computing, low errors per applied gate are needed for efficient error correction [266]. In quantum sensing, faulty gates can lead to a misinterpretation of the results [267] and error correction might bias the protocol [268]. To implement an operation on a quantum system, the needed gates are designed and then calibrated to provide the best performance within the given method for characterization, minimizing the single-gate errors. However, the accumulation of errors does not necessarily occur linearly for repeated applications of the gate [269, 270] or might differ, depending on the current state of the system. It can therefore be beneficial to regard the gate in the context of, e.g., the specific circuit and its position therein and the duration and actions before and after the applications of the gate. Different gates are often realized by similar drives, only varying in, e.g., the amplitude or phase of the external fields. To look at the whole gate-set at once, instead of singling out an individual operation, can thus also be of advantage. This can avoid a wrong estimation and aid to determine the performance in context of the effects of other gates and system configurations. During optimization, a set of gates is ideally found such that it performs well in any circuit it is being used in. In Ref. [3] we therefore investigate FoMs based on the gate(-set) evaluation metrics mentioned in Sec. 2.2, namely Quantum Process Tomography (QPT), Linear Inversion Gate-Set Tomography (LGST), Randomized Linear Gate-Set Tomography (RLGST), and Randomized Benchmarking for Immediate Tune-Up (ORBIT), for their suitability for closed-loop quantum optimal control.

As a test-bed, we use an ensemble of NV centers spread out with a concentration of 1.5 ppm in a layer of 10 µm thickness. The NVs are collectively driven by a microwave field transmitted though a gold antenna on the diamond surface. Optical readout and initialization is done by a laser with a 38 µm beam waist and a wavelength of 532 nm. The main advantage of the NV ensemble we exploit, is the fast signal accumulation for quick measurements. However, some disadvantages, such as large SPAM errors, a non-Markovian noise environment, and a variation of the observed microwave field by each single NV, are inherent on this setup. For our purpose, these disadvantages are intended and used as a feature to compare the impact of these effects on the optimization and evaluation with the different methods. Some approximations, e.g. in RLGST, might not hold during the pulse variation in the closed-loop search. This is also intended and part of the investigation of the suitability for optimization. For the optimization we choose to vary only one gate, the $-\mathcal{X}_{\pi/2}$ gate (see Sec. 2.2), in order to reduce the time needed for convergence and to favour more repetitions of optimization runs and number of experiments in general.

In the first part of the publication, we perform a basic investigation of the system and the FoMs, as defined in the methods section. A measurement of Rabi oscillations demonstrates some ensemble effects and the dependence of the correct pulse parameters on circuit length and sequence duration. A comparison between the performance of a guess pulse (30 ns) that is used as the input to the optimizations and a reference pulse ($\sim$ 14 ns) is made. Furthermore, a

variation of the pulse amplitude under constant duration, resulting in over- and under-rotations, show a convex behaviour of the FoMs around the expected target value. Since dCRAB usually performs large amplitude variations in the beginning of a search, this serves as a sanity check of our definitions. However, not all FoMs provide the same output (see Sec. 2.2). Thus for comparability, an optimization gain is introduced as

$$\text{Gain} = \frac{\text{FoM}_{\text{opt}} - \text{FoM}_{\text{guess}}}{\text{FoM}_{\text{ref}} - \text{FoM}_{\text{guess}}} \,. \tag{3.1}$$

By relating the FoM improvement of the optimized pulse and the reference pulse over the guess pulse, we can ensure a fair comparison between the different methods.

The FoMs based on QPT, LGST, RLGST and ORBIT are examined and compared. For that, we carry out several optimizations with each FoM and evaluate the optimized pulses with each method and an additional RB measurement. This way we can cross-compare the resulting pulses between all methods. The results show good performances for the methods with QPT, RLGST and ORBIT. LGST, in the form as implemented, is not able to achieve large gain values as well as consistent results throughout the evaluation methods. Therefore, a FoM based on LGST and defined via the expectation values of the method, called $\tilde{G}$, is also investigated. It displays a strong bias towards maximizing the gain resulting from the evaluation with this method itself, but cannot generally be reproduced by the evaluation with the remaining techniques. Furthermore, the comparison indicates differences in the contribution and weighting of ensemble effects to the distinct methods.
The FoM for QPT is based on fixed measurements, all with a relatively short circuit length. On the other hand, the average circuit length (L) for both, RLGST and ORBIT can be tuned arbitrarily and were selected much longer for the comparison. Therefore, the dependence on L for both methods is investigated in the latter part of the publication. Scans of the pulse amplitude (voltage) for different length parameters show a shifting optimum of the square guess pulse towards higher voltages for the two methods in accordance with the shifts in Rabi frequency. Optimizations at different L indicate improvements of the optimized pulse for longer circuits if optimized with ORBIT. The RLGST-based method is less conclusive but also suggests a better performance for optimization with larger circuit lengths. Overall, ORBIT provides the the most reproducible improvement and best gain values throughout the cross-comparison between all the methods.

In conclusion we find, that the specific gate-set evaluation metric for optimization has to be chosen based on the intended usage of the resulting gates and the characteristics of the setup. With higher circuit lengths, an optimization with RLGST or ORBIT is advantageous, since they capture incoherent errors well due to randomization and twirling. ORBIT displays a better performance compared to RLGST, but yields less information about the system, especially if it is not followed up by an RB measurement. In RLGST, additional gates and composite gates, such as building blocks for sensing sequences, or even an incomplete gate-set could be used in the scheme and more information about the individual gate-set elements is obtained. Both methods can be tuned to the intended application scenario and be further adapted to minimize the overhead due to, e.g., averaging over randomized instances. For shorter circuit lengths, QPT seems to be a valid alternative, at least for optimization. Furthermore, more advanced

strategies such as long-sequence GST [104] or randomized compiling [133] promise to provide a better insight into the actions of the gate-set and their suitability for optimization purposes needs to be investigated.

Title: Gate-set evaluation metrics for closed-loop optimal control on nitrogen-vacancy center ensembles in diamond

Authors: Philipp J. Vetter†, **Thomas Reisser**†, Maximilian G. Hirsch, Tommaso Calarco, Felix Motzoi, Fedor Jelezko, Matthias M. Müller

Journal: npj Quantum Information

Publisher: Springer Nature

Year: 2024

Volume: 10

Issue: 1

DOI: 10.1038/s41534-024-00893-y

Link: `https://doi.org/10.1038/s41534-024-00893-y`

† These authors contributed equally to this work.

3.3.2 Author's Contribution

Thomas Reisser contributed to the conceptualization of the project, the theory and made supporting simulations. He worked on the design of the measurements and optimizations and the writing of the manuscript. He analyzed the measurement data and composed most of the figures. Thomas provided support for the implementation of closed-loop optimization and implemented required features in the software QuOCS. In addition, Thomas helped on improvements to the experimental setup.

3.3.3 Data Availability

The experimental data and evaluated data shown in Publication [3] is stored on the backed-up data servers of PGI-8 at Forschungszentrum Jülich (FZJ) and available upon request to the author of this thesis or the Institute for Quantum Control (PGI-8). Further experimental raw data is stored at the Institute for Quantum Optics in Ulm and can be requested from Philipp Vetter (see publication).

npj | quantum information

Article

Published in partnership with The University of New South Wales

https://doi.org/10.1038/s41534-024-00893-y

Gate-set evaluation metrics for closed-loop optimal control on nitrogen-vacancy center ensembles in diamond

Philipp J. Vetter[1,2,7] ✉, Thomas Reisser[3,4,7], Maximilian G. Hirsch[1,2,6], Tommaso Calarco[3,4,5], Felix Motzoi[3,4], Fedor Jelezko[1,2] & Matthias M. Müller[3]

A recurring challenge in quantum science and technology is the precise control of their underlying dynamics that lead to the desired quantum operations, often described by a set of quantum gates. These gates can be subject to application-specific errors, leading to a dependence of their controls on the chosen circuit, the quality measure and the gate-set itself. A natural solution would be to apply quantum optimal control in an application-oriented fashion. In turn, this requires the definition of a meaningful measure of the contextual gate-set performance. Therefore, we explore and compare the applicability of quantum process tomography, linear inversion gate-set tomography, randomized linear gate-set tomography, and randomized benchmarking as measures for closed-loop quantum optimal control experiments, using a macroscopic ensemble of nitrogen-vacancy centers in diamond as a test-bed. Our work demonstrates the relative trade-offs between those measures and how to significantly enhance the gate-set performance, leading to an improvement across all investigated methods.

Be it quantum computing, information, communication or metrology, precise control over a quantum system is a prerequisite for any successful application. To ensure robust results and the ability to run long quantum circuits, a great effort is spent by, e.g., IBM and Google on a periodic re-calibration of their quantum chips[1–6]. To this end a plethora of error correction and error suppression schemes are developed to achieve fault tolerant quantum computing[7–12]. Another example is quantum sensing, where the measured signals can be biased by quantum error correction[13] or distorted by faulty gates that are not accounted for[14].

In general, the precision of the system often suffers under, e.g., erroneous operations, wrongly populated states or limited knowledge of the system. Moreover, these errors must not necessarily accumulate linearly[15–17], leading to a dependence of the optimal controls for specific operations on the chosen circuit and the corresponding point of time within the selected circuit[2,3]. Thus, the quality of an operation has to be viewed within the context of its application, rather than looking at isolated individual gates; the focus should be shifted to their performance with respect to the chosen circuit and the entire gate-set. The ideal scenario would be to find a set of gates that performs universally well, regardless of the planned experiment. Since such a gate-set will heavily depend on the chosen experimental system, Quantum Optimal Control (QOC)[18–22] is well suited to tackle this complex problem.

Several optimization algorithms[23–31] are available in dedicated software packages such as our Quantum Optimal Control Suite (QuOCS)[32] that allows for closed-loop black-box optimization employing the dCRAB algorithm[22,27] via an interface to the lab software Qudi[33]. Such closed-loop optimizations based on measurements on the quantum system have been employed for gate optimization in superconducting qubits via randomized benchmarking[34,35], to optimize the preparation and phase transitions of Bose-Einstein condensates[36,37], enhance the macroscopic hyperpolarization in pentacene-doped naphthalene crystals[38] and for autonomous calibration of single-qubit gates as well as robust magnetometry of nitrogen-vacancy (N-V) centers in diamond[39,40]. For N-V centers in general, QOC has become a valuable tool for a wide range of challenges[14,21,41–49].

Room-temperature accessibility and control of their electronic spin state makes N-V centers ideal sensors for magnetic and electric fields[50–53]. Ensembles of N-V centers have particularly become a focus of attention, as these allow to drastically improve the sensitivity[54–56], create spatially resolved images of, e.g., local magnetic fields[57–59] and can even be used to create new phases of matter[60,61]. Due to their macroscopic size, many individual

[1]Institute for Quantum Optics, Ulm University, Ulm, Germany. [2]Center for Integrated Quantum Science and Technology (IQST), Ulm, Germany. [3]Peter Grünberg Institute – Quantum Control (PGI-8), Forschungszentrum Jülich GmbH, Jülich, Germany. [4]Institute for Theoretical Physics, University of Cologne, Cologne, Germany. [5]Dipartimento di Fisica e Astronomia, Università di Bologna, Bologna, Italy. [6]Present address: NVision Imaging Technologies GmbH, Ulm, Germany. [7]These authors contributed equally: Philipp J. Vetter, Thomas Reisser. ✉e-mail: philipp.vetter@uni-ulm.de

https://doi.org/10.1038/s41534-024-00893-y **Article**

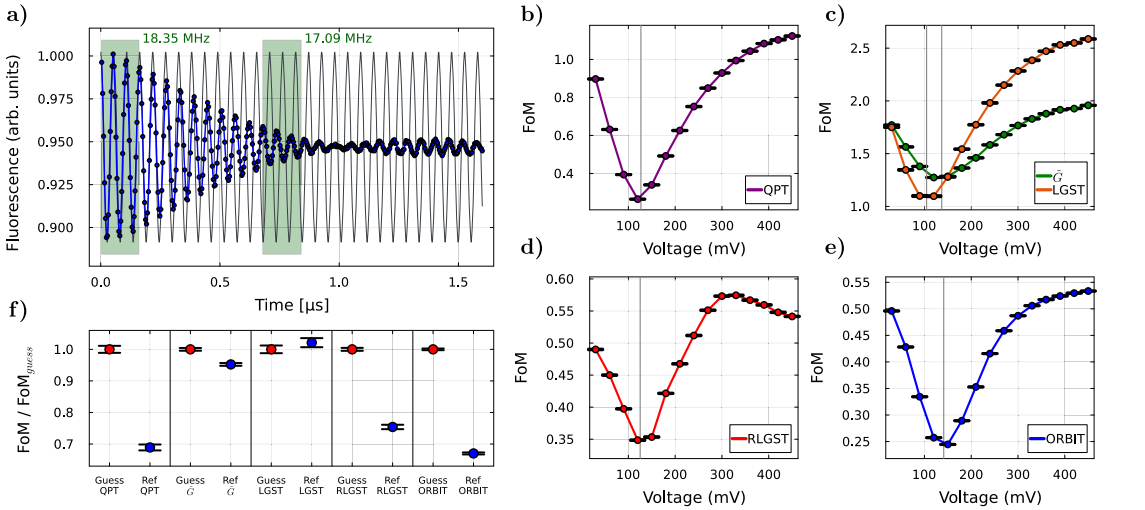

Fig. 1 | Ensemble dynamics and FoM validity measurements. a Rabi experiment with the N-*V* center ensemble, showing a strong beating due to the different Rabi oscillations of all individually contributing N-*V* centers. The green areas highlight the time dependence of the Rabi frequency and the black background oscillation visualizes the corresponding shift. **b** Linear sweep of the guess pulse amplitude for QPT, (**c**) LGST and $\tilde{G}$, (**d**) RLGST and (**e**) ORBIT. The ordinate shows the absolute value of the mean FoM from 20 measurements and the uncertainty. The minimum of the corresponding FoM is indicated by a gray line. **f** Comparison of the FoM definitions for the guess (red) and reference pulse (blue), normalized by FoM$_{guess}$. Each data point shows the mean value of 20 measurements with the corresponding standard deviation.

N-*V* centers contribute to the measurement, which ensures a very fast signal acquisition but can also result in strong detuning and large amplitude errors. These errors can negatively influence gate performances especially at different time-scales, as can be seen in Fig. 1a. The observed beating arises from the mixture of varying Rabi oscillation frequencies contributing to the measured signal. A macroscopic ensemble of N-*V* centers thus combines the effects of circuit- and length-dependent errors, large state preparation and measurement (SPAM) errors, a non-Markovian noise environment, and a high sensitivity to possible experimental drifts and distortions of the control pulses, making it an ideal test-bed to investigate the applicability of QOC for these kinds of inhomogeneous error mechanisms.

In order to find a universally well performing gate-set, a good measure is required, that reflects the quality of operations on the system in a holistic framework, being sensitive to the system dynamics on different time-scales and reliably accessible via measurements. To this end, we derive several measures of our gate-sets performance based on classical Quantum Process Tomography (QPT)[39,62–64], Linear-inversion Gate-Set Tomography (LGST)[65,66] and Randomized Linear Gate-Set Tomography (RLGST)[67] as well as Optimized Randomized Benchmarking for Immediate Tune-up (ORBIT)[35]. We experimentally asses their applicability for closed-loop optimizations in our test-bed and investigate how they reflect the system dynamics. We proceed by performing several optimization runs per method and cross-evaluate the performance of the optimized gate-set against all other methods as well as by Randomized Benchmarking (RB)[68–70]. Large improvements of the gate-set are observed in almost all optimization scenarios, significantly outperforming the provided guess and even outperforming the commonly used fastest possible rectangular shaped pulse. Moreover, we investigate how the chosen circuit length influences our obtained results for selected methods. Finally, we discuss the relative trade-offs of the individual methods applied on these types of systems and show how to best enhance the performance of the selected gate-set to find a universally well performing set.

Results

The experiments are performed with a CVD-grown diamond with a natural abundance (1.1%) of ^{13}C nuclei and a 10 µm thick layer of N-*V* centers. The layer contains an N-*V* concentration of roughly 1.5 ppm and is excited by a 532 nm laser with a beam waist of ≈38 µm. We apply a static magnetic field of 572 G to polarize the inherent nitrogen spin[71] and to create an effective qubit between the $|0\rangle$ and $|-1\rangle$ states. Gates are generated by microwave pulses sent through a straight microwave antenna made out of gold and placed on top of the diamond.

The figures of merit

We choose the gate-set

$$\begin{aligned}\mathcal{G} &= \{G_0, G_1, G_2, G_3, G_4, G_5, G_6\} \\ &= \{\mathbb{1}, \mathcal{X}_{\pi/2}, -\mathcal{X}_{\pi/2}, \mathcal{Y}_{\pi/2}, -\mathcal{Y}_{\pi/2}, \mathcal{X}_{\pi}, \mathcal{Y}_{\pi}\}\end{aligned} \tag{1}$$

for our experiments. Here, $\mathbb{1}$ is the identity and $\mathcal{X}$ and $\mathcal{Y}$ are the rotations around the *x*- and *y*- axis, where the rotation angle is given by the index. The gate-set is chosen such that we can generate the full Clifford group[72] needed for RB and ORBIT. We limit our optimizations to $G_2 = -\mathcal{X}_{\pi/2}$ to analyze how the change of an individual pulse affects the performance of our gate-set Eq. (1) and to ensure that the optimization converges quickly. All other gates are kept constant throughout all experiments, corresponding to rectangular pulses at maximum amplitude, whose pulse length is determined by a Rabi experiment. Except for QPT, all methods evaluate the performance of the entire gate-set, leading to the exact same measurements as if we would optimize all gates at once. Thus we do not expect a loss of generality of our results by limiting ourselves to one optimized gate. The initial state is set to $|\rho\rangle\rangle = |0\rangle\rangle$ and the POVM to $|E\rangle\rangle = |0\rangle\rangle$ for all of our experiments. Note that operators and states are given in Hilbert-Schmidt space to benefit from a simplified syntax (see supplementary information).

The performance of the gate-set is evaluated through measures based on QPT[39,62–64], LGST[65,66], RLGST[67] and ORBIT[35]. Additionally, we consider an adaption of LGST where we only take the targeted expectation values into account and label it $\tilde{G}$. The information extracted from these schemes is condensed down to a single real-valued number, called the Figure of Merit (FoM). The derivation and exact formula of the FoMs for each scheme can be found in the Methods "Definitions of the Figures of Merit". Note that the FoM is minimized in all experiments.

https://doi.org/10.1038/s41534-024-00893-y Article

Different types of errors can be present in the system. Incoherent errors, as, e.g., bit-flip errors[73], are stochastic errors that do not preserve the purity of the state[74]. They often arise from the interaction with the environment or noise on the control fields, leading, e.g., to non-unitary processes. Incoherent noise effects scale linearly with the circuit size[75,76]. Coherent errors, on the other hand, arise from, e.g., deterministic interactions of the system with surrounding spins and constant electromagnetic fields or imperfections due to miscalibrations of the control field[77]. In contrast to incoherent errors, they scale quadratically with the circuit size[75,76]. Furthermore, the system can be subject to errors classified as Markovian and non-Markovian[78], which can be contained in both, coherent and incoherent effects[79]. Errors which exhibit temporal correlations and memory effects are referred to as non-Markovian errors, while Markovian errors are given by irreversible, memory-less errors, e.g., white noise.

Not all of our FoMs are susceptible to these error sources in the same way. QPT, $\bar{G}$ and LGST, as employed here, will show a much stronger change of their corresponding FoM due to coherent errors in the form of over- and under-rotations than the other methods (see supplementary information). Due to their short circuit length, the correction of incoherent errors, as present in our system, like e.g., dephasing, will only lead to a slight change of their respective FoM. For RB on the other hand, the twirling condition[69] makes the method less sensitive to the full extend of coherent errors[74,80,81] and will thus weigh them differently. While ORBIT is based on RB, the method, and thus our FoM, directly measures the survival probability at a given circuit length. ORBIT does not perform a full-fledged RB experiment and therefore, a change of the coefficients that absorb SPAM errors or affect the final Clifford gate[70,82] can also lead to a change in our FoM. Despite the method, as employed in our studies, being mainly sensitive to incoherent errors, due to large circuit lengths, the FoM for ORBIT is still capable of detecting coherent errors. While RLGST is also based on randomized circuits, the method provides estimates of the gate-set, which is used to calculate our FoM. These estimates are only valid within the approximation of a linear-noise regime[67] and thus may suffer under large coherent errors. Due to the (potentially) significantly longer circuits, the method will be more sensitive to incoherent errors than the other methods with short circuit lengths. Like for LGST, incoherent errors can lead to a non-physical representation of the estimated gates. However, this must not be a problem for our application, as long as the FoM deteriorates for worse gates. In the case of RB and ORBIT, incoherent errors simply contribute to the observed exponential decay and they are also covered by the description of a process matrix in QPT.

Non-Markovian errors on the other hand will affect all FoMs. They can lead, for example, to a non-exponential decay in RB[80] and will negatively influence LGST[83]. Not only will coupling to surrounding nuclear spins lead to potentially non-Markovian errors during our measurements, but as we sum up the fluorescence signal of all N-V centers within our ensemble, specific sequences can exhibit strong temporal correlations, such as, e.g., seen by the beating of the Rabi oscillations in Fig. 1a. In our case, these errors arise from over- and under-rotations of the corresponding N-V centers attributed to the difference in driving field amplitude due to their varying distance to the microwave antenna, as well as their detunings due to the inhomogeneity of the external magnetic field. Thus, while some of our FoMs are by definition more sensitive to incoherent errors, due to their increased circuit length, these errors originate to a large degree from coherent dynamics, which if corrected, also lead to an improvement of the other FoMs. An effect that we more thoroughly analyze in "Optimizations with varying circuit length".

As QPT is unable to account for SPAM errors, all of the above mentioned errors can negatively influence the corresponding FoM even if they do not only act on the target gate.

During the closed-loop QOC experiments, QuOCS varies the S_x and S_y components of the microwave pulse amplitudes. To check the feasibility of our FoM definition, we sweep the pulse amplitude by varying the applied microwave voltage at a constant length $T = 30$ ns for a rectangular pulse, effectively creating a gate G_2 that either under- or over-rotates the spin instead of performing a $-\mathcal{X}_{\pi/2}$ operation. We select a circuit length of $L_R = 18$ for RLGST, which corresponds to a circuit length of $L_O = 10$ Cliffords for ORBIT. We average over 300 circuits to satisfy the twirling condition of RB and use the same number in RLGST and ORBIT for consistency, while ensuring that the number of circuits is significantly larger than the number of parameters to be estimated in RLGST[67]. The effect of this variation on the FoMs is shown in Fig. 1b–e. All curves show a distinct minimum from which the FoM increases upon deviation from the ideal voltage within the context of the individual technique. The obtained results again highlight the problem of circuit- and length-dependence of the optimal control parameters of our system, as we observe different minima, i.e., a different best amplitude, for all methods. This effect can be attributed to the previous discussion of coherent and incoherent errors and their influence on our FoMs.

Next, we investigate how a change in the pulse duration affects our FoMs. A short pulse with large amplitude is expected to outperform a long pulse with small amplitude because of its increased robustness against detuning errors as well as a smaller decoherence due to the shorter duration. In Fig. 1f the FoM of a 30 ns long rectangular pulse, which we from now on label as the "guess" pulse since it will be later handed to QuOCS as the guess at the start of our closed-loop QOC experiments, and the FoM of the shortest possible rectangular pulse of ≈14 ns, labeled as "reference" pulse, are shown. In both cases, the amplitude is determined through a Rabi experiment to match the selected pulse length. The shortest pulse is constrained by the maximal voltage that can be generated. Except for LGST, all methods show the expected behavior, that the short reference pulse achieves a significantly lower FoM than the guess pulse. While $\bar{G}$ shows a smaller difference when compared with QPT, RLGST and ORBIT, the observed difference is well above the margin of error. LGST indicates that the reference pulse performs slightly worse than the guess pulse and it appears that the method cannot be used for our macroscopic ensemble as it does not capture the expected dynamics of our effective spin correctly. Therefore, we drop LGST as a measure for the cross-comparison of the optimized gate-sets between the different methods but still explore how it competes as a FoM for closed-loop optimizations.

Optimization gain

When comparing different analysis methods with each other, it is important to not only consider the absolute change in their FoM but to compare the relative change between two fixed reference points in order to correctly interpret the measurement results. Therefore, we introduce the so-called gain

$$\text{Gain} = \frac{\text{FoM}_{\text{opt}} - \text{FoM}_{\text{guess}}}{\text{FoM}_{\text{ref}} - \text{FoM}_{\text{guess}}} \tag{2}$$

which displays the achieved improvement of the FoM_{opt} in relation to the FoM of the reference and guess pulse. If the gain exceeds 1, it outperforms the rectangular reference pulse with maximum amplitude and if it falls below 0, the analyzed pulse performs worse than the provided guess pulse. The gain is a valuable quantity to ensure a fair comparison between the different analysis methods, regardless of their absolute value at any given point. If the absolute value of the FoM would change over several days due to thermal shifts or mechanical disturbances, the calculated gain remains constant.

Optimization workflow

The pulse shape of the microwave pulses

$$\Omega(t) = a_x(t)\cos(\omega t) + a_y(t)\sin(\omega t) \tag{3}$$

can be expressed by the time-dependent amplitudes $a_x(t)$ and $a_y(t)$, which represent the S_x and S_y (x- and y- spin operator) component of the corresponding gate. During our closed-loop QOC experiments we vary those time-dependent amplitudes according to the dCRAB algorithm[21,22,27,39] (see Methods "dCRAB Algorithm and Settings").

https://doi.org/10.1038/s41534-024-00893-y **Article**

Figure 2 describes the workflow of such a closed-loop optimization. First, we select an analysis method, e.g., RLGST, which defines how the measurement sequence looks like and how the FoM is calculated. At the start of the optimization QuOCS[32] hands Qudi the initial guess pulse. The pulse is incorporated in the measurement sequence constructed by Qudi[33], our experimental control and data processing software. The full measurement sequence is uploaded via Qudi to the arbitrary waveform generator (Keysight M8195A) which generates the analog waveform and all required digital trigger signals. The analog waveform signal is sent through a 30 W amplifier (AR-30S1G6) at 80% gain and then through a straight gold microwave structure on the diamond's surface. The N-V centers are initialized and read out via a 532 nm green laser (Novanta Photonics gem 532) and their red fluorescence light is collected by a silicon photo-multiplier (Ketek PE3315-WB-TIA-SP). We use a digitizer (Spectrum Instrumentation M4i.4420-x8) to record the fluorescence signal which in turn is analyzed and evaluated by Qudi to obtain the N-V centers' spin state population. Once finished, Qudi calculates the FoM according to the selected analysis method, while treating the N-V ensemble as one effective qubit. The FoM is handed to QuOCS which in turn calculates a new pulse shape and the whole cycle repeats.

Following the closed-loop QOC experiment, the optimized pulse is benchmarked via all evaluation methods as well as a complete RB experiment.

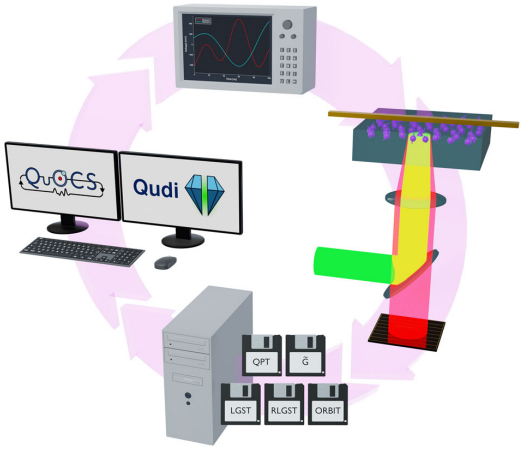

Fig. 2 | Workflow of the closed-loop QOC experiments. First, we select the analysis method, e.g., RLGST. Qudi then constructs the measurement sequence using the optimized pulse shape provided by QuOCS. The sequence is uploaded to the AWG to create the microwave signals. Finally, a green laser pulse is used to read out the N-V centers and the red fluorescence light is collected to calculate the corresponding FoM. The FoM is send to QuOCS which in return computes a new pulse shape and the cycle repeats.

Cross-comparison

Each optimization setting is repeated five times to investigate the stability and reproducibility of the optimization. The cross-evaluation of each experiment is shown in Fig. 3a displays an overview of all obtained gain values after optimization. Each column represents the method used for the FoM calculation during the closed-loop QOC experiment, each row represents the evaluation method and the height of the bars corresponds to the achieved gain, Eq. (2). For the evaluation with randomized benchmarking we use the extracted average error rate[69,70] instead of a FoM to calculate the corresponding gain. For a better comparison, we also show the average gain over all five optimizations for each method with the corresponding standard deviation in Fig. 3b. In Fig. 3c we show the gains of the pulse that performs best upon evaluation with its own optimization method for each of the five runs.

Optimization with QPT

For QPT, we observe a homogeneous gain progression across the whole column, i.e., for all evaluation methods. Evaluated with QPT, the achieved gain is on the same level as when evaluated by RLGST and RB. The first optimization run did not find a very good solution, which can happen because of the limited settings for the optimizer and can safely be marked as an outlier. Note, however, that this outlier leads to a large variance of the average values in Fig. 3b.

Optimization with $\tilde{G}$

Optimizing the pulse shape with $\tilde{G}$ leads to an outstanding improvement of the optimized pulse over the reference pulse when being evaluated with $\tilde{G}$ itself, resulting in an average gain of 1.34 and the highest achieved value of all

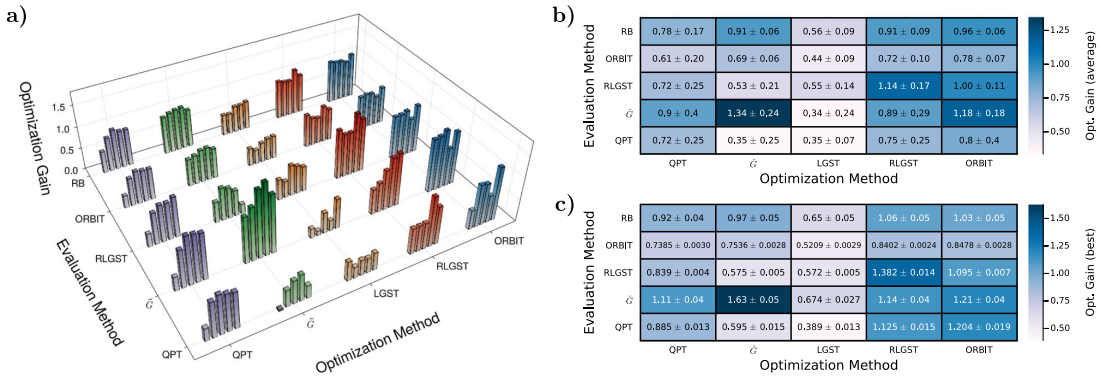

Fig. 3 | Cross-comparison of the closed-loop QOC experiments. a The x-axis shows the method selected to calculate the FoM during an optimization. We perform five optimization runs per method, represented by five bars, whose color denotes the optimization method. Their height corresponds to the achieved gain for the chosen evaluation method displayed in the y-axis and is is the average of 20 individual measurements. **b** Average gain of the five optimizations per method together with the standard deviation. The abscissa corresponds to the method selected for the FoM calculation during the optimization and the ordinate to the chosen evaluation method to calculate the gain. The color-scale indicated the achieved average gain. **c** The best performing pulse, when evaluated by its optimization method, is re-measured for all other evaluation methods. The error corresponds to the uncertainty of 20 measurements and the color-scale corresponds to the gain of the best performing pulse.

https://doi.org/10.1038/s41534-024-00893-y **Article**

measurements of 1.63. However, the large improvement in the gain compared to the reference pulse is not retained for the other evaluation methods. We obtain low performances for QPT and RLGST but high gain values if evaluated with ORBIT and RB.

Despite their similarities, a large improvement in ORBIT must not translate to a large improvement in RLGST and vice versa, as they, e.g., weight coherent errors differently. The evaluation with RLGST, while still showing an improvement, displays the lowest overall achieved gain for all optimization methods. The same applies to the evaluation with QPT together with the LGST-optimized pulses.

A possible explanation is that $\tilde{G}$, ORBIT and RB do not provide estimates of the gates, while RLGST and QPT do. $\tilde{G}$ can find a compromise between the contributions of the expectation values to its FoM that better fits the pulse in the basis given by the rest of the gate-set while shifting the focus away from the action of G_2 itself. Eq. (5) for QPT is just a subset of the full set of expectation values measured in Eq. (7) for $\tilde{G}$. Depending on the measurement of all other expectation values, this specific set of expectations values of QPT is not necessarily maximized when the gate is optimized via $\tilde{G}$. Furthermore, while the expectation values of $\tilde{G}$ are gauge invariant, QPT is not. RLGST, as employed here in our system, does not have to be gauge invariant[67]. A slight adjustment of the gauge, e.g., shifts of the rotation axes, can thus worsen the FoM of QPT and RLGST while improving the one of $\tilde{G}$.

Optimization with LGST

Next, we analyze the optimizations with LGST via $\mathrm{FoM}_{\mathrm{LGST}}$ defined by Eq. (9). As expected, we observe the lowest gain for all evaluation methods across all optimization methods. Still, we always observe a positive gain, i.e., QuOCS is able to improve the gate-set's performance by varying the pulse shape of G_2. A major problem for optimization with LGST is that it is not able to differentiate between the reference and guess pulse as shown in Fig. 1f and might therefore also misinterpret good QOC pulses. Additionally, small variations in the pulse shape and measurement errors can lead to an enormous change of the FoM due to the calculation of the estimates via the Gram matrix in Eq. (8). The inversion of a matrix filled with measured, and therefore noisy, values as well as constantly changing entries due to the variations during the dCRAB search, is propagating and amplifying small changes through the whole derivation[84]. This results in a strongly fluctuating FoM during the optimization (see supplementary information). QuOCS can deal with such experimental downsides but it still influences the search for an optimal solution negatively.

Optimization with RLGST

Optimizing the pulse shape via RLGST shows a large average gain for all methods. The average value of 0.75 in Fig. 3b and the highest value with 1.13 in Fig. 3c when being evaluated with QPT even exceeds the QPT optimization itself. Despite operating at a different time-scale connected to the circuit length, RLGST is thus able to capture errors influencing the individual gate performance measured by QPT. The short circuit length of QPT suggests that those errors are coherent errors that accumulate with increasing circuit length, enabling a more precise optimization via RLGST. Moreover, we are able to find an optimized gate-set that reaches gains exceeding a value of 1 for almost all evaluation methods, as shown by Fig. 3c. The optimized pulse shape is thus capable of combating coherent and incoherent errors, which is further seen by the high gains when evaluated with ORBIT and $\tilde{G}$.

However, the optimization with RLGST also shows a large variance in the obtained gain when evaluated with QPT and $\tilde{G}$. While the method can capture the errors that dominate at short circuit lengths, not every single RLGST-optimized pulse will necessarily perform equally well or better than one being optimized with the corresponding FoM directly.

Optimization with ORBIT

For the optimization with ORBIT we observe a similar effect, showing a large improvement across all evaluation methods. If we take the average over all evaluation methods, ORBIT provides the best performance.

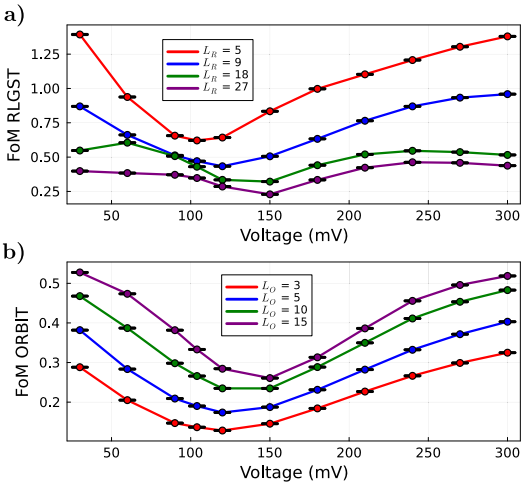

Fig. 4 | Dependence of the FoMs on the circuit length. Linear sweep of the guess pulse amplitude for different circuit lengths L for (**a**) RLGST and (**b**) ORBIT. The y-axis denotes the achieved FoM. Each data point represents the mean value of 20 measurements with the corresponding uncertainty and the chosen circuit length is visualized by the different colors.

For RLGST and $\tilde{G}$ we observe large improvements of the gain, reaching and even surpassing the performance of the reference pulse. The method also shows the highest average gain of all methods when evaluated with RB, which is only just below the reference pulse. Upon evaluation with QPT the optimized pulses on average outperform the ones achieved when being optimized via QPT itself.

Like the optimization with RLGST, the longer circuit lengths allows to better capture the main error contributions and optimize the pulse shape more precisely, leading to a robust gate-set at all evaluated circuit depths. Still, we observe a large variance between the different optimizations for the QPT evaluation. Again, the most plausible answer is that QPT is dominated by coherent errors in the form of over- or under-rotations, since incoherent errors only have a small influence on the FoM due to the short circuit length. As coherent errors are, to an extend, suppressed by twirling in RB[74,80,81] which partially translates to ORBIT, not every optimized pulse necessarily leads to a gate-set outperforming the reference pulse or the optimization with QPT itself. Additional measurements underlining this statement can be found in the supplementary information in sec. VII.

Circuit length dependence

The methods RLGST and ORBIT allow to easily probe how the system's dynamics at different time-scales affect the FoM by varying the selected circuit length. For this reason, we first examine how our defined FoMs for RLGST and ORBIT are affected by a linear change of the pulse amplitude for different L. The circuit length differs for the two methods: for RLGST it indicates the number of applied gates from the gate-set Eq. (1), while for ORBIT it stands for the number of applied Clifford gates. On average, one Clifford gate consists of ≈1.8 gates from our gate-set Eq. (1) and thus we choose the gate-string length of RLGST to match the average number of gates in ORBIT. Again we average over 300 random gate-strings per method. The measurement results are shown in Fig. 4a for RLGST and in Fig. 4b for ORBIT. We observe a shift of the minimum FoM, i.e., the best performing pulse amplitude, to larger amplitudes for increasing circuit length for both methods. This correlation can be explained by the strong beating observed in the Rabi experiment in Fig. 1a. Hopping from peak to peak of the Rabi oscillation is analogous to the application of a series of π-pulses on the system. If the π-pulse has a fixed pulse length, the amplitude of the pulse must be increased for subsequent applications to compensate for

https://doi.org/10.1038/s41534-024-00893-y **Article**

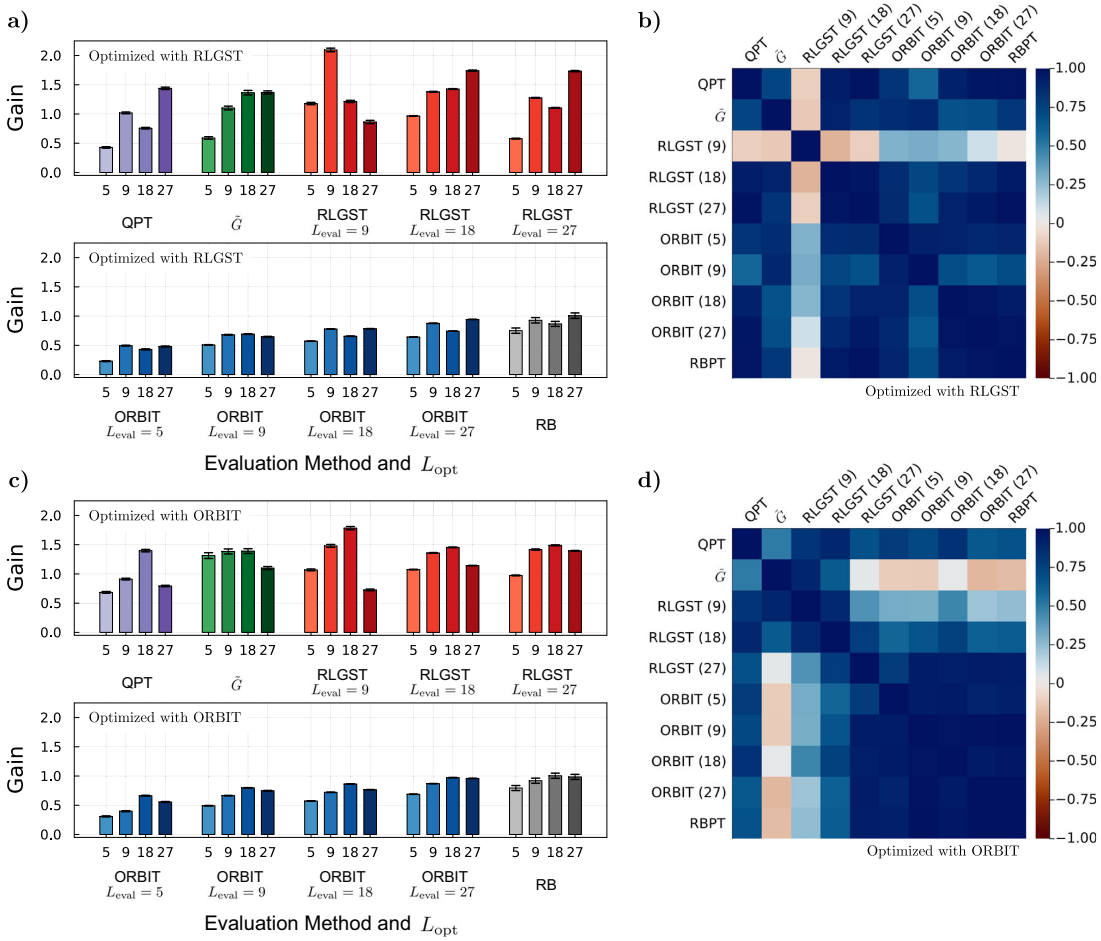

Fig. 5 | Influence of the circuit length on the optimization results. a Optimization runs with RLGST for four different circuit lengths $L = 5, 9, 18, 27$, represented by the four bars. The ordinate shows the gain achieved per optimization for the different evaluation methods displayed in the abscissa as an average of 20 measurements and the error bars denote the corresponding uncertainty. L_{eval} indicates the selected circuit length for the evaluation with RLGST and ORBIT. **b** Correlation matrix of the RLGST optimizations. The color-scale denotes the correlation between the different methods, i.e., if we observe the same dependence of the achieved gain on the circuit length. **c** Gain of the optimization runs for different circuit lengths with ORBIT. **d** Correlation matrix of the ORBIT optimizations. Again, the color-scale shows the correlation between the different methods.

the shift in the Rabi frequency caused by the beating. Thus, to find the best performing pulse for increasing number of repeated applications, a.k.a. L, the amplitude, in the form of a voltage in our case, needs to be adjusted upwards.

For ORBIT, the FoM gets worse (increases) with increasing circuit length as errors accumulate. This is expected as ORBIT evaluates the gate-set's performance at a fixed circuit length of the full RB curve, which exhibits an exponential decay with L. Therefore, increasing L samples the RB curve at a point of lower survival probability corresponding to a higher FoM per our definition. For RLGST we observe the exact opposite behavior, where an increased circuit length leads to a lower FoM. The FoM of RLGST in Eq. (14) in the Methods is based on the estimated error matrices for the initial state, POVM and the full gate-set, which are only accurate within the linear assumption[67]. Beyond this regime, the prediction error diverges[67] and the FoM decreases as the error matrices are under-estimated. Nonetheless, the argument of suitability of the FoM for our closed-loop QOC experiments holds due to the distinct minimum and the irrelevance of its absolute value as long as it guides the optimizer to a better solution. Importantly, both FoMs agree on the optimal amplitude for comparable L (minima of the curves with the same color code).

Optimizations with varying circuit length

Next, we investigate how a change of the circuit length affects the optimization result. A change in the circuit length can lead to a significant change in how different errors are weighted in the FoMs, e.g., the contribution of incoherent errors can be potentially increased through an increase of the circuit length. For example, L could be chosen such that it matches the intended circuit length of a desired experiment and thus might be tuned to give the best optimized gates for the given application. We therefore repeat the optimizations for RLGST and ORBIT once for different circuit lengths L. The results are shown in Fig. 5a for RLGST and Fig. 5c for ORBIT. We again choose the circuit length of RLGST such that it matches the average number of Clifford gates of ORBIT. For better readability we only display the average number of gates for ORBIT in Fig. 5c. The abscissa shows the chosen evaluation method, e.g., RLGST with a circuit length of $L_{\text{eval}} = 18$, the ordinate shows the achieved gain. The four bars per evaluation method

https://doi.org/10.1038/s41534-024-00893-y Article

represent the individual optimizations for a chosen circuit length. We omit the evaluation with $L_{eval} = 5$ for RLGST as the difference between the reference pulse and the guess pulse is within our measurement error and we are therefore not able to calculate the corresponding gain. Since we only perform one optimization per method and L_{opt}, we cannot exclude the possibility that some optimizations under- or over-performed due to the probabilistic nature of the optimization (caused by the measurement noise and the optimization algorithm). However, because of the small variance between different runs in Fig. 3, no significant change between repeated optimizations for the same L_{opt} is expected.

For both optimization methods, the overall achieved gain evaluated by ORBIT increases with increasing gate-string length L_{eval}. As the guess pulse is significantly longer than the reference pulse, the difference in their FoMs increases with the circuit length due to, inter alia, incoherent errors in the form of decoherence. This increases the distance between the FoMs of the reference and guess pulse. If the optimized pulse can compensate for this decoherence we observe an overall higher gain with increasing L_{eval} for the evaluation with ORBIT.

Figure 5b, d show the correlation matrices for the optimizations with different circuit lengths presented in Fig. 5a, c for RLGST and ORBIT, respectively. The correlation, described in the Methods "Correlation Matrix", looks at the behavior between the gains of different optimized pulses and compares it to other evaluation methods. E.g., if we observe that an increase of the circuit length leads to an increase of the gain when evaluated with ORBIT at $L = 27$, a high correlation with RB tells us that the method shows the same tendency.

When optimizing the gate-set via RLGST, we observe a high correlation between all evaluation methods except for the evaluation with RLGST at $L_{eval} = 9$, as shown by the correlation matrix in Fig. 5b. An increase of the circuit length L_{opt} leads to an increase of the achieved gain. At large L_{opt}, small errors accumulate and cause a stronger change of the FoM, leading to a more precise and overall better optimization. This is also reflected by the absolute value of the gain, which for large L_{opt} almost always exceeds 1, when evaluated with RLGST, $\tilde{G}$ and QPT. For RLGST at $L_{eval} = 9$ the gain even exceeds a value of 2, when optimized with the same circuit length. As the evaluation at this circuit length poorly correlates with all other evaluations, it can be assumed that the system exhibits certain dynamics exclusive to this time-scale and chosen measure.

The optimization with ORBIT at different circuit lengths shows again a high correlation between QPT, RB and the different ORBIT evaluations. The correlation matrix for ORBIT is shown in Fig. 5d. When evaluating the pulse with RLGST, we observe an increase of the correlation with ORBIT and RB for increasing L_{eval}. For $L_{eval} = 27$, the observed dependence of the gain on the circuit length correlates very well with that of ORBIT. At large circuit lengths, the FoM's of RLGST and ORBIT are dominated by the same dynamics and thus converge to similar solutions, i.e., similar performing gate-sets. We observe again, that an increase of L_{opt} leads to a higher gain. Through the high correlation between the methods we can conclude that the optimization with ORBIT at $L_{opt} = 27$ significantly under-performed and a higher gain is expected for repeated optimizations. Although showing high gains significantly exceeding 1, the evaluation with $\tilde{G}$ shows the smallest correlation with the other methods. Different circuit lengths during the optimization with ORBIT have thus no significant effect on the gain observed in $\tilde{G}$.

Evidently, it is favorable to perform optimizations with RLGST and ORBIT at higher L_{opt}. Apart from incoherent errors, a longer circuit length also allows for a higher precision when focusing on coherent errors prevalent at short time-scales. In our case, it does therefore provide no advantage to adapt L_{opt} to a desired experiment with, e.g., length L_{eval}, but it is simply better to choose the longest possible circuit length. Although this may seem surprising at first, it can be attributed to the ensemble nature of our system as we measure the collective fluorescence signal from all contributing individual N-V centers. The inhomogeneity of the microwave control field and external magnetic field heavily contribute to the observed dephasing (incoherent error) and apparent non-Markovianity in the Rabi measurement shown in Fig. 1a. Therefore, a pulse more robust to detuning and amplitude errors (coherent errors) can improve the performance for short and long sequences at the same time.

Discussion

Based on our detailed investigation, we can now discuss to what extent the individual methods are suitable for closed-loop optimizations with spin ensembles treated as one effective qubit or with qubits in general. We would like to emphasize that all methods have evidently been able to improve the performance of our gate-set.

Out of all investigated methods LGST achieves the lowest gains. Measurement errors dominate the provided estimates and therefore the calculated FoMs. More advance methods like long-sequence GST might help to overcome these shortcomings[83]. As a result, the optimizer sees no clear change for pulses that perform differently well, leading to an overall low optimization gain. If the FoM is calculated using solely the expectation values of LGST, i.e., $\tilde{G}$, significantly larger gains can be achieved. Since optimizations via $\tilde{G}$ maximize the overlap of the predefined expectation values to their target and allow to simply add additional gates to the gate-set, the method is particularly suitable if the gate-set is to be optimized for specific applications of the gates to arbitrary basis states. The method is heavily biased towards optimizing for its specific measurement sequence and the associated average circuit length.

QPT, unlike all the other methods, does not take SPAM errors into account. For larger SPAM errors, the correlation to other methods is expected to diminish as does its utility. Such is the case for our system, where an optimization based on QPT never beats the gate-set with the reference pulse. The optimization process is furthermore limited to one single gate at a time. While the optimization of an entire gate-set might be possible through iterative optimizations, the other methods offer a much better and clearer approach. Despite this, our FoM based on QPT is able to optimize the gate-set such that it shows improvements compared to the guess pulse for all investigated methods. Among all methods, QPT requires the fewest measurements, which can be beneficial when working with systems with low signal-to-noise ratio.

The overall best results are achieved by ORBIT. Not only does ORBIT show universally high gains across all methods, but the optimized gate-sets also outperform those of other optimization methods when evaluated with their own FoM, regardless of their time-scale. Although the method is mainly sensitive to incoherent errors, it also allows to correct those coherent errors that dominate the FoM for the other methods. As shown in the previous section, long circuit lengths are recommended for the optimization as errors accumulate, leading to larger changes in the defined FoM and therefore a more precise optimization. Too large L are not favorable, though, since information gets lost in noise and accumulated errors. When increasing the circuit length, we expect to find a sweet spot for the optimization where such dynamics are captured and weighed optimally. In our case we are limited by the fluence (see supplementary information) and therefore heating induced by long circuits.

One downside of ORBIT is that randomized benchmarking usually requires the use of Clifford gates which are generated by the over-full gate-set, Eq. (1). Additional gates that are to be optimized cannot simply be appended to the gate-set but need to be interleaved into the Clifford gates if possible.

This problem can largely be circumvented by the optimization via RLGST. Additional gates can simply be added to the gate-set. Optimizations via RLGST achieve similar high gains to ORBIT across all methods, i.e., are able to create a universally well-performing gate-set. Analogous to ORBIT, large circuit lengths are preferred when working with RLGST. At large circuit lengths, RLGST evaluates the system dynamics similar to ORBIT making the method ideal when working with a overfull gate-set as in our case. We show that the method can be used far beyond its intended linear (small error) working regime[67] to define a suitable FoM for closed-loop experiments. Moreover, while not directly investigated in our work, the method also allows to work with an incomplete gate-set[67], which can be of

https://doi.org/10.1038/s41534-024-00893-y **Article**

use for experimental systems with limited control. In addition, the method provides estimates of the gate-set and states which can be accessed during the optimization to obtain deeper insights into the system dynamics[85].

Nonetheless, as a large degree of our non-Markovian and incoherent errors originate from coherent dynamics due to the treatment of our micrometer-sized ensemble as one effective qubit, the recommendation for RLGST and ORBIT does not necessarily hold in other cases. For systems of a different nature such as ones measuring pure single qubits or physically different quantum platforms that have different error contributions, this might change. Short-circuit methods like QPT, $\tilde{G}$ and LGST could be selected over RLGST and ORBIT for other systems and shorter sequences in which the optimized gates are to be used. In general we expect, however, that RLGST and ORBIT with large L are suited well for applications that need longer circuit lengths. Further experiments that allow to strictly distinguish between coherent and incoherent errors[86] or even allow to, e.g., turn coherent errors into stochastic noise[74] would be of high interest to characterize the optimizations further or even optimize the gate-set with them.

In conclusion, through the definition of our FoMs based on RLGST and ORBIT we are able to create a gate-set that performs universally well across all investigated evaluation methods, regardless of their time-scale given by their circuit lengths and regardless of the different weighting of errors. We provide a detailed comparison of several gate and gate-set analysis methods and how these can be applied in a closed-loop QOC experiment, tested with a macroscopic ensemble of N-V centers. Since the occurring types of error are not exclusive to our system but exist in a wide variety of systems, our work can act as a useful handbook for experimentalists trying to overcome similar problems via QOC. The methods and the corresponding FoMs that work well for our system are expected to perform similar for other systems with comparable dynamics[59,87–90] and could also be applicable to systems with significantly smaller errors[91–93].

Methods

Definitions of the figures of merit

In addition to our gate-set Eq. (1), we define the SPAM-set to be

$$\begin{aligned}\mathcal{F} &= \{F_0, F_1, F_2, F_3\} \\ &= \{G_0, G_1, G_3, G_5\}\,.\end{aligned} \tag{4}$$

Starting with QPT, we measure the expectation values

$$p_{ij} = \langle\langle E|F_i G_2 F_j|\rho\rangle\rangle \tag{5}$$

for $F_{i,j} \in \mathcal{F}$ to evaluate the performance of G_2 along all axes and reconstruct the final states $|0\rangle$, $|-1\rangle$, $|+\rangle = 1/\sqrt{2}(|0\rangle + |-1\rangle)$ and $|-\rangle = 1/\sqrt{2}(|0\rangle + i|-1\rangle)$ after application of the gate. Finally, we calculate the process matrix χ according to[39,73], which defines the full linear map of our gate G_2. The FoM is then defined as the Frobenius norm of the distance between the measured and the target process matrix χ_T for the perfect gate:

$$\mathrm{FoM}_{\mathrm{QPT}} = \sqrt{\mathrm{tr}\Big(\big(\chi - \chi_T\big)^\dagger\big(\chi - \chi_T\big)\Big)}\,. \tag{6}$$

In contrast to QPT, quantum gate-set tomography[66,94] takes SPAM errors directly into account by measuring the expectation values of Eq. (5) for all $G_k \in \mathcal{G}$:

$$\begin{aligned}p_{ijk} &= \langle\langle E|F_i G_k F_j|\rho\rangle\rangle \\ &= (\tilde{G}_k)_{ij}.\end{aligned} \tag{7}$$

Following refs. 65,66, assuming a perfect idle gate $\mathbb{1}$ leads to the estimates

$$\begin{aligned}\hat{G}_k &= \tilde{G}_0^{-1}\tilde{G}_k, \\ |\hat{\rho}\rangle\rangle &= \tilde{G}_0^{-1}|\tilde{\rho}\rangle\rangle \\ |\hat{E}\rangle\rangle &= |\tilde{E}\rangle\rangle\,.\end{aligned} \tag{8}$$

using the inverse Gram matrix $\tilde{G}_0^{-1}$ to redistribute the errors to all other gates. As the expectation values (7) are gauge invariant, the estimates (8) need to be gauge-corrected. Following the derivations provided in refs. 65,66, we then obtain the gauge-transformed LGST estimates $\hat{G}_k^*$, $|\hat{\rho}^*\rangle\rangle$ and $|\hat{E}^*\rangle\rangle$. Usually, a maximum likelihood estimation (MLE) is used next to find the closest physically correct version of the obtained estimates, i.e., a $\hat{G}_k^*$ that corresponds to a CPTP map. However, such an MLE is computationally demanding, making it unsuitable for our closed-loop QOC experiments. We therefore use the estimates provided by LGST to evaluate the performance of our gates G_k through the difference to their target T_k:

$$\mathrm{FoM}_{\mathrm{LGST}} = \sqrt{\sum_{k=1}^{K+1}\mathrm{tr}\Big(\big(\hat{G}_k^* - T_k\big)^\dagger\big(\hat{G}_k^* - T_k\big)\Big)} \tag{9}$$

with $\hat{G}_{K+1}^* \equiv |\hat{\rho}^*\rangle\rangle\langle\langle\hat{E}^*|$. We sum up the squared norms for each gate difference similar to the sum of squared residuals in the least-squares method[95]. Additionally, we define another FoM

$$\mathrm{FoM}_{\tilde{G}} = \sqrt{\sum_{k=1}^{K}\mathrm{tr}\Big(\big(\tilde{G}_k - \tilde{T}_k\big)^\dagger\big(\tilde{G}_k - \tilde{T}_k\big)\Big)}\,, \tag{10}$$

based on the matrices $\tilde{G}_k$ of Eq. (7) filled with the measured expectation values and their difference to the corresponding target values $\tilde{T}_k$. While not providing an estimate, these expectation values are gauge invariant by definition.

Another method which takes SPAM errors into account is randomized benchmarking[68–70]. Randomized benchmarking uses Clifford gates, which are composed of gates from our gate-set Eq. (1)[72], to create multiple random circuits of length L, where the final gate flips the spin back to its initial state. The average recovered population, the so-called survival probability p_s, decays exponentially with the number of applied Clifford gates[69] and the average error per gate can be extracted from the decay parameter. ORBIT then allows to optimize the fidelity of the applied gates by increasing the survival probability at an arbitrary gate-string length L_{opt}[35]. Therefore, we define the corresponding FoM for our closed-loop QOC experiments with ORBIT by

$$\mathrm{FoM}_{\mathrm{ORBIT}} = 1 - p_s(L_{\mathrm{opt}})\,. \tag{11}$$

RLGST[67] combines the idea of gate-set tomography and randomized circuits to obtain an estimate of the gate-set with little computational overhead within a linear approximation. We start by measuring the expectation values

$$p_i = \langle\langle E|\mathcal{C}_i|\rho\rangle\rangle \tag{12}$$

for N randomly chosen circuits $\mathcal{C}_i$ of length L with $i = 1\ldots N$. Following the calculations provided in ref. 67, the expectation values of Eq. (12) are then used to obtain an estimate for the error matrices e_p, which describe how the measurement deviates from the expected target:

$$\begin{aligned}\hat{G}_k &= (\mathbb{1} + e_k)\cdot T_k, \\ |\hat{\rho}\rangle\rangle &= (\mathbb{1} + e_\rho)\cdot|\rho_T\rangle\rangle, \\ |\hat{E}\rangle\rangle &= (\mathbb{1} + e_E)\cdot|E_T\rangle\rangle\,.\end{aligned} \tag{13}$$

https://doi.org/10.1038/s41534-024-00893-y **Article**

Since we only vary a single gate during our optimizations, we expect to be reasonably close to the actual gauge for the estimates and defining the FoM for RLGST equivalent to Eq. (9) we obtain

$$\mathrm{FoM}_{\mathrm{RLGST}} = \sqrt{\sum_j \mathrm{tr}\left(e_j^\dagger e_j\right)}. \tag{14}$$

Correlation matrix

The correlation matrices are calculated according to ref. 96 via

$$M = \begin{pmatrix} 1 & r_{12} & r_{13} & \dots & r_{1p} \\ r_{21} & 1 & r_{23} & \dots & r_{2p} \\ r_{31} & r_{32} & 1 & \dots & r_{3p} \\ \vdots & \vdots & \vdots & \ddots & \vdots \\ r_{p1} & r_{p2} & r_{p3} & \dots & 1 \end{pmatrix} \tag{15}$$

with the correlation coefficient

$$r_{jk} = \frac{\sum_{i=1}^{n}\left(x_{ij} - \bar{x}_j\right)\left(x_{ik} - \bar{x}_k\right)}{\sqrt{\sum_{i=1}^{n}\left(x_{ij} - \bar{x}_j\right)^2}\sqrt{\sum_{i=1}^{n}\left(x_{ik} - \bar{x}_k\right)^2}} \tag{16}$$

where the bar indicates the average over the indexed column of the data matrix

$$X = \begin{pmatrix} x_{11} & x_{12} & \dots & x_{1p} \\ x_{21} & x_{22} & \dots & x_{2p} \\ \vdots & \vdots & \ddots & \vdots \\ x_{n1} & x_{n2} & \dots & x_{np} \end{pmatrix}. \tag{17}$$

The rows (n) of X are the four optimizations with varying L, i.e., the four pulses that are compared, and the columns (p) describe the different evaluation methods used.

dCRAB algorithm and settings

The dCRAB method expands updates to the amplitudes in a randomly selected sub-set of functions sampled from a "chopped" basis. We use the Fourier basis

$$a_k(t) = g(t) + \sum_{j=1}^{N_{\mathrm{SI}}}\sum_{i=1}^{N_b} c_{1,i}^j \sin\left(\nu_i^j t\right) + c_{2,i}^j \cos\left(\nu_i^j t\right), \tag{18}$$

where $g(t)$ is the provided guess. The frequencies ν_i^j for the update pulses are randomly selected from the interval $\left[0, \frac{2\pi \cdot n}{T}\right]$ where we choose $n = 4$ as the maximum allowed number of oscillations of the pulse envelope over the course of the pulse duration T. Several super-iterations (SI) with newly randomized basis vectors restart the search process by adding new search directions to avoid getting trapped in local minima. They are added to the best pulse shape of the previous SI. In our case we perform $N_{\mathrm{SI}} = 3$ super-iterations. We use the Nelder-Mead search method for the expansion parameters and select two basis vectors ($N_b = 2$) per pulse per super-iteration for the basis expansion. In this way, the search parameters for the optimization can be kept to a minimum, to ensure a quick convergence. If a potential improvement of the FoM does not exceed the measurement error, QuOCS will re-evaluate the evaluation step up to three times to ensure an accurate interpretation of the parameter landscape[32]. We determine the standard deviation by measuring the FoM for the guess pulse 100 times. A super-iteration stops, if the improvement of the FoM within the last 200 evaluation steps does not exceed the standard deviation. To account for experimental drifts in the FoM, the current best pulse is re-measured every 30 min.

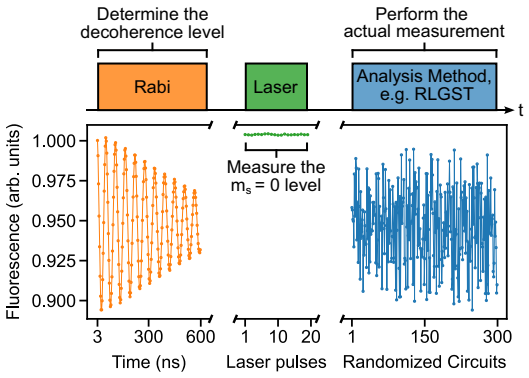

Fig. 6 | Measurement sequence. The measurement sequence for any experiment consists of three parts: a Rabi measurement to determine the decoherence level, a measurement of the $|0\rangle\rangle$ fluorescence level and the actual measurement sequence, e.g., RLGST, which is then converted to expectation values by the previously obtained fluorescence levels.

Data normalization and measurement sequence

For any performed experiment, the measurement sequence consists of three parts which are measured simultaneously, as depicted in Fig. 6. We start with a Rabi measurement at maximum amplitude for 600 ns to determine the decoherence level of our system and afterwards measure a series of 20 laser pulses to obtain the fluorescence level of the $|0\rangle\rangle$ state. Those levels are used to convert the fluorescence signal of the selected analysis method, to expectation values. Possible changes of the measurement contrast, through, e.g., laser power fluctuations, are thus taken into account by adjusting the measured expectation values such that 0 and 1 still correspond to the minimum and maximum achievable fluorescence.

Data availability

The data presented in this study is available from the corresponding authors on reasonable request.

Received: 21 March 2024; Accepted: 23 September 2024;
Published online: 02 October 2024

References

1. IBM. About calibration jobs. accessed: 19 January 2024. https://docs.quantum.ibm.com/admin/calibration-jobs.
2. Michielsen, K. et al. Benchmarking gate-based quantum computers. *Comput. Phys. Commun.* **220**, 44–55 (2017).
3. Papič, M., Auer, A. & de Vega, I. Fast estimation of physical error contributions of quantum gates. *arXiv preprint arXiv:2305.08916* (2023).
4. Tornow, C., Kanazawa, N., Shanks, W. E. & Egger, D. J. Minimum quantum run-time characterization and calibration via restless measurements with dynamic repetition rates. *Phys. Rev. Appl.* **17**, 064061 (2022).
5. Demirdjian, R., Gunlycke, D., Reynolds, C. A., Doyle, J. D. & Tafur, S. Variational quantum solutions to the advection–diffusion equation for applications in fluid dynamics. *Quantum Inform. Process.* **21**, 322 (2022).
6. Arute, F. et al. Quantum supremacy using a programmable superconducting processor. *Nature* **574**, 505–510 (2019).
7. Kelly, J. et al. State preservation by repetitive error detection in a superconducting quantum circuit. *Nature* **519**, 66–69 (2015).

https://doi.org/10.1038/s41534-024-00893-y **Article**

8. Terhal, B. M. Quantum error correction for quantum memories. *Rev. Mod. Phys.* **87**, 307–346 (2015).
9. Chiaverini, J. et al. Realization of quantum error correction. *Nature* **432**, 602–605 (2004).
10. Cory, D. G. et al. Experimental quantum error correction. *Phys. Rev. Lett.* **81**, 2152–2155 (1998).
11. Cai, Z. et al. Quantum error mitigation. *Rev. Mod. Phys.* **95**, 045005 (2023).
12. Endo, S., Benjamin, S. C. & Li, Y. Practical quantum error mitigation for near-future applications. *Phys. Rev. X* **8**, 031027 (2018).
13. Rojkov, I., Layden, D., Cappellaro, P., Home, J. & Reiter, F. Bias in error-corrected quantum sensing. *Phys. Rev. Lett.* **128**, 140503 (2022).
14. Vetter, P. J. et al. Zero- and low-field sensing with nitrogen-vacancy centers. *Phys. Rev. Appl.* **17**, 044028 (2022).
15. Willsch, D., Nocon, M., Jin, F., De Raedt, H. & Michielsen, K. Gate-error analysis in simulations of quantum computers with transmon qubits. *Phys. Rev. A* **96**, 062302 (2017).
16. Lagemann, H. et al. Fragility of gate-error metrics in simulation models of flux-tunable transmon quantum computers. *Phys. Rev. A* **108**, 022604 (2023).
17. Marxer, F. et al. Implementing and characterizing high-fidelity two-qubit gates with long-distance transmon coupler. *Bull. Am. Phys. Soc.* **2023**, Z75–010 (2023).
18. d'Alessandro, D. *Introduction to quantum control and dynamics* (Chapman and hall/CRC, 2021).
19. Brif, C., Chakrabarti, R. & Rabitz, H. Control of quantum phenomena: past, present and future. *N. J. Phys.* **12**, 075008 (2010).
20. Glaser, S. J. et al. Training schrödinger's cat: quantum optimal control. *Eur. Phys. J. D.* **69**, 1–24 (2015).
21. Rembold, P. et al. Introduction to quantum optimal control for quantum sensing with nitrogen-vacancy centers in diamond. *AVS Quantum Sci.* **2**, 024701 (2020).
22. Müller, M. M., Said, R. S., Jelezko, F., Calarco, T. & Montangero, S. One decade of quantum optimal control in the chopped random basis. *Rep. Prog. Phys.* **85**, 076001 (2022).
23. Khaneja, N., Reiss, T., Kehlet, C., Schulte-Herbrüggen, T. & Glaser, S. J. Optimal control of coupled spin dynamics: design of nmr pulse sequences by gradient ascent algorithms. *J. Magn. Reson.* **172**, 296–305 (2005).
24. Machnes, S. et al. Comparing, optimizing, and benchmarking quantum-control algorithms in a unifying programming framework. *Phys. Rev. A* **84**, 022305 (2011).
25. Motzoi, F., Gambetta, J. M., Merkel, S. & Wilhelm, F. Optimal control methods for rapidly time-varying hamiltonians. *Phys. Rev. A* **84**, 022307 (2011).
26. Caneva, T., Calarco, T. & Montangero, S. Chopped random-basis quantum optimization. *Phys. Rev. A* **84**, 022326 (2011).
27. Rach, N., Müller, M. M., Calarco, T. & Montangero, S. Dressing the chopped-random-basis optimization: a bandwidth-limited access to the trap-free landscape. *Phys. Rev. A* **92**, 062343 (2015).
28. Fortunato, E. M. et al. Design of strongly modulating pulses to implement precise effective hamiltonians for quantum information processing. *J. Chem. Phys.* **116**, 7599–7606 (2002).
29. Ciaramella, G., Borzì, A., Dirr, G. & Wachsmuth, D. Newton methods for the optimal control of closed quantum spin systems. *SIAM J. Sci. Comput.* **37**, A319–A346 (2015).
30. Leung, N., Abdelhafez, M., Koch, J. & Schuster, D. Speedup for quantum optimal control from automatic differentiation based on graphics processing units. *Phys. Rev. A* **95**, 042318 (2017).
31. Preti, F., Calarco, T. & Motzoi, F. Continuous quantum gate sets and pulse-class meta-optimization. *PRX Quantum* **3**, 040311 (2022).
32. Rossignolo, M. et al. Quocs: the quantum optimal control suite. *Comput. Phys. Commun.* **291**, 108782 (2023).
33. Binder, J. M. et al. Qudi: A modular python suite for experiment control and data processing. *SoftwareX* **6**, 85–90 (2017).
34. Chow, J. M. et al. Optimized driving of superconducting artificial atoms for improved single-qubit gates. *Phys. Rev. A* **82**, 040305 (2010).
35. Kelly, J. et al. Optimal quantum control using randomized benchmarking. *Phys. Rev. Lett.* **112**, 240504 (2014).
36. Heck, R. et al. Remote optimization of an ultracold atoms experiment by experts and citizen scientists. *Proc. Natl Acad. Sci. USA* **115**, E11231–E11237 (2018).
37. Rosi, S. et al. Fast closed-loop optimal control of ultracold atoms in an optical lattice. *Phys. Rev. A* **88**, 021601 (2013).
38. Marshall, A. et al. Macroscopic hyperpolarization enhanced with quantum optimal control. *Phys. Rev. Res.* **4**, 043179 (2022).
39. Frank, F. et al. Autonomous calibration of single spin qubit operations. *npj Quantum Inf.* **3**, 1–5 (2017).
40. Oshnik, N. et al. Robust magnetometry with single nitrogen-vacancy centers via two-step optimization. *Phys. Rev. A* **106**, 013107 (2022).
41. Said, R. S. & Twamley, J. Robust control of entanglement in a nitrogen-vacancy center coupled to a ^{13}C nuclear spin in diamond. *Phys. Rev. A* **80**, 032303 (2009).
42. Scheuer, J. et al. Precise qubit control beyond the rotating wave approximation. *N. J. Phys.* **16**, 093022 (2014).
43. Dolde, F. et al. High-fidelity spin entanglement using optimal control. *Nat. Commun.* **5**, 3371 (2014).
44. Poggiali, F., Cappellaro, P. & Fabbri, N. Optimal control for one-qubit quantum sensing. *Phys. Rev. X* **8**, 021059 (2018).
45. Häberle, T., Schmid-Lorch, D., Karrai, K., Reinhard, F. & Wrachtrup, J. High-dynamic-range imaging of nanoscale magnetic fields using optimal control of a single qubit. *Phys. Rev. Lett.* **111**, 170801 (2013).
46. Nöbauer, T. et al. Smooth optimal quantum control for robust solid-state spin magnetometry. *Phys. Rev. Lett.* **115**, 190801 (2015).
47. Ziem, F., Garsi, M., Fedder, H. & Wrachtrup, J. Quantitative nanoscale mri with a wide field of view. *Sci. Rep.* **9**, 1–9 (2019).
48. Konzelmann, P. et al. Robust and efficient quantum optimal control of spin probes in a complex (biological) environment. towards sensing of fast temperature fluctuations. *N. J. Phys.* **20**, 123013 (2018).
49. Müller, M. M., Gherardini, S. & Caruso, F. Noise-robust quantum sensing via optimal multi-probe spectroscopy. *Sci. Rep.* **8**, 14278 (2018).
50. Balasubramanian, G. et al. Nanoscale imaging magnetometry with diamond spins under ambient conditions. *Nature* **455**, 648–651 (2008).
51. Mamin, H. et al. Nanoscale nuclear magnetic resonance with a nitrogen-vacancy spin sensor. *Science* **339**, 557–560 (2013).
52. Schmitt, S. et al. Submillihertz magnetic spectroscopy performed with a nanoscale quantum sensor. *Science* **356**, 832–837 (2017).
53. Dolde, F. et al. Electric-field sensing using single diamond spins. *Nat. Phys.* **7**, 459–463 (2011).
54. Glenn, D. R. et al. High-resolution magnetic resonance spectroscopy using a solid-state spin sensor. *Nature* **555**, 351–354 (2018).
55. Barry, J. F. et al. Sensitivity optimization for nv-diamond magnetometry. *Rev. Mod. Phys.* **92**, 015004 (2020).
56. Balasubramanian, P. et al. dc magnetometry with engineered nitrogen-vacancy spin ensembles in diamond. *Nano Lett.* **19**, 6681–6686 (2019).
57. Horsley, A. et al. Microwave device characterization using a widefield diamond microscope. *Phys. Rev. Appl.* **10**, 044039 (2018).
58. Mizuno, K. et al. Wide-field diamond magnetometry with millihertz frequency resolution and nanotesla sensitivity. *Aip Adv.* **8**, 125316 (2018).
59. Scholten, S. et al. Widefield quantum microscopy with nitrogen-vacancy centers in diamond: strengths, limitations, and prospects. *J. Appl. Phys.* **130**, 150902 (2021).
60. Choi, S. et al. Observation of discrete time-crystalline order in a disordered dipolar many-body system. *Nature* **543**, 221–225 (2017).
61. Choi, J. et al. Probing quantum thermalization of a disordered dipolar spin ensemble with discrete time-crystalline order. *Phys. Rev. Lett.* **122**, 043603 (2019).
62. Poyatos, J. F., Cirac, J. I. & Zoller, P. Complete characterization of a quantum process: The two-bit quantum gate. *Phys. Rev. Lett.* **78**, 390–393 (1997).

https://doi.org/10.1038/s41534-024-00893-y **Article**

63. Chuang, I. L. & Nielsen, M. A. Prescription for experimental determination of the dynamics of a quantum black box. *J. Mod. Opt.* **44**, 2455–2467 (1997).
64. Leibfried, D. et al. Experimental determination of the motional quantum state of a trapped atom. *Phys. Rev. Lett.* **77**, 4281–4285 (1996).
65. Greenbaum, D. Introduction to quantum gate set tomography. *arXiv preprint arXiv:1509.02921* (2015).
66. Blume-Kohout, R. et al. Robust, self-consistent, closed-form tomography of quantum logic gates on a trapped ion qubit. *arXiv preprint arXiv:1310.4492* (2013).
67. Gu, Y., Mishra, R., Englert, B.-G. & Ng, H. K. Randomized linear gate-set tomography. *PRX Quantum* **2**, 030328 (2021).
68. Knill, E. et al. Randomized benchmarking of quantum gates. *Phys. Rev. A* **77**, 012307 (2008).
69. Magesan, E., Gambetta, J. M. & Emerson, J. Scalable and robust randomized benchmarking of quantum processes. *Phys. Rev. Lett.* **106**, 180504 (2011).
70. Magesan, E., Gambetta, J. M. & Emerson, J. Characterizing quantum gates via randomized benchmarking. *Phys. Rev. A* **85**, 042311 (2012).
71. Jacques, V. et al. Dynamic polarization of single nuclear spins by optical pumping of nitrogen-vacancy color centers in diamond at room temperature. *Phys. Rev. Lett.* **102**, 057403 (2009).
72. Epstein, J. M., Cross, A. W., Magesan, E. & Gambetta, J. M. Investigating the limits of randomized benchmarking protocols. *Phys. Rev. A* **89**, 062321 (2014).
73. Nielsen, M. A. & Chuang, I. *Quantum computation and quantum information* (Cambridge University Press, 2002).
74. Hashim, A. et al. Randomized compiling for scalable quantum computing on a noisy superconducting quantum processor. *Phys. Rev. X* **11**, 041039 (2021).
75. Wallman, J. J. & Emerson, J. Noise tailoring for scalable quantum computation via randomized compiling. *Phys. Rev. A* **94**, 052325 (2016).
76. Iverson, J. K. & Preskill, J. Coherence in logical quantum channels. *N. J. Phys.* **22**, 073066 (2020).
77. Kim, J.-S. et al. Hardware-efficient random circuits to classify noise in a multiqubit system. *Phys. Rev. A* **104**, 022609 (2021).
78. Haase, J. F. et al. Controllable non-markovianity for a spin qubit in diamond. *Phys. Rev. Lett.* **121**, 060401 (2018).
79. Penshin, P. et al. Realization of robust quantum noise characterization in the presence of coherent errors. *AVS Quantum Science 6.2* (2024).
80. Proctor, T., Rudinger, K., Young, K., Sarovar, M. & Blume-Kohout, R. What randomized benchmarking actually measures. *Phys. Rev. Lett.* **119**, 130502 (2017).
81. Boone, K., Carignan-Dugas, A., Wallman, J. J. & Emerson, J. Randomized benchmarking under different gate sets. *Phys. Rev. A* **99**, 032329 (2019).
82. Magesan, E. et al. Efficient measurement of quantum gate error by interleaved randomized benchmarking. *Phys. Rev. Lett.* **109**, 080505 (2012).
83. Nielsen, E. et al. Gate set tomography. *Quantum* **5**, 557 (2021).
84. Lefebvre, M., Keeler, R., Sobie, R. & White, J. Propagation of errors for matrix inversion. *Nucl. Instrum. Methods Phys. Res. Sect. A: Accelerators, Spectrometers, Detect. Associated Equip.* **451**, 520–528 (2000).
85. Wittler, N. et al. Integrated tool set for control, calibration, and characterization of quantum devices applied to superconducting qubits. *Phys. Rev. Appl.* **15**, 034080 (2021).
86. Feng, G. et al. Estimating the coherence of noise in quantum control of a solid-state qubit. *Phys. Rev. Lett.* **117**, 260501 (2016).
87. Gottscholl, A. et al. Spin defects in hbn as promising temperature, pressure and magnetic field quantum sensors. *Nat. Commun.* **12**, 4480 (2021).
88. Gong, R. et al. Coherent dynamics of strongly interacting electronic spin defects in hexagonal boron nitride. *Nat. Commun.* **14**, 3299 (2023).
89. Castelletto, S. & Boretti, A. Silicon carbide color centers for quantum applications. *J. Phys. Photon.* **2**, 022001 (2020).
90. Joas, T. et al. High-fidelity electron spin gates in a scalable diamond quantum register. *arXiv preprint arXiv:2406.04199* (2024).
91. Bartling, H. P. et al. Universal high-fidelity quantum gates for spin-qubits in diamond *arXiv preprint arXiv:2403.10633* (2024).
92. Werninghaus, M. et al. Leakage reduction in fast superconducting qubit gates via optimal control. *npj Quantum Inf.* **7**, 14 (2021).
93. Dehollain, J. P. et al. Optimization of a solid-state electron spin qubit using gate set tomography. *N. J. Phys.* **18**, 103018 (2016).
94. Merkel, S. T. et al. Self-consistent quantum process tomography. *Phys. Rev. A* **87**, 062119 (2013).
95. Van Huffel, S. & Vandewalle, J.*The Total Least Squares Problem* (Society for Industrial and Applied Mathematics, 1991). https://epubs.siam.org/doi/abs/10.1137/1.9781611971002.
96. Helwig, N. E. Data, covariance, and correlation matrix. *University of Minnesota (Twin Cities)* (2017).

Acknowledgements

We thank Ressa Said, Timo Joas, Marco Rossignolo and Maximilian Kraus for helpful discussions. This work was funded by the German Federal Ministry of Research (BMBF) by future cluster QSENS (No. 03ZK110AB) and projects DE-Brill (No. 13N16207), SPINNING (No. 13N16210 and No. 13N16215), DIAQNOS (No. 13N16463), quNV2.0 (No. 13N16707), QR.X (No. 16KISQ006) and Quamapolis (No. 13N15375), DLR via project QUASIMODO (No. 50WM2170), Deutsche Forschungsgemeinschaft (DFG) via Projects No. 386028944, No. 445243414, and No. 387073854 and Excellence Cluster POLiS (UP 33/1 Projekt-ID: 422053626), Excellence Cluster Matter and Light for Quantum Computing (ML4Q) EXC 2004/1 - 390534, and Helmholtz Validation Fund project “Qruise” (HVF-00096). This project has also received funding from the European Union’s HORIZON Europe program via projects QuMicro (No. 101046911), SPINUS (No. 101135699), C-QuENS (No. 101135359), QCIRCLE (No. 101059999), HORIZON-CL4-2021-DIGITALE-MERGING-02-10 QCFD (No. 101080085) and FLORIN (No. 101086142), European Research Council (ERC) via Synergy grant HyperQ (No. 856432) and Carl-Zeiss-Stiftung via the Center of Integrated Quantum Science and technology (IQST) and project Utrasens-Vir (No. P2022-06-007).

Author contributions

P.J.V. and T.R. contributed equally to the project. P.J.V., T.R., M.M.M., and F.M. conceived the experiments. P.J.V., T.R., and M.G.H. implemented the closed-loop optimizations. P.J.V. performed the measurement. P.J.V. and T.R. derived the figures of merit, analyzed the data and wrote the manuscript. M.M.M., F.M., T.C., and F.J. supervised the project. All authors read and commented on the manuscript.

Funding

Open Access funding enabled and organized by Projekt DEAL.

Competing interests

The authors declare no competing interests.

Additional information

Supplementary information The online version contains supplementary material available at https://doi.org/10.1038/s41534-024-00893-y.

Correspondence and requests for materials should be addressed to Philipp J. Vetter.

https://doi.org/10.1038/s41534-024-00893-y **Article**

Supplementary Information: Gate-set evaluation metrics for closed-loop optimal control on nitrogen-vacancy center ensembles in diamond

Philipp J. Vetter,[1,2,*] Thomas Reisser,[3,4,*] Maximilian G. Hirsch,[1,2,5] Tommaso Calarco,[3,4,6] Felix Motzoi,[3,4] Fedor Jelezko,[1,2] and Matthias M. Müller[3]

[1] *Institute for Quantum Optics, Ulm University, Albert-Einstein-Allee 11, 89081 Ulm, Germany*
[2] *Center for Integrated Quantum Science and Technology (IQST), 89081 Ulm, Germany*
[3] *Peter Grünberg Institute – Quantum Control (PGI-8), Forschungszentrum Jülich GmbH, D-52425 Germany*
[4] *Institute for Theoretical Physics, University of Cologne, D-50937 Germany*
[5] *Current address: NVision Imaging Technologies GmbH, Wolfgang-Paul-Straße 2, 89081 Ulm, Germany*
[6] *Dipartimento di Fisica e Astronomia, Università di Bologna, 40127 Bologna, Italy*

(Dated: March 2024)

CONTENTS

I. HILBERT-SCHMIDT SPACE

To simplify the notation throughout our manuscript we express our states and operations in the so-called *Hilbert-Schmidt* (HS) space [1, 2].
For this, we normalize the Pauli matrices by their dimension $P_i \to P_i/\sqrt{d}$ where $d = 2$ and choose them as our basis

$$P_k \in \left\{ \frac{\mathbb{1}}{\sqrt{2}}, \frac{\sigma_x}{\sqrt{2}}, \frac{\sigma_y}{\sqrt{2}}, \frac{\sigma_z}{\sqrt{2}} \right\}. \tag{1}$$

Density matrices are then written as d^2 vectors identified by double bra or ket brackets

$$|\rho\rangle\rangle = \sum_k |P_k\rangle\rangle\langle\langle P_k|\rho\rangle\rangle = \sum_k |P_k\rangle\rangle \, \mathrm{tr}\{P_k^\dagger \rho\}, \tag{2}$$

whereas the Hilbert-Schmidt inner product is given by

$$\langle\langle \alpha|\beta\rangle\rangle = \mathrm{tr}\{\alpha^\dagger \beta\} \, . \tag{3}$$

Operators describing linear maps can be written in the HS space as $d^2 \times d^2$ operators

$$\mathcal{O}_\Lambda = \sum_{jk} |P_j\rangle\rangle\langle\langle P_j|\hat{\mathcal{O}}_\Lambda|P_k\rangle\rangle\langle\langle P_k| \tag{4}$$

* These authors contributed equally to this work.
Corresponding author: philipp.vetter(at)uni-ulm.de

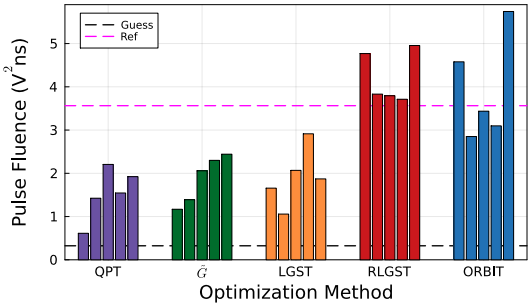

FIG. 1. Fluence of the optimized pulses. We perform five optimization runs per method shown in the x-axis. The fluence of the final optimized pulse is shown by the height of the individual bars. The black dashed line corresponds to the fluence of the guess pulse and the magenta one to the fluence of the reference pulse.

with $\langle\langle P_j|\hat{\mathcal{O}}_\Lambda|P_k\rangle\rangle = \mathrm{tr}\{P_j\Lambda(P_k)\}$. In our case, the linear map is simply given by the corresponding unitary pulse gate, $\Lambda(P_k) = UP_kU^\dagger$.
A measurement of a POVM $\langle\langle E|$ of the action of the gate G on the initial state $|\rho\rangle\rangle$ is then given by

$$p_G = \langle\langle E|G|\rho\rangle\rangle. \tag{5}$$

II. FLUENCE

To better understand why certain methods achieve significantly higher and consistent gains than others, we calculate the fluence of our optimized pulses. The fluence is given by

$$\Gamma = \int_0^{t_p} \left(a_x^2(t) + a_y^2(t)\right) \mathrm{d}t, \tag{6}$$

with the time-dependent amplitudes $a_x^2(t)$ and $a_y^2(t)$ of Eq. (3) from the main text and the pulse length t_p. While we ensure that at no point any pulse can have an amplitude larger then the reference pulse, the optimized pulse can achieve a higher fluence due to its longer pulse length.
The results for each optimization are shown in Fig. 1, where the height of the bars denote the fluence of the corresponding optimized pulse. For RLGST and ORBIT we observe on average a slightly higher fluence than for the reference pulse, while the fluence of all other methods is located between the one of the reference and the guess pulse. To achieve their enhanced robustness for any investigated method, RLGST and ORBIT thus require a significantly higher fluence than the other methods. The increased fluence seems to be a perquisite for the gate-set's successful application at long time-scales, which is in line with the observations in the main text. The connection between fluence and gate-performance stems from the higher amplitudes allowed for the corresponding pulses. While a low fluence restricts the pulse, a higher amplitude allows for a enhanced robustness with respect to frequency errors as they are suppressed in the effective Rabi frequency $\sqrt{\Omega^2 + \Delta^2}$, with Ω being the applied Rabi frequency (= microwave amplitude) and Δ the detuning.
The optimized pulses of $\tilde{G}$ show a much smaller fluence compared to the reference pulse. Yet, the method shows a significantly higher gain than the reference pulse when evaluated by itself. This makes the method particularly suitable if heating imposes an experimental limitation and the gate-set is to be optimized for specific applications of the gates to arbitrary basis states.

III. MAXIMUM-LIKELIHOOD ESTIMATION

Typically, the estimates provided by LGST are used as starting points for a maximum-likelihood estimation (MLE) to obtain real, physical estimates of the applied gates and states. For such an MLE we take the expectation values p_{ijk} (see Eq. (7) in the main text) measured with LGST and minimize

$$\sum_{ijk}\left(p_{ijk} - \sum_{mnrstu}(\chi_{F_i})_{tu}(\chi_{G_k})_{rs}(\chi_{F_j})_{mn}\,\mathrm{tr}\{EP_tP_rP_m\rho P_nP_sP_u\}\right) \tag{7}$$

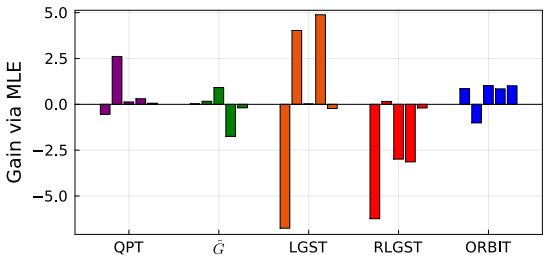

FIG. 2. Evaluation of the different optimization runs through MLE. The abscissa shows the chosen optimization method, the ordinate the achieved gain.

constrained by

$$\begin{aligned} &\sum_{mn} (\chi_G)_{mn} \operatorname{tr}(P_m P_r P_n) - \delta_{0r} = 0\,,\ \forall\, G \in \mathcal{G} \\ &\operatorname{tr}\{\rho\} = 1\,, \\ &\mathbb{1} - E \succcurlyeq 0 \end{aligned} \tag{8}$$

according to Ref. [2]. The process matrix χ_G describes the action of a gate on a given density matrix by

$$\Lambda(\rho) = \sum_{i,j=1}^{d^2} (\chi_G)_{ij}\ P_i \rho P_j \tag{9}$$

with the Pauli operators P_i, P_j. Performing the MLE for 20 repeated measurements of a fixed set of pulses results in a variance of about 1% for the obtained process matrix fidelities. From the LGST estimates of the gates one can calculate estimates for the process matrices, which are then used as a starting point for the minimization. We perform the MLE for the five optimization runs per method. The process matrices resulting from the MLE are compared to the target process matrices to determine their fidelity. Using the sum of the individual fidelities to calculate the optimization gain according to Eq. (2) in the main text leads to the results shown in Fig. 2. We observe a huge variance between different optimization runs for one method, as well as extremely large and small gain values. If we use the target process matrices as a starting point for the minimization such that the LGST estimates do not negatively influence the minimization, we obtain a similar result. This is in stark contrast to all other evaluation methods and is reminiscent of the results from the evaluation with LGST. The measurement errors of our experiment seem to strongly influence the MLE and do not allow us to to clearly distinguish between the gate-set of the guess, reference and optimized pulse. For this reason, the MLE is omitted as evaluation method.

IV. RANDOMIZED BENCHMARKING EXPERIMENTS

We additionally use randomized benchmarking (RB) [3–5] to evaluate our optimized gate-sets performance. An exemplary measurement is shown in Fig. 3, where the gate-set was optimized using ORBIT. Heating limits us to a maximum circuit length of 18 Cliffords and we average over 300 randomized circuits for each circuit length. The survival probability $p_s(m)$ is fitted with

$$p_s(m) = A \cdot q^m + B, \tag{10}$$

where m corresponds to the number of Cliffords. Due to our normalization, all SPAM errors are absorbed by A, leading to $B = 0.5$ by definition. The parameter q is used to calculate the average error per Clifford according to Ref. [4, 5]. For the shown example we obtain an average error rate per Clifford of $r = 0.0258 \pm 0.0007$ with $A = 0.430 \pm 0.008$.

Tab. I shows the average error rates per gate for the optimized gate-sets, i.e. the average error rate per Clifford, as extracted from RB, converted to native gates.

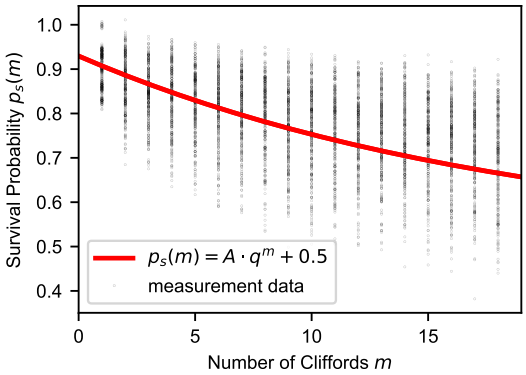

FIG. 3. Randomized benchmarking experiment for an optimized gate-set. The abscissa shows the number of applied Clifford gates m and the ordinate shows the corresponding survival probability $p_s\,(m)$. The data is fitted using a single exponential decay illustrated by the red line.

TABLE I. Average error rate per native gate for the optimized pulses.

opt. method	run 1	run 2	run 3	run 4	run 5
QPT	0.0142 ± 0.0005	0.0105 ± 0.0004	0.0089 ± 0.0004	0.0108 ± 0.0004	0.0100 ± 0.0005
$\tilde{G}$	0.0094 ± 0.0004	0.0105 ± 0.0005	0.0093 ± 0.0004	0.0094 ± 0.0004	0.0092 ± 0.0004
LGST	0.0131 ± 0.0005	0.0163 ± 0.0006	0.0133 ± 0.0005	0.0130 ± 0.0005	0.0127 ± 0.0005
RLGST	0.0088 ± 0.0004	0.0088 ± 0.0004	0.0088 ± 0.0004	0.0118 ± 0.0005	0.0096 ± 0.0004
ORBIT	0.0081 ± 0.0004	0.0091 ± 0.0004	0.0082 ± 0.0004	0.0093 ± 0.0004	0.0095 ± 0.0004

V. OPTIMIZATION METRICS

Tab. II shows the average number of evaluation steps of our optimizations for the selected method. RLGST and ORBIT require notably more evaluation steps than an optimization with QPT, $\tilde{G}$ or LGST. The parameter landscape of those two methods must thus be significantly more complex, requiring more evaluation steps until the optimizer converges according to the set stopping criteria.
In addition, the average duration of one evaluation step for ORBIT and RLGST is also significantly longer than for the other methods. To obtain the corresponding FoM of the two methods, we average over 300 circuits, i.e. we perform a measurement sequence which contains 236 more measurements than e.g. for $\tilde{G}$. These additional measurements increase the overall length of the measurement sequence, leading to a longer uploading time to the AWG and thus to a longer mean evaluation step duration.

TABLE II. Optimization Metrics. The average number of evaluation steps, their average duration and the average total optimization time per method is displayed together with the corresponding uncertainty.

method	mean number of evaluation steps	mean evaluation step duration (s)	mean optimization duration (h)
QPT	872 ± 26	40.524 ± 0.028	10.3 ± 0.4
$\tilde{G}$	880 ± 80	46.74 ± 0.17	14.1 ± 1.8
LGST	723 ± 9	47.25 ± 0.16	11.5 ± 0.8
RLGST	1220 ± 60	66.49 ± 0.25	32 ± 5
ORBIT	1100 ± 100	67.3 ± 0.4	28.0 ± 2.9

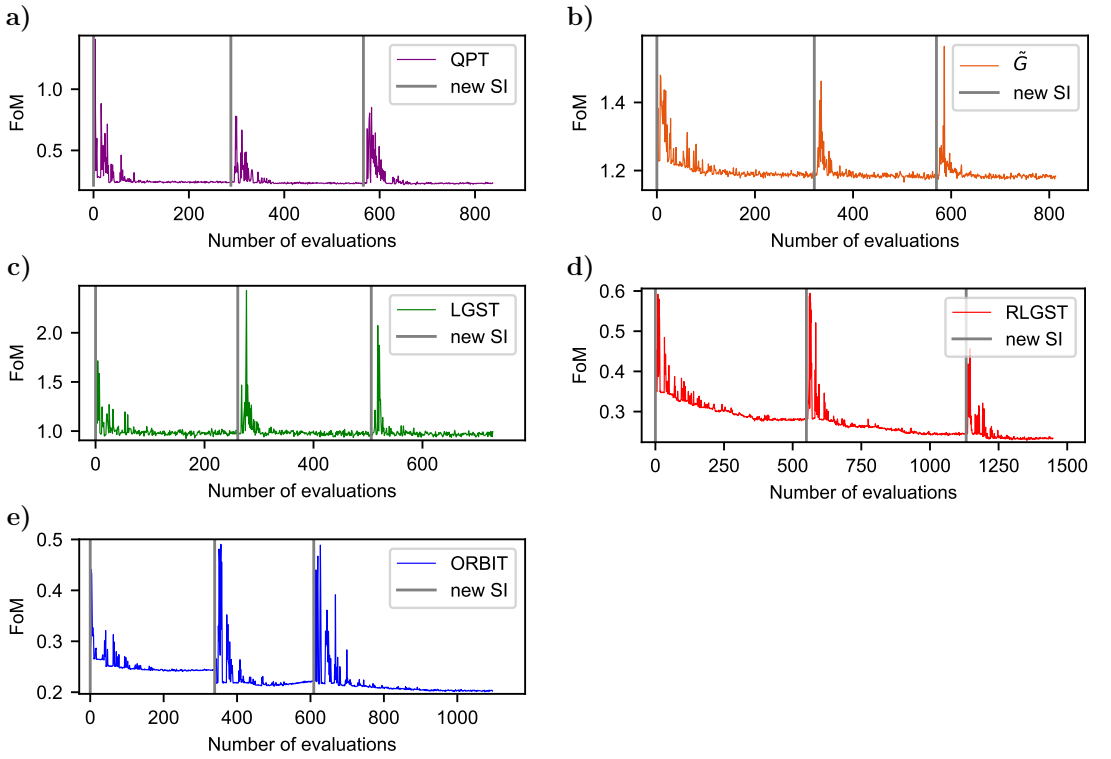

FIG. 4. FoM progression. Exemplary FoM progression during an optimization via **a)** QPT, **b)** $\tilde{G}$, **c)** LGST, **d)** RLGST and **e)** ORBIT. The abscissa shows the number of evaluations and the ordinate the absolute value of the corresponding FoM. The grey lines mark the beginning of a new super-iteration.

VI. FOM PROGRESSION DURING THE OPTIMIZATIONS

Fig. 4 shows the FoM progression during an optimization for the different analysis methods. The optimization via QPT in Fig. 4 a) shows a clear minimization of the FoM. We observe a strong modulation of the FoM during the beginning of a new super-iteration. In addition, the FoM converges very quickly and shows almost no variance between different super-iterations.
For the optimization via $\tilde{G}$ in Fig. 4 b) we also see a clear minimization but the ratio between the final FoM and the one of the initial guess is small compared to the other methods. Depending on the optimization run we can observe a further decrease of the FoM through additional super-iterations.
For LGST in Fig. 4 c) we observe again strong variations of the FoM at the beginning of a super-iteration. The improvement of the FoM is almost within the noise, due to the problems discussed in the main text. QuOCS is well equipped for such a task through the use of re-evaluation steps to correctly determine if the FoM truly improved or not. This allows us to enhance the gate-set's performance even for LGST.
For RLGST in Fig. 4 d) and ORBIT in Fig. 4 e) we observe a very clear minimization of the FoM from the initial guess. The FoM seems to be well defined such that QuOCS can easily improve the pulse shape and converge within the set boundaries. One can see a clear improvement of the FoM through the use of additional super-iterations. As we limit ourselves to three super-iterations due to time-limitations, we cannot exclude that the gains reported in the main text could be much higher for longer optimizations.

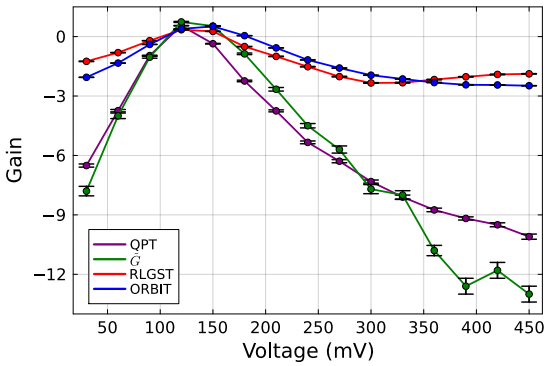

FIG. 5. Measured gain values for the different methods under a sweep of the applied voltage. Each data point shows the mean value of 20 measurements with the corresponding standard deviation.

VII. GAIN UNDER AMPLITUDE CHANGES

Fig. 5 shows the gain of the different evaluation methods for a sweep of the driving field voltage for the rectangular guess pulse. An increase or decrease from the ideal voltages corresponds to an over- or under-rotation of the gate and leads to a fall-off of the gain for each method.
As over- and under-rotations are classified as coherent errors, the steeper descent of QPT and $\tilde{G}$ indicates that these methods are more sensitive to those types of errors than RLGST and ORBIT. Due to the different weighting of these errors in the respective FoM, the curves also show different positions of the maxima.

[1] A. Y. Kitaev, A. H. Shen, and M. N. Vyalyi, Classical and Quantum Computation (American Mathematical Society, USA, 2002).
[2] D. Greenbaum, Introduction to quantum gate set tomography, arXiv preprint arXiv:1509.02921 (2015).
[3] E. Knill et al., Randomized benchmarking of quantum gates, Phys. Rev. A **77**, 012307 (2008).
[4] E. Magesan, J. M. Gambetta, and J. Emerson, Scalable and robust randomized benchmarking of quantum processes, Phys. Rev. Lett. **106**, 180504 (2011).
[5] E. Magesan, J. M. Gambetta, and J. Emerson, Characterizing quantum gates via randomized benchmarking, Phys. Rev. A **85**, 042311 (2012).

4 Conclusion

As single- and few-qubit quantum technologies evolve from research to commercial applications, the need for more precise control is more important then ever. Lower error rates, faster operations and higher sensitivity have become engineering tasks of high interest, both from the theoretical as well as the practical point of view. QOC can be used to tackle such challenges and also help to unlock new approaches and strategies to bring quantum applications to their full potential. In the research presented in this thesis, we have used QOC to enhance the macroscopic polarization of protons in a crystal [1], further developed and unified optimal control algorithms into a convenient software framework [2], and applied it to investigate gate-set evaluation metrics for their suitability in closed-loop optimization [3].

Polarized samples enable drastic improvements of the sensitivity in NMR experiments. We have set ourselves the goal to polarize the proton spins of a naphthalene crystal through DNP transfer from the optically accessible electron spin of deuterated pentacene doped into the host lattice. Manipulation of the electron spin state was performed through a microwave cavity and the polarization was measured via an NMR coil, to which the sample was shuttled after treatment in the cavity. The complex spin environment combined with incomplete knowledge of the true transfer function that results from distortions of the applied microwave field by the cavity as well as other hardware components, led us to choose a closed-loop optimization approach. Starting from a previously successfully applied strategy called ISE, the improved pulses found by the RedCRAB software were studied with the support of a simulated theoretical model. The identification of the relevant features of the optimized transfer pulses resulted in the introduction of the ARISE protocol in order to provide an effective strategy to find and tailor hyperpolarization sequences, also for other systems and setups. Following this scheme, we were able to improve the achieved polarization by 26 % while speeding up the transfer by a factor of 2.6 to reach 98 % of the saturation polarization obtained with the initial linear sweep approach. The optimized pulses were later used by Eichhorn et al. [243] to polarize a sample to 25 % for subsequent use in transfer to other organic molecules. Further development of the theoretical model, with a more refined characterization of the cavity and electronic hardware, including back-actions and distortions of the microwave pulse shapes, is of high interest. The ability for open-loop optimization and investigation of the results could lead to an improvement of the ARISE protocol. With a more detailed understanding of the system dynamics, adaptions to the dCRAB parameters, such as the type of basis functions, could be made and lead to an even faster calibration of the ideal hyperpolarization pulse shapes. Lastly, testing the ARISE protocol on other systems would be an interesting outlook for the future and a comparison to other DNP strategies could highlight its advantages and disadvantages.

Learning from the usage and application of the RedCRAB program in the previous project led to a further development of the optimal control software and the refinement of its features and code structure. With *QuOCS: The Quantum Optimal Control Suite* we have moved away from the communication with a remote server to ensure stable local optimization runs that do not require an internet connection. A more object-oriented and modular structure provides and easier maintenance. In combination with the open-source nature of the code, this can encourage contributions by the community and motivates users to adapt and extend the software with

their own ideas for, e.g., basis functions or search algorithms. We have also included a structure for gradient-based optimization that can also be used together with automatic differentiation. In the publication, we showcase a number of examples using simulations as well as a closed-loop experimental optimization. Features, such as drift compensation and dealing with measurement uncertainty, came in handy especially during the last project discussed in Sec. 3.3.

During the characterization phase of the NV ensemble setup in Ulm, we realized potential issues with the commonly used quantum process tomography for gate analysis. Therefore, we decided to investigate various methods for gate and gate-set evaluation and compared their suitability for closed-loop optimization of quantum operations. The NV ensemble setup with its large sensing volume served as an ideal test-bed with its coherent as well as incoherent and non-Markovian errors. It turns out, that a tailored selection of the evaluation method and its hyperparameters is crucial for gate-set optimization. These parameters, such as the average circuit length of the randomized test-circuits, depend on the type of errors contained in the system and the intended application scenario of the optimized gates. It would be very interesting to repeat the analysis with other samples with, e.g., a smaller sensing volume or a completely different system. Also, a simulation approach including only specific errors or noise sources could be used to investigate these effects on the different FoMs in more detail. Furthermore, even more sophisticated gate-set tomography methods should be investigated for their applicability in closed-loop optimal control.

In summary, this thesis highlights some of the most important ingredients for effective closed-loop QOC. The control algorithm alone is not enough to produce an optimal solution, but some additional design choices in the framework surrounding the control approach have to be made. Learning from the parameter landscape of the control parameters and dynamically adapting the control strategy, i.e. the search method or basis expansion function of the dCRAB method, could lead to an overall faster convergence and better optimization results. But also the control objective itself has to be suited to the problem to be solved. A simple contrast optimization of a π-pulse for population inversion does not necessarily act as a well functioning gate if applied on different states of the system. Methods that capture the properties of the intended target well, but are still experimentally feasible and fast enough to be economical, are needed. The last ingredient is the awareness that QOC is not a magical machine that always produces the best solutions automatically. To unlock its full potential, one has to learn from the results and use them to their advantage, here shown in the form of better guess inputs and adaption of the control strategy.

References

[1] A. Marshall et al. "Macroscopic hyperpolarization enhanced with quantum optimal control". In: *Phys. Rev. Res.* 4.4 (2022), p. 043179. DOI: 10.1103/PhysRevResearch.4.043179.

[2] M. Rossignolo et al. "QuOCS: The quantum optimal control suite". In: *Computer Physics Communications* 291 (2023), p. 108782. DOI: https://doi.org/10.1016/j.cpc.2023.108782.

[3] P. J. Vetter et al. "Gate-set evaluation metrics for closed-loop optimal control on nitrogen-vacancy center ensembles in diamond". In: *npj Quantum Information* 10.1 (2024), p. 96. DOI: 10.1038/s41534-024-00893-y.

[4] IBM. *The hardware and software for the era of quantum utility is here.* https://www.ibm.com/quantum/blog/quantum-roadmap-2033. Accessed: 2024/04/24.

[5] Nature 624, 238 (2023). *IBM releases first-ever 1,000-qubit quantum chip.* https://doi.org/10.1038/d41586-023-03854-1. Accessed: 2024/04/24.

[6] F. Arute et al. "Quantum supremacy using a programmable superconducting processor". In: *Nature* 574.7779 (2019), pp. 505–510. DOI: 10.1038/s41586-019-1666-5.

[7] H.-S. Zhong et al. "Quantum computational advantage using photons". In: *Science* 370.6523 (2020), pp. 1460–1463. DOI: 10.1126/science.abe8770. eprint: https://www.science.org/doi/pdf/10.1126/science.abe8770.

[8] L. S. Madsen et al. "Quantum computational advantage with a programmable photonic processor". In: *Nature* 606.7912 (2022), pp. 75–81. DOI: 10.1038/s41586-022-04725-x.

[9] A. D. King et al. *Computational supremacy in quantum simulation.* 2024. arXiv: 2403.00910 [quant-ph].

[10] P. W. Shor. "Polynomial-Time Algorithms for Prime Factorization and Discrete Logarithms on a Quantum Computer". In: *SIAM Review* 41.2 (1999), pp. 303–332. DOI: 10.1137/S0036144598347011. eprint: https://doi.org/10.1137/S0036144598347011.

[11] J. Ding, G. Spallitta, and R. Sebastiani. "Effective prime factorization via quantum annealing by modular locally-structured embedding". In: *Scientific Reports* 14.1 (2024), p. 3518. DOI: 10.1038/s41598-024-53708-7.

[12] P. Thomas, L. Ruscio, O. Morin, and G. Rempe. "Efficient generation of entangled multiphoton graph states from a single atom". In: *Nature* 608.7924 (2022), pp. 677–681. DOI: 10.1038/s41586-022-04987-5.

[13] C. E. Bradley et al. "A Ten-Qubit Solid-State Spin Register with Quantum Memory up to One Minute". In: *Phys. Rev. X* 9.3 (2019), p. 031045. DOI: 10.1103/PhysRevX.9.031045.

[14] A. Omran et al. "Generation and manipulation of Schrödinger cat states in Rydberg atom arrays". In: *Science* 365.6453 (2019), pp. 570–574. DOI: 10.1126/science.aax9743. eprint: https://www.science.org/doi/pdf/10.1126/science.aax9743.

[15] Z. Bao et al. *Schrödinger cats growing up to 60 qubits and dancing in a cat scar enforced discrete time crystal.* 2024. arXiv: 2401.08284 [quant-ph].

[16] IBM. *IBM and Daimler use quantum computer to develop next-gen batteries*. https://www.ibm.com/quantum/blog/next-gen-lithium-sulfur-batteries. Accessed: 2024/04/25.

[17] IonQ. *Improving Battery Chemistry with Quantum Computing*. https://ionq.com/resources/improving-battery-chemistry-with-quantum-computing. Accessed: 2024/04/25.

[18] Hyundai. *IonQ and Hyundai Motor partner to use Quantum Computing to advance effectiveness of Next-Gen Batteries*. https://www.hyundai.news/eu/articles/press-releases/ionq-and-hyundai-partner-to-use-quantum-computing-to-advance-effectiveness-of-next-gen-batteries.html. Accessed: 2024/04/25.

[19] J. E. Rice et al. "Quantum computation of dominant products in lithium–sulfur batteries". In: *The Journal of Chemical Physics* 154.13 (2021). DOI: 10.1063/5.0044068.

[20] Bosch. *Bosch Quantum Sensing*. https://www.bosch-quantumsensing.com/. Accessed: 2024/04/25.

[21] Bosch. *Quantum technologies: Bosch aims to use sensors to take a leading position*. https://www.bosch-presse.de/pressportal/de/en/quantum-technologies-bosch-aims-to-use-sensors-to-take-a-leading-position-258816.html. Accessed: 2024/04/25.

[22] T. Stollenwerk, E. Lobe, and M. Jung. "Flight Gate Assignment with a Quantum Annealer". In: *Quantum Technology and Optimization Problems*. Ed. by S. Feld and C. Linnhoff-Popien. Cham: Springer International Publishing, 2019, pp. 99–110.

[23] D. Willsch et al. "Benchmarking Advantage and D-Wave 2000Q quantum annealers with exact cover problems". In: *Quantum Information Processing* 21.4 (2022), p. 141. DOI: 10.1007/s11128-022-03476-y.

[24] A. Irbäck, L. Knuthson, S. Mohanty, and C. Peterson. "Folding lattice proteins with quantum annealing". In: *Phys. Rev. Res.* 4.4 (2022), p. 043013. DOI: 10.1103/PhysRevResearch.4.043013.

[25] A. Robert, P. K. Barkoutsos, S. Woerner, and I. Tavernelli. "Resource-efficient quantum algorithm for protein folding". In: *npj Quantum Information* 7.1 (2021), p. 38. DOI: 10.1038/s41534-021-00368-4.

[26] S. Woerner and D. J. Egger. "Quantum risk analysis". In: *npj Quantum Information* 5.1 (2019), p. 15. DOI: 10.1038/s41534-019-0130-6.

[27] R. Orús, S. Mugel, and E. Lizaso. "Quantum computing for finance: Overview and prospects". In: *Reviews in Physics* 4 (2019), p. 100028. DOI: https://doi.org/10.1016/j.revip.2019.100028.

[28] N. Stamatopoulos et al. "Option Pricing using Quantum Computers". In: *Quantum* 4 (2020), p. 291. DOI: 10.22331/q-2020-07-06-291.

[29] Y.-J. Chang, W.-T. Wang, H.-Y. Chen, S.-W. Liao, and C.-R. Chang. "A novel approach for quantum financial simulation and quantum state preparation". In: *Quantum Machine Intelligence* 6.1 (2024), p. 24. DOI: 10.1007/s42484-024-00160-5.

[30] C. H. Bennett, F. Bessette, G. Brassard, L. Salvail, and J. Smolin. "Experimental quantum cryptography". In: *Journal of Cryptology* 5.1 (1992), pp. 3–28. DOI: 10.1007/BF00191318.

[31] N. Gisin, G. Ribordy, W. Tittel, and H. Zbinden. "Quantum cryptography". In: *Rev. Mod. Phys.* 74.1 (2002), pp. 145–195. DOI: 10.1103/RevModPhys.74.145.

[32] S. Pirandola et al. "Advances in quantum cryptography". In: *Adv. Opt. Photon.* 12.4 (2020), pp. 1012–1236. DOI: 10.1364/AOP.361502.

[33] J. W. Webb et al. *Experimental anonymous quantum conferencing*. 2023. arXiv: 2311.14158 [quant-ph].

[34] S. Zaiser et al. "Enhancing quantum sensing sensitivity by a quantum memory". In: *Nature Communications* 7.1 (2016), p. 12279. DOI: 10.1038/ncomms12279.

[35] C. L. Degen, F. Reinhard, and P. Cappellaro. "Quantum sensing". In: *Rev. Mod. Phys.* 89.3 (2017), p. 035002. DOI: 10.1103/RevModPhys.89.035002.

[36] J. M. Boss, K. S. Cujia, J. Zopes, and C. L. Degen. "Quantum sensing with arbitrary frequency resolution". In: *Science* 356.6340 (2017), pp. 837–840. DOI: 10.1126/science.aam7009. eprint: https://www.science.org/doi/pdf/10.1126/science.aam7009.

[37] N. Aslam et al. "Quantum sensors for biomedical applications". In: *Nature Reviews Physics* 5.3 (2023), pp. 157–169. DOI: 10.1038/s42254-023-00558-3.

[38] Q.ANT. *Quantensensor verbessert Prozess- und Qualitätskontrolle durch Partikelanalyse in Echtzeit*. https://qant.com/de/pressemitteilung/quantensensor-verbessert-prozess-und-qualitaetskontrolle-durch-partikelanalyse-in-echtzeit/. Accessed: 2024/06/05.

[39] V. Giovannetti, S. Lloyd, and L. Maccone. "Quantum Metrology". In: *Phys. Rev. Lett.* 96.1 (2006), p. 010401. DOI: 10.1103/PhysRevLett.96.010401.

[40] V. Giovannetti, S. Lloyd, and L. Maccone. "Advances in quantum metrology". In: *Nature Photonics* 5.4 (2011), pp. 222–229. DOI: 10.1038/nphoton.2011.35.

[41] Y. L. Len, T. Gefen, A. Retzker, and J. Kołodyński. "Quantum metrology with imperfect measurements". In: *Nature Communications* 13.1 (2022), p. 6971. DOI: 10.1038/s41467-022-33563-8.

[42] A. G. J. MacFarlane, J. P. Dowling, and G. J. Milburn. "Quantum technology: the second quantum revolution". In: *Philosophical Transactions of the Royal Society of London. Series A: Mathematical, Physical and Engineering Sciences* 361.1809 (2003), pp. 1655–1674. DOI: 10.1098/rsta.2003.1227. eprint: https://royalsocietypublishing.org/doi/pdf/10.1098/rsta.2003.1227.

[43] H. E. Brandt. "Qubit devices and the issue of quantum decoherence". In: *Progress in Quantum Electronics* 22.5 (1999), pp. 257–370. DOI: https://doi.org/10.1016/S0079-6727(99)00003-8.

[44] M. Schlosshauer. "Quantum decoherence". In: *Physics Reports* 831 (2019). Quantum decoherence, pp. 1–57. DOI: https://doi.org/10.1016/j.physrep.2019.10.001.

[45] Q Ansel et al. “Introduction to theoretical and experimental aspects of quantum optimal control”. In: *Journal of Physics B: Atomic, Molecular and Optical Physics* 57.13 (2024), p. 133001. DOI: 10.1088/1361-6455/ad46a5.

[46] H. A. Fürst et al. “Controlling the transport of an ion: classical and quantum mechanical solutions”. In: *New Journal of Physics* 16.7 (2014), p. 075007. DOI: 10.1088/1367-2630/16/7/075007.

[47] C. P. Koch et al. “Quantum optimal control in quantum technologies. Strategic report on current status, visions and goals for research in Europe”. In: *EPJ Quantum Technology* 9.1 (2022), p. 19. DOI: 10.1140/epjqt/s40507-022-00138-x.

[48] N. Wittler et al. “Integrated Tool Set for Control, Calibration, and Characterization of Quantum Devices Applied to Superconducting Qubits”. In: *Phys. Rev. Appl.* 15.3 (2021), p. 034080. DOI: 10.1103/PhysRevApplied.15.034080.

[49] G. Galilei. *Discorsi e dimostrazioni matematiche intorno a due nuove scienze*. 1638.

[50] J. Bernoulli. “Problema novum ad cujus solutionem Mathematici invitantur”. In: *Acta Eruditorum* 15 (1696), p. 269.

[51] I. Newton. “De ratione temporis quo grave labitur per rectam data duo puncta conjungentem, ad tempus brevissimum quo, vi gravitatis, transit ab horum uno ad alterum per arcum cycloidis”. In: *Philosophical Transactions of the Royal Society of London* 19.225 (1697), pp. 424–425. DOI: 10.1098/rstl.1695.0074.

[52] G.-W. Leibniz. “De ratione temporis quo grave labitur per rectam data duo puncta conjungentem, ad tempus brevissimum quo, vi gravitatis, transit ab horum uno ad alterum per arcum cycloidis”. In: *Acta Eruditorum* 19 (1697), 201–205.

[53] M. de l’Hôpital. “Domini Marchionis Hospitalii solutio problematis de linea celerrimi descensus”. In: *Acta Eruditorum* 19 (1697), pp. 217–220.

[54] M. R. Lam et al. “Demonstration of Quantum Brachistochrones between Distant States of an Atom”. In: *Phys. Rev. X* 11.1 (2021), p. 011035. DOI: 10.1103/PhysRevX.11.011035.

[55] R. V. Gamkrelidze. “Discovery of the Maximum Principle”. In: *Journal of Dynamical and Control Systems* 5 (1999), pp. 437–451.

[56] H.-P. Breuer and F. Petruccione. *The Theory of Open Quantum Systems*. 2006. DOI: 10.1093/acprof:oso/9780199213900.001.0001.

[57] J. P. Palao and R. Kosloff. “Optimal control theory for unitary transformations”. In: *Phys. Rev. A* 68.6 (2003), p. 062308. DOI: 10.1103/PhysRevA.68.062308.

[58] P. Rembold et al. “Introduction to quantum optimal control for quantum sensing with nitrogen-vacancy centers in diamond”. In: *AVS Quantum Science* 2.2 (2020), p. 024701. DOI: 10.1116/5.0006785. eprint: https://pubs.aip.org/avs/aqs/article-pdf/doi/10.1116/5.0006785/19738886/024701_1_online.pdf.

[59] M. M. Müller, R. S. Said, F. Jelezko, T. Calarco, and S. Montangero. “One decade of quantum optimal control in the chopped random basis”. In: *Reports on Progress in Physics* 85.7 (2022), p. 076001. DOI: 10.1088/1361-6633/ac723c.

[60] R. Kaubruegger, D. V. Vasilyev, M. Schulte, K. Hammerer, and P. Zoller. "Quantum Variational Optimization of Ramsey Interferometry and Atomic Clocks". In: *Phys. Rev. X* 11.4 (2021), p. 041045. DOI: 10.1103/PhysRevX.11.041045.

[61] T.-X. Zheng et al. "Preparation of metrological states in dipolar-interacting spin systems". In: *npj Quantum Information* 8.1 (2022), p. 150. DOI: 10.1038/s41534-022-00667-4.

[62] F. Motzoi, J. M. Gambetta, P. Rebentrost, and F. K. Wilhelm. "Simple Pulses for Elimination of Leakage in Weakly Nonlinear Qubits". In: *Phys. Rev. Lett.* 103.11 (2009), p. 110501. DOI: 10.1103/PhysRevLett.103.110501.

[63] J. M. Gambetta, F. Motzoi, S. T. Merkel, and F. K. Wilhelm. "Analytic control methods for high-fidelity unitary operations in a weakly nonlinear oscillator". In: *Phys. Rev. A* 83.1 (2011), p. 012308. DOI: 10.1103/PhysRevA.83.012308.

[64] F. Motzoi and F. K. Wilhelm. "Improving frequency selection of driven pulses using derivative-based transition suppression". In: *Phys. Rev. A* 88.6 (2013), p. 062318. DOI: 10.1103/PhysRevA.88.062318.

[65] S. Shi, A. Woody, and H. Rabitz. "Optimal control of selective vibrational excitation in harmonic linear chain molecules". In: *The Journal of Chemical Physics* 88.11 (1988), pp. 6870–6883. DOI: 10.1063/1.454384. eprint: https://pubs.aip.org/aip/jcp/article-pdf/88/11/6870/18970162/6870_1_online.pdf.

[66] A. P. Peirce, M. A. Dahleh, and H. Rabitz. "Optimal control of quantum-mechanical systems: Existence, numerical approximation, and applications". In: *Phys. Rev. A* 37.12 (1988), pp. 4950–4964. DOI: 10.1103/PhysRevA.37.4950.

[67] R. Kosloff, S. Rice, P. Gaspard, S. Tersigni, and D. Tannor. "Wavepacket dancing: Achieving chemical selectivity by shaping light pulses". In: *Chemical Physics* 139.1 (1989), pp. 201–220. DOI: https://doi.org/10.1016/0301-0104(89)90012-8.

[68] R. Kosloff, A. D. Hammerich, and D. Tannor. "Excitation without demolition: Radiative excitation of ground-surface vibration by impulsive stimulated Raman scattering with damage control". In: *Phys. Rev. Lett.* 69.15 (1992), pp. 2172–2175. DOI: 10.1103/PhysRevLett.69.2172.

[69] D. J. Tannor, V. Kazakov, and V. Orlov. "Control of Photochemical Branching: Novel Procedures for Finding Optimal Pulses and Global Upper Bounds". In: *Time-Dependent Quantum Molecular Dynamics*. Ed. by J. Broeckhove and L. Lathouwers. Boston, MA: Springer US, 1992, pp. 347–360. DOI: 10.1007/978-1-4899-2326-4_24.

[70] A. I. Konnov and V. F. Krotov. "On global methods for the successive improvement of control processes". In: *Autom. Remote Control* 60.10 (1999), pp. 1427–1436.

[71] S. E. Sklarz and D. J. Tannor. "Loading a Bose-Einstein condensate onto an optical lattice: An application of optimal control theory to the nonlinear Schrödinger equation". In: *Phys. Rev. A* 66.5 (2002), p. 053619. DOI: 10.1103/PhysRevA.66.053619.

[72] N. Khaneja, T. Reiss, C. Kehlet, T. Schulte-Herbrüggen, and S. J. Glaser. "Optimal control of coupled spin dynamics: design of NMR pulse sequences by gradient ascent algorithms". In: *Journal of Magnetic Resonance* 172.2 (2005), pp. 296–305. DOI: https://doi.org/10.1016/j.jmr.2004.11.004.

[73] K. Kobzar, S. Ehni, T. E. Skinner, S. J. Glaser, and B. Luy. "Exploring the limits of broadband 90° and 180° universal rotation pulses". In: *Journal of Magnetic Resonance* 225 (2012), pp. 142–160. DOI: https://doi.org/10.1016/j.jmr.2012.09.013.

[74] P. E. Spindler et al. "Shaped optimal control pulses for increased excitation bandwidth in EPR". In: *Journal of Magnetic Resonance* 218 (2012), pp. 49–58. DOI: https://doi.org/10.1016/j.jmr.2012.02.013.

[75] M. Hirose and P. Cappellaro. "Time-optimal control with finite bandwidth". In: *Quantum Information Processing* 17.4 (2018), p. 88. DOI: 10.1007/s11128-018-1845-6.

[76] F. Motzoi, J. M. Gambetta, S. T. Merkel, and F. K. Wilhelm. "Optimal control methods for rapidly time-varying Hamiltonians". In: *Phys. Rev. A* 84.2 (2011), p. 022307. DOI: 10.1103/PhysRevA.84.022307.

[77] J. P. P. Daniel M. Reich and C. P. Koch. "Optimal control under spectral constraints: enforcing multi-photon absorption pathways". In: *Journal of Modern Optics* 61.10 (2014), pp. 822–827. DOI: 10.1080/09500340.2013.844866. eprint: https://doi.org/10.1080/09500340.2013.844866.

[78] J.-S. Li, J. Ruths, and D. Stefanatos. "A pseudospectral method for optimal control of open quantum systems". In: *The Journal of Chemical Physics* 131.16 (2009), p. 164110. DOI: 10.1063/1.3253796. eprint: https://pubs.aip.org/aip/jcp/article-pdf/doi/10.1063/1.3253796/13578867/164110_1_online.pdf.

[79] J. Ruths and J.-S. Li. "Optimal Control of Inhomogeneous Ensembles". In: *IEEE Transactions on Automatic Control* 57.8 (2012), pp. 2021–2032. DOI: 10.1109/TAC.2012.2195920.

[80] T. Caneva, T. Calarco, and S. Montangero. "Chopped random-basis quantum optimization". In: *Phys. Rev. A* 84.2 (2011), p. 022326. DOI: 10.1103/PhysRevA.84.022326.

[81] P. Doria, T. Calarco, and S. Montangero. "Optimal Control Technique for Many-Body Quantum Dynamics". In: *Phys. Rev. Lett.* 106.19 (2011), p. 190501. DOI: 10.1103/PhysRevLett.106.190501.

[82] A. Pagano, M. M. Müller, T. Calarco, S. Montangero, and P. Rembold. *The Role of Bases in Quantum Optimal Control*. 2024. arXiv: 2405.20889 [quant-ph].

[83] S. Lloyd and S. Montangero. "Information Theoretical Analysis of Quantum Optimal Control". In: *Phys. Rev. Lett.* 113.1 (2014), p. 010502. DOI: 10.1103/PhysRevLett.113.010502.

[84] S. Rosi et al. "Fast closed-loop optimal control of ultracold atoms in an optical lattice". In: *Phys. Rev. A* 88.2 (2013), p. 021601. DOI: 10.1103/PhysRevA.88.021601.

[85] J. Scheuer et al. "Precise qubit control beyond the rotating wave approximation". In: *New Journal of Physics* 16.9 (2014), p. 093022. DOI: 10.1088/1367-2630/16/9/093022.

[86] S. van Frank et al. "Interferometry with non-classical motional states of a Bose–Einstein condensate". In: *Nature Communications* 5.1 (2014), p. 4009. DOI: 10.1038/ncomms5009.

[87] N. Rach, M. M. Müller, T. Calarco, and S. Montangero. "Dressing the chopped-random-basis optimization: A bandwidth-limited access to the trap-free landscape". In: *Phys. Rev. A* 92.6 (2015), p. 062343. DOI: 10.1103/PhysRevA.92.062343.

[88] F. Frank et al. “Autonomous calibration of single spin qubit operations”. In: *npj Quantum Information* 3.1 (2017), p. 48. DOI: 10.1038/s41534-017-0049-8.

[89] F. Hoeb et al. “Amplification of the parametric dynamical Casimir effect via optimal control”. In: *Phys. Rev. A* 96.3 (2017), p. 033851. DOI: 10.1103/PhysRevA.96.033851.

[90] A. Pagano et al. “Error budgeting for a controlled-phase gate with strontium-88 Rydberg atoms”. In: *Phys. Rev. Res.* 4.3 (2022), p. 033019. DOI: 10.1103/PhysRevResearch.4.033019.

[91] R. Heck et al. “Remote optimization of an ultracold atoms experiment by experts and citizen scientists”. In: *Proceedings of the National Academy of Sciences* 115.48 (2018), E11231–E11237. DOI: 10.1073/pnas.1716869115. eprint: https://www.pnas.org/doi/pdf/10.1073/pnas.1716869115.

[92] F. Angaroni et al. “An Optimal Control Framework for the Automated Design of Personalized Cancer Treatments”. In: *Frontiers in Bioengineering and Biotechnology* 8 (2020). DOI: 10.3389/fbioe.2020.00523.

[93] N. Oshnik et al. “Robust magnetometry with single nitrogen-vacancy centers via two-step optimization”. In: *Phys. Rev. A* 106.1 (2022), p. 013107. DOI: 10.1103/PhysRevA.106.013107.

[94] P. T. Grochowski, H. Pichler, C. A. Regal, and O. Romero-Isart. *Quantum control of continuous systems via nonharmonic potential modulation*. 2023. arXiv: 2311.16819 [quant-ph].

[95] J. J. W. H. Sørensen, M. O. Aranburu, T. Heinzel, and J. F. Sherson. “Quantum optimal control in a chopped basis: Applications in control of Bose-Einstein condensates”. In: *Phys. Rev. A* 98.2 (2018), p. 022119. DOI: 10.1103/PhysRevA.98.022119.

[96] S. Machnes, E. Assémat, D. Tannor, and F. K. Wilhelm. “Tunable, Flexible, and Efficient Optimization of Control Pulses for Practical Qubits”. In: *Phys. Rev. Lett.* 120.15 (2018), p. 150401. DOI: 10.1103/PhysRevLett.120.150401.

[97] D. Lucarelli. “Quantum optimal control via gradient ascent in function space and the time-bandwidth quantum speed limit”. In: *Phys. Rev. A* 97.6 (2018), p. 062346. DOI: 10.1103/PhysRevA.97.062346.

[98] A. G. Baydin, B. A. Pearlmutter, A. A. Radul, and J. M. Siskind. “Automatic differentiation in machine learning: a survey”. In: *J. Mach. Learn. Res.* 18.1 (2017), 5595–5637.

[99] JuliaDiff. *Differentiation tools in Julia*. https://juliadiff.org/. Accessed: 2024/06/12.

[100] N. Leung, M. Abdelhafez, J. Koch, and D. Schuster. “Speedup for quantum optimal control from automatic differentiation based on graphics processing units”. In: *Phys. Rev. A* 95.4 (2017), p. 042318. DOI: 10.1103/PhysRevA.95.042318.

[101] M. Abdelhafez, D. I. Schuster, and J. Koch. “Gradient-based optimal control of open quantum systems using quantum trajectories and automatic differentiation”. In: *Phys. Rev. A* 99.5 (2019), p. 052327. DOI: 10.1103/PhysRevA.99.052327.

[102] D. Greenbaum. “Introduction to quantum gate set tomography”. In: *arXiv preprint arXiv:1509.02921* (2015).

[103] J. M. Epstein, A. W. Cross, E. Magesan, and J. M. Gambetta. "Investigating the limits of randomized benchmarking protocols". In: *Phys. Rev. A* 89.6 (2014), p. 062321. DOI: 10.1103/PhysRevA.89.062321.

[104] E. Nielsen et al. "Gate Set Tomography". In: *Quantum* 5 (2021), p. 557. DOI: 10.22331/q-2021-10-05-557.

[105] M. A. Nielsen and I. L. Chuang. *Quantum Computation and Quantum Information: 10th Anniversary Edition*. Cambridge University Press, 2010.

[106] A. Rivas and S. F. Huelga. *Open Quantum Systems: An Introduction*. en. SpringerBriefs in Physics. Berlin, Heidelberg: Springer Berlin Heidelberg, 2012. DOI: 10.1007/978-3-642-23354-8.

[107] F. Marquardt and A. Püttmann. *Introduction to dissipation and decoherence in quantum systems*. 2008. arXiv: 0809.4403 [quant-ph].

[108] R. Schmied. "Quantum state tomography of a single qubit: comparison of methods". In: *Journal of Modern Optics* 63.18 (2016), 1744–1758. DOI: 10.1080/09500340.2016.1142018.

[109] R. Blume-Kohout et al. *Robust, self-consistent, closed-form tomography of quantum logic gates on a trapped ion qubit*. 2013. arXiv: 1310.4492 [quant-ph].

[110] R. Blume-Kohout et al. "Demonstration of qubit operations below a rigorous fault tolerance threshold with gate set tomography". In: *Nature Communications* 8.1 (2017), p. 14485. DOI: 10.1038/ncomms14485.

[111] Y. Gu, R. Mishra, B.-G. Englert, and H. K. Ng. "Randomized Linear Gate-Set Tomography". In: *PRX Quantum* 2.3 (2021), p. 030328. DOI: 10.1103/PRXQuantum.2.030328.

[112] Qiskit Documentation. *Randomized Benchmarking in Qiskit*. https://qiskit.org/ecosystem/experiments/manuals/verification/randomized_benchmarking.html. Accessed: 2023/08/14.

[113] D. C. McKay, S. Sheldon, J. A. Smolin, J. M. Chow, and J. M. Gambetta. "Three-Qubit Randomized Benchmarking". In: *Phys. Rev. Lett.* 122.20 (2019), p. 200502. DOI: 10.1103/PhysRevLett.122.200502.

[114] M. Kononenko et al. "Characterization of control in a superconducting qutrit using randomized benchmarking". In: *Phys. Rev. Res.* 3.4 (2021), p. L042007. DOI: 10.1103/PhysRevResearch.3.L042007.

[115] Z. Li et al. "Error per single-qubit gate below 10^{-4} in a superconducting qubit". In: *npj Quantum Information* 9.1 (2023), p. 111. DOI: 10.1038/s41534-023-00781-x.

[116] J. M. Chow et al. "Universal Quantum Gate Set Approaching Fault-Tolerant Thresholds with Superconducting Qubits". In: *Phys. Rev. Lett.* 109.6 (2012), p. 060501. DOI: 10.1103/PhysRevLett.109.060501.

[117] E. Knill et al. "Randomized benchmarking of quantum gates". In: *Phys. Rev. A* 77.1 (2008), p. 012307. DOI: 10.1103/PhysRevA.77.012307.

[118] J. P. Gaebler et al. "Randomized Benchmarking of Multiqubit Gates". In: *Phys. Rev. Lett.* 108.26 (2012), p. 260503. DOI: 10.1103/PhysRevLett.108.260503.

[119] K. Wright et al. "Benchmarking an 11-qubit quantum computer". In: *Nature Communications* 10.1 (2019), p. 5464. DOI: 10.1038/s41467-019-13534-2.

[120] J.-S. Chen et al. *Benchmarking a trapped-ion quantum computer with 29 algorithmic qubits*. 2023. arXiv: 2308.05071 [id='quant-ph' full_name='Quantum Physics' is_active=True alt_name=None in_archive='quant-ph' is_general=False description=None].

[121] C. A. Ryan, M Laforest, and R Laflamme. "Randomized benchmarking of single- and multi-qubit control in liquid-state NMR quantum information processing". In: *New Journal of Physics* 11.1 (2009), p. 013034. DOI: 10.1088/1367-2630/11/1/013034.

[122] M. Jiang et al. "Experimental benchmarking of quantum control in zero-field nuclear magnetic resonance". In: *Science Advances* 4.6 (2018), eaar6327. DOI: 10.1126/sciadv.aar6327. eprint: https://www.science.org/doi/pdf/10.1126/sciadv.aar6327.

[123] J. Emerson, R. Alicki, and K. Życzkowski. "Scalable noise estimation with random unitary operators". In: *Journal of Optics B: Quantum and Semiclassical Optics* 7.10 (2005), S347. DOI: 10.1088/1464-4266/7/10/021.

[124] C. Dankert. *Efficient Simulation of Random Quantum States and Operators*. Master's Thesis. Available at https://arxiv.org/abs/quant-ph/0512217 (Accessed: 2024/06/21). Waterloo, Ontario, Canada, 2005.

[125] A. A. Mele. "Introduction to Haar Measure Tools in Quantum Information: A Beginner's Tutorial". In: *Quantum* 8 (2024), p. 1340. DOI: 10.22331/q-2024-05-08-1340.

[126] C. Dankert, R. Cleve, J. Emerson, and E. Livine. "Exact and approximate unitary 2-designs and their application to fidelity estimation". In: *Phys. Rev. A* 80.1 (2009), p. 012304. DOI: 10.1103/PhysRevA.80.012304.

[127] D. DiVincenzo, D. Leung, and B. Terhal. "Quantum data hiding". In: *IEEE Transactions on Information Theory* 48.3 (2002), pp. 580–598. DOI: 10.1109/18.985948.

[128] D. Gross, K. Audenaert, and J. Eisert. "Evenly distributed unitaries: On the structure of unitary designs". In: *Journal of Mathematical Physics* 48.5 (2007), p. 052104. DOI: 10.1063/1.2716992. eprint: https://pubs.aip.org/aip/jmp/article-pdf/doi/10.1063/1.2716992/14847389/052104_1_online.pdf.

[129] D. Gottesman. *The Heisenberg Representation of Quantum Computers*. 1998. arXiv: quant-ph/9807006 [id='quant-ph' full_name='Quantum Physics' is_active=True alt_name=None in_archive='quant-ph' is_general=False description=None].

[130] E. Magesan, J. M. Gambetta, and J. Emerson. "Scalable and Robust Randomized Benchmarking of Quantum Processes". In: *Phys. Rev. Lett.* 106.18 (2011), p. 180504. DOI: 10.1103/PhysRevLett.106.180504.

[131] E. Magesan et al. "Efficient Measurement of Quantum Gate Error by Interleaved Randomized Benchmarking". In: *Phys. Rev. Lett.* 109.8 (2012), p. 080505. DOI: 10.1103/PhysRevLett.109.080505.

[132] J. Kelly et al. "Optimal Quantum Control Using Randomized Benchmarking". In: *Phys. Rev. Lett.* 112.24 (2014), p. 240504. DOI: 10.1103/PhysRevLett.112.240504.

[133] A. Hashim et al. “Randomized Compiling for Scalable Quantum Computing on a Noisy Superconducting Quantum Processor”. In: *Phys. Rev. X* 11.4 (2021), p. 041039. DOI: 10.1103/PhysRevX.11.041039.

[134] M. W. Doherty et al. “Theory of the ground-state spin of the NV^- center in diamond”. In: *Phys. Rev. B* 85.20 (2012), p. 205203. DOI: 10.1103/PhysRevB.85.205203.

[135] J. H. N. Loubser and J. A. van Wyk. “Electron spin resonance in the study of diamond”. In: *Reports on Progress in Physics* 41.8 (1978), p. 1201. DOI: 10.1088/0034-4885/41/8/002.

[136] T. Iwasaki et al. “Germanium-Vacancy Single Color Centers in Diamond”. In: *Scientific Reports* 5.1 (2015), p. 12882. DOI: 10.1038/srep12882.

[137] C. D. Clark, H. Kanda, I. Kiflawi, and G. Sittas. “Silicon defects in diamond”. In: *Phys. Rev. B* 51.23 (1995), pp. 16681–16688. DOI: 10.1103/PhysRevB.51.16681.

[138] D. D. Sukachev et al. “Silicon-Vacancy Spin Qubit in Diamond: A Quantum Memory Exceeding 10 ms with Single-Shot State Readout”. In: *Phys. Rev. Lett.* 119.22 (2017), p. 223602. DOI: 10.1103/PhysRevLett.119.223602.

[139] J. N. Becker and E. Neu. “Chapter Seven - The silicon vacancy center in diamond”. In: *Diamond for Quantum Applications Part 1*. Ed. by C. E. Nebel, I. Aharonovich, N. Mizuochi, and M. Hatano. Vol. 103. Semiconductors and Semimetals. Elsevier, 2020, pp. 201–235. DOI: https://doi.org/10.1016/bs.semsem.2020.04.001.

[140] T. Iwasaki et al. “Tin-Vacancy Quantum Emitters in Diamond”. In: *Phys. Rev. Lett.* 119.25 (2017), p. 253601. DOI: 10.1103/PhysRevLett.119.253601.

[141] S. Castelletto and A. Boretti. “Silicon carbide color centers for quantum applications”. In: *Journal of Physics: Photonics* 2.2 (2020), p. 022001. DOI: 10.1088/2515-7647/ab77a2.

[142] S. Castelletto et al. “Silicon Carbide Photonics Bridging Quantum Technology”. In: *ACS Photonics* 9.5 (2022), pp. 1434–1457. DOI: 10.1021/acsphotonics.1c01775.

[143] M. W. Doherty et al. “The nitrogen-vacancy colour centre in diamond”. In: *Physics Reports* 528.1 (2013). The nitrogen-vacancy colour centre in diamond, pp. 1–45. DOI: https://doi.org/10.1016/j.physrep.2013.02.001.

[144] B. Grotz et al. “Charge state manipulation of qubits in diamond”. In: *Nature Communications* 3.1 (2012), p. 729. DOI: 10.1038/ncomms1729.

[145] S. Felton et al. “Hyperfine interaction in the ground state of the negatively charged nitrogen vacancy center in diamond”. In: *Phys. Rev. B* 79.7 (2009), p. 075203. DOI: 10.1103/PhysRevB.79.075203.

[146] N. B. Manson, J. P. Harrison, and M. J. Sellars. “Nitrogen-vacancy center in diamond: Model of the electronic structure and associated dynamics”. In: *Phys. Rev. B* 74.10 (2006), p. 104303. DOI: 10.1103/PhysRevB.74.104303.

[147] J. Harrison, M. Sellars, and N. Manson. “Measurement of the optically induced spin polarisation of N-V centres in diamond”. In: *Diamond and Related Materials* 15.4 (2006). Diamond 2005, pp. 586–588. DOI: https://doi.org/10.1016/j.diamond.2005.12.027.

[148] R. Schirhagl, K. Chang, M. Loretz, and C. L. Degen. "Nitrogen-Vacancy Centers in Diamond: Nanoscale Sensors for Physics and Biology". In: *Annual Review of Physical Chemistry* 65.Volume 65, 2014 (2014), pp. 83–105. DOI: https://doi.org/10.1146/annurev-physchem-040513-103659.

[149] A. Kiel and W. B. Mims. "Linear Electric Field Effect in Paramagnetic Resonance for CdS: Mn^{2+}". In: *Phys. Rev. B* 5.3 (1972), pp. 803–813. DOI: 10.1103/PhysRevB.5.803.

[150] E. Van Oort and M. Glasbeek. "Electric-field-induced modulation of spin echoes of N-V centers in diamond". In: *Chemical Physics Letters* 168.6 (1990), pp. 529–532. DOI: https://doi.org/10.1016/0009-2614(90)85665-Y.

[151] F. Jelezko and J. Wrachtrup. "Single defect centres in diamond: A review". In: *physica status solidi (a)* 203.13 (2006), pp. 3207–3225. DOI: https://doi.org/10.1002/pssa.200671403. eprint: https://onlinelibrary.wiley.com/doi/pdf/10.1002/pssa.200671403.

[152] I. Popa et al. "Energy levels and decoherence properties of single electron and nuclear spins in a defect center in diamond". In: *Phys. Rev. B* 70.20 (2004), p. 201203. DOI: 10.1103/PhysRevB.70.201203.

[153] P. Deines. "The carbon isotopic composition of diamonds: relationship to diamond shape, color, occurrence and vapor composition". In: *Geochimica et Cosmochimica Acta* 44.7 (1980), pp. 943–961. DOI: https://doi.org/10.1016/0016-7037(80)90284-7.

[154] A. P. Nizovtsev et al. "Non-flipping 13C spins near an NV center in diamond: hyperfine and spatial characteristics by density functional theory simulation of the C510[NV]H252 cluster". In: *New Journal of Physics* 20.2 (2018), p. 023022. DOI: 10.1088/1367-2630/aaa910.

[155] A. P. Nizovtsev et al. "Hyperfine Interactions in the NV-13C Quantum Registers in Diamond Grown from the Azaadamantane Seed". In: *Nanomaterials* 11.5 (2021). DOI: 10.3390/nano11051303.

[156] M. Mirdrikvand. "NMR methods for the characterization of mass transport and reaction processes in porous materials". PhD Thesis. Bremen, Germany: Universität Bremen, 2020. DOI: 10.13140/RG.2.2.20311.21925.

[157] P. Neumann. "Towards a room temperature solid state quantum processor — The nitrogen-vacancy center in diamond". PhD Thesis. Stuttgart, Germany: Universität Stuttgart, 2012. DOI: http://dx.doi.org/10.18419/opus-5067.

[158] P Neumann et al. "Excited-state spectroscopy of single NV defects in diamond using optically detected magnetic resonance". In: *New Journal of Physics* 11.1 (2009), p. 013017. DOI: 10.1088/1367-2630/11/1/013017.

[159] A. Dréau et al. "Avoiding power broadening in optically detected magnetic resonance of single NV defects for enhanced dc magnetic field sensitivity". In: *Phys. Rev. B* 84.19 (2011), p. 195204. DOI: 10.1103/PhysRevB.84.195204.

[160] G. Kucsko et al. "Nanometre-scale thermometry in a living cell". In: *Nature* 500.7460 (2013), pp. 54–58. DOI: 10.1038/nature12373.

[161] G. Balasubramanian, A. Lazariev, S. R. Arumugam, and D. wen Duan. "Nitrogen-Vacancy color center in diamond—emerging nanoscale applications in bioimaging and biosensing". In: *Current Opinion in Chemical Biology* 20 (2014). Molecular imaging, pp. 69–77. DOI: https://doi.org/10.1016/j.cbpa.2014.04.014.

[162] Y. Wu, F. Jelezko, M. B. Plenio, and T. Weil. "Diamond Quantum Devices in Biology". In: *Angewandte Chemie International Edition* 55.23 (2016), pp. 6586–6598. DOI: https://doi.org/10.1002/anie.201506556. eprint: https://onlinelibrary.wiley.com/doi/pdf/10.1002/anie.201506556.

[163] M. H. Abobeih et al. "One-second coherence for a single electron spin coupled to a multi-qubit nuclear-spin environment". In: *Nature Communications* 9.1 (2018), p. 2552. DOI: 10.1038/s41467-018-04916-z.

[164] L. Orphal-Kobin et al. "Optically Coherent Nitrogen-Vacancy Defect Centers in Diamond Nanostructures". In: *Phys. Rev. X* 13.1 (2023), p. 011042. DOI: 10.1103/PhysRevX.13.011042.

[165] E Schaefer-Nolte, F. Reinhard, M. Ternes, and K Kern. "A diamond-based scanning probe spin sensor operating at low temperature in ultra-high vacuum". In: *The Review of scientific instruments* 85 (2014), p. 013701. DOI: 10.1063/1.4858835.

[166] C.-C. Fu et al. "Characterization and application of single fluorescent nanodiamonds as cellular biomarkers". In: *Proceedings of the National Academy of Sciences* 104.3 (2007), pp. 727–732. DOI: 10.1073/pnas.0605409104. eprint: https://www.pnas.org/doi/pdf/10.1073/pnas.0605409104.

[167] H. Huang, E. Pierstorff, E. Osawa, and D. Ho. "Active Nanodiamond Hydrogels for Chemotherapeutic Delivery". In: *Nano Letters* 7.11 (2007), pp. 3305–3314. DOI: 10.1021/nl071521o.

[168] J. Aspinall, S. O. Adekanye, I. Brown, A. R. Dhawan, and J. M. Smith. "Instabilities in nanodiamond nitrogen-vacancy centre single photon sources under prolonged pulsed excitation". In: *Opt. Mater. Express* 10.2 (2020), pp. 332–341. DOI: 10.1364/OME.10.000332.

[169] F. Dolde et al. "Electric-field sensing using single diamond spins". In: *Nature Physics* 7.6 (2011), pp. 459–463. DOI: 10.1038/nphys1969.

[170] K. Bian et al. "Nanoscale electric-field imaging based on a quantum sensor and its charge-state control under ambient condition". In: *Nature Communications* 12.1 (2021), p. 2457. DOI: 10.1038/s41467-021-22709-9.

[171] M Hollendonner et al. "Quantum sensing of electric field distributions of liquid electrolytes with NV-centers in nanodiamonds". In: *New Journal of Physics* 25.9 (2023), p. 093008. DOI: 10.1088/1367-2630/acf392.

[172] J. R. Maze et al. "Nanoscale magnetic sensing with an individual electronic spin in diamond". In: *Nature* 455.7213 (2008), pp. 644–647. DOI: 10.1038/nature07279.

[173] J. M. Taylor et al. "High-sensitivity diamond magnetometer with nanoscale resolution". In: *Nature Physics* 4.10 (2008), pp. 810–816. DOI: 10.1038/nphys1075.

[174] G. Balasubramanian et al. "Ultralong spin coherence time in isotopically engineered diamond". In: *Nature Materials* 8.5 (2009), pp. 383–387. DOI: 10.1038/nmat2420.

[175] G. Balasubramanian et al. “Nanoscale imaging magnetometry with diamond spins under ambient conditions”. In: *Nature* 455.7213 (2008), pp. 648–651. DOI: 10.1038/nature07278.

[176] C. L. Degen. “Scanning magnetic field microscope with a diamond single-spin sensor”. In: *Applied Physics Letters* 92.24 (2008), p. 243111. DOI: 10.1063/1.2943282. eprint: https://pubs.aip.org/aip/apl/article-pdf/doi/10.1063/1.2943282/14395578/243111_1_online.pdf.

[177] J. H. Cole and L. C. L. Hollenberg. “Scanning quantum decoherence microscopy”. In: *Nanotechnology* 20.49 (2009), p. 495401. DOI: 10.1088/0957-4484/20/49/495401.

[178] A. Kuwahata et al. “Magnetometer with nitrogen-vacancy center in a bulk diamond for detecting magnetic nanoparticles in biomedical applications”. In: *Scientific Reports* 10.1 (2020), p. 2483. DOI: 10.1038/s41598-020-59064-6.

[179] P. Neumann et al. “High-Precision Nanoscale Temperature Sensing Using Single Defects in Diamond”. In: *Nano Letters* 13.6 (2013), pp. 2738–2742. DOI: 10.1021/nl401216y.

[180] D. M. Toyli, C. F. de las Casas, D. J. Christle, V. V. Dobrovitski, and D. D. Awschalom. “Fluorescence thermometry enhanced by the quantum coherence of single spins in diamond”. In: *Proceedings of the National Academy of Sciences* 110.21 (2013), pp. 8417–8421. DOI: 10.1073/pnas.1306825110. eprint: https://www.pnas.org/doi/pdf/10.1073/pnas.1306825110.

[181] M. W. Doherty et al. “Electronic Properties and Metrology Applications of the Diamond NV^- Center under Pressure”. In: *Phys. Rev. Lett.* 112.4 (2014), p. 047601. DOI: 10.1103/PhysRevLett.112.047601.

[182] H. P. Paudel, G. R. Lander, S. E. Crawford, and Y. Duan. “Sensing at the Nanoscale Using Nitrogen-Vacancy Centers in Diamond: A Model for a Quantum Pressure Sensor”. In: *Nanomaterials* 14.8 (2024). DOI: 10.3390/nano14080675.

[183] J. S. Hodges et al. “Timekeeping with electron spin states in diamond”. In: *Phys. Rev. A* 87.3 (2013), p. 032118. DOI: 10.1103/PhysRevA.87.032118.

[184] M Radtke, E Bernardi, A Slablab, R Nelz, and E Neu. “Nanoscale sensing based on nitrogen vacancy centers in single crystal diamond and nanodiamonds: achievements and challenges”. In: *Nano Futures* 3.4 (2019), p. 042004. DOI: 10.1088/2399-1984/ab5f9b.

[185] T. H. Taminiau, J. Cramer, T. van der Sar, V. V. Dobrovitski, and R. Hanson. “Universal control and error correction in multi-qubit spin registers in diamond”. In: *Nature Nanotechnology* 9.3 (2014), pp. 171–176. DOI: 10.1038/nnano.2014.2.

[186] T. H. Taminiau et al. “Detection and Control of Individual Nuclear Spins Using a Weakly Coupled Electron Spin”. In: *Phys. Rev. Lett.* 109.13 (2012), p. 137602. DOI: 10.1103/PhysRevLett.109.137602.

[187] X. Rong et al. “Experimental fault-tolerant universal quantum gates with solid-state spins under ambient conditions”. In: *Nature Communications* 6.1 (2015), p. 8748. DOI: 10.1038/ncomms9748.

[188] P. Neumann et al. “Single-Shot Readout of a Single Nuclear Spin”. In: *Science* 329.5991 (2010), pp. 542–544. DOI: 10.1126/science.1189075. eprint: https://www.science.org/doi/pdf/10.1126/science.1189075.

[189] I Aharonovich et al. “Diamond-based single-photon emitters”. In: *Reports on Progress in Physics* 74.7 (2011), p. 076501. DOI: 10.1088/0034-4885/74/7/076501.

[190] B. Rodiek et al. “Experimental realization of an absolute single-photon source based on a single nitrogen vacancy center in a nanodiamond”. In: *Optica* 4.1 (2017), pp. 71–76. DOI: 10.1364/OPTICA.4.000071.

[191] Y. Sekiguchi et al. “Geometric entanglement of a photon and spin qubits in diamond”. In: *Communications Physics* 4.1 (2021), p. 264. DOI: 10.1038/s42005-021-00767-1.

[192] B. Hensen et al. “Loophole-free Bell inequality violation using electron spins separated by 1.3 kilometres”. In: *Nature* 526.7575 (2015), pp. 682–686. DOI: 10.1038/nature15759.

[193] F. Rozpedek et al. “Near-term quantum-repeater experiments with nitrogen-vacancy centers: Overcoming the limitations of direct transmission”. In: *Physical Review A* 99.5 (2019), p. 052330. DOI: 10.1103/PhysRevA.99.052330.

[194] S. W. Smith. *The scientist and engineer’s guide to digital signal processing*. en. 2nd edition. OCLC: 493473234. San Diego (Calif.): California Technical Pub., 1999.

[195] P. L. Stanwix et al. “Coherence of nitrogen-vacancy electronic spin ensembles in diamond”. In: *Phys. Rev. B* 82.20 (2010), p. 201201. DOI: 10.1103/PhysRevB.82.201201.

[196] V. M. Acosta et al. “Diamonds with a high density of nitrogen-vacancy centers for magnetometry applications”. In: *Phys. Rev. B* 80.11 (2009), p. 115202. DOI: 10.1103/PhysRevB.80.115202.

[197] P. Balasubramanian et al. “dc Magnetometry with Engineered Nitrogen-Vacancy Spin Ensembles in Diamond”. In: *Nano Letters* 19.9 (2019), pp. 6681–6686. DOI: 10.1021/acs.nanolett.9b02993.

[198] J. F. Barry et al. “Sensitivity optimization for NV-diamond magnetometry”. In: *Rev. Mod. Phys.* 92.1 (2020), p. 015004. DOI: 10.1103/RevModPhys.92.015004.

[199] S. Sengottuvel et al. “Wide-field magnetometry using nitrogen-vacancy color centers with randomly oriented micro-diamonds”. In: *Scientific Reports* 12.1 (2022), p. 17997. DOI: 10.1038/s41598-022-22610-5.

[200] A. J. Healey et al. “Comparison of different methods of nitrogen-vacancy layer formation in diamond for wide-field quantum microscopy”. In: *Phys. Rev. Mater.* 4.10 (2020), p. 104605. DOI: 10.1103/PhysRevMaterials.4.104605.

[201] S. C. Scholten et al. “Widefield quantum microscopy with nitrogen-vacancy centers in diamond: Strengths, limitations, and prospects”. In: *Journal of Applied Physics* 130.15 (2021), p. 150902. DOI: 10.1063/5.0066733. eprint: https://pubs.aip.org/aip/jap/article-pdf/doi/10.1063/5.0066733/20031103/150902_1_5.0066733.pdf.

[202] K. Mizuno et al. “Wide-field diamond magnetometry with millihertz frequency resolution and nanotesla sensitivity”. In: *AIP Advances* 8.12 (2018), p. 125316. DOI: 10.1063/1.5048265. eprint: https://pubs.aip.org/aip/adv/article-pdf/doi/10.1063/1.5048265/12865028/125316_1_online.pdf.

[203] A. Hilberer et al. “Enabling quantum sensing under extreme pressure: Nitrogen-vacancy magnetometry up to 130 GPa”. In: *Phys. Rev. B* 107.22 (2023), p. L220102. DOI: 10.1103/PhysRevB.107.L220102.

[204] D. A. Simpson et al. “Magneto-optical imaging of thin magnetic films using spins in diamond”. In: *Scientific Reports* 6.1 (2016), p. 22797. DOI: 10.1038/srep22797.

[205] J.-P. Tetienne et al. “Quantum imaging of current flow in graphene”. In: *Science Advances* 3.4 (2017), e1602429. DOI: 10.1126/sciadv.1602429. eprint: https://www.science.org/doi/pdf/10.1126/sciadv.1602429.

[206] M. Block et al. “Optically Enhanced Electric Field Sensing Using Nitrogen-Vacancy Ensembles”. In: *Phys. Rev. Appl.* 16.2 (2021), p. 024024. DOI: 10.1103/PhysRevApplied.16.024024.

[207] S. Choi et al. “Observation of discrete time-crystalline order in a disordered dipolar many-body system”. In: *Nature* 543.7644 (2017), pp. 221–225. DOI: 10.1038/nature21426.

[208] J. Choi et al. “Probing Quantum Thermalization of a Disordered Dipolar Spin Ensemble with Discrete Time-Crystalline Order”. In: *Phys. Rev. Lett.* 122.4 (2019), p. 043603. DOI: 10.1103/PhysRevLett.122.043603.

[209] Healthcare in Europe. *14 Tesla: Researchers to build world’s strongest MRI scanner*. https://healthcare-in-europe.com/en/news/14-tesla-mri-strongest-scanner.html. Accessed: 2024/07/12.

[210] J. H. Ardenkjær-Larsen et al. “Increase in signal-to-noise ratio of > 10,000 times in liquid-state NMR”. In: *Proceedings of the National Academy of Sciences* 100.18 (2003), pp. 10158–10163. DOI: 10.1073/pnas.1733835100. eprint: https://www.pnas.org/doi/pdf/10.1073/pnas.1733835100.

[211] J. Kurhanewicz et al. “Analysis of cancer metabolism by imaging hyperpolarized nuclei: prospects for translation to clinical research”. en. In: *Neoplasia* 13.2 (2011), pp. 81–97.

[212] C. von Morze et al. “Simultaneous multiagent hyperpolarized (13)C perfusion imaging”. en. In: *Magn Reson Med* 72.6 (2013), pp. 1599–1609.

[213] T. Eichhorn et al. “Proton polarization above 70triplet states, a first step towards a broadband neutron spin filter”. In: *Nuclear Instruments and Methods in Physics Research Section A: Accelerators, Spectrometers, Detectors and Associated Equipment* 754 (2014), pp. 10–14. DOI: https://doi.org/10.1016/j.nima.2014.03.047.

[214] Quan, Yifan, Nekitic, Nemanja, van den Brandt, Ben, and Hautle, Patrick. “A novel broad-band neutron spin filter based on dynamically polarized protons using photo-excited triplet states”. In: *EPJ Web Conf.* 219 (2019), p. 10006. DOI: 10.1051/epjconf/201921910006.

[215] Y. Quan, B. van den Brandt, J. Kohlbrecher, W. Wenckebach, and P. Hautle. “A transportable neutron spin filter”. In: *Nuclear Instruments and Methods in Physics Research Section A: Accelerators, Spectrometers, Detectors and Associated Equipment* 921 (2019), pp. 22–26. DOI: https://doi.org/10.1016/j.nima.2018.12.047.

[216] S. Takada et al. “Polarized proton spin filter for epithermal neutrons based on dynamic nuclear polarization using photo-excited triplet electron spins”. In: *Progress of Theoretical and Experimental Physics* 2020.12 (2020), 123G01. DOI: 10.1093/ptep/ptaa111. eprint: https://academic.oup.com/ptep/article-pdf/2020/12/123G01/35611814/ptaa111.pdf.

[217] W. T. Wenckebach. "The Solid Effect". In: *Applied Magnetic Resonance* 34.3 (2008), pp. 227–235. DOI: 10.1007/s00723-008-0121-9.

[218] S. Kolkowitz, Q. P. Unterreithmeier, S. D. Bennett, and M. D. Lukin. "Sensing Distant Nuclear Spins with a Single Electron Spin". In: *Phys. Rev. Lett.* 109.13 (2012), p. 137601. DOI: 10.1103/PhysRevLett.109.137601.

[219] A. Henstra and W. Wenckebach. "Dynamic nuclear polarisation via the integrated solid effect I: theory". In: *Molecular Physics* 112.13 (2014), pp. 1761–1772. DOI: 10.1080/00268976.2013.861936. eprint: https://doi.org/10.1080/00268976.2013.861936.

[220] T. Eichhorn, B. van den Brandt, P. Hautle, A. Henstra, and T. Wenckebach. "Dynamic nuclear polarisation via the integrated solid effect II: Experiments on naphthalene-h8 doped with pentacene-d14". In: *Molecular Physics* 112.13 (2014), pp. 1773–1782. DOI: 10.1080/00268976.2013.863405. eprint: https://doi.org/10.1080/00268976.2013.863405.

[221] D. van den Heuvel, A. Henstra, T.-S. Lin, J. Schmidt, and W. Wenckebach. "Transient oscillations in pulsed dynamic nuclear polarization". In: *Chemical Physics Letters* 188.3 (1992), pp. 194–200. DOI: https://doi.org/10.1016/0009-2614(92)90008-B.

[222] A. Henstra and W. Wenckebach. "The theory of nuclear orientation via electron spin locking (NOVEL)". In: *Molecular Physics* 106.7 (2008), pp. 859–871. DOI: 10.1080/00268970801998262. eprint: https://www.tandfonline.com/doi/pdf/10.1080/00268970801998262.

[223] S. R. Hartmann and E. L. Hahn. "Nuclear Double Resonance in the Rotating Frame". In: *Phys. Rev.* 128.5 (1962), pp. 2042–2053. DOI: 10.1103/PhysRev.128.2042.

[224] A. Henstra. "The Integrated Solid Effect". Available at https://hyp23.org/assets/hyp23.pdf (Accessed: 2024/07/11). PhD Thesis. Leiden, Netherlands: Rijksuniversiteit te Leiden, 1990.

[225] P. London et al. "Detecting and Polarizing Nuclear Spins with Double Resonance on a Single Electron Spin". In: *Phys. Rev. Lett.* 111.6 (2013), p. 067601. DOI: 10.1103/PhysRevLett.111.067601.

[226] H. Brunner, R. H. Fritsch, and K. H. Hausser. "Notizen: Cross Polarization in Electron Nuclear Double Resonance by Satisfying the Hartmann-Hahn Condition". In: *Zeitschrift für Naturforschung A* 42.12 (1987), pp. 1456–1457. DOI: doi:10.1515/zna-1987-1217.

[227] A. Henstra, P. Dirksen, J. Schmidt, and W. Wenckebach. "Nuclear spin orientation via electron spin locking (NOVEL)". In: *Journal of Magnetic Resonance (1969)* 77.2 (1988), pp. 389–393. DOI: https://doi.org/10.1016/0022-2364(88)90190-4.

[228] J. Scheuer et al. "Optically induced dynamic nuclear spin polarisation in diamond". In: *New Journal of Physics* 18.1 (2016), p. 013040. DOI: 10.1088/1367-2630/18/1/013040.

[229] K. Akasaka. "Spin Diffusion". In: *Encyclopedia of Biophysics*. Ed. by G. C. K. Roberts. Berlin, Heidelberg: Springer Berlin Heidelberg, 2013, pp. 2427–2428. DOI: 10.1007/978-3-642-16712-6_349.

[230] A. Henstra, P. Dirksen, and W. Wenckebach. "Enhanced dynamic nuclear polarization by the integrated solid effect". In: *Physics Letters A* 134.2 (1988), pp. 134–136. DOI: https://doi.org/10.1016/0375-9601(88)90950-4.

[231] C. Zener and R. H. Fowler. "Non-adiabatic crossing of energy levels". In: *Proceedings of the Royal Society of London. Series A, Containing Papers of a Mathematical and Physical Character* 137.833 (1932), pp. 696–702. DOI: 10.1098/rspa.1932.0165. eprint: https://royalsocietypublishing.org/doi/pdf/10.1098/rspa.1932.0165.

[232] E. P. Glasbrenner and W. P. Schleich. "The Landau–Zener formula made simple". In: *Journal of Physics B: Atomic, Molecular and Optical Physics* 56.10 (2023), p. 104001. DOI: 10.1088/1361-6455/acc774.

[233] A. Henstra, T.-S. Lin, J. Schmidt, and W. Wenckebach. "High dynamic nuclear polarization at room temperature". In: *Chemical Physics Letters* 165.1 (1990), pp. 6–10. DOI: https://doi.org/10.1016/0009-2614(90)87002-9.

[234] Q. Chen, I. Schwarz, F. Jelezko, A. Retzker, and M. B. Plenio. "Optical hyperpolarization of ^{13}C nuclear spins in nanodiamond ensembles". In: *Phys. Rev. B* 92.18 (2015), p. 184420. DOI: 10.1103/PhysRevB.92.184420.

[235] J. Scheuer et al. "Robust techniques for polarization and detection of nuclear spin ensembles". In: *Phys. Rev. B* 96.17 (2017), p. 174436. DOI: 10.1103/PhysRevB.96.174436.

[236] A. Brillante and D. P. Craig. "Host and guest emission in pentacene-anthracene mixed crystals". In: *J. Chem. Soc., Faraday Trans. 2* 71.0 (1975), pp. 1457–1472. DOI: 10.1039/F29757101457.

[237] A. Van Strien and J. Schmidt. "An EPR study of the triplet state of pentacene by electron spin-echo techniques and laser flash excitation". In: *Chemical Physics Letters* 70.3 (1980), pp. 513–517. DOI: https://doi.org/10.1016/0009-2614(80)80115-1.

[238] W. Lambert and A. Zewail. "Intersystem crossing rates of pentacene in naphthalene at 1.9 K following single-mode laser excitation". In: *Chemical Physics Letters* 69.2 (1980), pp. 270–274. DOI: https://doi.org/10.1016/0009-2614(80)85061-5.

[239] M. Iinuma et al. "Proton Polarization with Naphthalene Crystals by Integrated Solid Effect on Photoexcited Triplet State". In: *Journal of the Physical Society of Japan* 74.9 (2005), pp. 2622–2630. DOI: 10.1143/JPSJ.74.2622. eprint: https://doi.org/10.1143/JPSJ.74.2622.

[240] D. J. Sloop, H. Yu, T. Lin, and S. I. Weissman. "Electron spin echoes of a photoexcited triplet: Pentacene in p-terphenyl crystals". In: *The Journal of Chemical Physics* 75.8 (1981), pp. 3746–3757. DOI: 10.1063/1.442520. eprint: https://pubs.aip.org/aip/jcp/article-pdf/75/8/3746/18932900/3746_1_online.pdf.

[241] T. Eichhorn, M. Haag, B. van den Brandt, P. Hautle, and W. Wenckebach. "High proton spin polarization with DNP using the triplet state of pentacene-d14". In: *Chemical Physics Letters* 555 (2013), pp. 296–299. DOI: https://doi.org/10.1016/j.cplett.2012.11.007.

[242] T. Eichhorn et al. "An apparatus for pulsed ESR and DNP experiments using optically excited triplet states down to liquid helium temperatures". In: *Journal of Magnetic Resonance* 234 (2013), pp. 58–66. DOI: https://doi.org/10.1016/j.jmr.2013.06.009.

[243] T. R. Eichhorn et al. “Hyperpolarized Solution-State NMR Spectroscopy with Optically Polarized Crystals”. In: *Journal of the American Chemical Society* 144.6 (2022). PMID: 35113568, pp. 2511–2519. DOI: 10.1021/jacs.1c09119. eprint: https://doi.org/10.1021/jacs.1c09119.

[244] H. H. Vallabhapurapu et al. “Fast Coherent Control of a Nitrogen-Vacancy-Center Spin Ensemble Using a $KTaO_3$ Dielectric Resonator at Cryogenic Temperatures”. In: *Phys. Rev. Appl.* 16.4 (2021), p. 044051. DOI: 10.1103/PhysRevApplied.16.044051.

[245] B. Julsgaard and K. Mølmer. “Dynamical evolution of an inverted spin ensemble in a cavity: Inhomogeneous broadening as a stabilizing mechanism”. In: *Phys. Rev. A* 86.6 (2012), p. 063810. DOI: 10.1103/PhysRevA.86.063810.

[246] K. R. Keshari and D. M. Wilson. “Chemistry and biochemistry of 13C hyperpolarized magnetic resonance using dynamic nuclear polarization”. In: *Chem. Soc. Rev.* 43.5 (2014), pp. 1627–1659. DOI: 10.1039/C3CS60124B.

[247] J. Eills et al. “Spin Hyperpolarization in Modern Magnetic Resonance”. In: *Chemical Reviews* 123.4 (2023), pp. 1417–1551. DOI: 10.1021/acs.chemrev.2c00534.

[248] L. T. Kuhn, ed. *Hyperpolarization Methods in NMR Spectroscopy*. en. Vol. 338. Topics in Current Chemistry. Berlin, Heidelberg: Springer Berlin Heidelberg, 2013. DOI: 10.1007/978-3-642-39728-8.

[249] S. Meier, P. Jensen, M. Karlsson, and M. Lerche. “Hyperpolarized NMR Probes for Biological Assays”. en. In: *Sensors* 14.1 (2014), pp. 1576–1597. DOI: 10.3390/s140101576.

[250] M. L. Mazzanti et al. “Distribution of Hyperpolarized Xenon in the Brain Following Sensory Stimulation: Preliminary MRI Findings”. en. In: *PLoS ONE* 6.7 (2011). Ed. by M. W. Brechbiel, e21607. DOI: 10.1371/journal.pone.0021607.

[251] NVISION IMAGING Technologies GmbH. *POLARIS*. https://www.nvision-imaging.com/polaris. Accessed: 2024/08/02.

[252] J. Zoller. “Optimal Quantum Engineering”. PhD Thesis. Ulm, Germany: Universität Ulm, 2018. DOI: 10.18725/OPARU-10199.

[253] H. Hogben, M. Krzystyniak, G. Charnock, P. Hore, and I. Kuprov. “Spinach – A software library for simulation of spin dynamics in large spin systems”. In: *Journal of Magnetic Resonance* 208.2 (2011), pp. 179–194. DOI: https://doi.org/10.1016/j.jmr.2010.11.008.

[254] S. Machnes et al. “Comparing, optimizing, and benchmarking quantum-control algorithms in a unifying programming framework”. In: *Phys. Rev. A* 84.2 (2011), p. 022305. DOI: 10.1103/PhysRevA.84.022305.

[255] J. Sørensen, J. Jensen, T. Heinzel, and J. Sherson. “QEngine: A C++ library for quantum optimal control of ultracold atoms”. In: *Computer Physics Communications* 243 (2019), pp. 135–150. DOI: https://doi.org/10.1016/j.cpc.2019.04.020.

[256] JuliaQuantumControl. *A Julia Framework for Quantum Optimal Control*. https://github.com/JuliaQuantumControl. Accessed: 2024/08/08.

[257] QuTiP - Quantum Toolbox in Python. *Quantum Optimal Control*. https://qutip.readthedocs.io/en/stable/guide/guide-control.html. Accessed: 2024/08/08.

[258] M. H. Goerz et al. “Krotov: A Python implementation of Krotov’s method for quantum optimal control”. In: *SciPost Phys.* 7 (2019), p. 080. DOI: 10.21468/SciPostPhys.7.6.080.

[259] A. S. Roy, K. Pack, N. Wittler, and S. Machnes. *Software tool-set for automated quantum system identification and device bring up*. 2022. arXiv: 2205.04829 [quant-ph].

[260] J. D. Teske, P. Cerfontaine, and H. Bluhm. “qopt: An Experiment-Oriented Software Package for Qubit Simulation and Quantum Optimal Control”. In: *Phys. Rev. Appl.* 17.3 (2022), p. 034036. DOI: 10.1103/PhysRevApplied.17.034036.

[261] Qruise. *We Accelerate your Quantum Hardware*. https://www.qruise.com/. Accessed: 2024/08/08.

[262] Q-CTRL. *Make quantum technology useful*. https://q-ctrl.com/. Accessed: 2024/08/08.

[263] J. Bradbury et al. *JAX: composable transformations of Python+NumPy programs*. Version 0.3.13. 2018.

[264] J. M. Binder et al. “Qudi: a modular python suite for experiment control and data processing”. In: *SoftwareX* 6 (2017), pp. 85–90. DOI: 10.1016/j.softx.2017.02.001.

[265] N. Grimm et al. *Coherent Control of a Long-Lived Nuclear Memory Spin in a Germanium-Vacancy Multi-Qubit Node*. 2024. arXiv: 2409.06313 [quant-ph].

[266] E. Knill, R. Laflamme, and W. H. Zurek. “Resilient Quantum Computation”. In: *Science* 279.5349 (1998), pp. 342–345. DOI: 10.1126/science.279.5349.342. eprint: https://www.science.org/doi/pdf/10.1126/science.279.5349.342.

[267] P. J. Vetter et al. “Zero- and Low-Field Sensing with Nitrogen-Vacancy Centers”. In: *Phys. Rev. Appl.* 17.4 (2022), p. 044028. DOI: 10.1103/PhysRevApplied.17.044028.

[268] I. Rojkov, D. Layden, P. Cappellaro, J. Home, and F. Reiter. “Bias in Error-Corrected Quantum Sensing”. In: *Phys. Rev. Lett.* 128.14 (2022), p. 140503. DOI: 10.1103/PhysRevLett.128.140503.

[269] D. Willsch, M. Nocon, F. Jin, H. De Raedt, and K. Michielsen. “Gate-error analysis in simulations of quantum computers with transmon qubits”. In: *Phys. Rev. A* 96.6 (2017), p. 062302. DOI: 10.1103/PhysRevA.96.062302.

[270] H. Lagemann et al. “Fragility of gate-error metrics in simulation models of flux-tunable transmon quantum computers”. In: *Phys. Rev. A* 108.2 (2023), p. 022604. DOI: 10.1103/PhysRevA.108.022604.

[271] Universität zu Köln. *Corporate Design Logo*. https://kommunikation-marketing.uni-koeln.de/marketing/corporate_design/logo_der_universitaet/index_ger.html. Accessed: 2024/03/12.

Acknowledgements

I would like to thank Tommaso Calarco for giving me the opportunity to work as one of his first PhD students in PGI-8 at Forschungszentum Jülich. His way of having open-minded discussions and asking the relevant questions have helped me focus on what was important in my projects. Secondly, I am grateful to Matthias M. Müller for being my direct advisor on a day-to-day basis and even replying to my e-mails during holidays or on weekends. I also want to thank Felix Motzoi for the valuable discussions and advice on many projects and the feedback and help whenever I was stuck. A big thank you also goes to Phila Rembold and Philipp J. Vetter, who were not only colleagues and collaborators but also friends and supported me with endless discussions, debates, input and a helping hand even beyond our common projects. I enjoyed the work on and development of RedCRAB and QuOCS together with Marco Rossignolo, Phila Rembold, Alastair Marshall and Alica Pagano and am grateful for the time we spent together on workshops and conferences. I also want to send many thanks to my brother, Danny, who supported me in the decision to start the PhD in the first place and I want to thank my parents for their support. Finally, I want to thank the Fighting Comrades for enduring extensive physics disputes on Discord, the Mindhunters for keeping our friendships even years after we started at the university together, and my flatmates in Jülich for keeping me company, also during the COVID lockdown.

Declaration

Hiermit versichere ich an Eides statt, dass ich die vorliegende Dissertation selbstständig und ohne die Benutzung anderer als der angegebenen Hilfsmittel und Literatur angefertigt habe. Alle Stellen, die wörtlich oder sinngemäß aus veröffentlichten und nicht veröffentlichten Werken dem Wortlaut oder dem Sinn nach entnommen wurden, sind als solche kenntlich gemacht. Ich versichere an Eides statt, dass diese Dissertation noch keiner anderen Fakultät oder Universität zur Prüfung vorgelegen hat; dass sie - abgesehen von unten angegebenen Teilpublikationen und eingebundenen Artikeln und Manuskripten - noch nicht veröffentlicht worden ist sowie, dass ich eine Veröffentlichung der Dissertation vor Abschluss der Promotion nicht ohne Genehmigung des Promotionsausschusses vornehmen werde. Die Bestimmungen dieser Ordnung sind mir bekannt. Darüber hinaus erkläre ich hiermit, dass ich die Ordnung zur Sicherung guter wissenschaftlicher Praxis und zum Umgang mit wissenschaftlichem Fehlverhalten der Universität zu Köln gelesen und sie bei der Durchführung der Dissertation zugrundeliegenden Arbeiten und der schriftlich verfassten Dissertation beachtet habe und verpflichte mich hiermit, die dort genannten Vorgaben bei allen wissenschaftlichen Tätigkeiten zu beachten und umzusetzen. Ich versichere, dass die eingereichte elektronische Fassung der eingereichten Druckfassung vollständig entspricht.

Teilpublikationen:

- Alastair Marshall, **Thomas Reisser**, Phila Rembold, Christoph Müller, Jochen Scheuer, Martin Gierse, Tim Eichhorn, Jakob M. Steiner, Patrick Hautle, Tommaso Calarco, Fedor Jelezko, Martin B. Plenio, Simone Montangero , Ilai Schwartz, Matthias M. Müller, Philipp Neumann; "*Macroscopic hyperpolarization enhanced with quantum optimal control*", In: Phys. Rev. Res. 4.4 (2022), p. 043179, DOI: `https://doi.org/10.1103/PhysRevResearch.4.043179`

- Marco Rossignolo, **Thomas Reisser**, Alastair Marshall, Phila Rembold, Alice Pagano, Philipp J. Vetter, Ressa S. Said, Matthias M. Müller, Felix Motzoi, Tommaso Calarco, Fedor Jelezko and Simone Montangero; "*QuOCS: The quantum optimal control suite*", In: Computer Physics Communications 291 (2023), p. 108782, DOI: `https://doi.org/10.1016/j.cpc.2023.108782`

- Philipp J. Vetter, **Thomas Reisser**, Maximilian G. Hirsch, Tommaso Calarco, Felix Motzoi, Fedor Jelezko and Matthias M. Müller; "*Gate-set evaluation metrics for closed-loop optimal control on nitrogen-vacancy center ensembles in diamond*", In: npj Quantum Information 10.1, 96 (2024), DOI: `https://doi.org/10.1038/s41534-024-00893-y`

Datum

Thomas Reisser